FEDERAL UNIVERSITY OF MINAS GERAIS (UFMG)
School of Engineering
Graduate Program in Structural Engineering (PROPEES)

Felipe Pereira dos Santos

SMOOTHED POINT INTERPOLATION METHODS FOR SHEAR-DEFORMABLE BEAMS

Belo Horizonte
2022

Felipe Pereira dos Santos

SMOOTHED POINT INTERPOLATION METHODS FOR SHEAR-DEFORMABLE BEAMS

Master's thesis submitted to the Graduate Program in Structural Engineering (PROPEES) of the School of Engineering at the FEDERAL UNIVERSITY OF MINAS GERAIS (UFMG), in partial fulfillment of the requirements for the master's degree in Structural Engineering

Supervisor: Prof. Dr. Lapo Gori

Co-supervisor: Prof. Dr. Enzo Marino

Belo Horizonte
2022

Santos, Felipe Pereira dos.
S237s Smoothed point interpolation methods for shear- deformable beams [recurso eletrônico] / Felipe Pereira dos Santos. - 2022.
1 recurso online (169 f. : il., color.) : pdf.

Orientador: Lapo Gori.
Coorientador: Enzo Marino.

Dissertação (mestrado) - Universidade Federal de Minas Gerais, Escola de Engenharia.

Apêndices: f. 141-169.

Bibliografia: f. 137-140.

1. Engenharia de estruturas - Teses. 2. Interpolação - Teses. 3. Vigas - Teses. 4. Cisalhamento - Teses. I. Gori, Lapo. II. Marino, Enzo. III. Universidade Federal de Minas Gerais. Escola de Engenharia. IV. Título.

CDU: 624(043)

Ficha catalográfica elaborada pelo bibliotecário Reginaldo César Vital dos Santos CRB/6 2165
Biblioteca Prof. Mário Werneck, Escola de Engenharia da UFMG

UNIVERSIDADE FEDERAL DE MINAS GERAIS

PROGRAMA DE PÓS-GRADUAÇÃO EM ENGENHARIA DE ESTRUTURAS

PROPEEs

UFMG

ATA DA DEFESA DE DISSERTAÇÃO DE MESTRADO EM ENGENHARIA DE ESTRUTURAS Nº: 389 DO ALUNO FELIPE PEREIRA DOS SANTOS.

Às **9:30** horas do dia **29** do mês de **agosto** de **2022**, reuniu-se em ambiente virtual, na Escola de Engenharia da Universidade Federal de Minas Gerais - UFMG, a Comissão Examinadora indicada pelo Colegiado do Programa em **14 de julho de 2022**, para julgar a defesa da Dissertação de Mestrado intitulada **"Smoothed Point Interpolation Methods for Shear-Deformable Beams"**, cuja aprovação é um dos requisitos para a obtenção do Grau de MESTRE EM ENGENHARIA DE ESTRUTURAS na área de ESTRUTURAS.

Abrindo a sessão, o Presidente da Comissão, **Prof. Dr. Lapo Gori**, após dar a conhecer aos presentes o teor das Normas Regulamentares passou a palavra ao candidato para apresentação de seu trabalho. Seguiu-se a argüição pelos examinadores, com a respectiva defesa do candidato. Logo após, a Comissão se reuniu, sem a presença do candidato e do público, para julgamento e expedição do resultado final. Foram atribuídas as seguintes indicações:

Prof. Dr. Lapo Gori - DEES - UFMG (Orientador): aprovado

Prof. Dr. Enzo Marino - DICEA - UNIFI (Coorientador): aprovado

Prof. Dr. Roque Luiz da Silva Pitangueira - DEES - UFMG: aprovado

Prof. Dr. Eduardo de Moraes Barreto Campello - USP: aprovado

Pelas indicações acima, o candidato foi considerado APROVADO, conforme pareceres em anexo.

O resultado final foi comunicado publicamente ao candidato pelo Presidente da Comissão.

Nada mais havendo a tratar, o Presidente encerrou a reunião e lavrou a presente ATA, que será assinada por todos os membros participantes da Comissão Examinadora.

Belo Horizonte, 29 de agosto de 2022.

Observações:

1. A aprovação do candidato na defesa da Dissertação de Mestrado não significa que o mesmo tenha cumprido todos os requisitos necessários para obtenção do Grau de Mestre em Engenharia de Estruturas;
2. Este documento não terá validade sem a assinatura e carimbo do Coordenador do Programa de Pós-Graduação.

Documento assinado eletronicamente por **Lapo Gori**, **Professor do Magistério Superior**, em 29/08/2022, às 12:32, conforme horário oficial de Brasília, com fundamento no art. 5º do Decreto nº 10.543, de 13 de novembro de 2020.

Documento assinado eletronicamente por **Eduardo de Morais Barreto Campello**, **Usuário Externo**, em 29/08/2022, às 14:30, conforme horário oficial de Brasília, com fundamento no art. 5º do Decreto nº 10.543, de 13 de novembro de 2020.

Documento assinado eletronicamente por **Roque Luiz da Silva Pitangueira**, **Professor do Magistério Superior**, em 29/08/2022, às 17:00, conforme horário oficial de Brasília, com fundamento no art. 5º do Decreto nº 10.543, de 13 de novembro de 2020.

Documento assinado eletronicamente por **Enzo Marino**, **Usuário Externo**, em 30/08/2022, às 04:06, conforme horário oficial de Brasília, com fundamento no art. 5º do Decreto nº 10.543, de 13 de novembro de 2020.

A autenticidade deste documento pode ser conferida no site https://sei.ufmg.br/sei/controlador_externo.php?acao=documento_conferir&id_orgao_acesso_externo=0, informando o código verificador **1692614** e o código CRC **F62A5D20**.

Referência: Processo nº 23072.249924/2022-88 SEI nº 1692614

Dedico esse trabalho aos meus pais, Luciene (in memoriam) e Valmir (in memoriam), que fizeram tudo o que podiam, ao seu modo, para oferecer aos seus filhos uma vida melhor. A caminhada é mais difícil quando se perde os pais tão cedo na vida. Mas tento seguir de cabeça erguida, e estou muito feliz em conseguir atingir o mais alto nível de educação da família, graças a vocês.

ACKNOWLEDGEMENTS

Gostaria de agradecer ao meu orientador Lapo Gori, pela dedicação, paciência e disponibilidade durante todo o tempo de mestrado. Agradeço pelo conhecimento compartilhado e por sempre estar disposto e acessível quando precisei. Agradeço também pelas (muitas) correções de texto, e que foram tão necessárias e criteriosas. Espero que este trabalho esteja a altura das suas expectivas. Estou escrevendo essa parte em Português para que pelo menos essa página não seja corrigida (risos).

I am profoundly grateful to my co-advisor Enzo Marino for the very good discussions during our meetings and to dedicate his precious time to enrich this work. Grazie di tutto!

Agradeço aos professores e demais funcionários do Departamento de Engenharia de Estruturas da UFMG. Agradeço também aos colegas de mestrado por todas as dicussões e sofrimentos compartilhados durante nosso processo de formação.

À minha namorada Regilene Pires pelo amor, companheirismo e paciência necessários para me aguentar. E principalmente por entender meus momentos de ausência.

Agradeço também à toda a minha família e amigos. Eu sei que todos torcem por mim e sou muito grato por isso.

To the Brazilian research agency *Conselho Nacional de Desenvolvimento Científico e Tecnológico* (CNPq) for the financial support during my master's degree.

É melhor, muito melhor, contentar-se com a realidade; se ela não é tão brilhante como os sonhos, tem pelo menos a vantagem de existir.

Machado de Assis

A Mão e a Luva (1874)

RESUMO

Esta dissertação de mestrado visa estender a aplicabilidade dos métodos do tipo *smoothed point interpolation* (SPIMs) para vigas deformáveis por cisalhamento. Esses métodos são de uma família de métodos sem malha onde os conceitos de domínios de suavização e formulação fraca-enfraquecida W^2 são introduzidos; seu uso é possibilitado pela extensão da forma fraca-enfraquecida em que se baseiam para as vigas objetos de estudo dessa dissertação. Este trabalho foca em dois modelos de viga, a viga linear de Timoshenko e um modelo geometricamente não linear. Dentre as possibilidades de divisões do domínio nos métodos SPIM, as simulações numéricas foram realizadas utilizando a abordagem baseada em arestas (ES-PIM). Além disso, as chamadas funções de forma αPIM foram investigadas dentro deste *framework*. As simulações da viga Timoshenko foram executadas na plataforma INSANE (INteractive Structural ANalysis Environment), um projeto de código aberto desenvolvido no Departamento de Estruturas da Universidade Federal de Minas Gerais. Os resultados de várias malhas foram comparados com o método dos elementos finitos (MEF) e com soluções analíticas. A abordagem de SPIMs proposta mostrou uma concordância muito boa com as soluções exatas para todos os exemplos de condições de contorno e casos de carga testados. As simulações da viga geometricamente não linear foram realizadas no MATLAB®, o código foi validado e os resultados foram comparados àqueles disponíveis na literatura. Conforme ilustrado neste trabalho, todas as simulações realizadas para o modelo não linear mostraram uma boa concordância com os resultados obtidos por outros autores. Por fim, as soluções numéricas fornecidas pelos SPIMs são livres de travamento (*shear-locking*), ou seja, nenhum tratamento adicional foi necessário para evitar o aparecimento da chamada *rigidez espúria*, como comumente acontece durante as simulações de vigas deformáveis por cisalhamento realizadas pelo método dos elementos finitos.

Palavras-chave: métodos sem malha; métodos de interpolação de pontos suavizados; vigas deformáveis por cisalhamento; viga de Timoshenko; viga geometricamente exata

ABSTRACT

This master's thesis aims to extend the applicability of the smoothed point interpolation methods (SPIMs) to shear-deformable beams. These methods are from a family of meshfree methods where the concepts of smoothing domains and weakened-weak W^2 formulation are introduced; their use is made possible by the extension of the weakened-weak form that they are based on to the case of the target beam models. This work focuses on two beam models, the linear Timoshenko beam and a geometrically nonlinear model. Among the possibilities of domain tessellations in the SPIM methods, the numerical simulations were performed using the edge-based approach (ES-PIM). In addition to that, the so-called αPIM shape functions were investigated within this framework. The simulations of the Timoshenko beam were executed in the INSANE (INteractive Structural ANalysis Environment) platform, an open-source project developed at the Structural Department of the Federal University of Minas Gerais. The results of several meshes were compared with the finite element method (FEM) and analytical solutions. The proposed SPIMs approach shown a very good agreement with the exact solutions for all examples of boundary conditions and load cases. The simulations of the geometrically nonlinear beam were executed in MATLAB®, the code was validated and the results were compared with the ones available in the literature. As illustrated in this work, all simulations performed for the nonlinear model shown a good agreement with the results obtained by other authors. Finally, the numerical solutions provided by the SPIMs are locking free, i.e. no additional treatment was necessary to avoid the *spurious stiffer behaviour*, as commonly happens with FEM during the simulations of shear-deformable beams.

Key-words: meshfree methods; smoothed point interpolation methods (SPIMs); shear-deformable beams; Timoshenko beam; geometrically exact beam

LIST OF FIGURES

LIST OF TABLES

LIST OF ABBREVIATIONS AND ACRONYMS

EFG	Element-Free Galerkin
ES-PIM	Edge-Based Point Interpolation Method
FDM	Finite Difference Method
FEM	Finite Element Method
INSANE	INteractive Structural ANalysis Environment
MLPG	Meshless Local Petrov-Galerkin
NS-PIM	Node-Based Point Interpolation Method
OOP	Object-Oriented Programming
PIM	Point Interpolation Method
RKPM	Reproducing Kernel Particle Method
RPIM	Radial Point Interpolation Method
SPH	Smoothed Particle Hydrodynamics
SPIM	Smoothed Point Interpolation Method
W^2	Weakened-Weak form

LIST OF SYMBOLS

$\boldsymbol{E}$	environment space
SO(3)	space of the rotation tensors
$\boldsymbol{D}$	domain of a body
$\partial\boldsymbol{D}$	boundary of a body
Γ_v	essential boundary for prescribed displacements
Γ_θ	essential boundary for prescribed rotations
Γ_Q	natural boundary for the prescribed shearing forces
Γ_M	natural boundary for the prescribed bending moments
$\boldsymbol{D}_k^S$	k-th smoothing domain
$\partial\boldsymbol{D}_k^S$	boundary of the k-th smoothing domain
v	displacement field
θ	rotation field
γ	shear strain measure
ω	bending strain measure
$a(\bar{\boldsymbol{w}}, \bar{\boldsymbol{u}})$	bilinear form
$f(\bar{\boldsymbol{w}})$	linear functional
φ_0	line of centroids
φ	admissible configurations
$\bar{\boldsymbol{t}}_I$	moving frame
$\bar{\boldsymbol{E}}_I$	reference frame
$\underline{\boldsymbol{\omega}}$	spatial curvature tensor
$\underline{\boldsymbol{\Omega}}$	material curvature tensor
$\bar{\boldsymbol{\omega}}$	spatial curvature vector
$\bar{\boldsymbol{\Omega}}$	material curvature vector
$\bar{\boldsymbol{\gamma}}$	spatial shear strain (account axial and shear deformations)
$\bar{\boldsymbol{\Gamma}}$	material shear strain (account axial and shear deformations)
$\vec{w}$	displacement test function
$\vec{u}$	displacement trial function
$\hat{\mathbf{E}}$	constitutive operator (classic stress/strain relation)
$\underline{\boldsymbol{C}}$	elastic constitutive tensor (material version)
$\underline{\boldsymbol{c}}$	elastic constitutive tensor (spatial version)

$\mathbf{1}$	identity matrix
$\underline{\boldsymbol{\theta}}$	skew-symmetric tensor (spatial version)
$\underline{\boldsymbol{\Theta}}$	skew-symmetric tensor (material version)
$\bar{\boldsymbol{\theta}}$	axial vector associated with $\underline{\boldsymbol{\theta}}$ (spatial version)
$\bar{\boldsymbol{\Theta}}$	axial vector associated with $\underline{\boldsymbol{\Theta}}$ (material version)
$\underline{\boldsymbol{R}}$	rotation tensor
$\boldsymbol{\eta}$	admissible variations
$\bar{\boldsymbol{m}}$	spatial stress measure (moments)
$\bar{\boldsymbol{f}}$	spatial stress measure (forces)
$\bar{\boldsymbol{M}}$	material stress measure (moments)
$\bar{\boldsymbol{N}}$	material stress measure (forces)
$\bar{\boldsymbol{q}}_{\bar{\boldsymbol{f}}}$	applied force per unit of reference arc length
$\bar{\boldsymbol{q}}_{\bar{\boldsymbol{m}}}$	applied moment per unit of reference arc length
$n^{(k)}$	unit normal "vector" field to k-th smoothing domain $\boldsymbol{D}_k^S$
E	Young's modulus
ν	Poisson's ratio
G	shear modulus
k_s	shear correction factor

TABLE OF CONTENTS

CHAPTER 1

INTRODUCTION

The Finite Element Method (FEM) is the most traditional numerical method to solve solid mechanics problems and requires a mesh to create a system of algebraic equations in order to find the nodal unknown variables. Meshfree methods, on the other hand, allow to assemble the system of algebraic equations without the need for a predefined mesh, or using a mesh in a more flexible way (Liu, 2009). An important motivation for the adoption of meshfree methods is to reduce the reliance on the use of "quality" meshes that can be difficult or expensive to create for some practical problems (Liu, 2009).

Many meshfree methods are available in the existing literature: smoothed particle hydrodynamics (SPH), element-free Galerkin (EFG) method, the meshless local Petrov-Galerkin (MLPG) method, reproducing kernel particle method (RKPM), the point interpolation method (PIM), the finite point method, the finite difference method (FDM) with arbitrary irregular grids, local point collocation methods and many others. A comprehensive discussion and applications of meshfree methods are available in Liu (2009). This treatise focuses on the smoothed point interpolation methods (SPIMs). These methods were developed by Liu and his research team (Liu, 2009), they use point interpolation (PIM) and radial point interpolation (RPIM) shape functions and a smoothing technique for the derivatives that appear in the weak form of the problem (see Liu (2009, 2010*a*,*b*), Liu and Zhang (2013)). Such shape functions exhibit desirable properties for solid mechanics applications, such as: linear independence, partition of unity, and Kronecker delta property. They suffer, however, from continuity issues, that do not allow them to fulfill the consistency requirements of the standard Galerkin weak form. Hence, a gradient smoothing technique is used by these methods in order to weaken this compatibility requirement, resulting in a so-called weakened-weak form (Liu, 2008, 2009).

The main aim of this work is to widen the applicability of smoothed point interpolation methods extending them to shear-deformable beam problems. In this treatise, two beam models are considered. The first one is the well-known linear Timoshenko[1] beam. As opposed to the Euler-Bernoulli model, this model takes into account the effect of transverse

[1]This theory was developed by Stephen Prokofievich Timoshenko and his co-author Paul Ehrenfest, however the theory is widely known with the name of the former, instead of Timoshenko-Ehrenfest beam theory or a similar name Elishakoff (2020). As usual, only the name Timoshenko will be used throughout this work to refer to the model.

shear deformation, and there is no direct relationship between the rotation and the derivative of the elastic curve. In addition to that, in the context of the finite element method it requires only C^0 continuity for the approximation function, while the Euler-Bernoulli beam requires C^1 continuity. A number of works investigated the application of meshfree methods to solve the Timoshenko beam problem. Liu and Gu (2002) developed a formulation of the local point interpolation method and local radial point interpolation method for Timoshenko beam problems. Xiao and McCarthy (2003) proposed a meshless method based on subdomain variational formulations and on a local Petrov–Galerkin approximation to solve the Timoshenko model. Panchore et al. (2016) solved a rotating Timoshenko beam free vibration problem using the meshless local Petrov-Galerkin method. Roque et al. (2011) applied the radial basis collocation method to the analysis of Timoshenko nanobeams. Hale (2013) used a meshfree method derived from the element-free Galerkin method for shear-deformable beams and plates.

The second model is the geometrically exact beam discussed by Simo (1985) and Simo and Vu-Quoc (1986) based on the work of Reissner (1972) for plane static problems. Despite being a three-dimensional model, the configurations of the beam are completely described by the motion of the line of centroids and the rotation of its cross-sections. In the first paper, the theory of the geometrically exact beam is derived for statics and dynamics problems, while the second paper addresses the computational aspects employing the finite element method, followed by many numerical simulations. A discussion concerning the update procedure based on the use of quaternions parameters is also illustrated by these authors. Their work was followed by a number of investigations devoted to improve different aspects of the problem formulation and its computational treatment, (see, for example, Geradin and Cardona (1988) and Mäkinen (2007)).

A number of papers also focused on the application of different numerical methods to this model and other geometrically nonlinear beam models. Marino (2016) extended the isogeometric collocation method to the geometrically nonlinear beam proposed by Simo (1985). Tiago and Pimenta (2005) applied a meshfree method, similar to the element-free Galerkin (EFG) method, to the geometrically exact analysis of spacial rods in the beam model discussed in Pimenta and Campello (2003) which is an extension of the model presented in Pimenta and Yojo (1993). He et al. (2019) used a class of meshfree methods known as point interpolation methods (PIM) to solve the intrinsic beam theory proposed by Hodges (1990).

In general, shear-deformable beams suffer from the so-called *shear locking* problem, which leads to undesirable *stiffer* solutions. Different strategies were proposed in the literature to overcome *shear locking* in finite element applications (see, e.g. the book by Oñate (2013)). As it will be shown later in this work, the proposed meshfree method exhibited a locking free behaviour, i.e. no additional treatment is necessary to avoid the *spurious stiffer* behaviour that commonly occurs in FEM simulations of shear-deformable

beams.

1.1 Objectives

The main goal of this master's thesis is to extend the meshless methods belonging to the family of smoothed point interpolation methods to shear-deformable beam problems, being them: (i) the linear Timoshenko beam, and (ii) the geometrically nonlinear beam proposed by Simo (1985) and Simo and Vu-Quoc (1986). This main goal, is composed by the following specific objectives:

- Carry on a fundamental study on the shear-deformable beam theories object of this work
- Derive a *weakened-weak* form for these models
- Discretise the beam models with smoothing domains and create SPIMs shape functions
- Implement the beam models using the SPIMs
- For the linear beam: validate and compare the obtained results with the finite element method and analytical solutions
- For the nonlinear beam: validate and compare the obtained results with those in the existing literature

1.2 Outline

The content of this master's thesis is organised in 8 chapters and five appendices. After this introduction (Chapter 1), in Chapter 2 the target shear-deformable beam models are introduced. In the first section, the basic concepts concerning the linear Timoshenko beam are presented, while the second section addresses the overall theory regarding the geometrically nonlinear beam (Simo, 1985, Simo and Vu-Quoc, 1986). The basic equations and the linearisation procedure considered in the latter are briefly outlined.

A short discussion on the FEM discretisation of the one-dimensional applications addressed in this work is treated in Chapter 3. The *isoparametric* elements for linear and quadratic shape functions are discussed.

In Chapter 4 the smoothed point interpolation methods are discussed considering two-dimensional cases. The concepts regarding domain tessellation, smoothing operation and weakened-weak form are recalled. Chapter 5 contains the main proposal of this work, that is the extension of SPIM formulations to the beam problems object of this study, reinterpreting the concepts illustrated in Chapter 4 for two-dimensional problems.

In Chapter 6 the numerical results concerning the Timoshenko beam are presented. Simulations using three load cases and four boundary conditions were performed with

both the finite element method and smoothed point interpolation methods. Analytical solutions were used to enhance and complement the comparisons.

The numerical results regarding the geometrically exact beam are presented in Chapter 7. The simulations encompass three classic examples, also presented in Simo and Vu-Quoc (1986), to validate the code and illustrate the obtained results by comparisons with the existing literature.

Finally, the main conclusions of this master's thesis are addressed in Chapter 8. In order to ease the reading, some demonstrations and complementary information are left out from the main text and are detailed in the Appendices.

1.3 Tools

In this work, some essential tools were used. The implementation and numerical simulations regarding the Timoshenko beam (see Chapter 6) were performed in INSANE [2], an open-source software based on the object-oriented programming paradigm and developed at the Structural Engineering Department of the Federal University of Minas Gerais. The implementation and numerical simulations regarding the geometrically nonlinear beam (see Chapter 7) were performed in MATLAB®. This text has been prepared in LaTeX, using the editor TeXMaker. The plots have been generated with the Tikz and Pgfplots libraries. Other figures have been prepared and edited with Inkscape.

1.4 Notation

Some standard notations used in this work, especially in Chapter 2 are summarized here. The symbol $\boldsymbol{D} \in \boldsymbol{\mathcal{E}}$ indicates the domain of a body embedded in the three-dimensional Euclidean space. $\boldsymbol{D}_i^S \subset \boldsymbol{D}$ is referred to the *smoothing domain* and it is a subset of the body domain. $\boldsymbol{D}_i^c \subset \boldsymbol{D}$ is referred to as *background cell domain* and it is also a subset of the body domain. In the *spatial configuration*, the lower case symbol $\bar{\boldsymbol{x}}$ represents vectors, while the the lower case symbol $\underline{\boldsymbol{x}}$ represents tensors. In the *material configuration* the upper case symbol $\bar{\boldsymbol{X}}$ represents vectors, while the the upper case symbol $\underline{\boldsymbol{X}}$ represents tensors. The symbol $\underline{\boldsymbol{R}}$ is referred to the *rotation tensor* in the three-dimensional space, a *two-point tensor*. The standard tensor product is expressed by the symbol $\otimes$. The dot product between vectors and the contraction between tensors are denoted by the symbol $\cdot$.

[2] INSANE stands for *INteractive Structural ANalysis Environment System*. For more information the reader may refer to: `http://www.insane.dees.ufmg.br`.

CHAPTER 2

SHEAR-DEFORMABLE BEAMS

In this chapter the two shear-deformable beam models treated on this work are introduced. The first one is the well-known linear Timoshenko beam, while the second is the geometrically exact beam model developed by Simo (1985) and Simo and Vu-Quoc (1986). Although the last model might undergoes large displacements due to its geometrically nonlinear nature, only a linear elastic constitutive behaviour is considered.

2.1 Timoshenko beam

As opposite to the Euler-Bernoulli theory, the Timoshenko beam accounts for the shear contribution on the deformation of the beam. The governing differential equations of the Timoshenko beam rely on the following assumptions:

- the beam axis is initially straight
- there is no elongation along the x-axis
- there is no torsion around the x-axis
- there is a single bending plane, corresponding to one of the principal axes of the cross-sections (i.e symmetrical plane bending)
- the deformations are small
- plane-cross sections that are initially orthogonal to the beam axis remain plane during the deformation of the beam, although not orthogonal to the beam axis

The plane bending problem of the Timoshenko beam is illustrated in Fig. 2.1. The domain of the problem is represented by $\boldsymbol{D} = [0, L]$, where L is the length of the beam, while its boundary $\boldsymbol{\Gamma} \coloneqq \partial \boldsymbol{D}$ is represented by the end-points of the beam.
Its kinematics is characterised by the deflection v and by the rotation θ, both of them functions of the coordinate x, and by the following deformation measures:

$$\gamma \coloneqq \frac{\partial v}{\partial x} - \theta, \qquad \omega \coloneqq \frac{\partial \theta}{\partial x} \tag{2.1}$$

referred to as *shear* and *bending* strains, respectively. In contrast with the Euler-Bernoulli beam theory, the equations above do not establish a direct relationship between the rotation θ and the derivative of the elastic curve $\partial v/\partial x$.

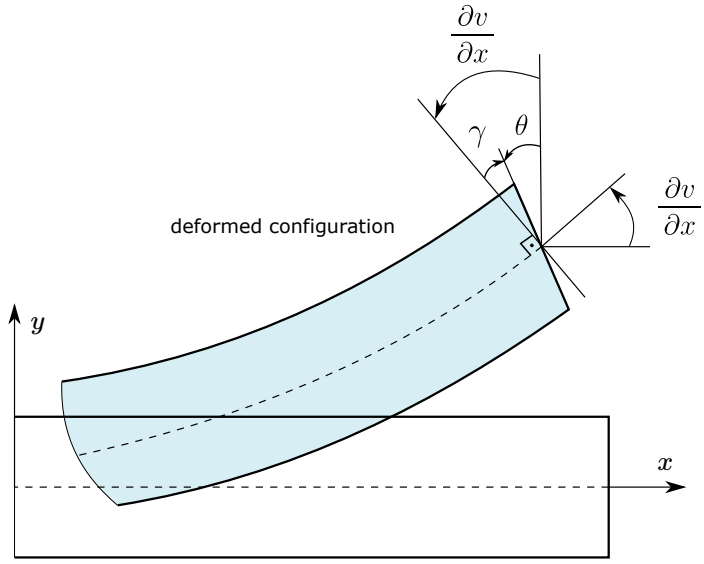

Figure 2.1: Timoshenko beam model. Adapted from Öchsner and Merkel (2018).

The stress measures associated to these deformation measures are the *shear force* Q and the *bending moment* M. Assuming a linear elastic material, this association is given by the following constitutive equations:

$$Q = k_s G A \gamma, \qquad M = EI\omega \tag{2.2}$$

where E is the Young's modulus, G the shear modulus, I the second moment of area of the cross-section, A the area of the cross-section, and k_s the shear correction factor.

Taking into account the assumptions of the model it is possible to show that the strong form of the Timoshenko beam problem is expressed by the following differential equations:

$$\frac{\partial}{\partial x}\left(EI\omega\right) + GA_s\gamma = 0 \tag{2.3}$$

$$\frac{\partial}{\partial x}\left(GA_s\gamma\right) = -q_y(x) \tag{2.4}$$

where q_y is the distributed load in the bending plane of the beam and $A_s = k_s A$ is the shear area of the cross-section. Equation 2.3 is the bending differential equation, while equation 2.4 is known as the shear differential equation. These equations are complemented by the following essential and natural boundary conditions:

$$v = v_\Gamma \text{ on } \Gamma_v, \qquad \theta = \theta_\Gamma \text{ on } \Gamma_\theta \tag{2.5}$$

$$Q = Q_\Gamma \text{ on } \Gamma_Q, \qquad M = M_\Gamma \text{ on } \Gamma_M \tag{2.6}$$

where the Γ_i, with $i = v,\ \theta,\ Q,\ M$, are the parts of the boundary where the different conditions are applied on.

The strong form of the problem expressed in Eqs. (2.3) and (2.4) can be recasted in a weak form[1], that consists in finding the couple $(v, \theta) \in \mathcal{V}(\boldsymbol{D})$ such that

$$a\left((\delta v, \delta\theta), (v, \theta)\right) = f(\delta v, \delta\theta), \quad \forall (\delta v, \delta\theta) \in \mathcal{V}^0(\boldsymbol{D}) \tag{2.7}$$

where a is a bilinear form, f a linear functional, and $\mathcal{V}(\boldsymbol{D})$ and $\mathcal{V}^0(\boldsymbol{D})$ the spaces of *trial* and *test* functions, respectively. The bilinear form a and the linear functional f appearing in the equation above are expressed by

$$a\left((\delta v, \delta\theta), (v, \theta)\right) := \int_0^L \delta\omega \; EI\omega \; dx + \int_0^L \delta\gamma \; GA_s\gamma \; dx \tag{2.8}$$

$$f(\delta v, \delta\theta) := \int_0^L \delta v \; q_y(x) dx + (\delta v \; GA_s\gamma)|_0^L + (\delta\theta \; EI\omega)|_0^L \tag{2.9}$$

where $\delta\gamma$ and $\delta\omega$ are given by

$$\delta\gamma := \frac{\partial \delta v}{\partial x} - \delta\theta, \qquad \delta\omega := \frac{\partial \delta\theta}{\partial x} \tag{2.10}$$

The spaces of *trial* and *test* functions, $\mathcal{V}(\boldsymbol{D})$ and $\mathcal{V}^0(\boldsymbol{D})$ are defined as

$$\mathcal{V}(\boldsymbol{D}) := \{(v, \theta) \in \mathcal{H}(\boldsymbol{D}) \times \mathcal{H}(\boldsymbol{D}) \mid v = v_\Gamma \text{ on } \Gamma_v, \; \theta = \theta_\Gamma \text{ on } \Gamma_\theta\} \tag{2.11}$$

$$\mathcal{V}^0(\boldsymbol{D}) := \{(\delta v, \delta\theta) \in \mathcal{H}(\boldsymbol{D}) \times \mathcal{H}(\boldsymbol{D}) \mid \delta v = 0 \text{ on } \Gamma_v, \; \delta\theta = 0 \text{ on } \Gamma_\theta\} \tag{2.12}$$

where $\mathcal{H}(\boldsymbol{D})$ is the space of square integrable functions with square integrable first derivative over the domain $\boldsymbol{D}$.

In possession of Eq. (2.8) and Eq. (2.9), it is possible to move towards a suitable numerical method that makes use of a weak form, for instance, the finite element method.

2.2 Geometrically exact model

This section focuses on the geometrically exact shear-deformable model developed in Simo (1985) (see also the paper Simo and Vu-Quoc (1986)), a three-dimensional beam model where displacements and rotations are allowed without any restriction in magnitude. The model will be presented in terms of:

- basic kinematics assumptions
- equations of motion
- deformation measures
- constitutive assumptions

The weak form of the problem and its linearisation will then be illustrated, using a proper set of admissible variations. This is a three-dimensional approach and should be

[1] See in Appendix A how can the weak form can be derived from Eq. (2.3) and Eq. (2.4).

regarded as a generalisation of the formulation originally developed by Reissner (1972) for plane static problems. This theory is also referred as the Simo-Reissner beam theory.

2.2.1 Kinematics

The motion of a generic three-dimensional body is given by the following map

$$\boldsymbol{\Phi} : \boldsymbol{D} \times \boldsymbol{\mathcal{T}} \to \boldsymbol{\mathcal{E}} : (p, t) \mapsto \boldsymbol{\Phi}(p, t) \in \boldsymbol{\mathcal{E}} \tag{2.13}$$

where $\boldsymbol{\mathcal{T}}$ is the one-dimensional affine space of time instants, $\boldsymbol{\mathcal{E}}$ is the affine environment space, $\boldsymbol{D}$ is a three-dimensional continuum body in its reference configuration ($\boldsymbol{D} \subset \boldsymbol{\mathcal{E}}$), p is a point belonging to $\boldsymbol{\mathcal{E}}$, and t is the time instant belonging to $\boldsymbol{\mathcal{T}}$. The set $\boldsymbol{\Phi}(\boldsymbol{D}, t)$ is the so-called current configuration of the body.

Due to its geometrical characteristics, the reference configuration $\boldsymbol{D}$ of a beam can be assumed to be composed by two objects: a family of cross sections and a line of centroids $\boldsymbol{I}$. The cross-sections are orthogonal to the line of centroids, and the line of centroids is constituted by the connection of all the centroids of the cross sections. For simplicity, in this work the line of centroids in the reference configuration is assumed to be a straight line, and the cross sections are assumed to be uniform; naturally, one could consider a more complex model with non-uniform cross sections and a line of centroids with an initial curvature in the reference configuration. In the current configuration the line of centroids is a curve defined on the open interval $\boldsymbol{I}$:

$$S \in \boldsymbol{I} \to \varphi_0(S, t) \in \mathbb{R}^3 \tag{2.14}$$

while the cross-sections are characterized by the following unit normal vector field

$$S \in \boldsymbol{I} \to \bar{\boldsymbol{n}}(S, t) \in \mathbb{R}^3 \tag{2.15}$$

The motion of the beam is obtained by assuming the following constraints on the general equation of motions presented in equation 2.13 Simo (1985):

- the cross-sections remain plane in the current (spatial) configuration (in other words, warping effects are not allowed)
- the cross-sections remain undeformed in their plane during the deformation, i.e they do not experience any change in shape or size

These assumptions mean that each cross-section may only rotate as a rigid body and it does not remain necessarily normal to the deformed line of centroids $\varphi_0(S, t)$.

In order to express the equation of motion of the beam model, it is often useful to introduce an *orthonormal frame* at each point of the curve $S \to \varphi_0(S, t)$ which will be referred to as *moving* or *intrinsic* frame: $\{\bar{\boldsymbol{t}}_1(S, t), \bar{\boldsymbol{t}}_2(S, t), \bar{\boldsymbol{n}}(S, t)\}$. This orthonormal frame is such that

$$\begin{array}{ll} \bar{\boldsymbol{t}}_3(S,t) \equiv \bar{\boldsymbol{n}}(S,t) & \bar{\boldsymbol{t}}_3(S,t) = \bar{\boldsymbol{t}}_1(S,t) \times \bar{\boldsymbol{t}}_2(S,t) \\ \|\bar{\boldsymbol{n}}(S,t)\| = 1 & \bar{\boldsymbol{n}}(S,t) \cdot \bar{\boldsymbol{t}}_\Gamma(S,t) = 0 \\ \|\bar{\boldsymbol{t}}_\Gamma(S,t)\| = 1 & \bar{\boldsymbol{t}}_1(S,t) \cdot \bar{\boldsymbol{t}}_2(S,t) = 0 \\ \Gamma = 1,2, & S \in \boldsymbol{I} \subset \mathbb{R} \end{array} \tag{2.16}$$

The admissible configurations of the beam $\varphi : \boldsymbol{A} \times \boldsymbol{I} \to \mathbb{R}^3$ where $\boldsymbol{A} \subset \mathbb{R}^2$ is compact have the explicit form

$$\varphi(\xi_1, \xi_2, S) \equiv \varphi_0(S,t) + \sum_{\Gamma=1}^{2} \xi_\Gamma \bar{\boldsymbol{t}}_\Gamma(S,t) \tag{2.17}$$

where the first term, $\varphi_0(S,t)$, represents the motion of the points lying on the line of centroids, while the other term represents the motion of the points of each cross-section with respect to the centroid.

Initially, any cross-section of the beam belongs to a plane normal to $\bar{\boldsymbol{E}}_3$. During the motion, the cross-sections exhibit a rigid body motion; the rotational component of the motion can be expressed in terms of an orthogonal transformation $S \to \underline{\boldsymbol{R}}(S,t) \in \mathrm{SO}(3)$[2] such that

$$\bar{\boldsymbol{t}}_I(S,t) = \underline{\boldsymbol{R}}(S,t)\bar{\boldsymbol{E}}_I, \quad \boldsymbol{I} = 1,2,3 \tag{2.18}$$

where $\underline{\boldsymbol{R}}(S,t)$ maps the *reference frame* into the *moving frame* as shown in Figure 2.2. In this context the *moving frame* is the reference frame rotated. The derivative of equation 2.18 results in

$$\frac{\partial}{\partial S}\bar{\boldsymbol{t}}_I(S,t) = \underline{\boldsymbol{\omega}}(S,t)\bar{\boldsymbol{t}}_I(S,t) \tag{2.19}$$

where $\underline{\boldsymbol{\omega}}(S,t)$ is a skew-symmetric (spatial) tensor field for each $S \in \boldsymbol{I}$, defined by

$$\underline{\boldsymbol{\omega}}(S,t) \equiv \left[\frac{\partial \underline{\boldsymbol{R}}(S,t)}{\partial S}\right] \underline{\boldsymbol{R}}^T(S,t) \tag{2.20}$$

The tensor $\underline{\boldsymbol{\omega}}(S,t)$ can be expressed in a matrix form relative to the *moving frame* as follows

$$\underline{\boldsymbol{\omega}}(S,t) = -\begin{bmatrix} 0 & \kappa_3(S,t) & -\kappa_2(S,t) \\ -\kappa_3(S,t) & 0 & \kappa_1(S,t) \\ \kappa_2(S,t) & -\kappa_1(S,t) & 0 \end{bmatrix} \tag{2.21}$$

The axial vector[3] field ($S \to \bar{\boldsymbol{\omega}}(S,t) \in \mathbb{R}^3$) associated with the skew-symmetric tensor

[2] This is the special orthogonal Lie group. See more in Geradin and Cardona (1988) and Appendix B.

[3] For every skew-symmetric tensor $\underline{\boldsymbol{T}}$ exists an associated axial vector $\bar{\boldsymbol{t}}$ such that for all vectors $\bar{\boldsymbol{x}}$ the following relation is verified: $\underline{\boldsymbol{T}} \cdot \bar{\boldsymbol{x}} = \bar{\boldsymbol{t}} \times \bar{\boldsymbol{x}}$. Note that the axial vector has the same number of degrees of freedom than the skew-symmetric tensor, (see equation 2.23).

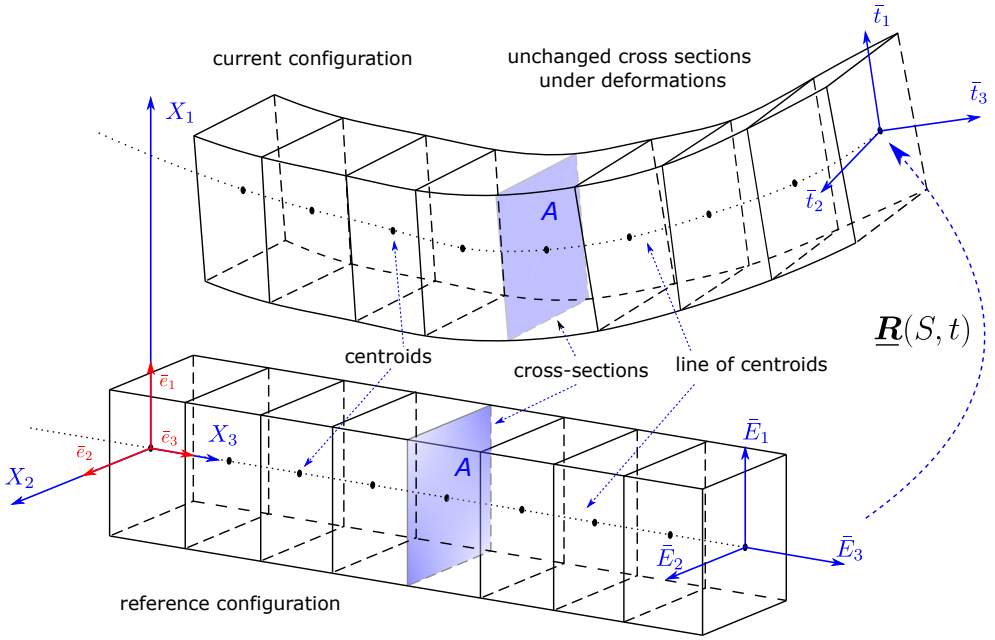

Figure 2.2: Reference and current configurations in a three-dimensional representation; reference frame $\{\bar{\boldsymbol{E}}_1, \bar{\boldsymbol{E}}_2, \bar{\boldsymbol{E}}_3\}$; current frame $\{\bar{\boldsymbol{t}}_1, \bar{\boldsymbol{t}}_2, \bar{\boldsymbol{t}}_3\}$; set of coordinates $\{X_1, X_2, X_3\}$; global reference system $\{\bar{\boldsymbol{e}}_1, \bar{\boldsymbol{e}}_2, \bar{\boldsymbol{e}}_3\}$.

relative to the *moving frame* is now introduced as

$$\frac{\partial}{\partial S}\bar{\boldsymbol{t}}_I(S,t) = \underline{\boldsymbol{\omega}}(S,t)\bar{\boldsymbol{t}}_I = \bar{\boldsymbol{\omega}}(S,t) \times \bar{\boldsymbol{t}}_I(S,t), \quad I = 1,2,3 \tag{2.22}$$

The vector $\bar{\boldsymbol{\omega}}(S,t)$ is referred to the *curvature* of the beam. Now one can write the following equation in a *spatial* representation

$$\bar{\boldsymbol{\omega}}(S,t) = \kappa_1(S,t)\bar{\boldsymbol{t}}_1(S,t) + \kappa_2(S,t)\bar{\boldsymbol{t}}_2(S,t) + \kappa_3(S,t)\bar{\boldsymbol{n}}(S,t) \tag{2.23}$$

or in a *material* representation

$$\bar{\boldsymbol{\Omega}}(S,t) \equiv \kappa_I(S,t)\bar{\boldsymbol{E}}_I \tag{2.24}$$

The spatial and material vector fields are related directly by the orthonormal transformation

$$\bar{\boldsymbol{\omega}}(S,t) = \underline{\boldsymbol{R}}(S,t)\bar{\boldsymbol{\Omega}}(S,t) \tag{2.25}$$

The *deformation gradient* is denoted by $\underline{\boldsymbol{F}}$. This quantity distinguishes rigid body motion (i.e. translation and rotation) from deformation. It maps all material line elements $(d\bar{\boldsymbol{X}})$ in the reference configuration into all spatial line elements $(d\bar{\boldsymbol{x}})$ in the current configuration. Using equations 2.17 and 2.22 one can show that for the beam model treated here the deformation gradient assumes the form

$$\underline{\boldsymbol{F}} = \sum_{\Gamma=1}^{2} \bar{\boldsymbol{t}}_\Gamma \otimes \bar{\boldsymbol{E}}_\Gamma + \left[\frac{\partial \varphi_0}{\partial S} + \bar{\boldsymbol{\omega}} \times (\varphi - \varphi_0) \right] \otimes \bar{\boldsymbol{E}}_3 \tag{2.26}$$

2.2.2 Stress measures and equilibrium equations

Beam models are characterized by two different stress measures, the internal forces and internal couples. As in the standard beam theory, the stress measures of this geometrically exact model can be defined in terms of integrals of one of the stress tensors over the beam cross sections $A(S,t)$.

As pointed out by Simo (1985), the internal forces are the resultant contact forces per unit of reference length over the cross section, and in a Lagrangian description can be represented in terms of the first Piola-Kirchhoff tensor as

$$\bar{\boldsymbol{f}}(S,t) \equiv \int_A \underline{\boldsymbol{P}}(\xi,S,t)\bar{\boldsymbol{E}}_3 \, d\xi \tag{2.27}$$

while the internal couples are the resultant of contact moment per unit of reference length over the cross-section

$$\bar{\boldsymbol{m}}(S,t) = \int_A [\varphi(S,t) - \varphi_0(S,t)] \times \underline{\boldsymbol{P}}(\xi,S)\bar{\boldsymbol{E}}_3 \, d\xi \tag{2.28}$$

The quantities $\bar{\boldsymbol{f}}(S,t)$ and $\bar{\boldsymbol{m}}(S,t)$ are spatial stress measures, i.e. stress measures acting on the current configuration.

As pointed out by Simo (1985), it is often more convenient to use a *material* form of the beam model in applications. Material stress measures belong to the reference configuration, and can be obtained from the spatial measures through a *pull-back* operation, performed with the rotation tensor $\underline{\boldsymbol{R}}(S,t)$:

$$\begin{aligned} \bar{\boldsymbol{N}}(S,t) &= \underline{\boldsymbol{R}}^T(S,t)\bar{\boldsymbol{f}}(S,t) \\ \bar{\boldsymbol{M}}(S,t) &= \underline{\boldsymbol{R}}^T(S,t)\bar{\boldsymbol{m}}(S,t) \end{aligned} \tag{2.29}$$

Taking into account the representation in components of the stress measures in the current moving frame, the following representation is obtained

$$\bar{\boldsymbol{f}} = f_i \bar{\boldsymbol{t}}_i \quad \text{and} \quad \bar{\boldsymbol{m}} = m_i \bar{\boldsymbol{t}}_i \tag{2.30}$$

It can be shown that these components are the same in both the current and reference frames. One can demonstrate that the beam stress measures must satisfy the following linear and angular momentum balance equations

$$\frac{\partial \bar{\boldsymbol{f}}}{\partial S} + \bar{\boldsymbol{q}}_{\bar{\boldsymbol{f}}} = 0 \tag{2.31}$$

$$\frac{\partial \bar{\boldsymbol{m}}}{\partial S} + \frac{\partial \varphi_0}{\partial S} \times \bar{\boldsymbol{f}} + \bar{\boldsymbol{q}}_{\bar{\boldsymbol{m}}} = 0 \qquad S \in \boldsymbol{I} \tag{2.32}$$

where $\bar{\boldsymbol{q}}_{\bar{\boldsymbol{f}}}$ is the (applied) force per unit of reference arc length and $\bar{\boldsymbol{q}}_{\bar{\boldsymbol{m}}}$ is the (applied) moment per unit of reference arc length.

2.2.3 Internal power and conjugated strain measures

In the target three-dimensional beam model, the internal power is expressed by

$$\mathcal{P} = \int_{A\times I} \underline{\boldsymbol{P}} : \underline{\dot{\boldsymbol{F}}}\, d\xi dS \tag{2.33}$$

Taking into account equation 2.26, it can be shown that the internal power can be expressed in terms of the spatial stress measures $\bar{\boldsymbol{f}}(S,t)$ and $\bar{\boldsymbol{m}}(S,t)$, and of the spatial strain measures $\bar{\boldsymbol{\gamma}}(S,t)$ and $\bar{\boldsymbol{\omega}}(S,t)$, as

$$\mathcal{P} = \int_I [\bar{\boldsymbol{f}} \cdot \overset{\triangledown}{\bar{\boldsymbol{\gamma}}} + \bar{\boldsymbol{m}} \cdot \overset{\triangledown}{\bar{\boldsymbol{\omega}}}] dS \tag{2.34}$$

The beam strain measure $\bar{\boldsymbol{\gamma}}(S,t)$, conjugated with the stress measure $\bar{\boldsymbol{f}}(S,t)$ in the sense of the internal power, is expressed by

$$\bar{\boldsymbol{\gamma}}(S,t) \equiv \frac{\partial \varphi_0(S,t)}{\partial S} - \bar{\boldsymbol{n}}(S,t) \tag{2.35}$$

the vector $\bar{\boldsymbol{\gamma}}(S,t)$ takes into account axial and shear deformations, while the strain measure $\bar{\boldsymbol{\omega}}(S,t)$ is the one defined in equation 2.23, and takes into account bending and torsional deformations.

Both strain measures appear in equation 2.33 in terms of the objective derivative defined as (see Appendix B.2)

$$\overset{\triangledown}{(\cdot)} = \frac{\partial}{\partial t}(\cdot) - \bar{\boldsymbol{w}} \times (\cdot) \tag{2.36}$$

Like for the stress measures, a material counterpart of the strain measures can be introduced. The *pull-back* of $\bar{\boldsymbol{\gamma}}$ is the material vector

$$\bar{\boldsymbol{\Gamma}}(S,t) \equiv \underline{\boldsymbol{R}}^T \frac{\partial \varphi_0(S,t)}{\partial S} - \bar{\boldsymbol{E}}_3(S) \tag{2.37}$$

while the *pull-back* of $\bar{\boldsymbol{\omega}}(S,t)$ is the one expressed in equation 2.25. Using the material stress and strain measures, the internal power can be expressed as

$$\mathcal{P} \equiv \int_I [\bar{\boldsymbol{N}} \cdot \dot{\bar{\boldsymbol{\Gamma}}} + \bar{\boldsymbol{M}} \cdot \dot{\bar{\boldsymbol{\Omega}}}] dS \tag{2.38}$$

2.2.4 Constitutive equations

The constitutive equation presented in this section is limited to the elastic case. This is not a limitation of the model, but a simplification adopted in the context of this work; other constitutive models for hyperelastic or elasto-plastic materials, for example, could be introduced in the beam model of Simo (1985). Let us define a stored energy function in a material description, $\Psi(S, \bar{\boldsymbol{\Gamma}}, \bar{\boldsymbol{\Omega}})$, such that

$$\bar{\boldsymbol{N}} = \frac{\partial \Psi(S, \bar{\boldsymbol{\Gamma}}, \bar{\boldsymbol{\Omega}})}{\partial \bar{\boldsymbol{\Gamma}}}, \quad \bar{\boldsymbol{M}} = \frac{\partial \Psi(S, \bar{\boldsymbol{\Gamma}}, \bar{\boldsymbol{\Omega}})}{\partial \bar{\boldsymbol{\Omega}}}, \quad S \in \boldsymbol{I} \tag{2.39}$$

Therefore, the material version of the constitutive law can be represented by

$$\left\{ \begin{array}{c} \bar{\boldsymbol{N}}(S,t) \\ \bar{\boldsymbol{M}}(S,t) \end{array} \right\} = \underline{\boldsymbol{C}} \left\{ \begin{array}{c} \bar{\boldsymbol{\Gamma}}(S,t) \\ \bar{\boldsymbol{\Omega}}(S,t) \end{array} \right\} \tag{2.40}$$

where the tangent constitutive tensor assumes the form

$$\underline{\boldsymbol{C}} = \left[\begin{array}{cc} \dfrac{\partial^2 \Psi}{\partial \bar{\boldsymbol{\Gamma}} \partial \bar{\boldsymbol{\Gamma}}} & \dfrac{\partial^2 \Psi}{\partial \bar{\boldsymbol{\Gamma}} \partial \bar{\boldsymbol{\Omega}}} \\ \dfrac{\partial^2 \Psi}{\partial \bar{\boldsymbol{\Gamma}} \partial \bar{\boldsymbol{\Omega}}} & \dfrac{\partial^2 \Psi}{\partial \bar{\boldsymbol{\Omega}} \partial \bar{\boldsymbol{\Omega}}} \end{array} \right] \tag{2.41}$$

In this treatise our attention will be confined to the Saint-Venant–Kirchhoff material. This is a common assumption in beams that may experience arbitrarily large rotations, but small strains. In addition to that, the material is assumed to be homogeneous and isotropic. For a particular case where the beam axis coincides with the cross-sectional centroids and the cross-sectional axis is parallel to the principal axis of inertia, the tensor $\underline{\boldsymbol{C}}$ is constant and diagonal, as follows

$$\underline{\boldsymbol{C}} = \left[\begin{array}{cc} \underline{\boldsymbol{C}}_1 & \boldsymbol{0} \\ \boldsymbol{0} & \underline{\boldsymbol{C}}_2 \end{array} \right] \tag{2.42}$$

That being said, the material version of the constitutive law can be rewritten as

$$\bar{\boldsymbol{N}}(S,t) = \underline{\boldsymbol{C}}_1 \bar{\boldsymbol{\Gamma}}(S,t) \tag{2.43}$$

$$\bar{\boldsymbol{M}}(S,t) = \underline{\boldsymbol{C}}_2 \bar{\boldsymbol{\Omega}}(S,t) \tag{2.44}$$

In the reference configuration the *constitutive operators* $\underline{\boldsymbol{C}}_1$ and $\underline{\boldsymbol{C}}_2$ take the form

$$\underline{\boldsymbol{C}}_1 = \left[\begin{array}{ccc} GA_1 & 0 & 0 \\ 0 & GA_2 & 0 \\ 0 & 0 & EA \end{array} \right] \tag{2.45}$$

$$\underline{\boldsymbol{C}}_2 = \begin{bmatrix} EI_1 & 0 & 0 \\ 0 & EI_2 & 0 \\ 0 & 0 & GJ_t \end{bmatrix} \tag{2.46}$$

where E, G are the elastic modulus and shear modulus respectively, EA is the axial stiffness, EI_1, EI_2 are the principal bending stiffnesses relative to the cross-section along the principal directions, GA_1, GA_2 are the shear stiffnesses with respect to the cross-section in principal directions. Note that A_1 and A_2 include the shear factor k_s, and GJ_t is the torsional stiffness with $J_t = I_1 + I_2$.

The rate forms of equations 2.43 and 2.44 are often needed for computational applications (Simo, 1985); in order to obtain these forms, the time derivative combined with the chain rule is used (Simo, 1985). The result for the material description is presented as follows

$$\begin{Bmatrix} \dot{\boldsymbol{N}}(S,t) \\ \dot{\boldsymbol{M}}(S,t) \end{Bmatrix} = \underline{\boldsymbol{C}} \begin{Bmatrix} \dot{\boldsymbol{\Gamma}}(S,t) \\ \dot{\boldsymbol{\Omega}}(S,t) \end{Bmatrix} \tag{2.47}$$

All equations of this section presented in a material form can be recasted in the spatial form. The rate form of the spatial version is obtained similarly with the material version case by taking the time derivative combined with the chain rule. For the stored energy function $\psi(S, \bar{\boldsymbol{\gamma}}, \bar{\boldsymbol{\omega}})$, one can write

$$\bar{\boldsymbol{f}} = \frac{\partial \psi(S, \bar{\boldsymbol{\gamma}}, \bar{\boldsymbol{\omega}})}{\partial \bar{\boldsymbol{\gamma}}}, \quad \bar{\boldsymbol{m}} = \frac{\partial \psi(S, \bar{\boldsymbol{\gamma}}, \bar{\boldsymbol{\omega}})}{\partial \bar{\boldsymbol{\omega}}}, \quad S \in \boldsymbol{I} \tag{2.48}$$

Similarly, equations for the spatial description are presented as follows

$$\begin{Bmatrix} \overset{\triangledown}{\bar{\boldsymbol{f}}} \\ \overset{\triangledown}{\bar{\boldsymbol{m}}} \end{Bmatrix} = \underline{\boldsymbol{c}} \begin{Bmatrix} \overset{\triangledown}{\bar{\boldsymbol{\gamma}}} \\ \overset{\triangledown}{\bar{\boldsymbol{\omega}}} \end{Bmatrix} \tag{2.49}$$

$$\underline{\boldsymbol{c}} = \begin{bmatrix} \dfrac{\partial^2 \psi}{\partial \bar{\boldsymbol{\gamma}} \partial \bar{\boldsymbol{\gamma}}} & \dfrac{\partial^2 \psi}{\partial \bar{\boldsymbol{\gamma}} \partial \bar{\boldsymbol{\omega}}} \\ \dfrac{\partial^2 \psi}{\partial \bar{\boldsymbol{\gamma}} \partial \bar{\boldsymbol{\omega}}} & \dfrac{\partial^2 \psi}{\partial \bar{\boldsymbol{\omega}} \partial \bar{\boldsymbol{\omega}}} \end{bmatrix} \tag{2.50}$$

In the spatial version 2.43, 2.44 and 2.42 are represented as follows

$$\bar{\boldsymbol{f}}(S,t) = \underline{\boldsymbol{c}}_1 \bar{\boldsymbol{\gamma}}(S,t) \tag{2.51}$$

$$\bar{\boldsymbol{m}}(S,t) = \underline{\boldsymbol{c}}_2 \bar{\boldsymbol{\omega}}(S,t) \tag{2.52}$$

$$\underline{\boldsymbol{c}} = \begin{bmatrix} \underline{\boldsymbol{c}}_1 & \mathbf{0} \\ \mathbf{0} & \underline{\boldsymbol{c}}_2 \end{bmatrix} \tag{2.53}$$

where the constitutive operators $\underline{\boldsymbol{c}}_1$ and $\underline{\boldsymbol{c}}_2$ obey the following relation

$$\underline{\boldsymbol{c}}_1 = \underline{\boldsymbol{R}}(S,t)\underline{\boldsymbol{C}}_1\underline{\boldsymbol{R}}^T(S,t) \tag{2.54}$$

$$\underline{\boldsymbol{c}}_2 = \underline{\boldsymbol{R}}(S,t)\underline{\boldsymbol{C}}_2\underline{\boldsymbol{R}}^T(S,t) \tag{2.55}$$

2.2.5 Beam configuration and admissible variations

In the previous sections the three-dimensional beam model developed by Simo (1985) was presented. The present section is devoted to the concepts of configuration and admissible variations of the beam, which are essential to obtain the weak form of the beam model and the subsequent numerical formulation [4]. In this model the current configuration of the three-dimensional beam is expressed in terms of the position of the line of centroids and the rotation of the cross-sections. The set of all possible configurations of the beam can then be expressed as

$$\mathcal{C} = \{(\varphi_0, \underline{\boldsymbol{R}}) | \, \varphi_0 : S \to \mathbb{R}^3, \underline{\boldsymbol{R}} : S \to \mathrm{SO}(3)\} \tag{2.56}$$

Due to the presence of the special orthogonal group SO(3), the space of configurations is a nonlinear differentiable manifold, rather than a linear space as in standard beam theories. An admissible variation is a superposed change of configuration that allows to obtain a perturbed configuration of the beam, compatible with the applied boundary conditions, and expressed by $\mathcal{C}_\varepsilon = (\varphi_{0\varepsilon}, \underline{\boldsymbol{R}}_\varepsilon)$, with $\varepsilon > 0$. The perturbed motion of the line of centroids and the rotation of the cross-sections are given by

$$\varphi_{0\varepsilon}(S,t) = \varphi_0(S,t) + \varepsilon\bar{\boldsymbol{\eta}}_0(S,t) \tag{2.57}$$

$$\underline{\boldsymbol{R}}_\varepsilon(S,t) = \exp[\varepsilon\underline{\boldsymbol{\theta}}(S,t)]\underline{\boldsymbol{R}}(S,t) \tag{2.58}$$

The form of Equation 2.57 is compatible with the fact that the line of centroids belongs to a subset of the affine space $\boldsymbol{\mathcal{E}}$, which is a linear space. On the other hand equation 2.58 belongs to the nonlinear space SO(3), therefore a perturbed configuration is achieved by means of the concept of *compound rotations*. Equation 2.58 is termed as *left translation map*; alternatively, the perturbed configuration could be given by the right-application of

[4] As will be shown in chapter Chapter 5, for the smoothed point interpolation methods the starting point to develop the weakened-weak formulation can be the weak form.

an incremental rotation operator, a *right translation map*, which is represented as follows[5]

$$\underline{\boldsymbol{R}}_{\varepsilon}(S,t) = \underline{\boldsymbol{R}}(S,t)\exp[\varepsilon\underline{\boldsymbol{\Theta}}(S,t)] \tag{2.59}$$

It is important to highlight that $\underline{\boldsymbol{R}}_{\varepsilon}(S,t)$ remains orthogonal and therefore the equation above is a suitable orientation of the moving frame. The superposed infinitesimal displacement and rotation can be written in terms of their components as follows

$$\bar{\boldsymbol{\eta}}_0(S,t) = \eta_{0i}(S,t)\boldsymbol{e}_i \quad \underline{\boldsymbol{\theta}}(S,t) = \theta_{ij}\boldsymbol{e}_i \otimes \boldsymbol{e}_j \tag{2.60}$$

One can recall that every skew-symmetric tensor is associated with an axial vector, that is to say, for a $\underline{\boldsymbol{\theta}}(S,t) \in \mathrm{so}(3)$ [6] exists an associated axial vector $\bar{\boldsymbol{\theta}}(S,t) \in \mathbb{R}^3$ such that the following equality stands for a given vector $\bar{\boldsymbol{h}}$

$$\underline{\boldsymbol{\theta}}\bar{\boldsymbol{h}} = \bar{\boldsymbol{\theta}} \times \bar{\boldsymbol{h}} \quad \text{for any } \bar{\boldsymbol{h}} \in \mathbb{R}^3 \tag{2.61}$$

In some situations it is convenient to use the axial vector instead the skew-symmetric tensor. Let us define a set of kinematically admissible variations $T_{\varphi}\mathcal{C}$ as

$$\begin{gathered} T_{\varphi}\mathcal{C} \equiv \{\bar{\boldsymbol{\eta}}(S,t) \equiv (\bar{\boldsymbol{\eta}}_0(S,t), \bar{\boldsymbol{\theta}}(S,t))\} \\ \bar{\boldsymbol{\eta}}(S,t) \in \mathbb{R}^3 \times \mathbb{R}^3 | \bar{\boldsymbol{\eta}}_0 \equiv \bar{\boldsymbol{\theta}} = 0 \text{ on } \partial D_c \end{gathered} \tag{2.62}$$

∂D_c is where the essential boundary conditions are evaluated. By taking the directional derivatives below, it can be shown that $\bar{\boldsymbol{\eta}}_0$ and $\bar{\boldsymbol{\theta}}$ are kinematically admissible variations of the beam configuration:

$$D\varphi_0 \cdot \bar{\boldsymbol{\eta}}_0 \coloneqq \left.\frac{\partial \varphi_{0\varepsilon}}{\partial \varepsilon}\right|_{\varepsilon=0} = \bar{\boldsymbol{\eta}}_0(S,t) \tag{2.63}$$

$$D\underline{\boldsymbol{R}} \cdot \underline{\boldsymbol{\theta}} \coloneqq \left.\frac{\partial \underline{\boldsymbol{R}}_{\varepsilon}}{\partial \varepsilon}\right|_{\varepsilon=0} = \underline{\boldsymbol{\theta}}(S,t)\underline{\boldsymbol{R}}(S,t) \tag{2.64}$$

As pointed out by Simo and Vu-Quoc (1986), in a geometric perspective the superposed infinitesimal rotation $\underline{\boldsymbol{\theta}}(S,t)$ defines an incremental tangent field onto the current configuration given by $\underline{\boldsymbol{R}}(S,t)$ such that a subsequent configuration is obtained by simply considering the exponential map $\underline{\boldsymbol{R}}_{n+1} = \exp[\underline{\boldsymbol{\theta}}]\underline{\boldsymbol{R}}_n$. Recalling equation 2.59 an equivalent update procedure is obtained by $\underline{\boldsymbol{R}}_{n+1} = \underline{\boldsymbol{R}}_n \exp[\underline{\boldsymbol{\Theta}}]$. For a broader discussion about finite rotations applied to nonlinear beams, see Argyris (1982), Geradin and Cardona (1988)

[5] See Appendix B.

[6] Lie algebra for all skew-symmetric tensors. See Appendix B.

and Moreira (2009).

2.2.6 Linearisation of the strain measures

In the previous section, a linearisation of the beam configuration has been performed using the concept of directional derivative, resulting in the space of admissible variations (equations 2.57 and 2.58). The same linearisation can be propagated to the other relevant quantities of the beam model, namely the stress and strain measures.

The linearisation of the strain measures can be achieved by means of the spatial infinitesimal rotation $\underline{\boldsymbol{\theta}}$ or using its material counterpart $\underline{\boldsymbol{\Theta}}$, (equations 2.58 and 2.59). Here, we will present the results of the linearisation procedure using the *spatial* infinitesimal rotation only. Equivalent equations can be obtained making use of the *material* infinitesimal rotation as presented in equation 2.59. In order to obtain the linearisation of $\underline{\boldsymbol{\omega}}(S,t)$ and $\underline{\boldsymbol{\Omega}}(S,t)$ one can start with their perturbed expressions

$$\underline{\boldsymbol{\omega}}_\varepsilon = \frac{\partial \underline{\boldsymbol{R}}_\varepsilon}{\partial S}\boldsymbol{R}_\varepsilon^T, \qquad \underline{\boldsymbol{\Omega}}_\varepsilon = \boldsymbol{R}_\varepsilon^T \frac{\partial \underline{\boldsymbol{R}}_\varepsilon}{\partial S} \tag{2.65}$$

and proceed with the linearisation by applying the directional derivative, resulting in

$$D\underline{\boldsymbol{\omega}} \cdot \underline{\boldsymbol{\theta}} \coloneqq \left.\frac{\partial \underline{\boldsymbol{\omega}}_\varepsilon}{\partial \varepsilon}\right|_{\varepsilon=0} = \frac{\partial \underline{\boldsymbol{\theta}}}{\partial S} + \underline{\boldsymbol{\theta}}\underline{\boldsymbol{\omega}} - \underline{\boldsymbol{\omega}}\underline{\boldsymbol{\theta}} \tag{2.66}$$

$$D\underline{\boldsymbol{\Omega}} \cdot \underline{\boldsymbol{\theta}} \coloneqq \left.\frac{\partial \underline{\boldsymbol{\Omega}}_\varepsilon}{\partial \varepsilon}\right|_{\varepsilon=0} = \underline{\boldsymbol{R}}^T \frac{\partial \underline{\boldsymbol{\theta}}}{\partial S}\underline{\boldsymbol{R}} \tag{2.67}$$

Table 2.1 illustrates the linearised strain measures using both, the spatial and material rotation increments ($\underline{\boldsymbol{\theta}}$ and $\underline{\boldsymbol{\Theta}}$).
For further details on the mathematical procedure used to obtain equations 2.66, 2.67 and those of Table 2.1, the reader may refer to Appendix B.3.

2.2.7 Weak form of balance equations

In what follows, attention will be focused on obtaining a weak form for the beam problem restricted to the static case[7]. Let us consider an arbitrary admissible variation $\bar{\boldsymbol{\eta}}(S,t) \equiv (\bar{\boldsymbol{\eta}}_0(S,t), \bar{\boldsymbol{\theta}}(S,t)) \in T_\varphi \mathcal{C}$ as presented in equation 2.62. Starting from the equations 2.31 and 2.32 and using the admissible variations as test functions in a weighted residual procedure (see Appendix B.4), a functional $G(\varphi, \bar{\boldsymbol{\eta}})$ can be introduced, in its spatial version

[7] The original model presented by Simo (1985) and Simo and Vu-Quoc (1986) also accounts for dynamic effects.

SPATIAL STRAIN MEASURES	
$(D\bar{\boldsymbol{\gamma}} \cdot \bar{\boldsymbol{\eta}}_0) = \dfrac{\partial \bar{\boldsymbol{\eta}}_0}{\partial S} - \bar{\boldsymbol{\theta}} \times \bar{\boldsymbol{n}}$ $(D\bar{\boldsymbol{\omega}} \cdot \bar{\boldsymbol{\theta}}) = \dfrac{\partial \bar{\boldsymbol{\theta}}}{\partial S} + \bar{\boldsymbol{\theta}} \times \bar{\boldsymbol{\omega}}$	Via spatial rotation increment
$(D\bar{\boldsymbol{\gamma}} \cdot \bar{\boldsymbol{\eta}}_0) = \dfrac{\partial \bar{\boldsymbol{\eta}}_0}{\partial S} - \underline{\boldsymbol{R}}(\bar{\boldsymbol{\Theta}} \times \bar{\boldsymbol{E}}_3)$ $(D\bar{\boldsymbol{\omega}} \cdot \bar{\boldsymbol{\Theta}}) = \underline{\boldsymbol{R}} \dfrac{\partial \bar{\boldsymbol{\Theta}}}{\partial S}$	Via material rotation increment
MATERIAL STRAIN MEASURES	
$(D\bar{\boldsymbol{\Gamma}} \cdot \bar{\boldsymbol{\eta}}_0) = \underline{\boldsymbol{R}}^T \left(\dfrac{\partial \bar{\boldsymbol{\eta}}_0}{\partial S} - \bar{\boldsymbol{\theta}} \times \dfrac{\partial \varphi_0}{\partial S} \right)$ $(D\bar{\boldsymbol{\Omega}} \cdot \underline{\boldsymbol{\theta}}) = \underline{\boldsymbol{R}}^T \dfrac{\partial \bar{\boldsymbol{\theta}}}{\partial S}$	Via spatial rotation increment
$(D\bar{\boldsymbol{\Gamma}} \cdot \bar{\boldsymbol{\eta}}_0) = -\underline{\boldsymbol{\Theta}\boldsymbol{R}}^T \dfrac{\partial \varphi_0}{\partial S} + \underline{\boldsymbol{R}}^T \dfrac{\partial \bar{\boldsymbol{\eta}}_0}{\partial S}$ $(D\bar{\boldsymbol{\Omega}} \cdot \underline{\boldsymbol{\Theta}}) = \dfrac{\partial \bar{\boldsymbol{\Theta}}}{\partial S} + \bar{\boldsymbol{\Omega}} \times \bar{\boldsymbol{\Theta}}$	Via material rotation increment

Table 2.1: Summary table of the strain measures

$$G(\varphi, \bar{\boldsymbol{\eta}}) \coloneqq \int_{[0,L]} \left\{ \bar{\boldsymbol{f}} \cdot \left[\frac{\partial \bar{\boldsymbol{\eta}}_0}{\partial S} - \bar{\boldsymbol{\theta}} \times \frac{\partial \varphi_0}{\partial S} \right] + \bar{\boldsymbol{m}} \cdot \frac{\partial \bar{\boldsymbol{\theta}}}{\partial S} \right\} dS - \int_{[0,L]} (\bar{\boldsymbol{q}}_{\bar{\boldsymbol{f}}} \cdot \bar{\boldsymbol{\eta}}_0 + \bar{\boldsymbol{q}}_{\bar{\boldsymbol{m}}} \cdot \bar{\boldsymbol{\theta}})\, dS \quad (2.68)$$

and in its material version

$$\begin{aligned} G(\varphi, \bar{\boldsymbol{\eta}}) \coloneqq & \int_{[0,L]} \left\{ \bar{\boldsymbol{N}} \cdot \underline{\boldsymbol{R}}^T \left[\frac{\partial \bar{\boldsymbol{\eta}}_0}{\partial S} - \bar{\boldsymbol{\theta}} \times \frac{\partial \varphi_0}{\partial S} \right] + \bar{\boldsymbol{M}} \cdot \underline{\boldsymbol{R}}^T \frac{\partial \bar{\boldsymbol{\theta}}}{\partial S} \right\} dS \\ & - \int_{[0,L]} (\bar{\boldsymbol{q}}_{\bar{\boldsymbol{f}}} \cdot \bar{\boldsymbol{\eta}}_0 + \bar{\boldsymbol{q}}_{\bar{\boldsymbol{m}}} \cdot \bar{\boldsymbol{\theta}})\, dS \end{aligned} \quad (2.69)$$

The weak form of the beam problem consists then into find a configuration $\varphi \in \mathcal{C}$ such that $G = 0, \forall \bar{\boldsymbol{\eta}} \in T_\varphi \mathcal{C}$.

In order to apply a numerical method to the beam model developed in this work it is

convenient to express equation 2.68 (or 2.69) in a matrix form. To achieve this goal we will introduce the following notation

$$\boldsymbol{\Sigma} = \left\{ \begin{array}{c} \bar{\boldsymbol{N}} \\ \bar{\boldsymbol{M}} \end{array} \right\}, \quad \boldsymbol{\sigma} = \left\{ \begin{array}{c} \bar{\boldsymbol{f}} \\ \bar{\boldsymbol{m}} \end{array} \right\} \equiv \boldsymbol{\Pi}\boldsymbol{\Sigma} \tag{2.70}$$

where

$$\boldsymbol{\Pi} \coloneqq \left[\begin{array}{cc} \underline{\boldsymbol{R}} & 0 \\ 0 & \underline{\boldsymbol{R}} \end{array} \right] \tag{2.71}$$

where $\boldsymbol{\Sigma}$ and $\boldsymbol{\sigma}$ are the material and spatial vectors of resultant stresses and stress couples respectively. Let us define now the matrix differential operator $\boldsymbol{\xi}$, such that

$$\boldsymbol{\xi}^T \coloneqq \left[\begin{array}{cc} \dfrac{\partial}{\partial S}\mathbf{1} & [\varphi_0'\times] \\ \mathbf{0} & \dfrac{\partial}{\partial S}\mathbf{1} \end{array} \right] \tag{2.72}$$

In equation 2.72 $(\cdot)'$ is the differentiation with respect to S; $\mathbf{1} = Diag[1,1,1]$ is the identity matrix, $(\partial/\partial S)\mathbf{1}$ is a diagonal operator defined in equation 2.74, and $[\varphi_0'\times]$ is the skew symmetric matrix associated with axial vector $\varphi_0' = \varphi_{0i}'\boldsymbol{e}_i$, as follows

$$[\boldsymbol{\varphi}_0'\times] \coloneqq \left[\begin{array}{ccc} 0 & -\varphi_{03}' & \varphi_{02}' \\ \varphi_{03}' & 0 & -\varphi_{01}' \\ -\varphi_{02}' & \varphi_{01}' & 0 \end{array} \right] \tag{2.73}$$

$$\frac{\partial}{\partial S}\mathbf{1} \coloneqq Diag\left[\begin{array}{ccc} \dfrac{\partial}{\partial S} & \dfrac{\partial}{\partial S} & \dfrac{\partial}{\partial S} \end{array} \right] \tag{2.74}$$

The relations defined previously allow us to rephrase equation 2.68 (or 2.69) in a compacted format as follows

$$G(\varphi, \bar{\boldsymbol{\eta}}) = \int_{[0,L]} [(\boldsymbol{\xi}^T(S,t)\bar{\boldsymbol{\eta}}(S,t)) \cdot \boldsymbol{\sigma}(S,t) - \bar{\boldsymbol{\eta}}(S,t) \cdot \boldsymbol{q}(S,t)]\, dS \tag{2.75}$$

where $\boldsymbol{q}$ carries the applied forces and moments as

$$\boldsymbol{q}^T \coloneqq \{\bar{\boldsymbol{q}}_{\bar{\boldsymbol{f}}}, \bar{\boldsymbol{q}}_{\bar{\boldsymbol{m}}}\}^T \tag{2.76}$$

In order to obtain a solution algorithm for the geometrically nonlinear beam problem, the weak form must be linearised. In this work, the *proofs* of some equations concerning the target model are neglected. A comprehensible treatise with all demonstrations of *spatial* and *material* equations versions involved in the geometrically exact model can be find in Simo and Vu-Quoc (1986), Gori (2014) and Lozzo (2010).

The linearisation procedure of the functional $G(\varphi, \bar{\boldsymbol{\eta}})$ is achieved by considering its

tangent approximation at the configuration $\varphi = \hat{\varphi}$ (see (Wriggers, 2008, p. 96)) as follows[8]

$$L[G(\hat{\varphi}, \bar{\boldsymbol{\eta}})] = G(\hat{\varphi}, \bar{\boldsymbol{\eta}}) + DG(\hat{\varphi}, \bar{\boldsymbol{\eta}}) \cdot \Delta\varphi \tag{2.77}$$

As already seen in this work the directional derivative is used to obtain the required results in above equation. Taking into account the last term in equation 2.77 results in

$$DG(\hat{\varphi}, \bar{\boldsymbol{\eta}}) \cdot \Delta\varphi = \left. \frac{\partial G(\hat{\varphi}_\varepsilon, \bar{\boldsymbol{\eta}})}{\partial \varepsilon} \right|_{\varepsilon=0} \tag{2.78}$$

where $\Delta\varphi \equiv (\boldsymbol{u}_0, \boldsymbol{\psi}) \in T_\varphi \mathcal{C}$ is an admissible variation.

Now, we proceed to obtain the linear part of equation 2.75. To achieve this goal we note that the linearised internal force can be expressed as

$$D\boldsymbol{\Sigma} \cdot \Delta\bar{\boldsymbol{\theta}} = \underline{\hat{\boldsymbol{C}}} \left\{ \begin{array}{c} D\bar{\boldsymbol{\Gamma}} \cdot \boldsymbol{u} \\ D\bar{\boldsymbol{\Omega}} \cdot \boldsymbol{\psi} \end{array} \right\} = \underline{\hat{\boldsymbol{C}}} \hat{\boldsymbol{\Pi}}^T \hat{\boldsymbol{\xi}}^T \Delta\varphi \tag{2.79}$$

where the quantities $\hat{\boldsymbol{\Sigma}}$, $\hat{\boldsymbol{\Pi}}$ and $\hat{\boldsymbol{\xi}}$ are the representation of $\boldsymbol{\Sigma}$, $\boldsymbol{\Pi}$ and $\boldsymbol{\xi}$ for the configuration $\varphi = \hat{\varphi}$, and $\underline{\hat{\boldsymbol{C}}}$ is the material tangent elastic tensor presented in 2.42. In addition to that, the following relation should be highlighted

$$\left\{ \begin{array}{c} D\bar{\boldsymbol{\Gamma}} \cdot \boldsymbol{u} \\ D\bar{\boldsymbol{\Omega}} \cdot \bar{\boldsymbol{\theta}} \end{array} \right\} = \hat{\boldsymbol{\Pi}}^T \hat{\boldsymbol{\xi}}^T \left\{ \begin{array}{c} \boldsymbol{u}_0 \\ \boldsymbol{\psi} \end{array} \right\} \equiv \hat{\boldsymbol{\Pi}}^T \hat{\boldsymbol{\xi}}^T \Delta\varphi \tag{2.80}$$

The linearisation of the functional $G(\hat{\varphi}, \bar{\boldsymbol{\eta}})$ is composed by three parts. The first one is the material part of the tangent stiffness matrix due to the linearisation procedure applied to the internal forces $\boldsymbol{\Sigma}$. The second is the geometric part of the tangent stiffness matrix obtained by means of the linearisation of the operator $[\boldsymbol{\xi}\boldsymbol{\Pi}]$, which was defined previously. In other words one can write

$$DG(\hat{\varphi}, \bar{\boldsymbol{\eta}}) \cdot \Delta\varphi = D_M G(\hat{\varphi}, \bar{\boldsymbol{\eta}}) \cdot \Delta\varphi_s + D_G G(\hat{\varphi}, \bar{\boldsymbol{\eta}}) \cdot \Delta\varphi_s + D_L G(\hat{\varphi}, \bar{\boldsymbol{\eta}}) \cdot \Delta\varphi_s \tag{2.81}$$

the sub-indices M and G refer, respectively, to the *material* and *geometric* part of the *tangent stiffness* matrix, while the sub-index L refers to the *load stiffness*, and in $\Delta\varphi_s$ the sub-index s refers to *spatial*. The terms from equation 2.81 can be expressed as follows

$$D_M G(\hat{\varphi}, \bar{\boldsymbol{\eta}}_s) \cdot \Delta\varphi = \int_{[0,L]} (\hat{\boldsymbol{\xi}}^T \bar{\boldsymbol{\eta}}) \cdot (\underline{\hat{\boldsymbol{c}}} \hat{\boldsymbol{\xi}}^T \Delta\varphi_s)\, dS \tag{2.82}$$

$$D_G G(\hat{\boldsymbol{\phi}}, \bar{\boldsymbol{\eta}}_s) \cdot \Delta\varphi = \int_{[0,L]} (\hat{\beta} \bar{\boldsymbol{\eta}}_s) \cdot (\hat{\boldsymbol{b}} \hat{\beta} \Delta\varphi_s)\, dS \tag{2.83}$$

[8] For a broader and more formal overview regarded to the linearisation procedure, see Marsden and Hughes (1994).

$$D_L G(\hat{\boldsymbol{\phi}}, \bar{\boldsymbol{\eta}}_s) \cdot \Delta\varphi = \int_{[0,L]} \bar{\boldsymbol{\eta}}_s \cdot (\hat{\boldsymbol{l}} \Delta\varphi_s)\, dS \tag{2.84}$$

where $\hat{\beta}$ is the matrix differential operator

$$\hat{\beta} \coloneqq \begin{bmatrix} \dfrac{\partial}{\partial S}\mathbf{1} & \mathbf{0} \\ \mathbf{0} & \dfrac{\partial}{\partial S}\mathbf{1} \\ \mathbf{0} & \mathbf{1} \end{bmatrix} \tag{2.85}$$

$\hat{\boldsymbol{b}}$ is the *geometric stiffness* matrix

$$\hat{\boldsymbol{b}} \coloneqq \begin{bmatrix} \mathbf{0} & \mathbf{0} & [-\bar{\boldsymbol{f}}\times] \\ \mathbf{0} & \mathbf{0} & [-\bar{\boldsymbol{m}}\times] \\ \left[\bar{\boldsymbol{f}}\times\right] & \mathbf{0} & [\bar{\boldsymbol{f}} \otimes \varphi_0' - (\bar{\boldsymbol{f}} \cdot \varphi_0')\mathbf{1}] \end{bmatrix} \tag{2.86}$$

the operator $\hat{\boldsymbol{l}}$ is defined as

$$\boldsymbol{l} \coloneqq \begin{bmatrix} \mathbf{0} & [-\bar{\boldsymbol{q}}^{fl}_{\bar{\boldsymbol{f}}}(S,t)\times] \\ \mathbf{0} & [-\bar{\boldsymbol{q}}^{fl}_{\bar{\boldsymbol{m}}}(S,t)\times] \end{bmatrix} \tag{2.87}$$

the sub-index fl appearing in Eq. (2.87) is referring to a *follower* load. The term $\hat{\underline{\boldsymbol{c}}} \coloneqq \hat{\boldsymbol{\Pi}}\underline{\hat{\boldsymbol{C}}}\hat{\boldsymbol{\Pi}}^T$ is the spatial form of the elastic tensor. We recall again that the quantities with a hat sign $\hat{(\cdot)}$ stand for the configuration $\varphi = \hat{\varphi}$.

Due to the nonlinear character of the geometrically exact model, in this master's thesis the Newton method is used to solve the equilibrium equations using the *material* version of the involved quantities. Therefore, aiming the further implementation, it is preferable to represent the linearised weak form components in their *material* version.

Taking into account Eq. (2.77) the first portion of the linearised form is represented in its *material* version as

$$G(\hat{\varphi}, \bar{\boldsymbol{\eta}}) = \int_{[0,L]} [(\boldsymbol{\Xi}^T(S,t)\bar{\boldsymbol{\eta}}(S,t)) \cdot \boldsymbol{\Sigma}(S,t) - \bar{\boldsymbol{\eta}}(S,t) \cdot \boldsymbol{Q}(S,t)] dS \tag{2.88}$$

where $\boldsymbol{Q}$ gathers the external loads, forces and moments, applied on the beam

$$\boldsymbol{Q}(S,t) \coloneqq \begin{pmatrix} \bar{\boldsymbol{Q}}_f(S,t) \\ \bar{\boldsymbol{Q}}_m(S,t) \end{pmatrix} \equiv \begin{pmatrix} \bar{\boldsymbol{q}}^{fx}_f(S,t) \\ \underline{\boldsymbol{R}}^T(S,t)\bar{\boldsymbol{q}}^{fx}_m(S,t) \end{pmatrix} + \begin{pmatrix} \bar{\boldsymbol{q}}^{fl}_f(S,t) \\ \underline{\boldsymbol{R}}^T(S,t)\bar{\boldsymbol{q}}^{fl}_m(S,t) \end{pmatrix} \tag{2.89}$$

the sub-indices in above equation have the following meaning: f = *forces*, m = *moments*, fx = *fixed* and fl = *follower*. As discussed in Simo (1985), this model also allows *follower* applied loads.

The *material tangent stiffness* of the linearised form can be represented as

$$D_M G(\hat{\varphi}, \bar{\boldsymbol{\eta}}) \cdot \Delta\varphi = \int_{[0,L]} (\hat{\boldsymbol{\Xi}}^T \bar{\boldsymbol{\eta}}) \cdot (\hat{\underline{\boldsymbol{C}}} \hat{\boldsymbol{\Xi}}^T \Delta\varphi_M) dS \tag{2.90}$$

where the kinematic operator is introduced as

$$\hat{\boldsymbol{\Xi}}^T \coloneqq \begin{bmatrix} \underline{\boldsymbol{R}}^T(S,t) \dfrac{\partial}{\partial S} \mathbf{1} & [\underline{\boldsymbol{R}}^T(S,t) \varphi_0' \times] \\ \mathbf{0} & \dfrac{\partial}{\partial S} \mathbf{1} + \underline{\boldsymbol{\Omega}}(S,t) \end{bmatrix} \tag{2.91}$$

The *geometric tangent stiffness* is the part of the tangent operator given by the linearisation of the *rotation* and the *kinematic* operators. In a material form it assumes the following representation

$$D_G G(\hat{\varphi}, \bar{\boldsymbol{\eta}}) \cdot \Delta\varphi = \int_{[0,L]} (\hat{\beta} \bar{\boldsymbol{\eta}}) \cdot (\hat{\boldsymbol{B}} \hat{\beta} \Delta\varphi_G) dS \tag{2.92}$$

where the following quantities are defined

$$\boldsymbol{B} \coloneqq \begin{bmatrix} \mathbf{0} & \mathbf{0} & -\underline{\boldsymbol{R}}(S,t) [\bar{\boldsymbol{N}}(S,t) \times] \\ \mathbf{0} & \mathbf{0} & \mathbf{0} \\ \left[\bar{\boldsymbol{N}}(S,t) \times\right] \underline{\boldsymbol{R}}^T(S,t) & [-\bar{\boldsymbol{M}}(S,t) \times] & [A] \end{bmatrix} \tag{2.93}$$

with the sub-matrix represented $[A]$ by

$$\begin{aligned} [A] \coloneqq\ & \bar{\boldsymbol{N}}(S,t) \otimes \left(\underline{\boldsymbol{R}}^T(S,t) \frac{\partial \varphi_0(S,t)}{\partial S} \right) - \bar{\boldsymbol{N}}(S,t) \cdot \left(\underline{\boldsymbol{R}}^T(S,t) \frac{\partial \varphi_0(S,t)}{\partial S} \right) \\ & + \bar{\boldsymbol{M}}(S,t) \otimes \bar{\boldsymbol{\Omega}}(S,t) - \bar{\boldsymbol{M}}(S,t) \cdot \bar{\boldsymbol{\Omega}}(S,t) \end{aligned} \tag{2.94}$$

Lastly, the *material* version of the *load stiffness* can be represented as follows

$$D_L G(\hat{\varphi}, \bar{\boldsymbol{\eta}}) \cdot \Delta\varphi = \int_{[0,L]} \bar{\boldsymbol{\eta}} \cdot (\hat{\boldsymbol{L}} \Delta\boldsymbol{\varphi}_L) dS \tag{2.95}$$

where the operator $\boldsymbol{L}(S,t)$ appearing in above equation is introduced as

$$\boldsymbol{L} \coloneqq \begin{pmatrix} 0 & -\left[\boldsymbol{q}_f^{fl}(S,t) \times\right] \underline{\boldsymbol{R}}(S,t) \\ 0 & -\left[\underline{\boldsymbol{R}}^T(S,t) \boldsymbol{q}_m^{fx}(S,t) \times\right] \end{pmatrix} \tag{2.96}$$

where the sub-indices fx and fl refer to a *fixed* and a *follower* load respectively.

CHAPTER 3

FINITE ELEMENT METHOD

This chapter addresses the basic aspects of the finite element discretisation oriented to the target beam models, considering linear and quadratic elements. At the end of this chapter, a brief discussion about the *shear-locking* issue is also presented.

3.1 Preliminaries

In the finite element method, the problem domain is discretised in a finite number of subdomains called *elements*. In typical one-dimensional beam elements, a *local* coordinate system is usually defined with the x axis oriented along the beam axis. If the beam length is L, the following domain discretisation is created:

$$\boldsymbol{D} \in [0\ L] \simeq \bigcup_{e=1}^{N_{e\ell}} \boldsymbol{D}_e^{e\ell} \quad \text{with} \quad \boldsymbol{D}_i^{e\ell} \bigcap \boldsymbol{D}_j^{e\ell} = \emptyset, \forall i, j = 1, \ldots, N_{e\ell} \tag{3.1}$$

where $N_{e\ell}$ is the number of elements, $\boldsymbol{D}_e^{e\ell} \in [0\ L_e]$ is the element domain, and L_e is the element length. In finite element implementations, the so-called *isoparametric* formulation is usually adopted. In this case, a *natural* coordinate system is defined such that the *local* coordinate x and the *natural* coordinate ξ (see Fig. 3.1) are related by the following expression:

$$\xi(x) = \frac{2x - L_e}{L_e} \tag{3.2}$$

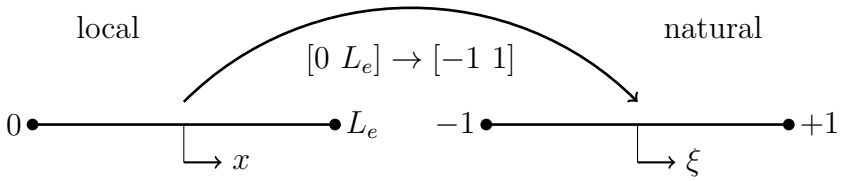

Figure 3.1: Local and natural coordinate systems representation

Within each element, the field variables can be interpolated through the shape functions obtained from the *natural* coordinate system. The Lagrange polynomials are usually

employed to obtain the *isoparametric* shape functions:

$$N_i = \prod_{j=1 \wedge j \neq i}^{h} \frac{\xi_j - \xi}{\xi_j - \xi_i} \tag{3.3}$$

where h is the number of element nodes, which is also referred to the element *incidence*. The terms ξ_i and ξ_j are the values of the *natural coordinate* ξ on the nodes i and j respectively.

Using Eq. (3.3) it is possible to obtain different orders of approximation, depending on the number of nodes of each element. Two-nodes elements results in the linear shape functions depicted in Fig. 3.2, while three-nodes elements results in the quadratic shape functions illustrated in Fig. 3.3.

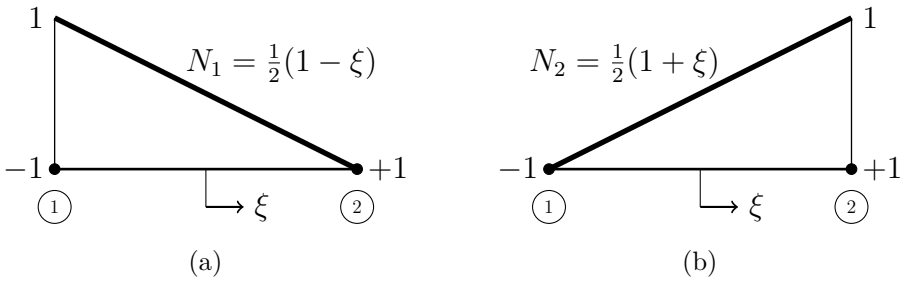

Figure 3.2: Linear FEM shape functions

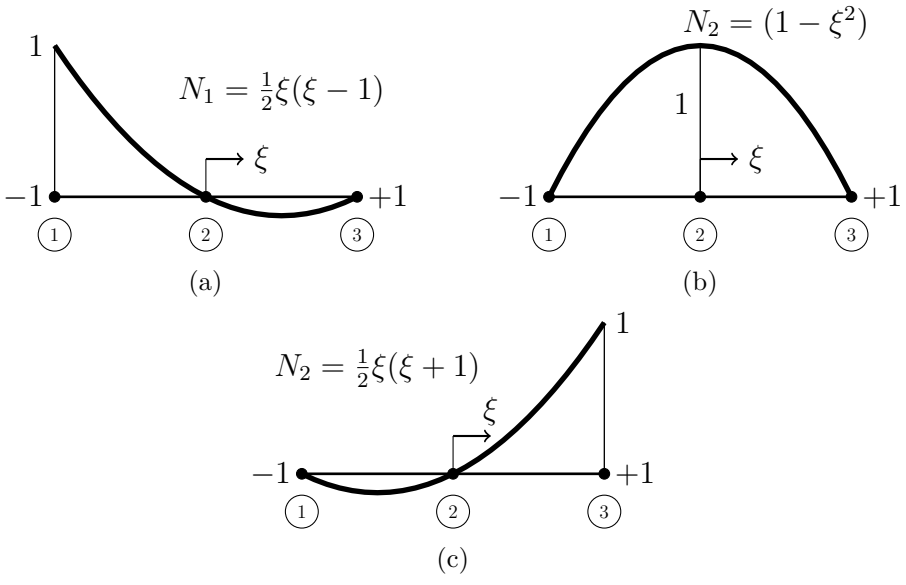

Figure 3.3: Quadratic FEM shape functions

Due to the transformation between the *local* and *natural* coordinate systems, it is necessary to obtain the determinant of the *Jacobian*[1] and its inverse, this is necessary for the use of the numerical integration commonly employed in FEM implementations. For beam applications, they are easily determined from Eq. (3.2):

[1]This is the Jacobian matrix that commonly appears in coordinate system transformations.

$$|J| = \frac{\partial x}{\partial \xi} = \frac{L_e}{2}, \quad |J|^{-1} = \frac{\partial \xi}{\partial x} = \frac{2}{L_e} \tag{3.4}$$

3.2 Discretisation

In the finite element method the field variables are approximated in terms of nodal values and shape functions. In what follows, the discretisation of the target beam models is briefly discussed considering the *isoparametric* formulation.

3.2.1 Timoshenko beam

For the Timoshenko beam model, the deflection v and rotation θ within each element are interpolated as

$$v \simeq \sum_{i=1}^{h} N_i^v(\xi) d_i^v, \quad \theta \simeq \sum_{i=1}^{h} N_i^\theta(\xi) d_i^\theta \tag{3.5}$$

where the index i indicates the ith node of the element *incidence*, N_i^v and N_i^θ are the shape functions used to interpolate the nodal values d_i^v and d_i^θ of deflections and rotations, respectively. The superscripts v and θ are just to emphasise that different shape functions can be adopted to approximate different nodal variables.

The shear and bending strains appearing in Eq. (2.1) can be expressed as

$$\omega = \frac{\partial \theta}{\partial x} = \frac{\partial \xi}{\partial x}\frac{\partial \theta}{\partial \xi} \simeq \frac{\partial \xi}{\partial x} \sum_{i=1}^{h} \frac{\partial N^v(\xi)}{\partial \xi} d_i^\theta \tag{3.6}$$

$$\gamma = \frac{\partial v}{\partial x} - \theta \simeq \frac{\partial \xi}{\partial x} \sum_{i=1}^{h} \frac{\partial N^v(\xi)}{\partial \xi} d_i^v - \sum_{i=1}^{h} N^\theta(\xi) d_i^\theta \tag{3.7}$$

Recalling that $d\xi/dx = 2/L_e$, the above strain measures can be recasted in the following array

$$\{\varepsilon(\xi)\} \coloneqq \begin{pmatrix} \omega(\xi) \\ \gamma(\xi) \end{pmatrix} = \frac{2}{L_e} \sum_{i=1}^{h} \begin{pmatrix} 0 & \dfrac{\partial N_i^\theta(\xi)}{\partial \xi} \\ \dfrac{\partial N_i^v(\xi)}{\partial \xi} & -N_i^\theta(\xi)\dfrac{L_e}{2} \end{pmatrix} \begin{pmatrix} d_i^v \\ d_i^\theta \end{pmatrix} = \sum_{i=1}^{h} [B]_i(\xi)\{d_i\} \tag{3.8}$$

The constitutive law can also be recasted in a matrix form as[2]:

[2]Here the constitutive matrix has been represented as a constant term. However, the case of variable properties along the beam axis can be easily obtained by considering a constitutive matrix that is constant within a single element (i.e. piecewise constant along the beam axis).

$$\begin{pmatrix} M \\ Q \end{pmatrix} = [E]\{\varepsilon\}; \quad [E] := \begin{pmatrix} EI & 0 \\ 0 & GA_s \end{pmatrix} \tag{3.9}$$

where the constitutive matrix $[E]$ has been introduced. Finally, the bilinear form of Eq. (2.8) can be expressed as

$$a\left((\delta v, \delta\theta), (v, \theta)\right) = \int_{-1}^{1} \left(\varepsilon^T(\xi)[E]\varepsilon(\xi)\right) |J| \, d\xi \tag{3.10}$$

where $|J|$ is the *determinant* of the jacobian matrix. The representation in terms of shape functions and nodal parameters results in an algebraic system representing the behaviour of the whole discrete model:

$$[K] \{X\} = \{R\} \tag{3.11}$$

where $[K]$ is the global stiffness matrix of the system, $\{X\}$ the nodal parameters vector collecting all the nodal parameters $\{d_i\}$, and $\{R\}$ the vector of nodal dual parameters (i.e. nodal forces and moments). The stiffness matrix $[K]$ can be evaluated starting from the stiffness matrix $[K_{e\ell}]$ of the single elements

$$[K_{e\ell}] = \int_{-1}^{1} [B(\xi)]^T [E] [B(\xi)] |J| \, d\xi \tag{3.12}$$

where the matrix $[B(\xi)]$ is composed by the submatrices $[B_i(\xi)]$ as

$$[B(\xi)] = ([B_1(\xi)] \dots [B_i(\xi)] \dots [B_h(\xi)]) \tag{3.13}$$

In Eq. (3.12) the stiffness matrix gathers the contributions of the shear and bending strains. However, it is also common to split Eq. (3.12) revealing the contributions of the shear and bending strains separately:

$$[K_b] = \int_{-1}^{1} [B_b(\xi)]^T [E_b] [B_b(\xi)] \, |J| \, d\xi \quad [K_s] = \int_{-1}^{1} [B_s(\xi)]^T [E_s] [B_s(\xi)] \, |J| \, d\xi \tag{3.14}$$

where the subscript b refers to bending, while the subscript s refers to shear. In the above equation the following relations can be identified

$$[B] = \begin{pmatrix} [B_b] \\ [B_s] \end{pmatrix} = \frac{2}{L_e} \sum_{i=1}^{h} \begin{pmatrix} 0 & \dfrac{\partial N_i^\theta(\xi)}{\partial \xi} \\ \dfrac{\partial N_i^v(\xi)}{\partial \xi} & -N_i^\theta(\xi) \dfrac{L_e}{2} \end{pmatrix} \tag{3.15}$$

and

$$[E] = \begin{pmatrix} [E_b] & [0] \\ [0] & [E_s] \end{pmatrix} = \begin{pmatrix} EI & 0 \\ 0 & GA_s \end{pmatrix} \tag{3.16}$$

3.2.2 Geometrically exact beam

As shown in Section 2.2, the geometrically exact beam is charaterised by the position of the line of centroids and the rotation of the cross-sections:

$$\mathcal{C} \equiv (\varphi_0, \underline{\boldsymbol{R}}) \tag{3.17}$$

In this beam model, the *local* coordinate system is defined by the variable S, i.e. the relation between the *local* and *natural* charts are expressed as

$$\xi(S) = \frac{2S - L_e}{L_e} \tag{3.18}$$

Using the *isoparametric* shape functions previously defined, the line of centroids is interpolated through its nodal values as follows

$$\varphi_0(\xi) \simeq \sum_{i=1}^{h} \boldsymbol{N}_i^{\varphi_0}(\xi)\ \boldsymbol{d}_i^{\varphi_0} \tag{3.19}$$

where the index i indicates a node i in the element *incidence*, $\boldsymbol{d}_i^{\varphi_0}$ gathers the nodal values of the line of centroids, and the operator $\boldsymbol{N}_i^{\varphi_0}(\xi)$ collects the shape functions used in the interpolation. Again, the superscript φ_0 is just to emphasise that the shape functions can be different depending of the quantity to be approximated, in this case, the line of centroids. It is worth noting that $\varphi_0(S,t)$ is composed by three values $\varphi_0(S,t) = [\varphi_{01}, \varphi_{02}, \varphi_{03}]$, therefore the shape functions of a particular *incidence node* can be expressed in the following matrix form

$$\varphi_0(\xi) = \begin{bmatrix} N_i^{\varphi_0}(\xi) & 0 & 0 \\ 0 & N_i^{\varphi_0}(\xi) & 0 \\ 0 & 0 & N_i^{\varphi_0}(\xi) \end{bmatrix} \begin{bmatrix} d_i^{\varphi_{01}} \\ d_i^{\varphi_{02}} \\ d_i^{\varphi_{03}} \end{bmatrix} \tag{3.20}$$

The derivative of the line of centroids is necessary to compute the shear deformation, taking into account the *natural* coordinates, this derivative is expressed by

$$\frac{\partial \varphi_0(\xi)}{\partial S} = \frac{\partial \boldsymbol{N}_i^{\varphi_0}}{\partial S}\boldsymbol{d}_i^{\varphi_0} = \frac{\partial \boldsymbol{N}_i^{\varphi_0}}{\partial \xi}\frac{\partial \xi}{\partial S}\boldsymbol{d}_i^{\varphi_0} \tag{3.21}$$

where

$$\frac{\partial \boldsymbol{N}_i^{\varphi_0}}{\partial S} = \begin{pmatrix} N_i^{\varphi_0}(\xi) & 0 & 0 \\ 0 & N_i^{\varphi_0}(\xi) & 0 \\ 0 & 0 & N_i^{\varphi_0}(\xi) \end{pmatrix} \frac{\partial \xi}{\partial S} \tag{3.22}$$

The *configuration increments* are interpolated through their nodal values, as follows

$$\bar{\boldsymbol{\eta}} \simeq \sum_{i=1}^{h} \boldsymbol{N}_{i,S}\, \bar{\boldsymbol{\eta}}_i \equiv \sum_{i=1}^{h} \begin{pmatrix} \boldsymbol{N}_i(\xi) & 0 \\ 0 & \boldsymbol{N}_i(\xi) \end{pmatrix} \begin{pmatrix} \bar{\boldsymbol{\eta}}_{0i} \\ \bar{\boldsymbol{\theta}}_i \end{pmatrix} \tag{3.23}$$

$$\Delta\varphi \simeq \sum_{i=1}^{h} \boldsymbol{N}_{i,S}\, \Delta\varphi_i \equiv \sum_{i=1}^{h} \begin{pmatrix} \boldsymbol{N}_i(\xi) & 0 \\ 0 & \boldsymbol{N}_i(\xi) \end{pmatrix} \begin{pmatrix} \bar{\boldsymbol{u}}_{0i} \\ \bar{\boldsymbol{\psi}}_i \end{pmatrix} \tag{3.24}$$

while the derivatives of the above expressions with respect to S can be written as

$$\frac{\partial \bar{\boldsymbol{\eta}}}{\partial S} \simeq \sum_{i=1}^{h} \boldsymbol{N}_{i,S}\, \bar{\boldsymbol{\eta}}_i \equiv \sum_{i=1}^{h} \begin{pmatrix} \boldsymbol{N}_{i,S}(\xi) & 0 \\ 0 & \boldsymbol{N}_{i,S}(\xi) \end{pmatrix} \begin{pmatrix} \bar{\boldsymbol{\eta}}_{0i} \\ \bar{\boldsymbol{\theta}}_i \end{pmatrix} \tag{3.25}$$

$$\frac{\partial \Delta\varphi}{\partial S} \simeq \sum_{i=1}^{h} \boldsymbol{N}_{i,S}\, \Delta\varphi_i \equiv \sum_{i=1}^{h} \begin{pmatrix} \boldsymbol{N}_{i,S}(\xi) & 0 \\ 0 & \boldsymbol{N}_{i,S}(\xi) \end{pmatrix} \begin{pmatrix} \bar{\boldsymbol{u}}_{0i} \\ \bar{\boldsymbol{\psi}}_i \end{pmatrix} \tag{3.26}$$

With this framework, it is possible to show that Eq. (2.77) assumes the following *material* representation

$$\begin{aligned} L[G(\varphi, \bar{\boldsymbol{\eta}}] = & \int_{-1}^{1} \left[\boldsymbol{N}^T(\xi)\boldsymbol{Q}(\xi) - \left(\boldsymbol{\Xi}^T(\xi)\boldsymbol{N}(\xi)\right)^T \boldsymbol{\Sigma}(\xi) \right] d\xi \\ & + \int_{-1}^{1} \left[\left(\boldsymbol{\Xi}^T(\xi)\boldsymbol{N}(\xi)\right)^T \underline{\boldsymbol{C}} \left(\boldsymbol{\Xi}^T(\xi)\boldsymbol{N}(\xi)\right) \right] d\xi \\ & + \int_{-1}^{1} \left[\left(\beta\boldsymbol{N}(\xi)\right)^T \boldsymbol{B}^T(\xi) \left(\beta\boldsymbol{N}(\xi)\right) \right] d\xi \\ & - \int_{-1}^{1} \boldsymbol{N}^T(\xi)\boldsymbol{L}(\xi)\boldsymbol{N}(\xi)\, d\xi \end{aligned} \tag{3.27}$$

All quantities appearing in Eq. (3.27) are defined in Section 2.2. In an implementation perspective, the integrals above are commonly solved using the *Gaussian quadrature*. For linear shape functions two integration points are employed to integrate the shape functions exactly, while three integration points are used for quadratic shape functions.

3.3 Shear locking effect

In this section the *shear-locking* phenomenon will be presented and briefly discussed. The following ideas are oriented to the Timoshenko beam, however they are valid for other models that share the same principles.

The finite element method applied to the Timoshenko beam model using linear shape

functions for the displacement $v(x)$ and the rotation $\theta(x)$ is considered the simplest element for this model. However when the beam is arbitrarily thin, that is to say, the length-to-thickness ratio become large, the resultant displacements are much smaller than the exact ones, in other words, the element used in the discretisation is *overly stiff* (Wang et al., 2000). This phenomenon arises due to the inconsistency of the interpolation used in $v(x)$ and $\theta(x)$ (Wang et al., 2000), and it is a well-known issue named as *shear-locking* (Bathe, 1996). In fact, this is a common numerical behaviour in shear-deformable beams.

Many authors proposed a way to overcome the shear locking in finite element applications. The two most common acceptable approaches are (Reddy, 2010)

- Reduced integration technique, consisting in a reduced integration for the evaluation of the transverse shear stiffness coefficients
- Consistent interpolation, that consists in the use of an approximation of $v(x)$ and $\theta(x)$ in a way that dv/dx and $\theta(x)$ possess the same polynomial degree

In addition to that, the *shear locking* can also be avoided using the *assumed shear strain* technique, which consists into assuming "a priori" a polynomial transverse shear strain field compatible to the model field variables (Oñate, 2013).

Hale (2013) demonstrated that *shear locking* problem remains in meshfree methods by contrasting the Timoshenko beam theory using the finite element method with the same model solved by a meshfree method. In addition, the shear locking behaviour is sensible to the discretisation parameters in meshfree methods, consequently this is a key information necessary to design locking-free meshfree method (Hale, 2013, p. 85). The meshfree methods used in Hale (2013) can be considered descendants of the element-free Galerkin method of Belytschko et al. (1995). The papers of Tiago and Pimenta (2005) and Marino (2016) cited in Chapter 1 are addressed to nonlinear beam models and the formulation approached in these works are *locking free*.

In order to overcome this problem, in all FEM numerical simulations throughout this work, the *reduced integration* technique is adopted for both, linear and geometrically nonlinear beam models. It is worth mentioning that the *shear locking* problem appears also in plate and shell models, however such discussion is not a matter to this work.

CHAPTER 4

SMOOTHED POINT INTERPOLATION METHODS

In this chapter the main concepts of the smoothed point interpolation methods are recalled. A vast and detailed information regarding the theory and applications of these methods can be found in Liu (2009) and Liu and Zhang (2013).

After introducing the meshfree methods and some basic aspects of them in Chapter 1, in this chapter the smoothed point interpolation methods (SPIMs) are presented. While the proposed SPIM model for shear-deformable beams is one-dimensional (Chapter 5), SPIM models are first introduced considering a more general two-dimensional case, that, due to its practical graphical representation, allows for a better illustration of the formulation. All this section is based primarily on the work of Liu (2009) and his research team.

As it will be pointed out in the following, SPIMs strategies are based on:

- shape functions obtained with the point interpolation and radial point interpolation methods
- different support nodes selection strategies
- different techniques for the domain tessellation
- a smoothing operation for the field variables derivatives

Similarly to the finite element method, field variables are approximated in terms of nodal values and shape functions; however, the concept of elements and its incidence, are replaced by the concepts of smoothing domains and support nodes. In addition to that PIM shape functions can be build including nodes beyond the integration cells, on the contrary of FEM shape functions that are constructed using only the nodes of the elements (Liu, 2009).

4.1 PIM shape functions

The point interpolation method (PIM) is one of the shape function construction strategies that can be adopted within the family of smoothed point interpolation methods, and makes use of polynomial basis functions. Other strategies are represented by the radial point interpolation method (RPIM) Wang and Liu (2000, 2002), Liu (2009) and the radial

point interpolation method with polynomial reproduction (RPIMp) Liu (2009). In the following, for brevity, only the PIM strategy will be illustrated; for a broader presentation, including radial basis functions and radial basis functions with polynomial reproduction, the reader may refer to Liu (2009). Let $u(p)$ be a field variable in the problem domain $\boldsymbol{D}$ with a number of scattered field nodes. The following series representation is used to approximate the function for a point of interest p:

$$u^h(p) = \sum_{i=1}^{n} p_i(p) a_i = \boldsymbol{p}^T(p)\boldsymbol{a} \tag{4.1}$$

where $\boldsymbol{p}^T(p)$ is the basis function of monomials, n is the number of *support* nodes selected in a local support domain, a_i is the coefficient for the monomial $p_i(p)$, and the vector $\boldsymbol{a}$ is expressed as follows

$$\boldsymbol{a} = [a_1, a_2, \ldots, a_n]^T \tag{4.2}$$

In the vicinity of p the coefficients a_i are constants; only when the support nodes associated with p change, the coefficients are updated. As explained by Liu (2009),

> "[...], in any finite discretization of the problem domain with nonduplicated nodes, $u^h(p)$ is consistent in finite local domains where these support nodes do not change. The order of the consistency depends on the polynomial basis functions used." (Liu, 2009, p. 61).

In general, the monomial $p_i(p)$ is chosen in a top-down approach from the Pascal triangle shown in Figure 4.1 particularised for a 2D case.

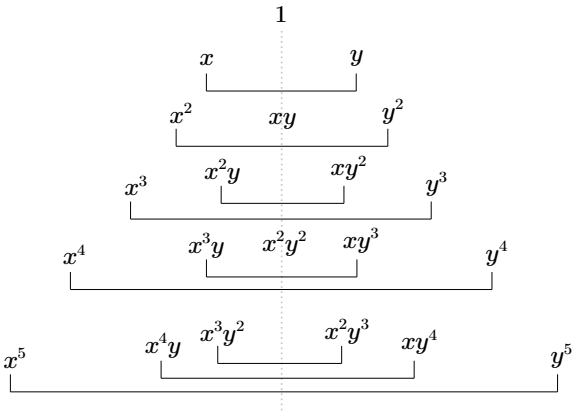

Figure 4.1: Pascal triangle of monomials, 2D case.

This process leads to a complete basis of the desired order. In Table 4.1 the basis used for 1D, 2D and 3D problems are presented.

At each point p, the unknown coefficient $\boldsymbol{a}_i$ can be obtained by imposing the interpolation condition of equation 4.1 at the n support nodes in the vicinity of p. For a generic node i it is possible to write

Dimension	Polynomial basis
1D	$\boldsymbol{p}^T(x) = \{1, x, x^2, x^3, x^4, \ldots, x^n\}$
2D	$\boldsymbol{p}^T = \boldsymbol{p}^T(x, y) = \{1, x, y, xy, x^2, y^2, \ldots, x^n, y^n\}$
3D	$\boldsymbol{p}^T = \boldsymbol{p}^T(x, y, z) = \{1, x, y, z, xy, yz, zx, xyz, x^2, y^2, z^2, \ldots, x^n, y^n, z^n\}$

Table 4.1: Complete polynomial basis for order n

$$u_i = \boldsymbol{p}^T(p_i)\boldsymbol{a} \qquad i = 1, 2, \ldots, n \tag{4.3}$$

where u_i is the nodal value of $\boldsymbol{u}$ at $p = p_i$.
The above equation can be rewritten in matrix form as follows:

$$\boldsymbol{d}_s = \boldsymbol{P}_Q\boldsymbol{a} \tag{4.4}$$

where $\boldsymbol{d}_s$ is a vector containing the nodal values of the field variable at the n support node

$$\boldsymbol{d}_s = \{u_1, u_2, \ldots, u_n\}^T \tag{4.5}$$

and $\boldsymbol{P}_Q$ is the moment matrix, expressed by

$$\boldsymbol{P}_Q = \begin{bmatrix} \boldsymbol{p}^T(p_1) \\ \boldsymbol{p}^T(p_2) \\ \vdots \\ \boldsymbol{p}^T(p_n) \end{bmatrix} \tag{4.6}$$

that for a 2D problem assumes the form

$$\boldsymbol{P}_Q = \begin{bmatrix} 1 & x_1 & y_1 & x_1y_1 & x_1^2 & y_1^2 & \ldots \\ 1 & x_2 & y_2 & x_2y_2 & x_2^2 & y_2^2 & \ldots \\ \vdots & \vdots & \vdots & \vdots & \vdots & \vdots & \vdots \\ 1 & x_n & y_n & x_ny_n & x_n^2 & y_n^2 & \ldots \end{bmatrix} \tag{4.7}$$

Assuming the matrix $\boldsymbol{P}_Q$ to be non-singular, it is possible to write the vector $\boldsymbol{a}$ as

$$\boldsymbol{a} = \boldsymbol{P}_Q^{-1}\boldsymbol{d}_s \tag{4.8}$$

Entering Equation 4.8 into Equation 4.1, results in

$$u^h(p) = \sum_{i=1}^{n} \phi_i(p)u_i = \boldsymbol{\varphi}(p)\boldsymbol{d}_s \tag{4.9}$$

where $\boldsymbol{\varphi}(p)$ is a matrix of PIM shape functions $\phi_i(p)$ defined by

$$\boldsymbol{\varphi}(p) = \boldsymbol{p}^T(p)\boldsymbol{P}_Q^{-1} = [\phi_1(p), \phi_2(p), \ldots, \phi_n(p)] \tag{4.10}$$

All the functions involved in the shape functions are polynomials, therefore their derivatives can be obtained without further complications; for the ℓth derivative

$$\boldsymbol{\varphi}_i^{\ell}(p) = [\boldsymbol{p}^{\ell}(p)]^T\boldsymbol{P}_Q^{-1} \tag{4.11}$$

As long as the moment matrix is invertible and linear terms are included in the basis (Table 4.1), it can be shown Liu (2009) that the PIM shape functions

- are linearly independent;
- possess the delta Kronecker property;
- form a partition of unity: $\sum_{i=1}^{n} \phi_i(p) = 1$;
- possess the linear reproduction property;
- present compact support (as long as they are constructed using compact support domains);
- are not compatible, meaning that they may present discontinuities when passing from a support domain to another

The moment matrix $\boldsymbol{P}_Q$ presented earlier might be singular for a certain node distribution on the support domain [1]. In order to avoid singularities some support nodes selection schemes have been proposed, for instance: T-schemes, K-nearest neighbors (KNN) algorithms with irregularly distributed nodes and radial basis for shape function creation.

4.2 Smoothing operation

In order to solve the issue of lack compatibility of PIM and RPIM shape functions, Liu Liu (2010*a*,*b*) proposed the use of a *weakened-weak form* where the continuity requirement is reduced. In a short description, this is a form obtained after performing the smoothing operation over the smoothing domains (see Section 4.3). For a comprehensive treatment to this matter the reader is referred to Liu (2009, 2010*a*,*b*).

Let us consider the derivative of a field variable f at a point $x \in \boldsymbol{D}_k^s$, next we replace its derivative by the *smoothed derivative* defined[2] in equation 4.12:

$$f_{i,j}(x) \approx \widetilde{f}_{i,j}(p_k) \coloneqq \int_{\boldsymbol{D}_k^S} f_{i,j}(\xi)\widetilde{W}(p_k - \xi)dV, \quad x \in \boldsymbol{D}_k^S \tag{4.12}$$

constant within a smoothing domain, where $\widetilde{W}$ is a *smoothing function* and where p_k is the centre of the smoothing domain. If the field variable f is continuous, the Green's divergence theorem can be applied, resulting in

[1] The existence of the inverse of the moment matrix depends not only on the node distribution, but also on the coordinate system.

[2] See Liu (2009, 2010*a*,*b*), Liu and Zhang (2013).

$$\widetilde{f}_{i,j}(p_k) = \int_{\partial \boldsymbol{D}_k^S} \left(f_i(\xi) \otimes n_j^k(\xi) \right) \widetilde{W}(p_k - \xi) dS - \int_{\boldsymbol{D}_k^S} f_i(\xi) \otimes \widetilde{W}_{,j}(p_k - \xi) dV \tag{4.13}$$

in above equation $\bar{\boldsymbol{n}}^k$ is the unitary outward normal on the boundary $\partial \boldsymbol{D}_k^S$. The *smoothing function* $\widetilde{W}$ is usually assumed to be the following Heaviside type function as follows

$$\widetilde{W}(p_k - \xi) \coloneqq \begin{cases} 1/A_k & \text{if } \xi \in \boldsymbol{D}_k^S \\ 0 & \text{if } \xi \notin \boldsymbol{D}_k^S \end{cases} \tag{4.14}$$

where $A_k = \int_{\boldsymbol{D}_k^s} dV$ is the area of the smoothing domain associated with the point at k, $\partial \boldsymbol{D}_k^S$ is the boundary of the smoothing domain associated with k. Substituting equation 4.14 in 4.13 leads to

$$\widetilde{f}_{i,j}(p_k) = \frac{1}{A_k} \int_{\partial \boldsymbol{D}_k^S} f_i(\xi) \otimes n_j^k(\xi) dS \tag{4.15}$$

This derivative is constant within the smoothing domain $\boldsymbol{D}_k^S$. As pointed out by Liu (2009) this approximation is not rigorous in theory, because the possibility of discontinuous field variables; however it is possible to implement and no differentiation of field variables is required. Hence it is assumed to be valid for both continuous and discontinuous field variables, i.e. whether the application of Green's theorem in Eq. (4.12) is licit or not.

4.3 Domain tessellation

At the beginning of Chapter 4, it has been pointed out that SPIMs strategies are based on peculiar tessellations of the problem domain in a set of smoothing domains. Focusing on 2D problems, this section illustrates three different strategies for domain tessellation, a node-based, an edge-based and a cell-based strategy, that results in the node-based smoothed point interpolation method (NS-PIM), edge-based smoothed point interpolation method (ES-PIM), and cell-based smoothed point interpolation method (CS-PIM), respectively. The first step consists in the discretisation of the domain $\boldsymbol{D}$ in a set of, non-overlapping, N_e *background cells* $\boldsymbol{D}_i^c$ $(i = 1, 2, 3, \ldots, N_e)$ whose vertices correspond to a set of N_n scattered nodes. The shape of these cells can be generic, however a triangular shape is generally used, due to the availability of efficient triangulation algorithms and due to the fact that the triangular cells can also be used for support nodes selection (Liu, 2009). The entire problem domain is tessellated in such way that $\cup_{i=1}^{n} \boldsymbol{D}_i^S = \boldsymbol{D}$ stands; in other words, the problem domain is completely covered by the smoothing domains.

In the NS-PIM, each smoothing domain is associated to a **node** of the background triangulation. Node-based smoothing domains can be created by the *equal-shared* or *Voroni*

strategies; however, only the former is illustrated in this section. With this technique, the generic smoothing domain $\boldsymbol{D}_i^S$, associated to the ith node, is generated by connecting the mid-edge points to the centroids of the surrounding triangular cells sharing this same node, as illustrated in Figure 4.2a.

In the ES-PIM each smoothing domain is associated to an **edge** of the background triangulation. The jth smoothing domain is obtained by connecting the nodes at the ends of the edge j with the centroids of the two triangular cells that share the same edge j, as illustrated in Figure 4.2b.

In the CS-PIM the triangular backgrounds **cells** usually constructed for 2D applications are used as smoothing domains. In other words after dividing the problem domain in triangles there is no need of an additional operation to construct the smoothing domains, as illustrated in Figure 4.2c.

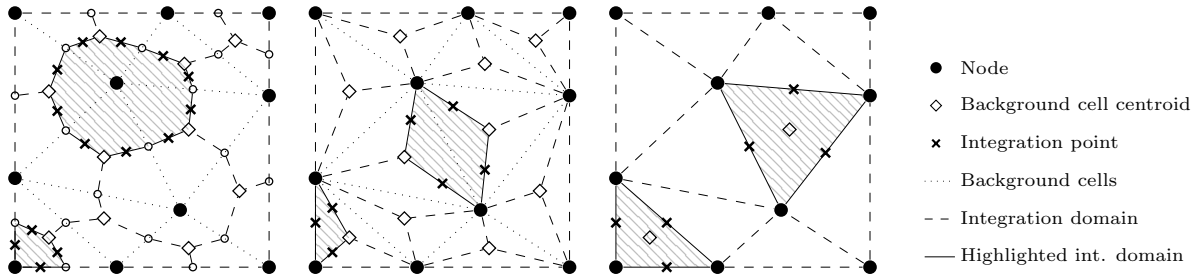

(a) Node-based (b) Edge-based (c) Cell-based

Figure 4.2: Two-dimensional smoothing domains

For all tessalation procedures the smoothing domains follow the no-sharing rule[3] and they are non-overlapping. As already pointed out, the problem domain is usually divided into a set of N_s smoothing domains using the triangulation as reference. However for two-dimensional applications quadrilateral background cells are also practical for implementations, as shown in Gori (2018).

4.4 Weakened-weak form

The theory and fundamentals regarding the weakened-weak (W^2) formulation, as well as the applications in solid mechanics problems, were established in the papers Liu (2010*a*) and Liu (2010*b*). This formulation is applicable to any problems where the standard formulation is also applicable. In order to illustrate the overall idea, first a classic weak form of an elasticity problem is considered:

$$a(\bar{\boldsymbol{w}}, \bar{\boldsymbol{u}}) = f(\bar{\boldsymbol{w}}) \tag{4.16}$$

[3]According to Liu (2009), the no-sharing rule means that the boundaries of smoothing domains do not share any finite portion with interfaces of the surrounding triangular cells. This property is fundamental for the numerical integration of SPIMs models.

The *bilinear form* $a(\bar{\boldsymbol{w}}, \bar{\boldsymbol{u}})$ and the *linear functional* $f(\bar{\boldsymbol{w}})$ appearing in expressions above are

$$a(\bar{\boldsymbol{w}}, \bar{\boldsymbol{u}}) \coloneqq \int_{\boldsymbol{D}} \underline{\boldsymbol{\varepsilon}}(\bar{\boldsymbol{w}}) \cdot \left(\underline{\underline{\hat{\boldsymbol{E}}}} \cdot \underline{\boldsymbol{\varepsilon}}(\bar{\boldsymbol{u}}) \right) \mathrm{d}\mathcal{V} \tag{4.17}$$

$$f(\bar{\boldsymbol{w}}) \coloneqq \int_{\partial \boldsymbol{D}} \bar{\boldsymbol{w}} \cdot \bar{\boldsymbol{t}} \, \mathrm{d}\mathcal{S} + \int_{\boldsymbol{D}} \bar{\boldsymbol{w}} \cdot \bar{\boldsymbol{b}}_V \, \mathrm{d}\mathcal{V} \tag{4.18}$$

where $\bar{\boldsymbol{u}}$ and $\bar{\boldsymbol{w}}$ are, respectively, the *trial* and *test* functions, $\bar{\boldsymbol{t}}$ is the vector of prescribed tractions, $\bar{\boldsymbol{b}}_V$ the vector of body forces, $\underline{\boldsymbol{\varepsilon}}$ the deformation tensor, and $\underline{\underline{\hat{\boldsymbol{E}}}}$ the elastic constitutive tensor.

Through the use of the smoothing operation introduced in Section 4.2 the weakened-weak form of a classic generic problem in elasticity is obtained by replacing the strain tensor $\underline{\boldsymbol{\varepsilon}}$ with its *smoothed version* $\underline{\tilde{\boldsymbol{\varepsilon}}}$, i.e. by replacing the derivatives of the displacement field by the smoothed derivative defined in Eq. (4.15).

Within each smoothing domain the strain field is assumed to be constant, hence the domain integral $\int_{\boldsymbol{D}}$ can be transformed in a summation over the N_S smoothing domains composing the discrete model. Therefore the *bilinear form* of Eq. (4.17) is converted into a *smoothed bilinear form* as follows

$$\tilde{a}(\bar{\boldsymbol{w}}, \bar{\boldsymbol{u}}) = \int_{\boldsymbol{D}} \underline{\tilde{\boldsymbol{\varepsilon}}}(\bar{\boldsymbol{w}}) \cdot \left(\underline{\underline{\hat{\boldsymbol{E}}}} \cdot \underline{\tilde{\boldsymbol{\varepsilon}}}(\bar{\boldsymbol{u}}) \right) \mathrm{d}\mathcal{S} \equiv \sum_{i=1}^{N_S} A_k \left[\underline{\tilde{\boldsymbol{\varepsilon}}}(\bar{\boldsymbol{w}}(p_k)) \cdot \left(\underline{\underline{\hat{\boldsymbol{E}}}} \cdot \underline{\tilde{\boldsymbol{\varepsilon}}}(\bar{\boldsymbol{u}}(p_k)) \right) \right] \tag{4.19}$$

4.5 Voigt notation and discretisation

Aiming to solve problems with discrete numerical methods, the *bilinear form* of Eq. (4.17) is here discretised and recasted in the Voigt notation. In order to illustrate the idea of the smoothing operation, a plane stress case is considered. In this case the strains can be represented in matrix form as follows

$$\{\underline{\boldsymbol{\varepsilon}}(\bar{\boldsymbol{u}})\} = [L]\{\bar{\boldsymbol{u}}\} = \begin{pmatrix} \varepsilon_{xx} \\ \varepsilon_{yy} \\ \varepsilon_{xy} \end{pmatrix} = \begin{pmatrix} \partial_x & 0 \\ 0 & \partial_y \\ \partial_y & \partial_x \end{pmatrix} \begin{pmatrix} u_x \\ u_y \end{pmatrix} \tag{4.20}$$

Combining the strains representation of Eq. (4.20) together with the bilinear form of Eq. (4.17) in a finite element method setting, it is possible to show that the stiffness matrix of a particular element $[K]_{e\ell}$ can be written as

$$[K]_{e\ell} = \int_{\boldsymbol{D}_{e\ell}} [B(p)]^T [\underline{\underline{\boldsymbol{E}}}(p)][B(p)] \, \mathrm{d}\mathcal{V} \tag{4.21}$$

where p is a point belonging to the element domain, and $\boldsymbol{D}_{e\ell}$ represents the element

domain. The matrix $[B(p)] = \left[\begin{array}{ccc} B_1(p) & ... & B_{N_{e\ell}}(p) \end{array} \right]$ is formed by $N_{e\ell}$ submatrices, such that

$$\{\underline{\boldsymbol{\varepsilon}}(p)\} = \sum_{i=1}^{N} [B_i(p)]\{d_i\} = \begin{pmatrix} \partial_x N_i(p) & 0 \\ 0 & \partial_y N_i(p) \\ \partial_y N_i(p) & \partial_x N_i(p) \end{pmatrix} \begin{pmatrix} d_{xi} \\ d_{yi} \end{pmatrix} \tag{4.22}$$

where $N_{e\ell}$ is the number of element nodes, and $N_i(p)$ is the shape function of the ith element node.

In order to achieve the weakened-weak form to be used in one of the SPIMs, the smoothing operation can be applied to the strain field resulting in a smoothed strain field

$$\{\widetilde{\underline{\boldsymbol{\varepsilon}}}(\bar{\boldsymbol{u}}(p_k)\} = \frac{1}{A_k} \int_{\partial \boldsymbol{D}_k^S} \left[\widetilde{L}_n(\xi)\right] [\bar{\boldsymbol{u}}(\xi)] \, \mathrm{d}\mathcal{S} \tag{4.23}$$

In the expression above, the matrix $[L]$ that gathers the derivatives is transformed according to Eq. (4.15) into the matrix $[\widetilde{L}_n]$, that gathers the components of the unit normal vector $\bar{\boldsymbol{n}}$. After performing the smoothing operation the strains in Eq. (4.20) are rewritten as follows[4]

$$\begin{pmatrix} \widetilde{\varepsilon}_{xx} \\ \widetilde{\varepsilon}_{yy} \\ \widetilde{\varepsilon}_{xy} \end{pmatrix} = \frac{1}{A_k} \int_{\partial \boldsymbol{D}_k^S} \begin{pmatrix} n_x^{(k)}(\xi) & 0 \\ 0 & n_y^{(k)}(\xi) \\ n_y^{(k)}(\xi) & n_x^{(k)}(\xi) \end{pmatrix} \begin{pmatrix} u_x(\xi) \\ u_y(\xi) \end{pmatrix} \mathrm{d}\mathcal{S} \tag{4.24}$$

Assuming that the constitutive operator $\underline{\boldsymbol{E}}$ is constant within each smoothing domain and recalling that the strains are also constant, the integral above can be replaced by a summation over the smoothing domains, as follows

$$\widetilde{a}(\bar{\boldsymbol{w}}, \bar{\boldsymbol{u}}) = \sum_{k=1}^{S} A_k \left(\widetilde{\underline{\boldsymbol{\varepsilon}}}(\bar{\boldsymbol{w}}(p_k)) \cdot (\underline{\boldsymbol{E}} \cdot \widetilde{\underline{\boldsymbol{\varepsilon}}}(\bar{\boldsymbol{u}}(p_k)))\right) \tag{4.25}$$

Using PIM and/or RPIM shape functions $\phi_i(x)$ the field variable $\bar{\boldsymbol{u}}$ can be approximated as

$$\bar{\boldsymbol{u}} \simeq \sum_{i \in S_d} [\phi_i(x)] \{d_i\} \tag{4.26}$$

where $\{d_i\}$ gathers the nodal parameters at the node i, and S_d is the support domain of the point $x \in \boldsymbol{D}$. At this point it is possible to express the smoothed strains in terms of the smoothed strain-displacement matrix

$$\{\widetilde{\underline{\boldsymbol{\varepsilon}}}(\bar{\boldsymbol{u}}(p_k)\} = \sum_{i \in S_d} \left[\widetilde{B}_i(p_k)\right] \{d_i\} \tag{4.27}$$

[4]Instead of the concept of element, in SPIM the concept of smoothing domains takes place.

where matrix $\left[\widetilde{B}_i(p_k)\right]$ assumes the following form for a plane stress state

$$\begin{aligned}\left[\widetilde{B}_i(p_k)\right] &= \frac{1}{A_k}\int_{\partial \boldsymbol{D}_k^S}\left[\widetilde{L}_n(\xi)\right]\left[\phi_i(\xi)\right]\,\mathrm{d}\mathcal{S} \\ &= \frac{1}{A_k}\int_{\partial \boldsymbol{D}_k^S}\begin{pmatrix} n_x^{(k)}(\xi)\phi_i(\xi) & 0 \\ 0 & n_y^{(k)}(\xi)\phi_i(\xi) \\ n_y^{(k)}(\xi)\phi_i(\xi) & n_x^{(k)}(\xi)\phi_i(\xi)\end{pmatrix} \\ &= \begin{pmatrix} \widetilde{\phi}_{i,x}(p_k) & 0 \\ 0 & \widetilde{\phi}_{iy}(p_k) \\ \widetilde{\phi}_{i,y}(p_k) & \widetilde{\phi}_{i,x}(p_k)\end{pmatrix}\end{aligned} \tag{4.28}$$

where the *smoothed derivatives* are expressed as

$$\widetilde{\phi}_{i,\ell}(p_k) = \frac{1}{A_k}\int_{\partial \boldsymbol{D}_k^S} n_\ell^{(k)}(\xi)\phi_i(\xi)\,\mathrm{d}\mathcal{S}, \quad \ell = x, y \tag{4.29}$$

In contrast with a finite element application, in the present method the stiffness matrix is computed for each *smoothing domain*

$$[K(p_k)]_{S_d} = A_k[\widetilde{B}(p_k)]^T[\underline{\boldsymbol{E}}(p_k)][\widetilde{B}(p_k)] \tag{4.30}$$

where $[\widetilde{B}_i(p_k)]$ is a submatrix computed for a particular node of the support domain S_d at the point p_k and $[\widetilde{B}(p_k)] = [\ \widetilde{B}_1(p_k)\ \ \ldots\ \ \widetilde{B}_N(p_k)\ ]$, and N is the number of support nodes.

4.6 Support node selection

As pointed out in the previous section, the creation of PIM, RPIM and RPIMp approximations at a given point depends on a certain number n of nodes in the neighbourhood of p, the so-called support nodes. While there exist different strategies for support nodes selection, in the present section only the so-called T-schemes will be illustrated.

As it will be illustrated in the following sections, SPIMs strategies are based on peculiar domain tessellations, built on triangular background cells (in 2D problem); as pointed out by Liu (2009), the same triangular cells can be used for the selection of support nodes. T-schemes stands for triangular cell-based node selection schemes and as explained in Liu (2009) they "have been found most practical, robust, reliable, and efficient for local supporting node selection"; in addition to that, PIMs works particularly well with these schemes for node selection. Liu (2009) presented five T-schemes, which are T3-scheme, T6/3-scheme, T6-scheme, T4-scheme and T2L-scheme. However, only the first two will be presented, which are illustrated in Figures 4.3 and 4.4. In general, given a point of interest p, its home cell is the background cell where the point of interest belongs to. If

this cell has no edge on the boundary of the problem domain it is termed as interior cell, otherwise boundary cell. A cell which shares one edge with the home cell is termed as neighbouring cell.

- T3-scheme: The same number of nodes is chosen for an interior home cell or for a boundary home cell. PIM linear shape functions can be created using this methodology. As the name suggests, in a T3-scheme three nodes are selected to compose the support domain.
- T6/3-scheme: given a point of interest six nodes are selected, three from the home cell and the others from the remote vertices of the three cells at the neighbourhood. For a boundary home cell only three nodes are used, which are the vertices of the home cell that hosts the point p.

Figures 4.3 and 4.4 presents the visual idea for both T-schemes presented.

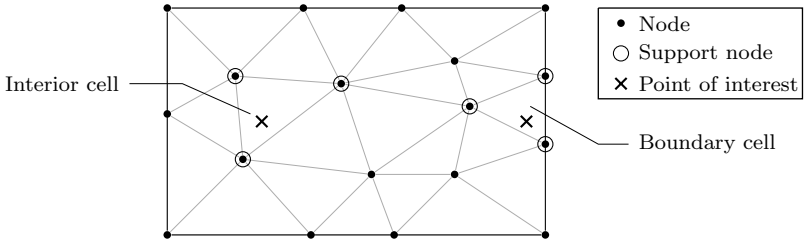

Figure 4.3: Support nodes selection via T3-scheme (2D case).

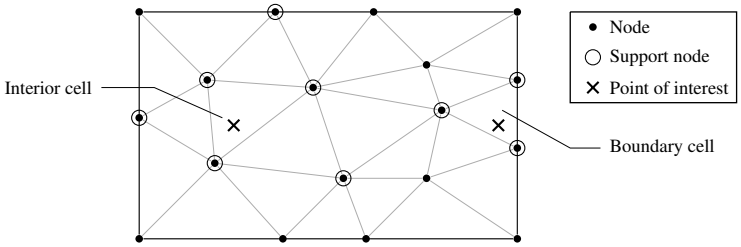

Figure 4.4: Support nodes selection via T6/3-scheme (2D case).

4.7 αPIM shape functions

In general SPIM models are able to offer a *softer* behaviour, in contrast with linear PIM that is able to reproduce the linear finite element method, which is often *stiffer* when compared to the exact solution. Using a scaling factor $\alpha \in [0\ 1]$ Liu et al. (2013) proposed the so called αPIM shape functions that combine the softer and stiffer models into an intermediary behaviour according to the α value, potentially improving the convergence to the analytical solution.

The procedure create the αPIM shape functions, starts with two sets of nodal PIM shape functions $S^{(I)}$ and $S^{(II)}$ available for a point of interest p:

$$\boldsymbol{\Phi}^{(I)}(p) = [\ \phi_1^{(I)}(p) \quad \phi_2^{(I)}(p) \quad \dots \quad \phi_n^{(I)}(p)\ ] \tag{4.31}$$

$$\boldsymbol{\Phi}^{(II)}(p) = [\ \phi_1^{(II)}(p) \quad \phi_2^{(II)}(p) \quad \dots \quad \phi_n^{(II)}(p)\ ] \tag{4.32}$$

These two sets does not have to be identical, however it is required that $S^{(I)}$ and $S^{(II)}$ possess some shared nodes. A function u at a point p can be interpolated using the nodes of the set of shape functions $S^{(I)}$

$$u(p) = \sum_{i=1}^{I_n} \phi_i^{(I)}(p) u_i \tag{4.33}$$

or the nodes of the set $S^{(II)}$

$$u(p) = \sum_{i=1}^{II_n} \phi_i^{(II)}(p) u_i \tag{4.34}$$

where I_n and II_n are, respectively, the number of support nodes in the two sets of $S^{(I)}$ and $S^{(II)}$. These sets of shape functions can be combined to approximate the field variable u as follows

$$u(p) = \alpha \left(\sum_{i=1}^{I_n} \phi_i^{(I)}(p) u_i \right) + (1-\alpha) \left(\sum_{i=1}^{II_n} \phi_i^{(II)}(p) u_i \right) \tag{4.35}$$

where $\alpha \in [0,1]$. The equation above can be recasted as follows

$$\begin{aligned} u(p) &= \alpha \left(\sum_{i=1}^{I_n} \phi_i^{(I)}(p) u_i \right) + (1-\alpha) \left(\sum_{i=1}^{II_n} \phi_i^{(II)}(p) u_i \right) \\ &= \sum_{i \in S^{(I)} \cap S^{(II)}} \left[\alpha \phi_i^{(I)}(p) + (1-\alpha) \phi_i^{(II)}(p)] u_i \right] \\ &+ \sum_{i \in S^{(I)} \setminus S^{(II)}} \alpha \phi_i^{(I)}(p) u_i + \sum_{i \in S^{(II)} \setminus S^{(I)}} (1-\alpha) \phi_i^{(II)} u_i(p) \end{aligned} \tag{4.36}$$

therefore

$$u(p) = \sum_{i \in S^{(\alpha)}} \phi_i^{(\alpha)}(p) u_i = \boldsymbol{\Phi}^{(\alpha)}(p) \boldsymbol{d} \tag{4.37}$$

For convenience the following set is termed as αPIM shape functions

$$\boldsymbol{\Phi}^{(\alpha)}(p) = [\ \phi_1^{(\alpha)}(p) \quad \phi_2^{(\alpha)}(p) \quad \dots \quad \phi_{n^{(\alpha)}}^{(\alpha)}(p)\ ] \tag{4.38}$$

where $n^{(\alpha)}$ is the number of nodes in the set of $S^{(\alpha)} = S^{(I)} \cup S^{(II)}$, with

$$\phi_i^{(\alpha)}(p) = \begin{cases} \alpha\phi_i^{(I)}(p) + (1-\alpha)\phi_i^{(II)}(p) & \forall i \in S^{(I)} \cap S^{(II)} \\ \alpha\phi_i^{(I)}(p) & \forall i \in S^{(I)} \setminus S^{(II)} \\ (1-\alpha)\phi_i^{(II)}(p) & \forall i \in S^{(II)} \setminus S^{(I)} \end{cases} \tag{4.39}$$

Liu et al. (2013) used a cell-based smoothed alpha radial point interpolation method (CS-αRPIM) approach, aiming to obtain better results by combining the "condensed RPIM (RPIM-Cd) shape functions and the linear PIM shape functions, where the former often leads to a "softer" CS-RPIM model, and the latter a "stiffer" linear CS-RPIM model (which is the same as linear FEM), compared to the exact one." A motivation to use αPIM shape functions is trying to control the stiffness/softness of the solution and obtain results closer to the exact one. In Liu et al. (2013) the authors proposed a way to estimate an *alpha* value that produces a solution "close" to exact one (see Liu et al. (2013)). The reader is referred to Liu et al. (2013) and Liu and Zhang (2013) to obtain more information regarding the numerical examples of 2D and 3D using CS-αRPIM.

CHAPTER 5

ONE-DIMENSIONAL SPIM FOR SHEAR-DEFORMABLE BEAMS

In Chapter 4, the smoothed point interpolation methods were introduced and illustrated for 2D applications. In this chapter, the SPIM will be extended to shear-deformable beams, hence a one-dimensional SPIM is discussed. As pointed out in Chapter 1, this work targets two models: (i) the linear Timoshenko beam, and (ii) the geometrically exact shear-deformable beam developed by Simo (1985) and Simo and Vu-Quoc (1986). To the knowledge of the author, this is the first application of smoothed point interpolation methods to shear-deformable beams (linear and nonlinear).

5.1 PIM shape functions

In Chapter 4 the PIM shape function generation was illustrated for 2D case, at this point the process will be particularised for 1D applications. Among the possibilities of shape functions creation (Chapter 4), this work focuses on PIM shape functions; later on this concept is also extended to the so-called αPIM shape functions (Section 5.7).

As already pointed out in the previous chapter, the interpolation of a field variable is represented at each point x as the following series representation (here a generic scalar field variable u is considered)

$$u(x) \simeq \sum_{i \in S_d} p_i(x)\ a_i = \{\mathbf{p}(\mathbf{x})\}^T \{\mathbf{a}\} \tag{5.1}$$

where the terms $p_i(x)$ are a set of monomials evaluated at x (see Table 4.1), each one associated to a coefficient a_i, and S_d is the set of *support nodes*. The set of monomials forms a polynomial basis, that depends on the number n of support nodes at x

$$\{\boldsymbol{p}(x)\}^T = \begin{pmatrix} 1 & x & x^2 & \dots & x^{n-1} \end{pmatrix} \tag{5.2}$$

Similarly to the 2D case, the unknown coefficients a_i are evaluated by imposing the interpolation condition $u(x_i) = d_i^u$, of the series representation, at each node of the support domain, resulting in the following matrix expression:

$$\{\mathbf{d^u}\} = [\mathbf{P}]\{\mathbf{a}\} \tag{5.3}$$

where $\{\mathbf{d^u}\} = (u_1 \ \dots \ u_n)^T$ is the vector of nodal parameters of the field variable u while $[\mathbf{P}]$ is the *moment matrix* expressed by

$$[\mathbf{P}] = \begin{pmatrix} \{\boldsymbol{p}(x_1)\}^T \\ \vdots \\ \{\boldsymbol{p}(x_n)\}^T \end{pmatrix} \tag{5.4}$$

Assuming the moment matrix to be invertible, the coefficients can be calculated as $\{\mathbf{a}\} = [\mathbf{P}]^{-1}\{\mathbf{d^u}\}$. Once replaced into Eq. (5.1), it is possible to express the shape functions ϕ_i^u as

$$\phi_i^u(x) = p_j(x)[\mathbf{P}]^{-1}_{ji} \tag{5.5}$$

It is worth to note that, contrary to the 2D case, the fact the all the nodes lies on the same straight line does not result in a singular *moment matrix*, as long as there are no duplicated nodes Liu (2009).

In general, in order to evaluate meshfree shape functions at a certain interest point, the numerical inversion of the *moment matrix* must be computed. With PIM shape functions however, it is possible to obtain analytical expressions, that can be used directly to evaluate the value of the shape functions at the interest points, avoiding the matrix inversion operation. In this work, PIM shape functions will be evaluated for support domains containing 2, 3, or 4 nodes; the process to obtain the shape functions are illustrated in Appendix C, where these functions are also plotted. In following equations, the shape functions obtained using two and three *support nodes* are represented, respectively

$$\boldsymbol{\Phi}^{(L2)}(x) = \begin{bmatrix} \dfrac{x_2 - x}{x_2 - x_1} & \dfrac{x - x_1}{x_2 - x_1} \end{bmatrix} \tag{5.6}$$

$$\boldsymbol{\Phi}^{(L3)}(x) = \begin{bmatrix} \dfrac{(x - x_2)(x - x_3)}{(x_1 - x_2)(x_1 - x_3)} & -\dfrac{(x - x_1)(x - x_3)}{(x_1 - x_2)(x_2 - x_3)} & \dfrac{(x - x_1)(x - x_2)}{(x_1 - x_3)(x_2 - x_3)} \end{bmatrix} \tag{5.7}$$

5.2 Smoothing operation

The first step of this strategy consists in the tessellation of the problem domain into a set of N_S non-overlapping *smoothing domains* $\boldsymbol{D}_k^S$, with $k = 1, \dots, N_S$; more details will be provided in Section 5.3 for the one-dimensional approach. The second step is the *smoothing operation* Liu (2008). At each point $x \in \boldsymbol{D}_k^S$ the derivative $f_{,x}$ of a generic function $f(x)$ is replaced by a *smoothed derivative* $\widetilde{f_{,x}}$ *constant* within a smoothing domain,

defined as

$$f_{,x} \simeq \widetilde{f_{,x}} := \int_{\boldsymbol{D}_k^S} f_x(\xi)\ \widetilde{W}(x_k - \xi)\ dx, \quad x \in \boldsymbol{D}_k^S \tag{5.8}$$

where x_k is the centre of $\boldsymbol{D}_k^S$, and $\widetilde{W}$ is a *smoothing function*, similarly to the 2D case, it is usually assumed to be the following Heaviside-type function:

$$\widetilde{W}(x_k - \xi) := \begin{cases} 1/\ell_k & \xi \in \boldsymbol{D}_k^S \\ 0 & \xi \notin \boldsymbol{D}_k^S \end{cases} \tag{5.9}$$

where $\ell_k = \int_{\boldsymbol{D}_k^S} dx$ is the length of the smoothing domain. For the 2D case it was the area A_k of the smoothing domain. If the function $f(x)$ is continuous, Green's divergence theorem can be applied, and the domain integral $\int_{\boldsymbol{D}_k^S}$ can be replaced by

$$\widetilde{f_{,x}} = \frac{1}{\ell_k}\ f(\xi)\ n_x^{(k)}(\xi)\Big|_{\boldsymbol{\Gamma}_k := \partial \boldsymbol{D}_k^S} \tag{5.10}$$

where $n_x^{(k)}$ is the unitary outward normal on the boundary $\boldsymbol{\Gamma}_k := \partial \boldsymbol{D}_k^S$. It's worth it to note that, while in more general 2D and 3D SPIM models a unit normal vector would appear in Eq. (5.10), here $n_x^{(k)}$ is a scalar, assuming values -1 or $+1$, when pointing in the negative and positive directions of the x-axis. It is important to highlight again that the application of Green's theorem is used whether it is licit or not, since Eq. (5.10) requires no differentiation of $f(x)$, opening the possibility to use PIM and RPIM *incompatible* functions for the approximation.

5.2.1 Timoshenko beam

Analogous to the 2D case shown in Chapter 4, the smoothing operation is applied to the shear $\gamma(x)$ and bending $\omega(x)$ strains, recalled here in the following

$$\{\varepsilon(x)\} = \begin{bmatrix} \omega(x) \\ \gamma(x) \end{bmatrix} = \begin{bmatrix} \dfrac{\partial \theta(x)}{\partial x} \\ \dfrac{\partial v(x)}{\partial x} - \theta(x) \end{bmatrix} \tag{5.11}$$

At each point x of a certain smoothing domain $\boldsymbol{D}_k^S$, $\gamma = \gamma(x)$ and $\omega = (x)$ are replaced by the smoothed shear strain $\widetilde{\gamma} = \widetilde{\gamma}(x_k)$ and by the smoothed curvature $\widetilde{\omega} = \widetilde{\omega}(x_k)$ that depend on the value of the field variables at the centre x_k of the smoothing domain $\boldsymbol{D}_k^S$, and that are defined by

$$\gamma(x) \simeq \widetilde{\gamma}(x_k) = \int_{\boldsymbol{D}_k^S} \left(\frac{\partial v(\xi)}{\partial x} - \theta(\xi) \right) \widetilde{W}(x_k - \xi)\, dx, \quad x \in \boldsymbol{D}_k^S \tag{5.12}$$

$$\omega(x) \simeq \widetilde{\omega}(x_k) = \int_{\boldsymbol{D}_k^S} \frac{\partial \theta(\xi)}{\partial x}\, \widetilde{W}(x_k - \xi)\, dx, \quad x \in \boldsymbol{D}_k^S \tag{5.13}$$

Applying the integration by parts associated to the Green's divergence theorem, equations above become

$$\begin{aligned}\widetilde{\gamma}(x_k) = v(\xi)\ \widetilde{W}(x_k-\xi)\ n_x^{(k)}(\xi)\Big|_{\boldsymbol{\Gamma}_k} \\ - \int_{\boldsymbol{D}_k^S} v(\xi)\ \frac{\partial \widetilde{W}(x_k-\xi)}{\partial x}\,dx - \int_{\boldsymbol{D}_k^S} \theta(\xi)\ \widetilde{W}(x_k-\xi)\ dx\end{aligned} \tag{5.14}$$

$$\widetilde{\omega}(x_k) = \theta(\xi)\ \widetilde{W}(x_k-\xi)\ n_x^{(k)}(\xi)\Big|_{\boldsymbol{\Gamma}_k} - \int_{\boldsymbol{D}_k^S} \theta(\xi)\ \frac{\partial \widetilde{W}(x_k-\xi)}{\partial x}\,dx \tag{5.15}$$

Assuming the same Heaviside-type smoothing function illustrated in Eq. (5.9), Eqs. (5.14) and (5.15) reduce to

$$\widetilde{\gamma}(x_k) = \frac{1}{\ell_k} v(\xi)\ n_x^{(k)}(\xi)\Big|_{\boldsymbol{\Gamma}_k} - \widetilde{\theta}(x_k) \tag{5.16}$$

$$\widetilde{\omega}(x_k) = \frac{1}{\ell_k} \theta(\xi)\ n_x^{(k)}(\xi)\Big|_{\boldsymbol{\Gamma}_k} \tag{5.17}$$

where $\widetilde{\theta}(x_k)$ is a smoothed version of the rotation θ, constant over the smoothing domain $\boldsymbol{D}_k^S$, and defined as[1]

$$\widetilde{\theta}(x_k) := \frac{1}{\ell_k} \int_{\boldsymbol{D}_k^S} \theta(\xi)\ dx \tag{5.18}$$

As it can be observed in Eqs. (5.16) and (5.17), with the application of Green's divergence theorem, all the domain integrals where the field variables appeared in terms of their derivatives have been transformed into a function evaluation on the boundary of each smoothing domain. However, due to the presence of the field variable θ, the smoothed shear strain $\widetilde{\gamma}(x_k)$ (Eq. (5.16)) still contains a domain integral (Eq. (5.18)), which requires a special treatement for the construction of a Timoshenko weakened-weak form. This problem is not new to SPIM strategies, and more in general to methods that require strain smoothing operations (e.g. for nodal integration), and has been already dealt with for *axisymmetric* problems Chen et al. (2002), Tootoonchi and Khoshghalb (2016) and for the *micropolar* continuum theory Gori et al. (2019). According to the results available in the literature, two approaches can be followed. Tootoonchi and Khoshghalb (2016) considered axisymmetric problems with the application of the cell-based smoothed point interpolation method (see Chapter 4). The strain terms depending on the field variable were treated by the authors by performing a numerical integration of the domain integral, using integration points inside each smoothing domain. Applying this approach to the smoothed Timoshenko shear strain of Eq. (5.16) would require to perform the numerical

[1]Based on the idea of defining a function by an integral as presented in Eq. (5.8)

integration of Eq. (5.18), in order to evaluate the smoothed rotation. Chen et al. (2002) instead, proposed a nodal integration strategy for Galerkin meshfree methods applied to geometrical non-linearities and elasto-plasticity. The case of axisymmetric problems was briefly mentioned, stating that the strain terms containing the field variable should be evaluated nodally. Within this approach the following approximation should be introduced

$$\widetilde{\theta}(x_k) = \theta(x_k) \tag{5.19}$$

which consists in approximating the smoothed field variable appearing in Eq. (5.16) with its value at the centre x_k of each smoothing domain. The latter approach was also considered by Gori et al. (2019) for the application of the SPIM strategy to the micropolar continuum theory. Just like the Timoshenko shear strain, one of the micropolar deformation measures contains a field variable (i.e. the microrotation of the material points), besides the derivatives of other field values (i.e. the displacements of the material points). In the present work the approach by Chen et al. (2002) and by Gori et al. (2019) has been preferred on the one by Tootoonchi and Khoshghalb (2016), since it led to a more simple treatement of the shear strain measure, also from a computational point of view. Then, replacing Eq. (5.19) into Eq. (5.16), the smoothed Timoshenko shear strain can be expressed as

$$\widetilde{\gamma}(v(x_k)) = \frac{1}{\ell_k} v(\xi)\ n_x^{(k)}(\xi)\Big|_{\mathbf{\Gamma}_k} - \theta(x_k) \tag{5.20}$$

Introducing Eqs. (5.17) and (5.20) into the weak form of the Timoshenko beam allows to obtain the so-called weakened-weak form, with a reduced requirement of continuity for the trial and test functions. More details are provided in Section 5.4.1, where the discretisation of the weakened-weak form with PIM shape functions is also discussed.

5.2.2 Geometrically exact beam

Following the same principles discussed before, the smoothing operation is applied to the strain measures of the geometrically exact beam. Since the implementation constructed[2] to solve the nonlinear model deals only with material quantities, the smoothing operation is performed taking into account only the *material* strain measures. In what follows, the expressions of the *material* curvature and shear strains are recalled

$$\underline{\boldsymbol{\Omega}}(S,t) = \underline{\boldsymbol{R}}^T(S,t)\underline{\boldsymbol{\omega}}(S,t)\underline{\boldsymbol{R}}(S,t) = \underline{\boldsymbol{R}}^T(S,t)\frac{\partial \underline{\boldsymbol{R}}(S,t)}{\partial S} \tag{5.21}$$

[2]For this master's thesis purposes. In general, it is also possible to implement a code taking into account the *spatial* configuration of the beam during its motion.

$$\bar{\boldsymbol{\Gamma}}(S,t) = \underline{\boldsymbol{R}}^T(S,t)\bar{\boldsymbol{\gamma}}(S,t) = \underline{\boldsymbol{R}}^T(S,t)\frac{\partial\boldsymbol{\varphi}_0(S,t)}{\partial S} - \boldsymbol{\partial E}_3(S) \tag{5.22}$$

Similarly[3] to the Timoshenko beam case, at each point x of a certain smoothing domain[4] $\boldsymbol{D}_k^S$, $\bar{\boldsymbol{\Gamma}} = \bar{\boldsymbol{\Gamma}}(S)$ and $\underline{\boldsymbol{\Omega}} = \underline{\boldsymbol{\Omega}}(S)$ are replaced by the smoothed shear strain $\widetilde{\bar{\boldsymbol{\Gamma}}} = \widetilde{\bar{\boldsymbol{\Gamma}}}(x_k)$ and by the smoothed curvature $\underline{\widetilde{\boldsymbol{\Omega}}} = \underline{\widetilde{\boldsymbol{\Omega}}}(x_k)$ that depend on the value of the field variables at the centre x_k of the smoothing domain $\boldsymbol{D}_k^S$. First, the smoothed curvature is introduced as

$$\underline{\widetilde{\boldsymbol{\Omega}}}(x_k) = \int_{\boldsymbol{D}_k^S} \underline{\boldsymbol{\Omega}}\, \widetilde{W}(x_k - \xi)d\xi = \int_{\boldsymbol{D}_k^S} \left[\underline{\boldsymbol{R}}^T(\xi)\frac{\partial\underline{\boldsymbol{R}}(\xi)}{\partial S}\right] \widetilde{W}(x_k - \xi)\, d\xi \tag{5.23}$$

Assuming the weight function to be the one defined in Eq. (5.9) results in

$$\underline{\widetilde{\boldsymbol{\Omega}}}(x_k) = \frac{1}{\ell_k}\int_{\boldsymbol{D}_k^S} \underline{\boldsymbol{\Omega}}\, d\xi = \frac{1}{\ell_k}\int_{\boldsymbol{D}_k^S} \left[\underline{\boldsymbol{R}}^T(\xi)\frac{\partial\underline{\boldsymbol{R}}(\xi)}{\partial S}\right] d\xi \tag{5.24}$$

In the expression above, the presence of the rotation tensor premultiplying its derivative, does not allow for a straightforward application of the Green's theorem, aiming to transform the domain integral into a boundary integral. For this purpose, Eq. (5.24) is simplified by assuming the rotation tensor (though not its derivative) to be constant within each smoothing domain, and equal to the value corresponding to the centre of the smoothing domain. This is somehow similar to the procedure illustrated in Eq. (5.18) and adopted for the Timoshenko beam. With this assumption, the term $\underline{\boldsymbol{R}}^T(\xi)$ can be removed from the domain integral, resulting in

$$\underline{\widetilde{\boldsymbol{\Omega}}}(x_k) = \frac{\underline{\boldsymbol{R}}^T(x_k)}{\ell_k}\int_{\boldsymbol{D}_k^S} \frac{\partial\underline{\boldsymbol{R}}(\xi)}{\partial S}\, d\xi \tag{5.25}$$

Now it is possible to apply the Green's theorem to the integral of Eq. (5.25), resulting in the following expression of the smoothed curvature tensor:

$$\underline{\widetilde{\boldsymbol{\Omega}}}(x_k) = \frac{\underline{\boldsymbol{R}}^T(x_k)}{\ell_k}\left[\underline{\boldsymbol{R}}(\xi)\; n_S^{(k)}(\xi)\right]\Big|_{\boldsymbol{\Gamma}_k} \tag{5.26}$$

Likewise, the smoothing operation is applied to the shear strain measure $\bar{\boldsymbol{\Gamma}}(S)$

$$\bar{\boldsymbol{\Gamma}}(S) \simeq \widetilde{\bar{\boldsymbol{\Gamma}}}(x_k) = \int_{\boldsymbol{D}_k^S} \left[\underline{\boldsymbol{R}}^T(\xi)\frac{\partial\boldsymbol{\varphi}_0(\xi)}{\partial S} - \boldsymbol{\partial E}_3(\xi)\right] \widetilde{W}(x_k - \xi)\, d\xi \tag{5.27}$$

In agreement with the procedure performed for the material curvature, the rotation tensor $\underline{\boldsymbol{R}}^T(\xi)$ appearing in Eq. (5.27) is assumed to be constant, and equal to the value corresponding to the centre of the smoothing domain, resulting in

[3] The variable t is omitted in the following equations.

[4] The letter S appearing in $\boldsymbol{D}_k^S$ to represent the smoothing domain should not be confused with the variable S employed in the geometrically exact beam formulation.

$$\tilde{\bar{\boldsymbol{\Gamma}}}(x_k) = \frac{\underline{\boldsymbol{R}}^T(x_k)}{\ell_k} \int_{\boldsymbol{D}_k^S} \left[\frac{\partial \varphi_0(\xi)}{\partial S} - \partial E_3(\xi) \right] d\xi \tag{5.28}$$

and then in

$$\tilde{\bar{\boldsymbol{\Gamma}}}(x_k) = \frac{\underline{\boldsymbol{R}}^T(x_k)}{\ell^S} \int_{\boldsymbol{D}_k^S} \frac{\partial \varphi_0(\xi)}{\partial S} d\xi - \widetilde{\partial E_3(\xi)} \tag{5.29}$$

with $\widetilde{\partial E_3(\xi)} = \int_{\boldsymbol{D}_k^S} \partial E_3(\xi)\, d\xi$. The smoothing vector will be approximated to the vector itself $\widetilde{\partial E_3(S)} \approx \partial E_3(S)$, therefore

$$\tilde{\bar{\boldsymbol{\Gamma}}}(x_k) = \frac{\underline{\boldsymbol{R}}^T(x_k)}{\ell_k} \left[\varphi_0(\xi)\ n_S^{(k)}(\xi) \right] \Big|_{\boldsymbol{\Gamma}_k} - \partial E_3(S) \tag{5.30}$$

5.3 Domain tessellation

In a one-dimensional problem, as beam-like structures, there are two possible tessellations, that can be seen as degenerations of the ones depicted in Figs. 4.2a to 4.2c. The first one is a node-based tessellation, analogous to the one of the two-dimensional case depicted in Fig. 4.2a. The other is a degeneration of both the edge- and cell-based tessellations of the two-dimensional case.

The node-based one-dimensional tessellation has already been used in the literature by Liu and his co-authors (Cui et al., 2008, Liu, 2009, Du et al., 2018), for the static and dynamic analysis of Euler-Bernoulli beams. As illustrated in Fig. 5.1, the beam axis is divided into a set of background cells, whose end-points are the nodes of the discretisation. The smoothing domain $\boldsymbol{D}_k^S$ associated to the node x_k (the centre of the smoothing domain where to evaluate the rotation θ appearing in Eq. (5.20)) is delimited by the mid-points of the background cells adjacent to x_k. These mid-points are then the boundary $\boldsymbol{\Gamma}_k$ of the smoothing domain, and serve as integration points to evaluate the smoothed deformation measures of the beam problems. While this holds for the internal smoothing domains, the ones at the end-points of the beam are delimited by a mid-point and by a node, i.e. one of the integration points corresponds to a node (Fig. 5.1).

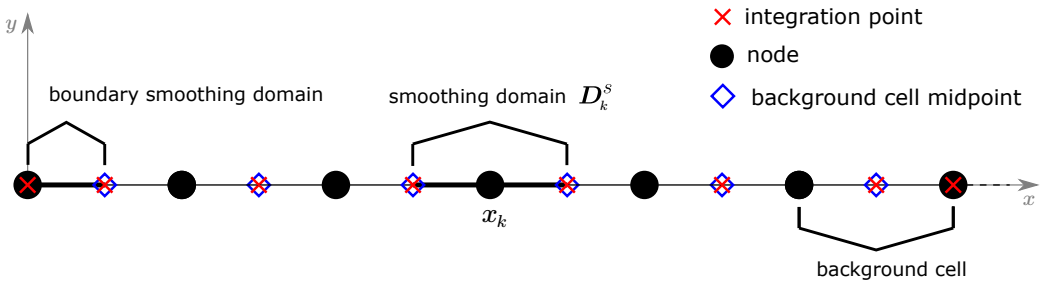

Figure 5.1: Node-based one-dimensional smoothing domain

This work also proposes the use of an edge-based one-dimensional tessellation. As the node-based tessellation depicted in Fig. 5.1, the edge-based tessellation illustrated in Fig. 5.2 is obtained as a degeneration of the corresponding two-dimensional tessellation (though in this case, both the edge- and cell-based cases degenerate to the same one-dimensional tessellation). The beam axis is divided into the same background cells already adopted for the node-based case. Each smoothing domain $\boldsymbol{D}_k^S$ is now associated to the mid-point x_k of a background cell (that is also the centre of the smoothing domain where to evaluate the rotation θ appearing in Eq. (5.20)), and its boundary $\boldsymbol{\Gamma}_k$ is represented by the two nodes that constitute the end-points of the background cell. These two nodes also serve as integration points for the evaluation of the smoothed deformation measures. In this case, there is no distinction between internal and boundary smoothing domains.

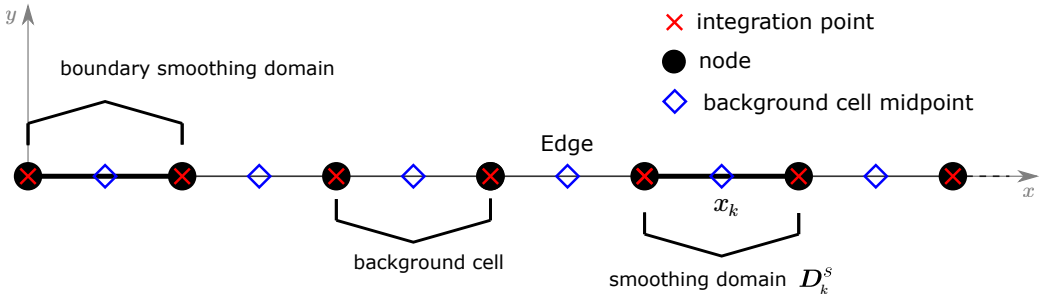

Figure 5.2: Edge-based one-dimensional smoothing domain

As illustrated in Section 4.3, for the same background cells dividing the problem domain, it is possible to create different smoothing domains strategies in SPIM.

5.4 Weakened-weak form

With the concept of smoothing operation in hands, it is possible to obtain the weakened-weak form of the target beam models.

5.4.1 Timoshenko beam

The weakened-weak form of the Timoshenko beam problem can be obtained from the standard weak form of Eq. (2.7), by replacing the deformation measures γ and ω with the corresponding smoothed deformation measures $\widetilde{\gamma}$ and $\widetilde{\omega}$. This substitution results in the following *smoothed bilinear form*

$$\widetilde{a}\left((\delta v, \delta\theta), (v, \theta)\right) = \int_0^L \widetilde{\delta\omega}\; EI\; \widetilde{\omega}\; dx + \int_0^L \widetilde{\delta\gamma}\; GA_s\; \widetilde{\gamma}\; dx \tag{5.31}$$

Recalling that the smoothed *shear* and *bending* strains defined in Section 5.2.1 are *constant* within each smoothing domain $\boldsymbol{D}_k^S$, and also assuming the constitutive terms EI and GA_s to be constant within each smoothing domain, the domain integral $\int_0^L$ can

be transformed in a summation over the N_S smoothing domains composing the discrete model, resulting in the following expressions for the smoothed bilinear form

$$\widetilde{a}\left((\delta v, \delta\theta), (v, \theta)\right) = \sum_{i=1}^{N_S} l_k \left(\widetilde{\delta\omega}(x_k)\ EI\ \widetilde{\omega}(x_k)\right) + \sum_{i=1}^{N_S} l_k \left(\widetilde{\delta\gamma}(x_k)\ GA_s\ \widetilde{\gamma}(x_k)\right) \tag{5.32}$$

The weakened-weak form of the Timoshenko beam can then be expressed as follows: find the set $(v, \theta) \in \mathcal{V}_h(\boldsymbol{D})$ such that

$$\widetilde{a}\left((\delta v, \delta\theta), (v, \theta)\right) = f(\delta u, \delta\theta), \quad \forall (\delta v, \delta\theta) \in \mathcal{V}_h^0(\boldsymbol{D}) \tag{5.33}$$

where $\mathcal{V}_h(\boldsymbol{D})$ and $\mathcal{V}_h^0(\boldsymbol{D})$ are, respectively, the spaces of *trial* and *test* functions, defined as

$$\mathcal{V}_h(\boldsymbol{D}) := \{(v, \theta) \in \mathcal{G}(\boldsymbol{D}) \times \mathcal{G}(\boldsymbol{D}) \mid v = v_\Gamma \text{ on } \Gamma_v,\ \theta = \theta_\Gamma \text{ on } \Gamma_\theta\} \tag{5.34}$$

$$\mathcal{V}_h^0(\boldsymbol{D}) := \{(\delta v, \delta\theta) \in \mathcal{G}(\boldsymbol{D}) \times \mathcal{G}(\boldsymbol{D}) \mid \delta v = 0 \text{ on } \Gamma_v,\ \delta\theta = 0 \text{ on } \Gamma_\theta\} \tag{5.35}$$

In the expressions above, $\mathcal{G}(\boldsymbol{D})$ indicates a special space of square integrable functions, well-suited for PIM shape function, and referred to as *G-space* in the literature of smoothed methods (see the papers by Liu Liu (2010*a*,*b*) for further details).

5.4.2 Geometrically exact beam

As pointed out in Section 2.2.7, the weak form of the beam problem consists then into find a configuration $\varphi \in \mathcal{C}$ such that $G = 0, \forall \bar{\boldsymbol{\eta}} \in T_\varphi \mathcal{C}$, with

$$T_\varphi \mathcal{C} \equiv \{\bar{\boldsymbol{\eta}}(S, t) \equiv (\bar{\boldsymbol{\eta}}_0(S, t), \bar{\boldsymbol{\theta}}(S, t))\} \tag{5.36}$$

The linearised weak form of the geometrically exact beam is recalled in the following

$$\begin{aligned} L[G(\varphi, \bar{\boldsymbol{\eta}})] &= G(\hat{\varphi}, \bar{\boldsymbol{\eta}}) + DG(\hat{\varphi}, \bar{\boldsymbol{\eta}}) \cdot \Delta\varphi \\ &= \int_{[0,L]} [(\boldsymbol{\Xi}^T \bar{\boldsymbol{\eta}}) \cdot \boldsymbol{\Sigma} - \bar{\boldsymbol{\eta}} \cdot \boldsymbol{Q}] dS + \int_{[0,L]} (\hat{\boldsymbol{\Xi}}^T \bar{\boldsymbol{\eta}}) \cdot (\underline{\hat{\boldsymbol{C}}} \hat{\boldsymbol{\Xi}}^T \Delta\varphi_M) dS \\ &+ \int_{[0,L]} (\hat{\boldsymbol{\beta}} \bar{\boldsymbol{\eta}}) \cdot (\hat{\boldsymbol{B}} \hat{\boldsymbol{\beta}} \Delta\varphi_G) dS + \int_{[0,L]} \bar{\boldsymbol{\eta}} \cdot (\hat{\boldsymbol{L}} \Delta\varphi_L) dS \end{aligned} \tag{5.37}$$

where the terms appearing above are defined in Section 2.2.7.

Similarly with what was made for the Timoshenko model, considering that the smoothed strains defined in Section 5.2.2 are *constant* within each smoothing domain $\boldsymbol{D}_k^S$, and also assuming the constitutive terms in Eq. (2.45) and Eq. (2.46) to be constant within each

smoothing domain, the domain integral $\int_{[0,L]}$ can be transformed in a summation over the N_S smoothing domains composing the discrete model, resulting in the weakened-weak form of the geometrically exact model

$$\widetilde{L}[G(\varphi, \bar{\boldsymbol{\eta}})] = \widetilde{G}(\hat{\varphi}, \bar{\boldsymbol{\eta}}) + \widetilde{DG}(\hat{\varphi}, \bar{\boldsymbol{\eta}}) \cdot \Delta\varphi \tag{5.38}$$

5.5 Discretisation

Focusing on SPIMs applications, in what follows the discretisation procedure for the target beam models is presented.

5.5.1 Timoshenko beam

In SPIMs, the field variables are approximated in terms of nodal values and shape functions, as in the finite element method. In the Timoshenko beam model, the deflection v and rotation θ are then approximated as

$$v(x) \simeq \sum_{i \in S_d} \phi_i^v(x)\ d_i^v, \qquad \theta(x) \simeq \sum_{i \in S_d} \phi_i^\theta(x)\ d_i^\theta \tag{5.39}$$

where the index i indicates a node x_i in the *support domain* S_d, i.e. the set of nodes in the neighbourhood of the point x, $\phi_i^v(x)$ and $\phi_i^\theta(x)$ are meshless shape functions used to interpolate the nodal values d_i^v and d_i^θ of deflections and rotations, respectively.

In order to obtain a discretised weakened-weak form, the approximated deflection and rotation appearing in Eq. (5.39) are introduced in the smoothed deformation measures of Eqs. (5.16) and (5.17), resulting in the following expressions:

$$\widetilde{\gamma}(x_k) = \frac{1}{l_k} \sum_{i \in S_d} \left(\phi_i^v(\xi)\ n_x^{(k)}(\xi) \right) \Big|_{\boldsymbol{\Gamma}_k}\ d_i^v - \sum_{i \in S_d} \phi_i^\theta(x_k)\ d_i^\theta \tag{5.40}$$

$$\widetilde{\omega}(x_k) = \frac{1}{l_k} \sum_{i \in S_d} \left(\phi_i^\theta(\xi)\ n_x^{(k)}(\xi) \right) \Big|_{\boldsymbol{\Gamma}_k}\ d_i^\theta \tag{5.41}$$

By introducing the following smoothed derivatives of the shape function

$$\widetilde{\phi}_{i,x}^v(x_k) := \frac{1}{l_k} \left(\phi_i^v(\xi)\ n_x^{(k)}(\xi) \right) \Big|_{\boldsymbol{\Gamma}_k}, \qquad \widetilde{\phi}_{i,x}^\theta(x_k) := \frac{1}{l_k} \left(\phi_i^\theta(\xi)\ n_x^{(k)}(\xi) \right) \Big|_{\boldsymbol{\Gamma}_k} \tag{5.42}$$

the discretised deformation measures of Eqs. (5.40) and (5.41) can be recasted as

$$\widetilde{\gamma}(x_k) = \sum_{i \in S_d} \widetilde{\phi}^v_{i,x}(x_k)\ d^v_i - \sum_{i \in S_d} \phi^\theta_i(x_k)\ d^\theta_i \tag{5.43}$$

$$\widetilde{\omega}(x_k) = \sum_{i \in S_d} \widetilde{\phi}^\theta_{i,x}(x_k)\ d^\theta_i \tag{5.44}$$

By collecting the deformation measures in the following array

$$\{\widetilde{\varepsilon}(\mathbf{x_k})\} := \begin{pmatrix} \widetilde{\omega}(x_k) \\ \widetilde{\gamma}(x_k) \end{pmatrix} = \sum_{i \in S_d} \begin{pmatrix} 0 & \widetilde{\phi}^\theta_{i,x}(x_k) \\ \widetilde{\phi}^v_{i,x}(x_k) & -\phi^\theta_i(x_k) \end{pmatrix} \begin{pmatrix} d^v_i \\ d^\theta_i \end{pmatrix} = \sum_{i \in S_d} [\widetilde{\mathbf{B}}_\mathbf{i}(\mathbf{x_k})]\{\mathbf{d_i}\} \tag{5.45}$$

and the constitutive terms in the following matrix[5]

$$[E] := \begin{pmatrix} EI & 0 \\ 0 & GA_s \end{pmatrix} \tag{5.46}$$

the bilinear form of Eq. (5.32) can be recasted as

$$\widetilde{a}\left((\delta u, \delta\theta), (u, \theta)\right) = \sum_{i=1}^{N_S} l_k \left(\{\widetilde{\delta\varepsilon}(\mathbf{x_k})\}^T\ [E]\ \{\widetilde{\varepsilon}(\mathbf{x_k})\} \right) \tag{5.47}$$

The representation in terms of shape functions and nodal parameters results in an algebraic system representing the behaviour of the whole discrete model

$$[K]\ \{X\} = \{R\} \tag{5.48}$$

where $[K]$ is the global stiffness matrix of the system, $\{X\}$ the nodal parameters vector collecting all the nodal parameters $\{d_i\}$, and $\{R\}$ the vector of nodal dual parameters (i.e. nodal forces and moments). The stiffness matrix $[K]$ can be evaluated through the contribution of each *smoothing domain* $\boldsymbol{D}^S_k$

$$[K(x_k)]_{Sd} = l_k\ [\widetilde{B}(x_k)]^T\ [E]\ [\widetilde{B}(x_k)] \tag{5.49}$$

where the matrix $[\widetilde{B}(x_k)]$ is composed by the submatrices $[\widetilde{B}_i(x_k)]$ as

$$[\widetilde{B}(x_k)] = \left([\widetilde{B}_1(x_k)] \dots [\widetilde{B}_i(x_k)] \dots [\widetilde{B}_N(x_k)] \right) \tag{5.50}$$

where N is the number of nodes in the support domain S_d at the point x_k.

[5]Similarly to finite element applications, the case of variable properties along the beam axis can be obtained by considering a constitutive matrix that is constant within a single smoothing domain (i.e. piecewise constant along the beam axis).

5.5.2 Geometrically exact beam

In the geometrically exact model, we recall that the configuration of the beam is represented through the position of the line of centroids and the rotation of the cross-sections

$$\mathcal{C} \equiv (\varphi_0, \underline{\boldsymbol{R}}) \tag{5.51}$$

The rotation operation $\underline{\boldsymbol{R}}$ is not directly interpolated through its nodal values, hence attention will be directed to the line of centroids that can be approximated as follows

$$\varphi_0(S,t) \simeq \sum_{i \in S_d} \boldsymbol{\phi}_i^{\varphi_0}(S)\ \boldsymbol{d}_i^{\varphi_0}, \tag{5.52}$$

where the index i indicates a node x_i in the support domain S_d, $\boldsymbol{\phi}_i^{\varphi_0}(S,t)$ is the (PIM) shape function used to interpolate the nodal values of the line of centroids, and $\boldsymbol{d}_i^{\varphi_0}$ is vector that gathers these nodal values of the line o centroids. It is worth noting that $\varphi_0(S,t)$ is composed by three values $\varphi_0(S,t) = [\varphi_{01}, \varphi_{02}, \varphi_{03}]$, therefore the shape functions of a particular *support node* can be represented in the following matrix

$$\boldsymbol{\phi}_i^{\varphi_0}(S,t) = \begin{bmatrix} \phi_i^{\varphi_0}(S,t) & 0 & 0 \\ 0 & \phi_i^{\varphi_0}(S,t) & 0 \\ 0 & 0 & \phi_i^{\varphi_0}(S,t) \end{bmatrix} \quad \text{with } \boldsymbol{d}_i^{\varphi_0} = \begin{bmatrix} d_i^{\varphi_{01}} \\ d_i^{\varphi_{02}} \\ d_i^{\varphi_{03}} \end{bmatrix} \tag{5.53}$$

In order to evaluate the derivatives of the line of centroids, the derivatives of the shape functions are replaced by their smoothed version

$$\begin{aligned} \frac{\partial \boldsymbol{\phi}_i^{\varphi_0}(S,t)}{\partial S} &= \begin{bmatrix} \dfrac{\partial \phi_i^{\varphi_0}(S,t)}{\partial S} & 0 & 0 \\ 0 & \dfrac{\partial \phi_i^{\varphi_0}(S,t)}{\partial S} & 0 \\ 0 & 0 & \dfrac{\partial \phi_i^{\varphi_0}(S,t)}{\partial S} \end{bmatrix} \\ &\equiv \begin{bmatrix} \widetilde{\phi}_{i,S}^{\varphi_0}(S,t) & 0 & 0 \\ 0 & \widetilde{\phi}_{i,S}^{\varphi_0}(S,t) & 0 \\ 0 & 0 & \widetilde{\phi}_{i,S}^{\varphi_0}(S,t) \end{bmatrix} \end{aligned} \tag{5.54}$$

the components of above matrix are computed in same way as presented in Eq. (5.42). In this work, all derivatives of the shape functions are transformed into their smoothed versions to approximate the target quantities

$$\frac{\partial \phi_i}{\partial S} \coloneqq \widetilde{\phi}_{i,S} \tag{5.55}$$

The *configuration increments* are approximated through their nodal values, as follows

$$\bar{\boldsymbol{\eta}} \simeq \sum_{i \in S_d} \boldsymbol{\phi}_i(x_k) \bar{\boldsymbol{\eta}}_i \equiv \sum_{i \in S_d} \begin{pmatrix} \boldsymbol{\phi}_i(x_k) & 0 \\ 0 & \boldsymbol{\phi}_i(x_k) \end{pmatrix} \begin{pmatrix} \bar{\boldsymbol{\eta}}_{0i} \\ \bar{\boldsymbol{\theta}}_i \end{pmatrix} \tag{5.56}$$

$$\Delta\varphi \simeq \sum_{i \in S_d} \boldsymbol{\phi}_i(x_k) \Delta\varphi_i \equiv \sum_{i \in S_d} \begin{pmatrix} \boldsymbol{\phi}_i(x_k) & 0 \\ 0 & \boldsymbol{\phi}_i(x_k) \end{pmatrix} \begin{pmatrix} \bar{\boldsymbol{u}}_{0i} \\ \bar{\boldsymbol{\psi}}_i \end{pmatrix} \tag{5.57}$$

while the derivatives of above expressions with respect to S can be written as

$$\frac{\partial \bar{\boldsymbol{\eta}}}{\partial S} \simeq \sum_{i \in S_d} \widetilde{\boldsymbol{\phi}}_{i,S} \bar{\boldsymbol{\eta}}_i \equiv \sum_{i \in S_d} \begin{pmatrix} \widetilde{\boldsymbol{\phi}}_{i,S} & 0 \\ 0 & \widetilde{\boldsymbol{\phi}}_{i,S} \end{pmatrix} \begin{pmatrix} \bar{\boldsymbol{\eta}}_{0i} \\ \bar{\boldsymbol{\theta}}_i \end{pmatrix} \tag{5.58}$$

$$\frac{\partial \Delta\varphi}{\partial S} \simeq \sum_{i \in S_d} \widetilde{\boldsymbol{\phi}}_{i,S} \Delta\varphi_i \equiv \sum_{i \in S_d} \begin{pmatrix} \widetilde{\boldsymbol{\phi}}_{i,S} & 0 \\ 0 & \widetilde{\boldsymbol{\phi}}_{i,S} \end{pmatrix} \begin{pmatrix} \bar{\boldsymbol{u}}_{0i} \\ \bar{\boldsymbol{\psi}}_i \end{pmatrix} \tag{5.59}$$

In this framework, it is possible to show that Eq. (5.38) assumes the following *material* representation

$$\begin{aligned} \widetilde{L}[G(\varphi, \bar{\boldsymbol{\eta}}] = \ell_k & \left[\boldsymbol{\phi}^T(x_k) \boldsymbol{Q} - \left(\boldsymbol{\Xi}^T \boldsymbol{\phi}(x_k) \right)^T \boldsymbol{\Sigma} \right] \\ & + \ell_k \left[\left(\boldsymbol{\Xi}^T(x_k) \boldsymbol{\phi}(x_k) \right)^T \underline{\boldsymbol{C}} \left(\boldsymbol{\Xi}^T(x_k) \boldsymbol{\phi}(x_k) \right) \right] \\ & + \ell_k \left[\left(\beta(x_k) \boldsymbol{\phi}(x_k) \right)^T \boldsymbol{B}^T(x_k) \left(\beta(x_k) \boldsymbol{\phi}(x_k) \right) \right] \\ & - \ell_k \left[\left(\boldsymbol{\phi}^T(x_k) \boldsymbol{L}(x_k) \boldsymbol{\phi}(x_k) \right) \right] \end{aligned} \tag{5.60}$$

all quantities appearing in $\widetilde{L}[G(\varphi, \bar{\boldsymbol{\eta}}]$ are defined in Section 2.2.

5.6 Support nodes strategies

The approximation of the field variables illustrated in SPIM takes into account, for each point, a certain number of *support nodes*, the so-called *support domain* S_d at that point. While there are different techniques for the choice of the support nodes at each interest point, SPIM strategies usually rely on the same background cells used to build the domain tessellation. In the two-dimensional tessellation depicted in Section 4.3, for example, support domains are usually assembled using background triangular cells, with the so-called *T-schemes* (see, for example, the book by Liu and Zhang (2013)); the support domain of a point lying in a certain cell can be assembled considering the three nodes of that cell (T3-scheme), and eventually three additional nodes from the neighbouring cells (T6-scheme).

As discussed in Section 5.3, Liu and his co-authors (Cui et al., 2008, Liu, 2009, Du et al., 2018), already investigated a one-dimensional SPIM strategy for the static and dynamic analysis of Euler-Bernoulli beams. In their studies they focused on linear shape

functions, built using only two nodes at each integration point. In the present work, two different approaches are considered.

The first one, referred to as *L2-scheme*, is analogous to the one already adopted in the aforementioned papers. Within this approach, illustrated in Fig. 5.3, the support domain at each integration point on the boundary of a smoothing domain is built using two nodes. For internal node-based domains, since each integration point corresponds to the centroid of a background cell, the two nodes are the end-points of the cell (Fig. 5.3a); it is worth noting that the two integration points of each smoothing domain will have two different support domains (the *left* and *right* supports indicated in Fig. 5.3a). The exception of a smoothing domain lying on the end-point of the beam is treated as illustrated in Fig. 5.3a, considering the same two nodes for both integration points. For the edge-based strategy, as illustrated in Fig. 5.3b, since each smoothing domain corresponds to a background cell, each integration point will receive the same support nodes, namely the nodes at the end-points of the cell.

As indicated in Eq. (5.45), it is necessary to evaluate the approximation function also at the centre of each smoothing domain, due to the presence of the "field variables" in the deformation measures[6]. The support domain at the centre of each smoothing domain will be built as the *union* of the *left* and *right* supports of the same smoothing domain; it is worth noting that, due to this choice, the centre of internal node-based smoothing domain will present three support nodes, while the other configurations will be characterised by two nodes.

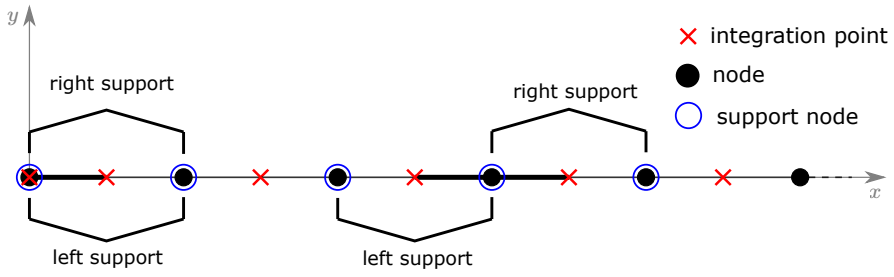

(a) NSPIM

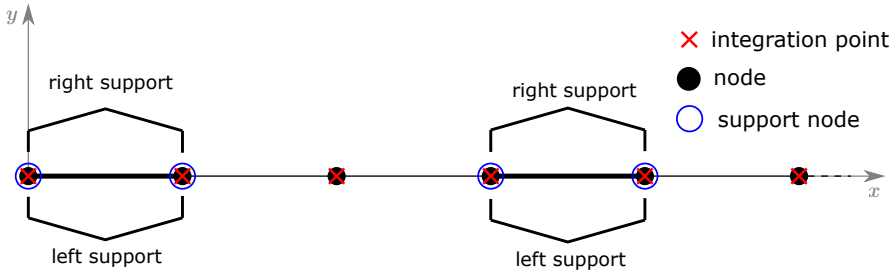

(b) ESPIM

Figure 5.3: L2-schemes for support domains

[6]The rotation $\theta(x)$ in the Timoshenko beam and the rotation tensor $\underline{\boldsymbol{R}}(S,t)$ for the geometrically exact model, for instance.

The second approach, referred to as *L3/2-scheme*, is a variation of the previous L2-scheme, that aims to widen the size of the support domains. As it can be observed in Fig. 5.4, at each integration point, the support domain is built considering three nodes, except for the integration points at the beam boundaries, that receive only two nodes (hence the name L3/2-scheme). For node-based smoothing domains, as illustrated in Fig. 5.4a, at each integration point these three nodes are choosen considering the same two nodes of the L2-scheme (i.e. the two nodes of the background cell which the integration point belongs to), with the additional node of the neighbouring background cell at the opposite side of the smoothing domain centre. In edge-based smoothing domains, as depicted in Fig. 5.4b, the three nodes of the support domain are the nodes belonging to the two background cells connected through the integration point. The support domain at the centre of each smoothing domain will still be built as the *union* of the *left* and *right* supports of the same smoothing domain. Internal node-based smoothing domains will receive five support nodes at their centre, while internal edge-based smoothing domains will receive four nodes. Smoothing domains lying on the boundary will receive three support nodes at their centre, for both node- and edge-based strategies.

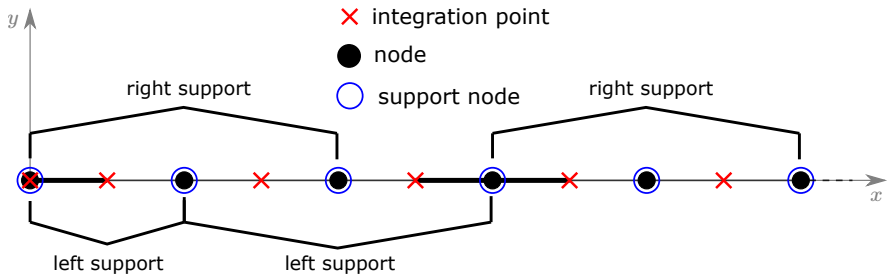

(a) NSPIM

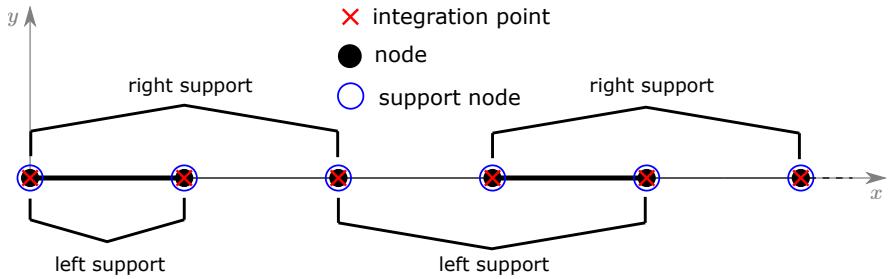

(b) ESPIM

Figure 5.4: L3/2-schemes for support domains

In the current beam model, the shape functions must be evaluated at the end-points and at the centre of each smoothing domain. The value of the shape functions at the end-points is used to solve the boundary integral appearing in the expressions of the smoothed strain measures (Eqs. (5.40) and (5.41)), while the value at the centre is used for the rotation term appearing the expression of the smoothed shear strain (Eq. (5.40)). It is worth noting that it is not necessary to apply the analytical expressions of the PIM shape functions each time that their values are needed. Indeed, since PIM shape functions

possess the Kronecker delta property, they assume values of 0 or 1 at the nodes, and must be explicitly evaluated only at the integration points that do not lie on a node, i.e. the end-points of node-based smoothing domains and the centre of edge-based smoothing domains. The cost needed to evaluate the shape functions for each smoothing domain is then comparable to the cost of a two-nodes finite element.

5.7 αPIM shape functions

In Section 4.7 the concept of αPIM shape function was introduced. Since it is possible to obtain analytical solutions for the one-dimensional Timoshenko beam, in this section, the αPIM notion is particularised for this case. However, the overall idea is independent of the model, it suffices to satisfy the conditions that was discussed in Section 4.7 (see also Liu et al. (2013)).

As it will be shown in Chapter 6, simulations performed with L2 and L3/2 schemes provide different bounds to the analytical solution. One-dimensional SPIM models that adopt the L2-scheme reproduce the behaviour of two-nodes finite elements, i.e. a behaviour that is *stiffer* than the analytical solution. On the other hand, when the L3/2-scheme is adopted, the resulting behaviour is *softer* than the analytical solution. Since the analytical solution is bounded by these two numerical schemes, it is possible to adopt the so-called α-PIM shape functions discussed by Liu and Zhang (2013), in order to achieve a better convergence to the analytical solution.

The starting point is two sets of support nodes, $S_d^{(I)}$ and $S_d^{(II)}$, at the same interest point x, used to build two different sets PIM shape functions

$$\Phi^{(I)}(x) = \begin{pmatrix} \phi_1^{(I)}(x) & \phi_2^{(I)}(x) & \dots & \phi_{N_I}^{(I)}(x) \end{pmatrix} \tag{5.61}$$

$$\Phi^{(II)}(x) = \begin{pmatrix} \phi_1^{(I)}(x) & \phi_2^{(I)}(x) & \dots & \phi_{N_{II}}^{(I)}(x) \end{pmatrix} \tag{5.62}$$

where N_I and N_{II} are, respectively, the number of nodes of $S_d^{(I)}$ and $S_d^{(II)}$. While the two sets may have a different number of nodes, they must have some shared nodes.

In the present work, these two sets will be build using, at each interest point, the L2 and L3/2 schemes, where the L2 support domain is always contained in the L3/2 support domain, $S_d^{(L3/2)} \supseteq S_d^{(L2)}$.

The corresponding shape functions $\phi_i^{(L2)}(x)$ and $\phi_i^{(L3/2)}(x)$ can be used to obtain different approximations of the field variables of the Timoshenko beam[7]

[7]In Eqs. (5.63) and (5.64), for simplicity, no distinction has been made for shape functions approximating the deflection and the rotation fields.

$$v^{(L2)}(x) = \sum_{i \in S_d^{(L2)}} \phi_i^{(L2)}(x)\ d_i^v, \qquad \theta^{(L2)}(x) = \sum_{i \in S_d^{(L2)}} \phi_i^{(L2)}(x)\ d_i^\theta \tag{5.63}$$

$$v^{(L3/2)}(x) = \sum_{i \in S_d^{(L3/2)}} \phi_i^{(L3/2)}(x)\ d_i^v, \qquad \theta^{(L3/2)}(x) = \sum_{i \in S_d^{(L3/2)}} \phi_i^{(L3/2)}(x)\ d_i^\theta \tag{5.64}$$

Since the approximated fields of Eqs. (5.63) and (5.64) result in different bounds to the analytical solution they can be combined in order to obtain a better convergence to the analytical solution

$$v(x) = \alpha \left(\sum_{i \in S_d^{(L2)}} \phi_i^{(L2)}(x)\ d_i^v \right) + (1-\alpha) \left(\sum_{i \in S^{(L3/2)}} \phi_i^{(L3/2)}(x)\ d_i^v \right) \tag{5.65}$$

$$\theta(x) = \alpha \left(\sum_{i \in S_d^{(L2)}} \phi_i^{(L2)}(x)\ d_i^\theta \right) + (1-\alpha) \left(\sum_{i \in S_d^{(L3/2)}} \phi_i^{(L3/2)}(x)\ d_i^\theta \right) \tag{5.66}$$

The variable $\alpha \in [0,1]$ appearing in the expressions above indicates how the two different approximations are blended. Eqs. (5.65) and (5.66) can be recasted as follows

$$v(x) = \sum_{i \in S^{(\alpha)}} \phi_i^{(\alpha)}(x)\ d_i^v, \qquad \theta(x) = \sum_{i \in S^{(\alpha)}} \phi_i^{(\alpha)}(x)\ d_i^\theta \tag{5.67}$$

where each $\phi_i^{(\alpha)}(x)$ is an αPIM shape function, defined as

$$\phi_i^{(\alpha)}(x) = \begin{cases} \alpha\phi_i^{(L2)}(x) + (1-\alpha)\phi_i^{(L3/2)}(x) & \forall i \in S^{(L2)} \cap S^{(L3/2)} \\ \alpha\phi_i^{(L2)}(x) & \forall i \in S^{(L2)} \setminus S^{(L3/2)} \\ (1-\alpha)\phi_i^{(L3/2)}(x) & \forall i \in S^{(L3/2)} \setminus S^{(L2)} \end{cases} \tag{5.68}$$

5.8 Numerical simulations

Although it is possible to employ radial basis functions and use a node-based PIM approach when using SPIM methods, the numerical simulations performed in this master's thesis focused on the polynomial basis functions, and the edge-based technique for the domain tessellation, i.e. the smoothing domains are created adopting this strategy. Therefore, in the following two chapters addressed to the numerical simulations, whenever the SPIMs are mentioned, above delimitation is implied. Additionally, regarding the geometrically exact beam code, the resulting nonlinear system of equations is treated by a Newton-like algorithm with load control.

CHAPTER 6

NUMERICAL SIMULATIONS: TIMOSHENKO BEAM

The present chapter is devoted to the simulations regarding the linear Timoshenko model. Classic beam boundary conditions were chosen to validate the proposed SPIM application. Numerical results using the αPIM shape functions are also presented.

6.1 Preliminaries

The simulations are illustrated for four boundary conditions: pinned-pinned, fixed-fixed, fixed-pinned and fixed-free each of them with three load cases, an uniformly distributed load, a point force load, and a linearly distributed load. The parameters adopted for the numerical simulations are: Young's modulus $E = 2 \cdot 10^{11}\text{N/m}^2$, Poisson's ratio $\nu = 0.3$, beam length $L = 10\,\text{m}$, form factor $k = 5/6$ and rectangular cross section with a fixed thickness of $b = 0.2\,\text{m}$. The slenderness ratio (h/L) was varied according to the values in table 6.1. The load values chosen for the simulations are also presented in this table. Due to the distinct (h/L) ratios, the load values had to be adjusted in order to avoid very small displacements or very large ones. As the cantilever beam is more flexible compared to the other beams, the values of table 6.1 were divided by ten to perform its simulations.

h/L	$P\,[N]$	$q\,[N/m]$	$q_i - q_f\,[N/m]$
0.10	350000	35000	50000-10000
0.50	45000000	4500000	5000000-1000000
1.00	100000000	10000000	50000000-10000000

Table 6.1: Slenderness ratio

In order to compare the proposed strategy with a consolidated method, the FEM model of the Timoshenko beam was also simulated. Aiming to avoid the shear locking problem, the *reduced integration* technique was adopted for the finite element simulations.

With the intention of performing comparisons of the numerical results with the exact ones, the analytical expressions for the Timoshenko beam were derived. The general procedure to obtain these analytical expressions is described in Appendix D and encompasses all boundary conditions and load cases.

The error of all simulations was estimated with equation 6.1 in the following

$$e = \left[\frac{\sum_{i=1}^{N_n} (v_i^{ref} - v_i^{num})^2 + \sum_{i=1}^{N_n} (\theta_i^{ref} - \theta_i^{num})^2}{\sum_{i=1}^{N_n} (v_i^{ref})^2 + \sum_{i=1}^{N_n} (\theta_i^{ref})^2} \right]^{\frac{1}{2}} \tag{6.1}$$

where v_i^{ref} and θ_i^{ref} are the reference solutions for the displacements and rotations at a node i, respectively, while v_i^{num} and θ_i^{num} gather the numerical solutions for the displacement and rotation for a node i, respectively, and N_n is the total number of field nodes used in the problem domain discretisation.

The simulations of the present chapter are organised in the following two sections. In Section 6.2 the results are presented in terms of (i) displacements and rotations along the beam axis and (ii) error norm computed with Eq. (6.1). In the first analysis, a mesh with 5 equally spaced nodes is shown for each load case varying the values of h/L ratio exhibited in Table 6.1, while in the second analysis the error is computed using nine meshes, where the nodes discretisation are ranging from 5 to 53 nodes equally spaced by 6 plus an additional mesh with 95 nodes. In this case, the L2-scheme, L3/2-scheme and the linear FEM are compared.

In Section 6.3 the application of the αPIM is illustrated. A procedure to estimate an adequate alpha value is proposed, and its results are added to the error comparisons performed in Section 6.2. The variation of the error while the alpha parameter is changed is also shown.

6.2 L2 and L3/2 simulations

In what follows, the results of deflections and rotations using both L2 and L3/2 schemes are shown for all boundary conditions (see Fig. 6.1). The correspondent analytical solutions are also presented. As already pointed out, three load cases are used in the simulations: a point force load, an uniformly distributed load and a linearly distributed load over the beam, as illustrated in Fig. 6.1. In Figs. 6.2 to 6.13, each page corresponds to the results of a particular load case associated with a boundary condition.

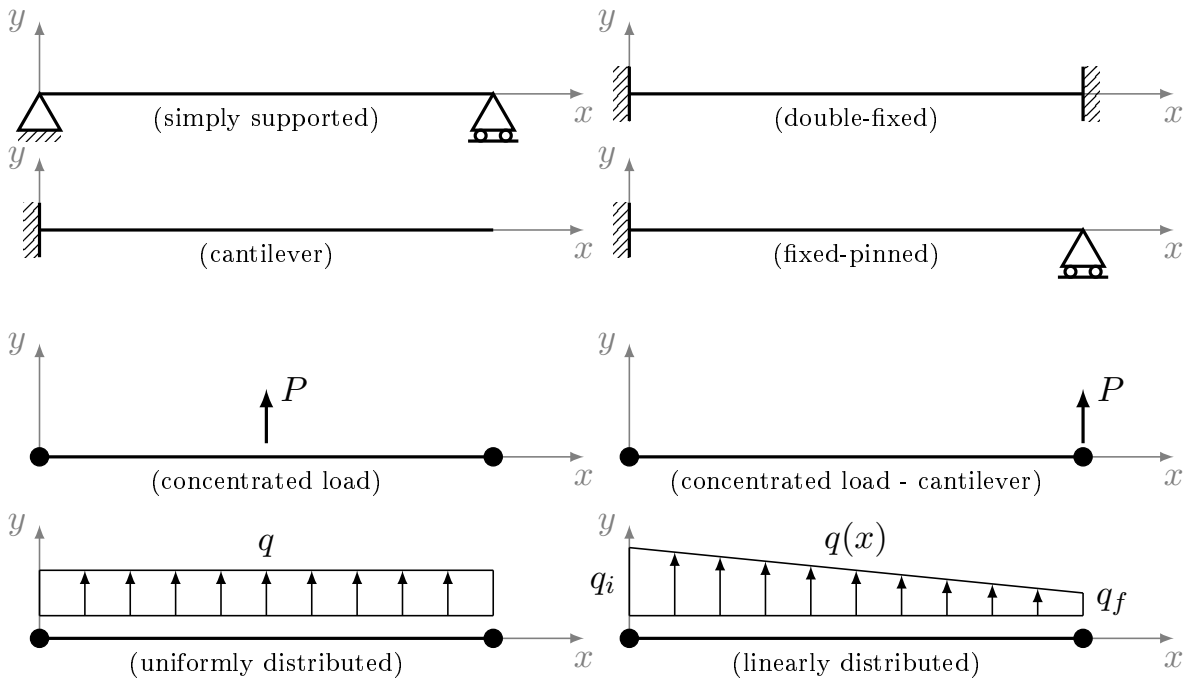

Figure 6.1: Beam boundary conditions and load cases

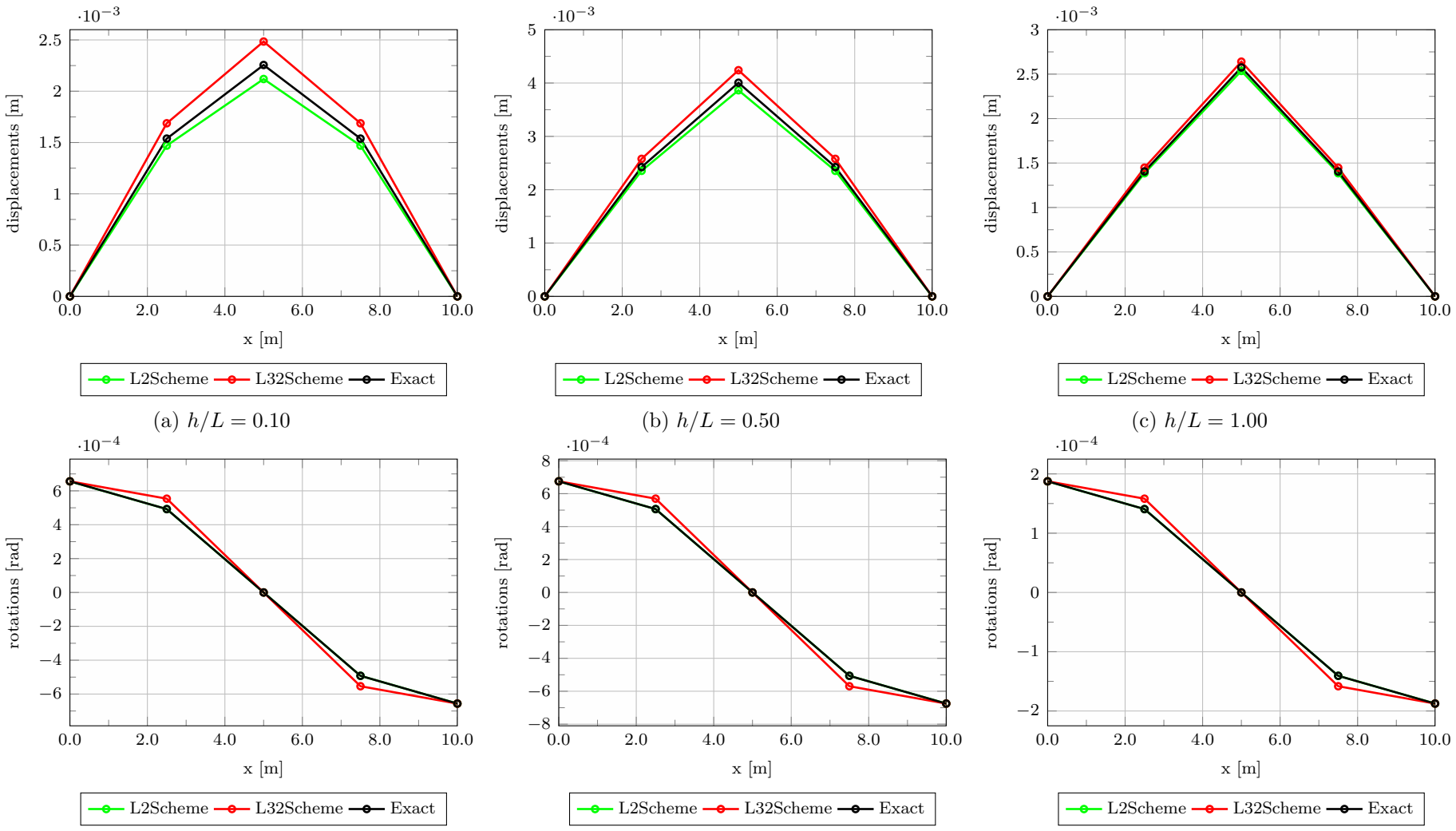

(a) $h/L = 0.10$ (b) $h/L = 0.50$ (c) $h/L = 1.00$

(d) $h/L = 0.10$ (e) $h/L = 0.50$ (f) $h/L = 1.00$

Figure 6.2: Simply supported beam: force load results

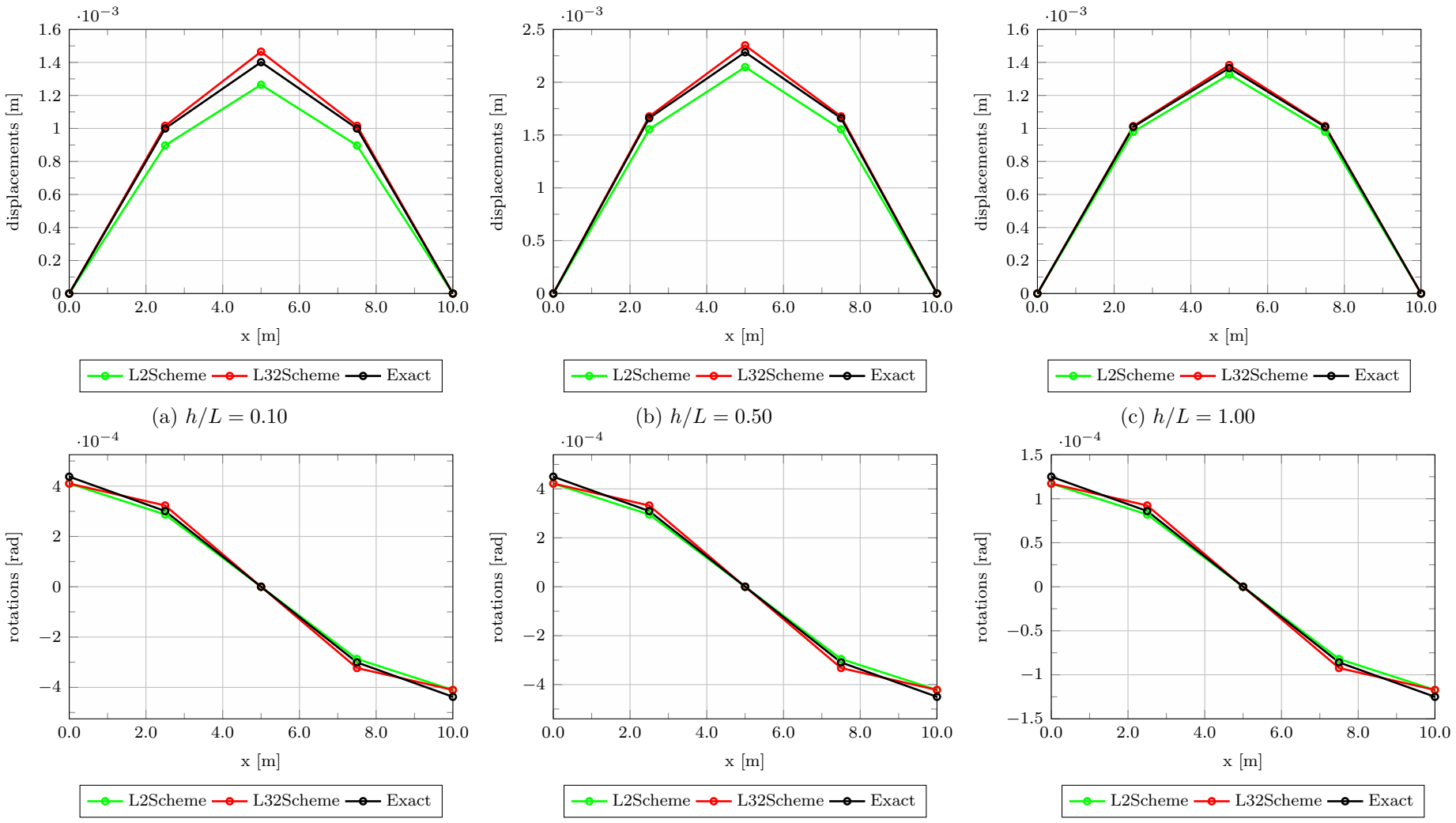

(a) $h/L = 0.10$ (b) $h/L = 0.50$ (c) $h/L = 1.00$

(d) $h/L = 0.10$ (e) $h/L = 0.50$ (f) $h/L = 1.00$

Figure 6.3: Simply supported beam: uniformly distributed load results

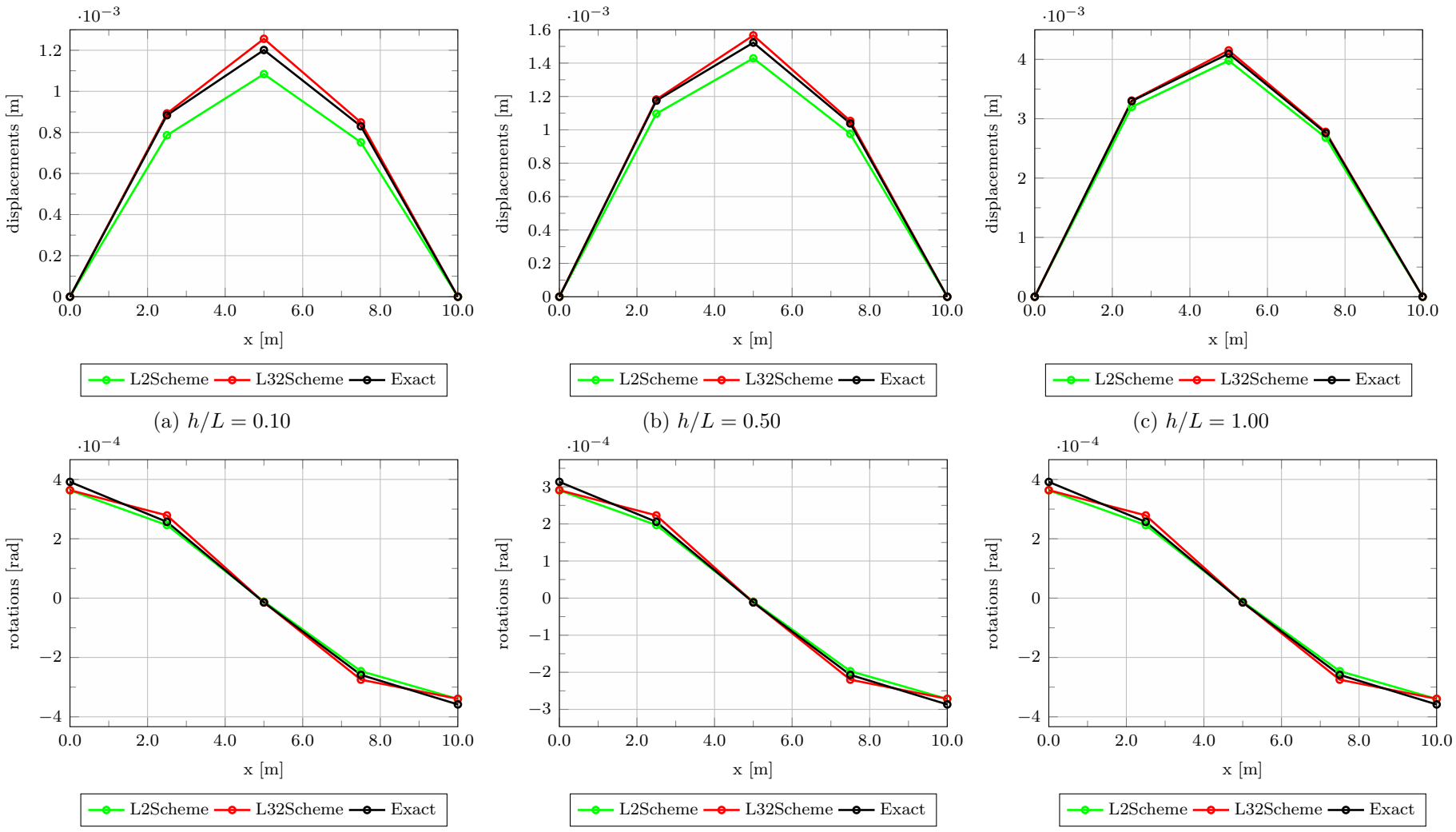

(a) $h/L = 0.10$ (b) $h/L = 0.50$ (c) $h/L = 1.00$

(d) $h/L = 0.10$ (e) $h/L = 0.50$ (f) $h/L = 1.00$

Figure 6.4: Simply supported beam: linearly distributed load results

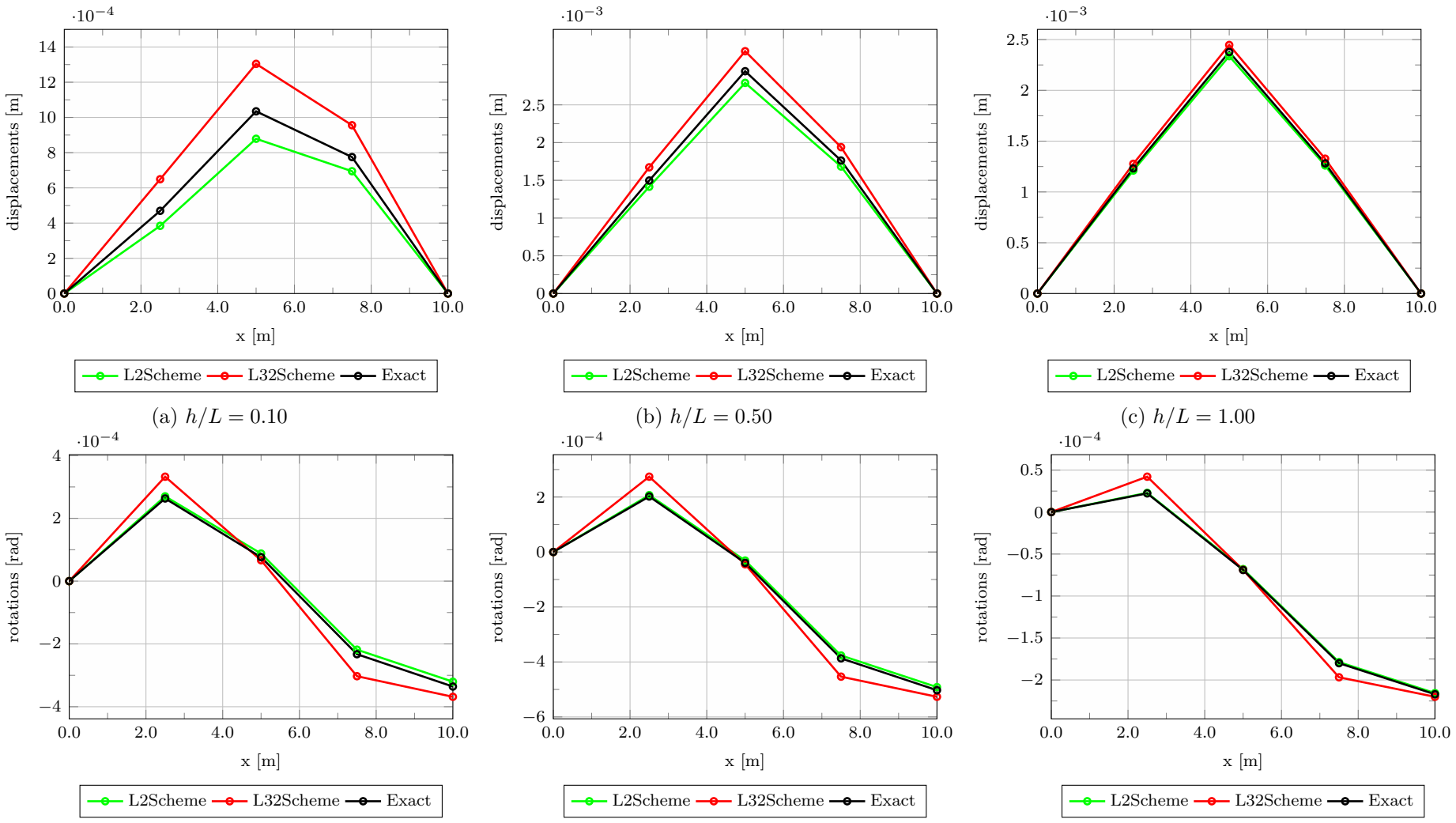

(a) $h/L = 0.10$ (b) $h/L = 0.50$ (c) $h/L = 1.00$

(d) $h/L = 0.10$ (e) $h/L = 0.50$ (f) $h/L = 1.00$

Figure 6.5: Fixed-pinned beam: force load results

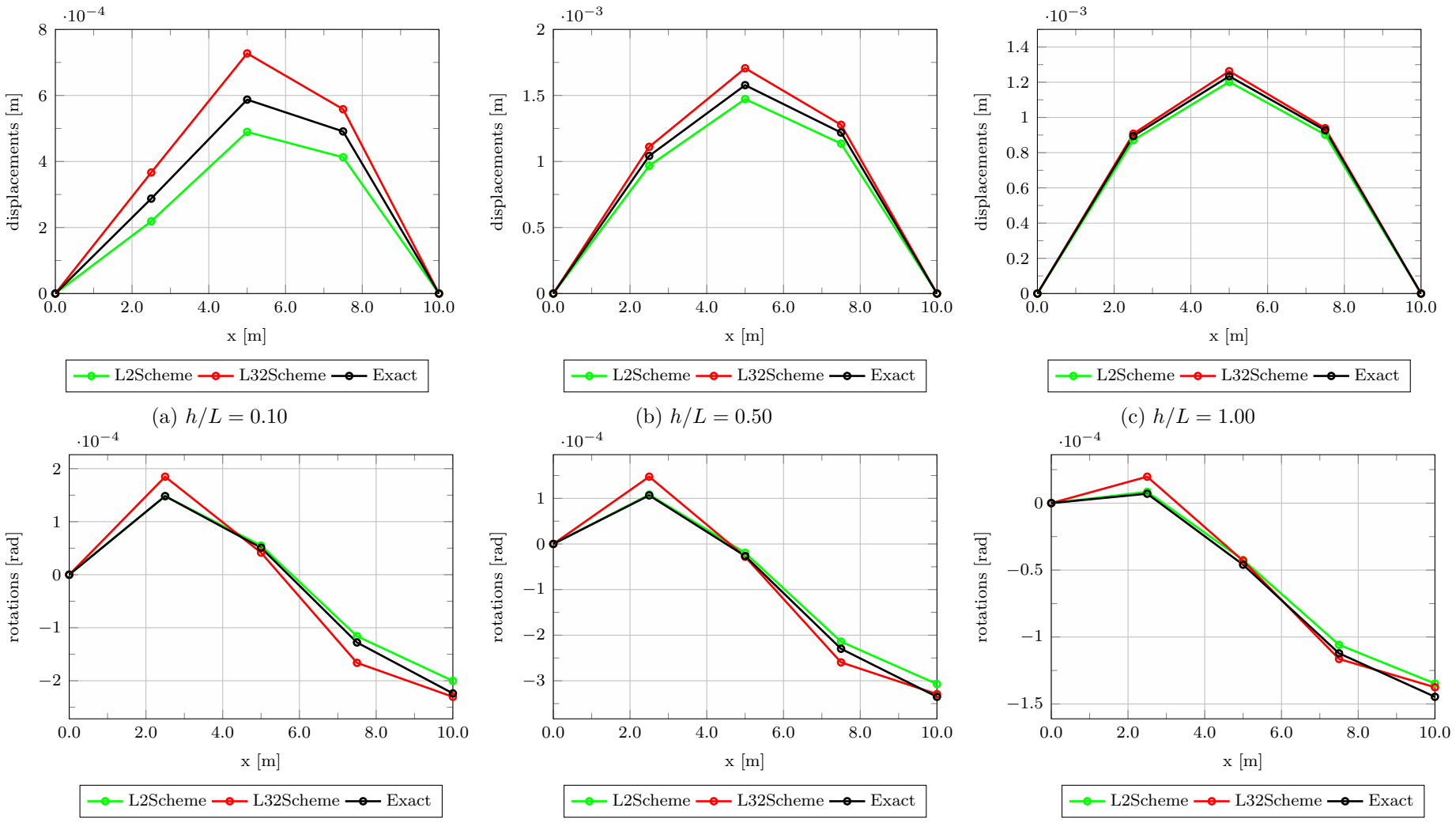

(a) $h/L = 0.10$ (b) $h/L = 0.50$ (c) $h/L = 1.00$

(d) $h/L = 0.10$ (e) $h/L = 0.50$ (f) $h/L = 1.00$

Figure 6.6: Fixed-pinned beam: uniformly distributed load results

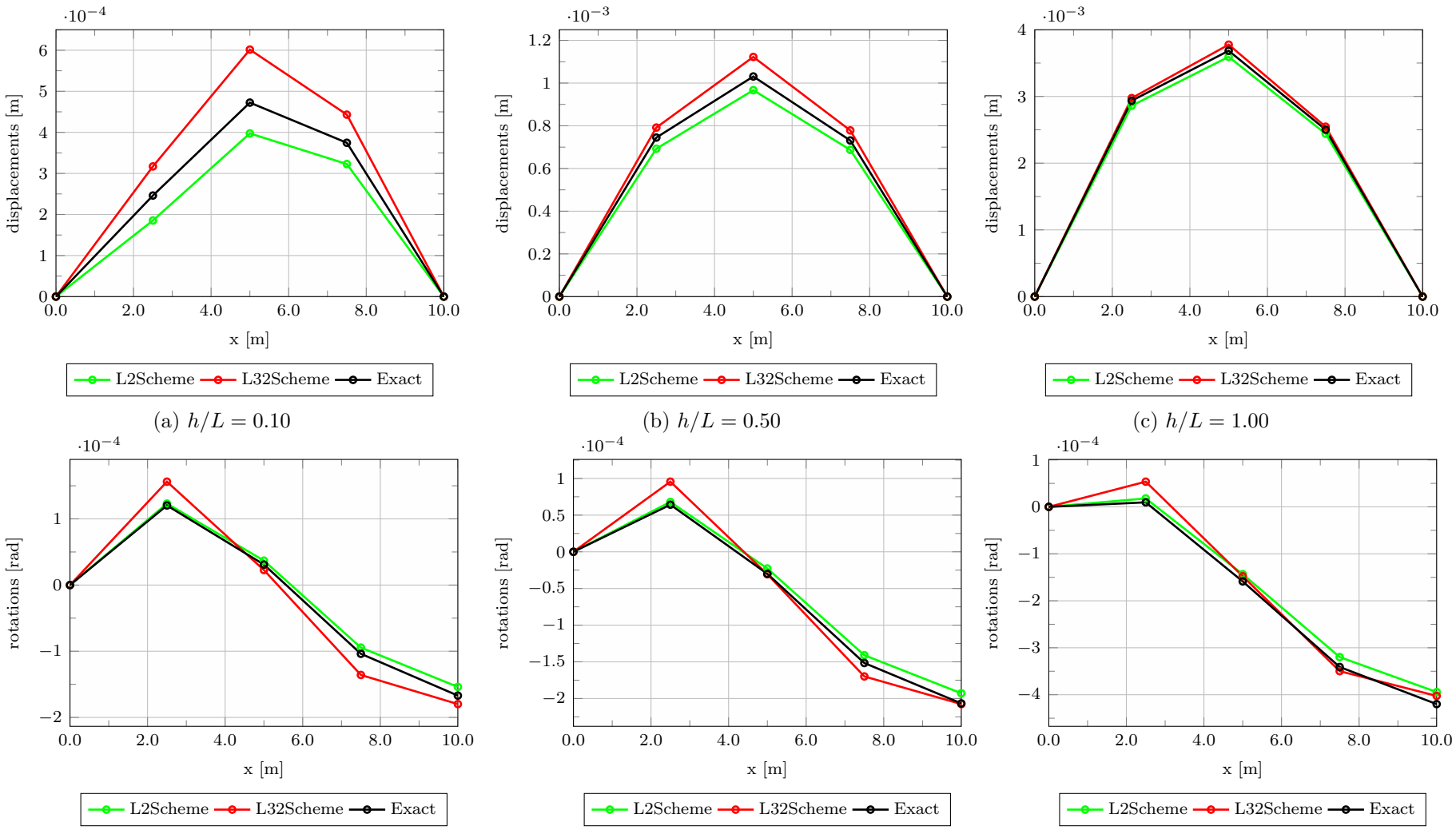

(a) $h/L = 0.10$ (b) $h/L = 0.50$ (c) $h/L = 1.00$

(d) $h/L = 0.10$ (e) $h/L = 0.50$ (f) $h/L = 1.00$

Figure 6.7: Fixed-pinned beam: linearly distributed load results

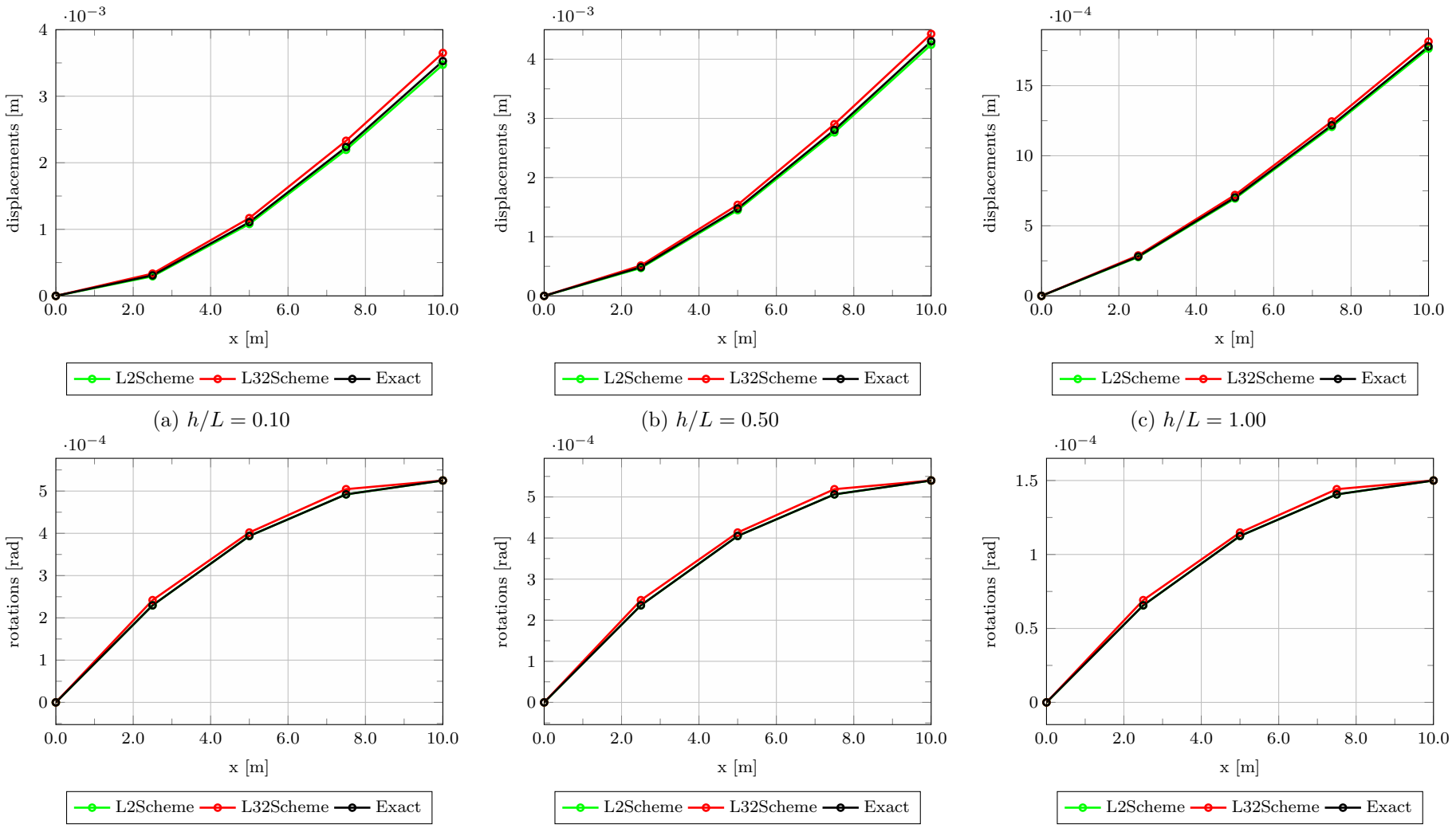

(a) $h/L = 0.10$ (b) $h/L = 0.50$ (c) $h/L = 1.00$

(d) $h/L = 0.10$ (e) $h/L = 0.50$ (f) $h/L = 1.00$

Figure 6.8: Cantilever beam: force load results

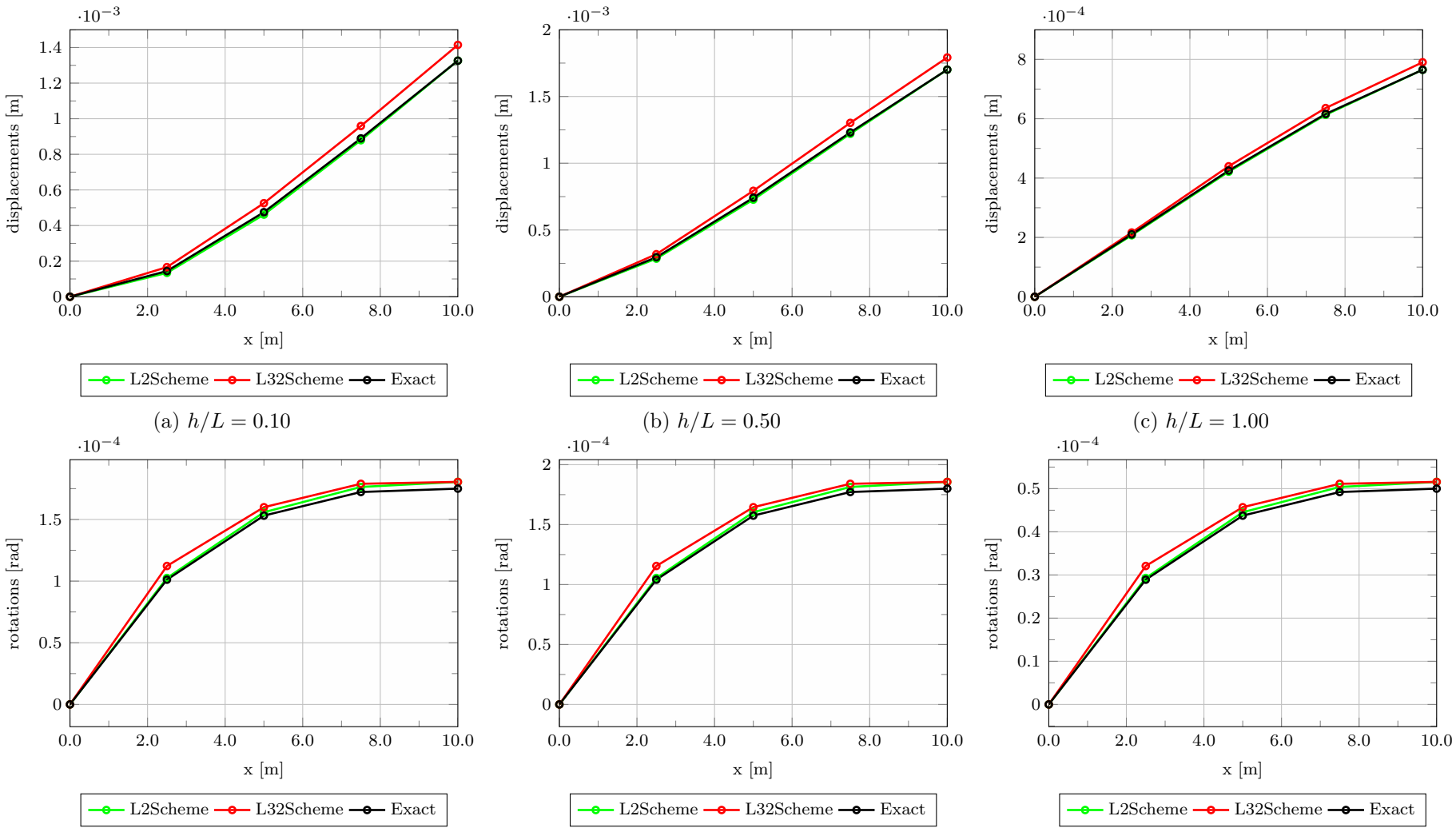

(a) $h/L = 0.10$ (b) $h/L = 0.50$ (c) $h/L = 1.00$

(d) $h/L = 0.10$ (e) $h/L = 0.50$ (f) $h/L = 1.00$

Figure 6.9: Cantilever beam: uniformly distributed load results

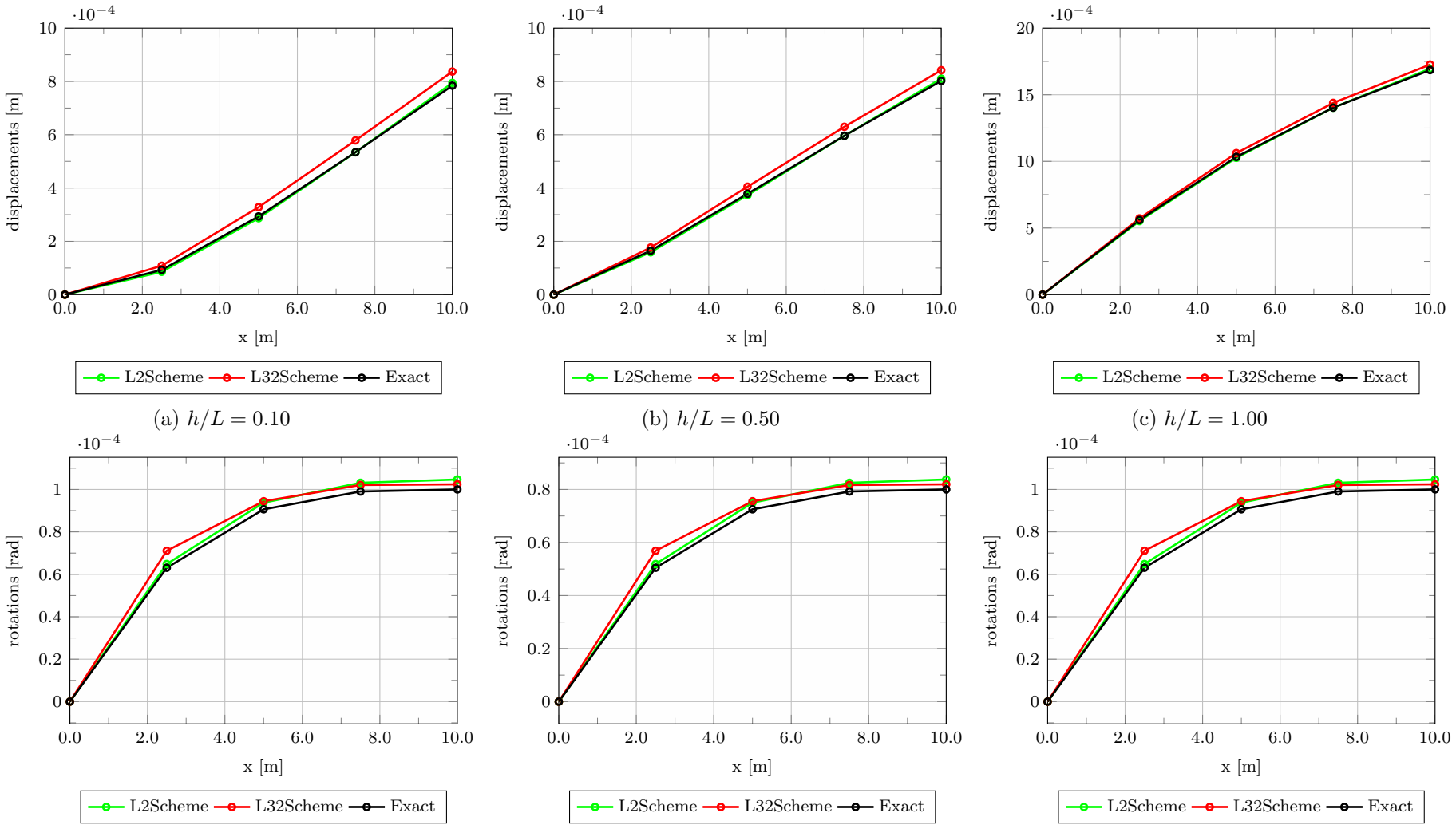

(a) $h/L = 0.10$ (b) $h/L = 0.50$ (c) $h/L = 1.00$

(d) $h/L = 0.10$ (e) $h/L = 0.50$ (f) $h/L = 1.00$

Figure 6.10: Cantilever beam: linearly distributed load results

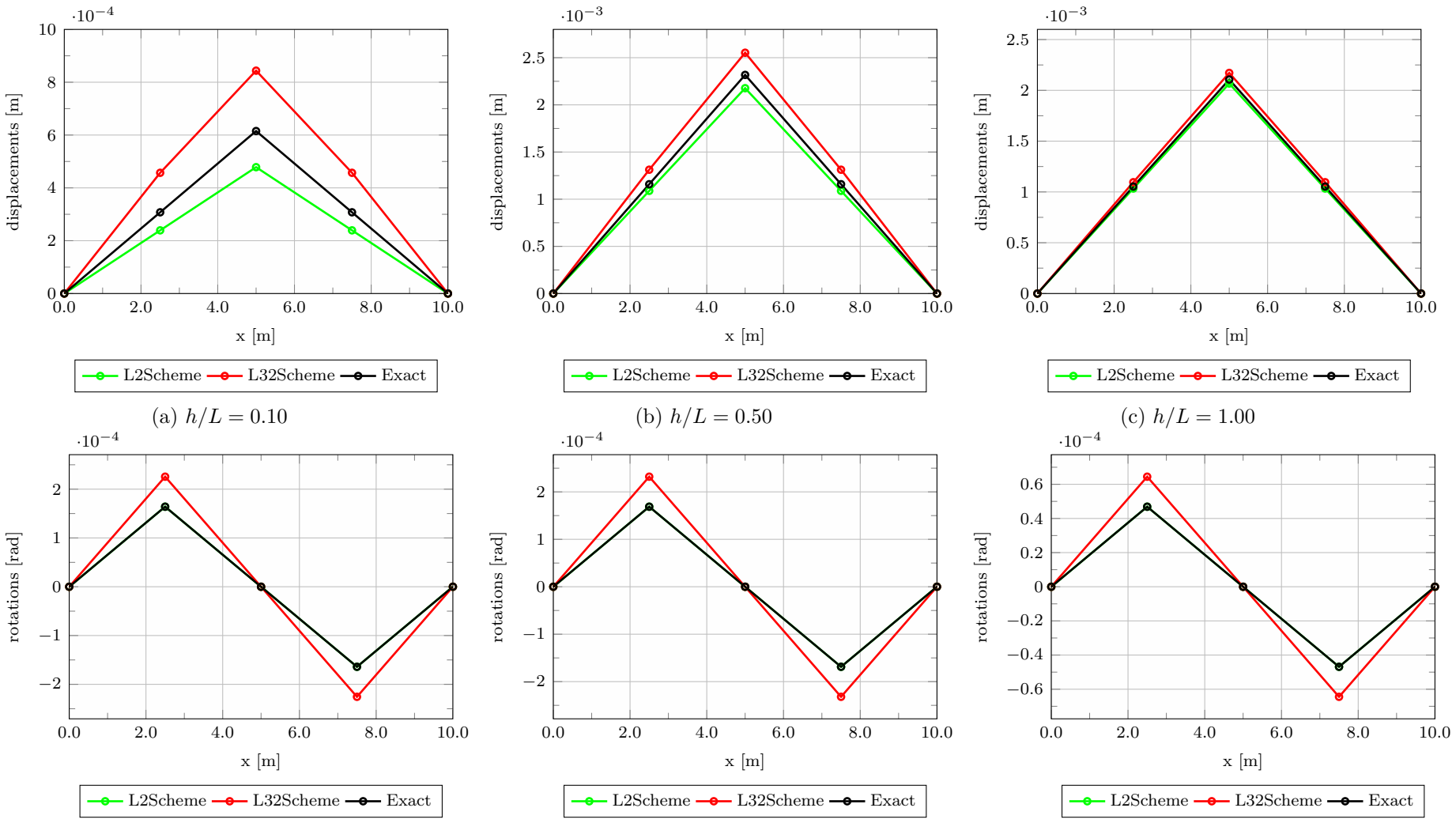

(a) $h/L = 0.10$ (b) $h/L = 0.50$ (c) $h/L = 1.00$

(d) $h/L = 0.10$ (e) $h/L = 0.50$ (f) $h/L = 1.00$

Figure 6.11: Fixed-fixed beam: force load results

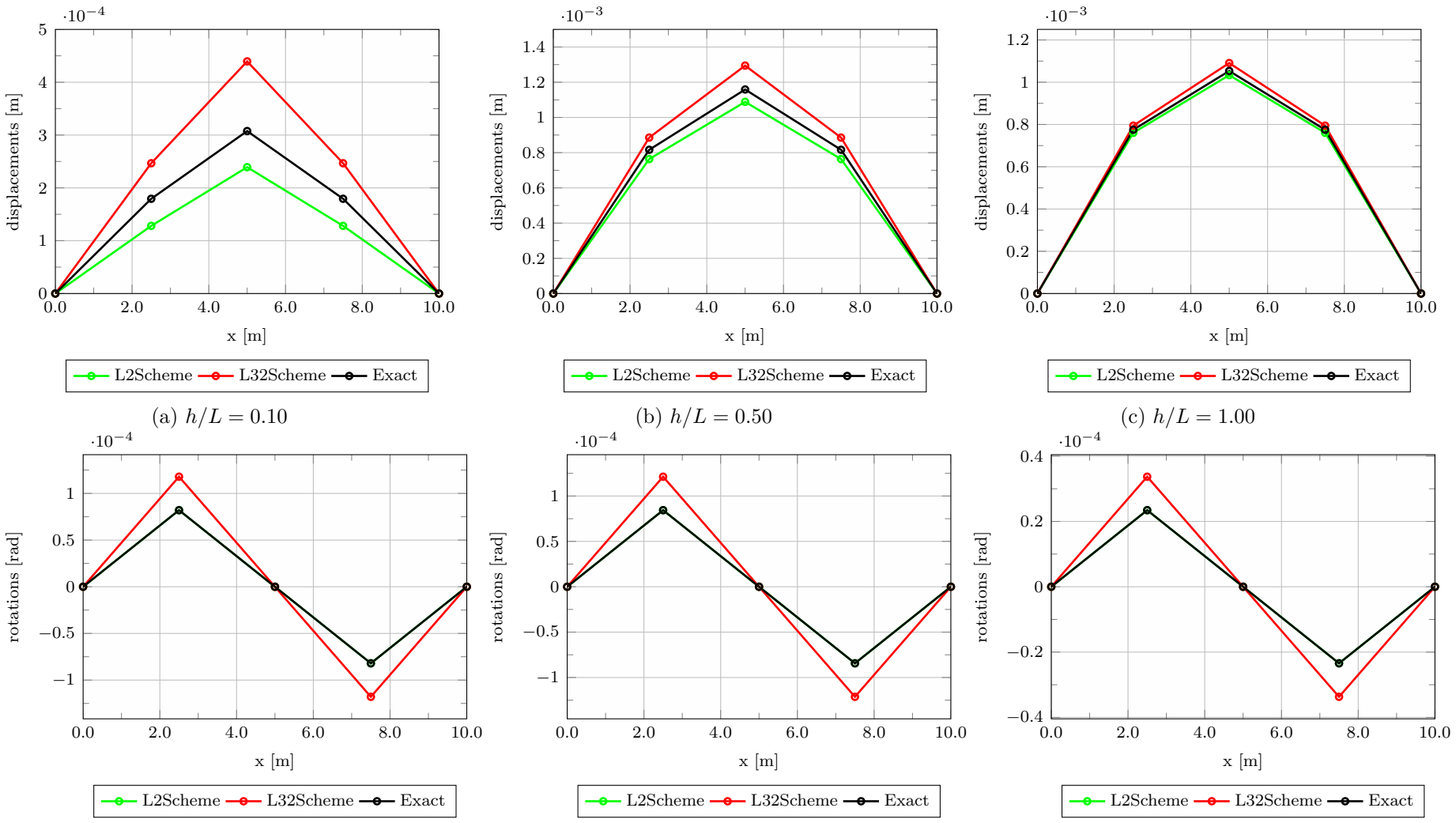

(a) $h/L = 0.10$ (b) $h/L = 0.50$ (c) $h/L = 1.00$

(d) $h/L = 0.10$ (e) $h/L = 0.50$ (f) $h/L = 1.00$

Figure 6.12: Fixed-fixed beam: uniformly distributed load results

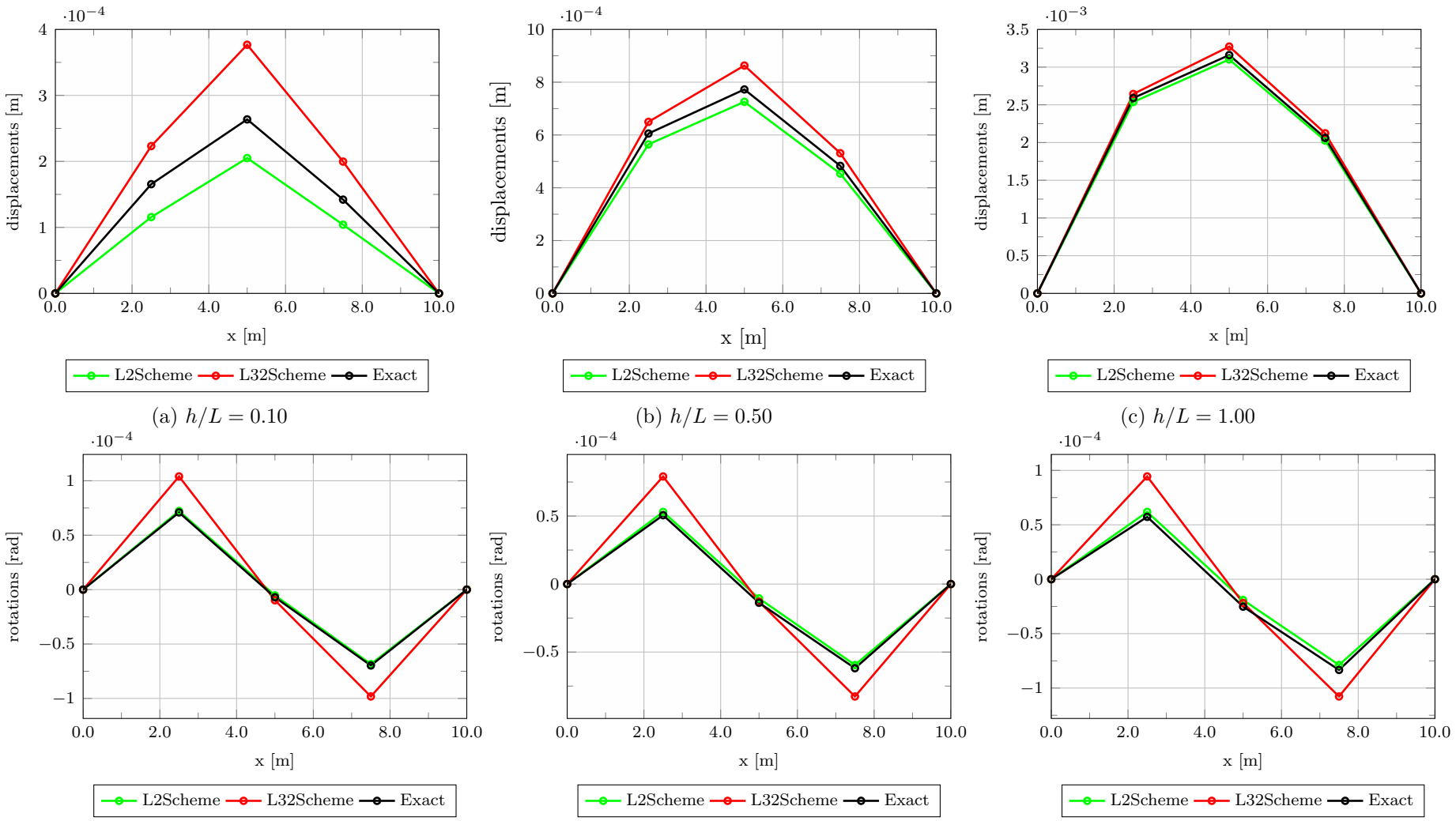

(a) $h/L = 0.10$ (b) $h/L = 0.50$ (c) $h/L = 1.00$

(d) $h/L = 0.10$ (e) $h/L = 0.50$ (f) $h/L = 1.00$

Figure 6.13: Fixed-fixed beam: linearly distributed load results

As can be observed in the previous plots, the numerical solutions showed a good agreement with the exact one. In terms of deflections, the L2-scheme exhibited a *lower bound solution*, while the L3/2-scheme exhibited an *upper bound solution*. Moreover, the numerical solutions provided for the force load case recover the exact rotation obtained from the analytical expressions for all boundary conditions, except for the fixed-pinned beam. Additionally, it is worth mentioning that the numerical solutions in terms of deflections tend to be closer to the exact solution when the slenderness ratios (h/L) increase, in other words, the results obtained with the $h/L = 1.00$ are better than the results obtained with $h/L = 0.10$. However, this tendency did not occur with the rotation results. Other than that the proposed SPIM models are locking-free, i.e. no additional treatment was necessary to avoid the *spurious stiffer behaviour*, as commonly happens with FEM during the simulations of shear-deformable beams. In Fig. 6.14 the results of displacements and rotations of the simply supported beam for the force load case are illustrated with a mesh with 11 nodes and the slenderness ratio of $h/L = 0.10$. The linear finite elements were simulated with 2 integration points. In fact, in this scenario the *stiffer* behaviour of the FEM simulation is clearly observed, in other words the displacement are smaller than expected, and the accuracy of the rotations are also affected.

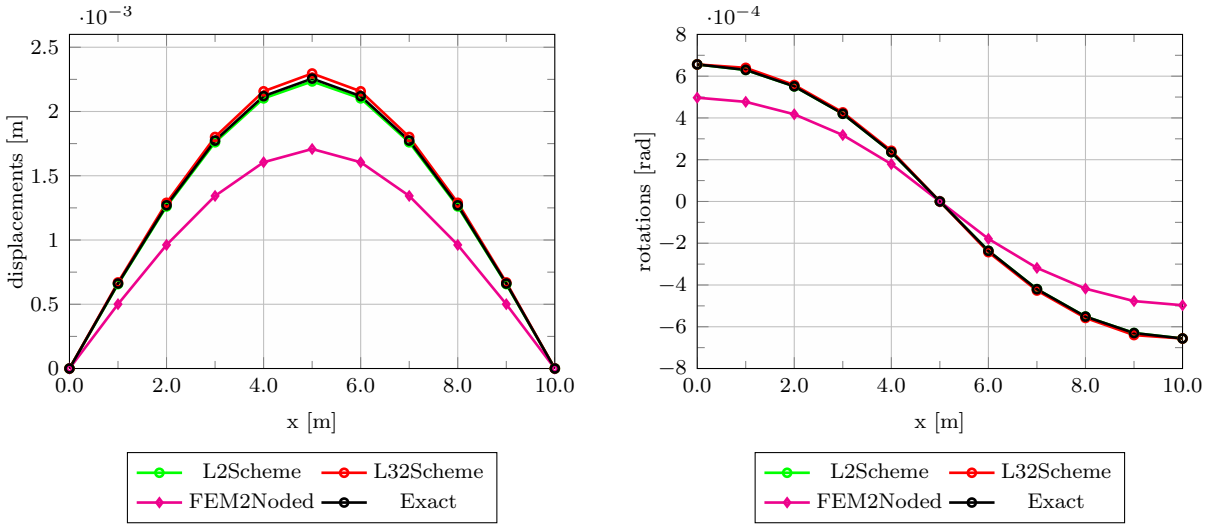

(a) (b)

Figure 6.14: Shear locking behaviour

In the sequel, the simulations of the error (see Eq. (6.1)) are shown in Figs. 6.15 to 6.18. The L2 and L3/2 schemes are compared with the results of the linear finite element method using several meshes. As already pointed out, the reference solutions used in Eq. (6.1) are the analytical solutions of the Timoshenko beam.

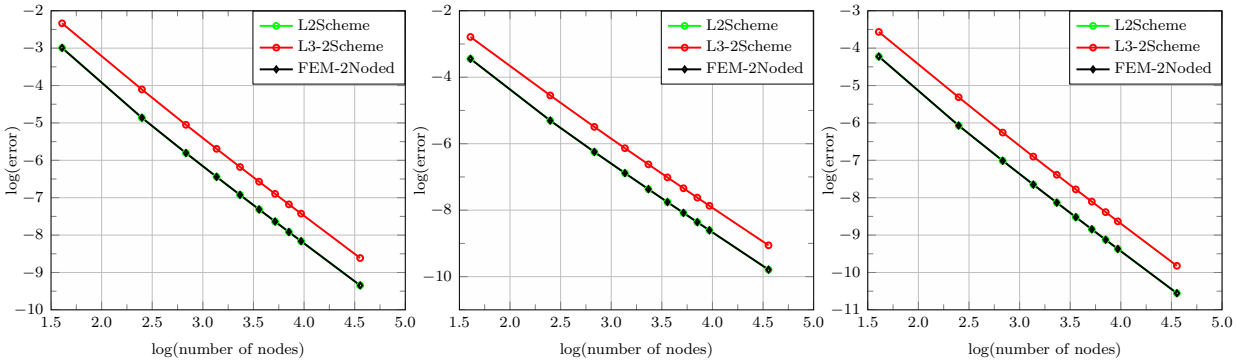

(a) Force load: $h/L = 0.10$ (b) Force load: $h/L = 0.50$ (c) Force load: $h/L = 1.00$

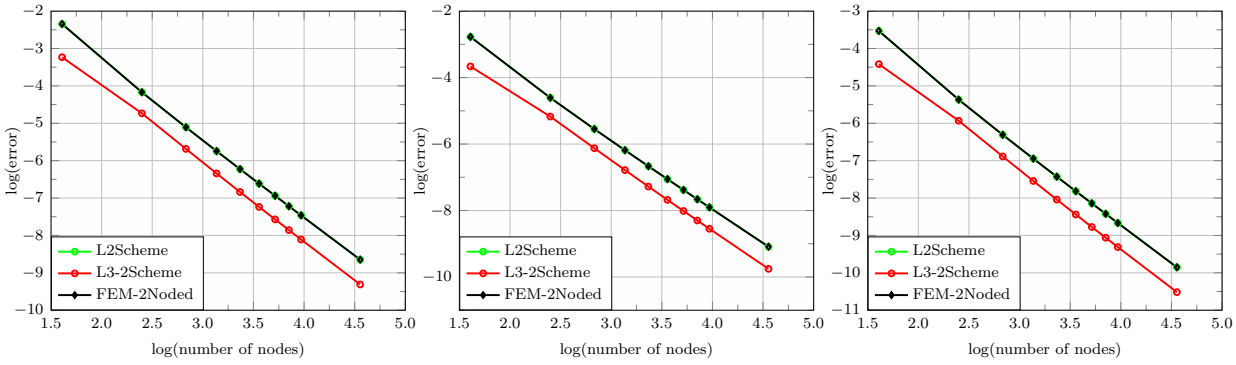

(d) Constant load: $h/L = 0.10$ (e) Constant load: $h/L = 0.50$ (f) Constant load: $h/L = 1.00$

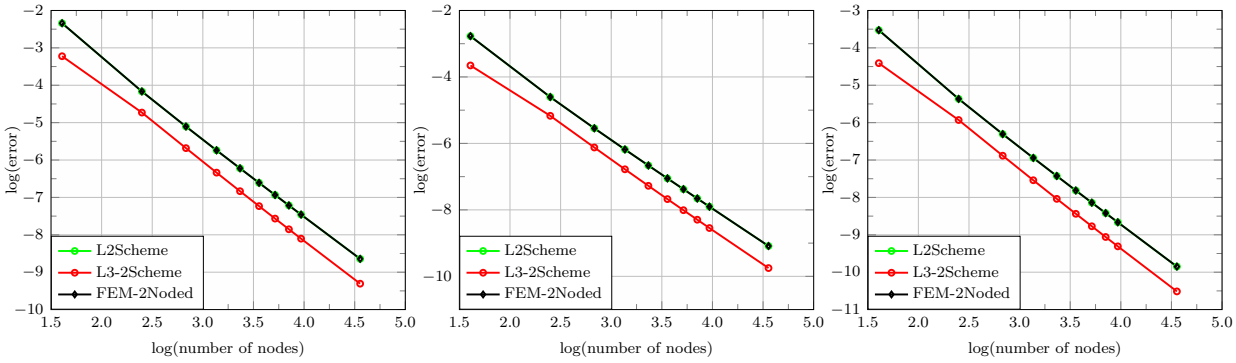

(g) Linear load: $h/L = 0.10$ (h) Linear load: $h/L = 0.50$ (i) Linear load: $h/L = 1.00$

Figure 6.15: Error norm simulations for the simply supported beam

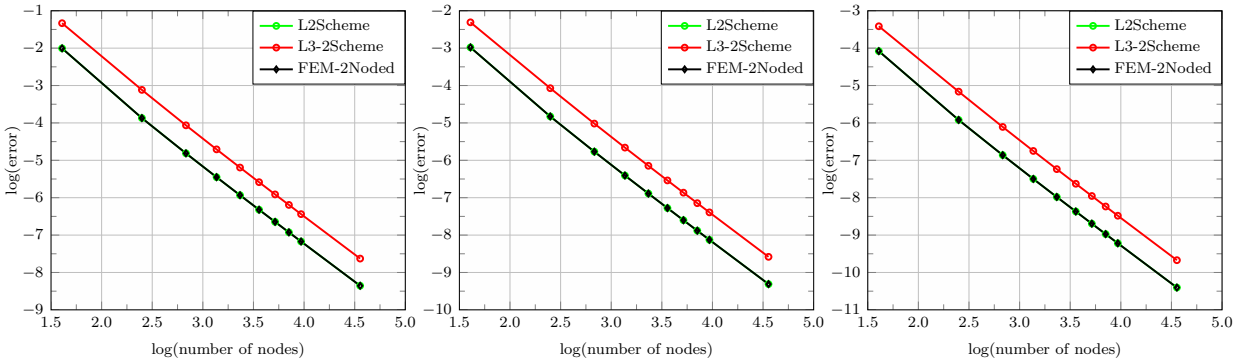

(a) Force load: $h/L = 0.10$ (b) Force load: $h/L = 0.50$ (c) Force load: $h/L = 1.00$

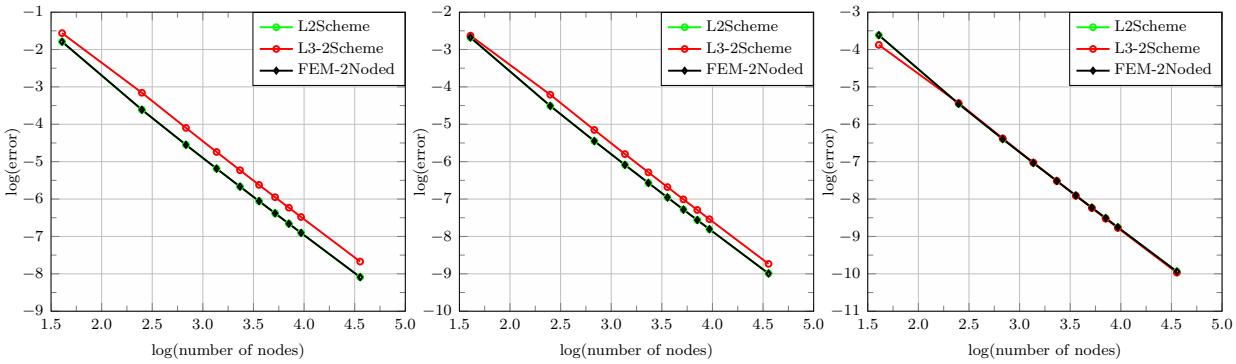

(d) Constant load: $h/L = 0.10$ (e) Constant load: $h/L = 0.50$ (f) Constant load: $h/L = 1.00$

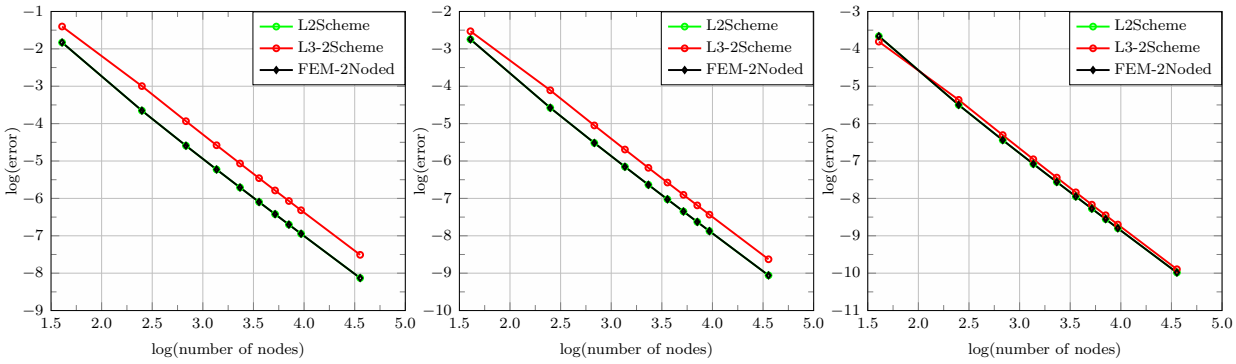

(g) Linear load: $h/L = 0.10$ (h) Linear load: $h/L = 0.50$ (i) Linear load: $h/L = 1.00$

Figure 6.16: Error norm simulations for the fixed-pinned beam

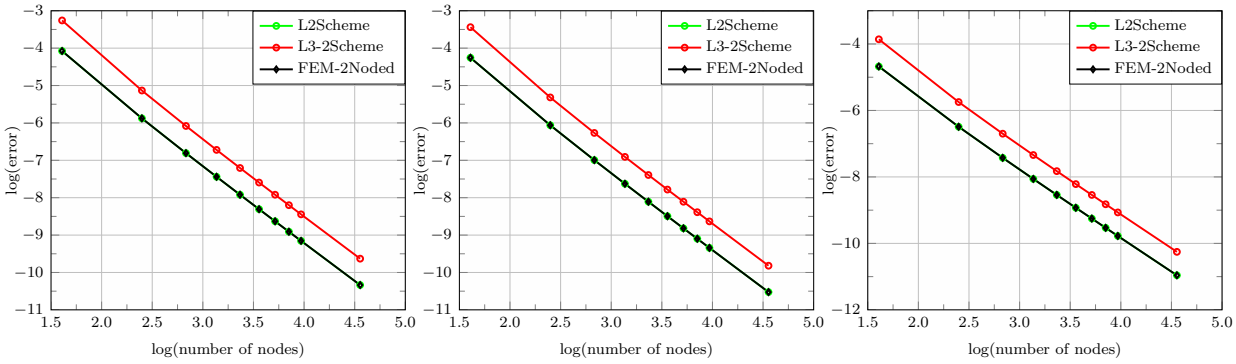

(a) Force load: $h/L = 0.10$ (b) Force load: $h/L = 0.50$ (c) Force load: $h/L = 1.00$

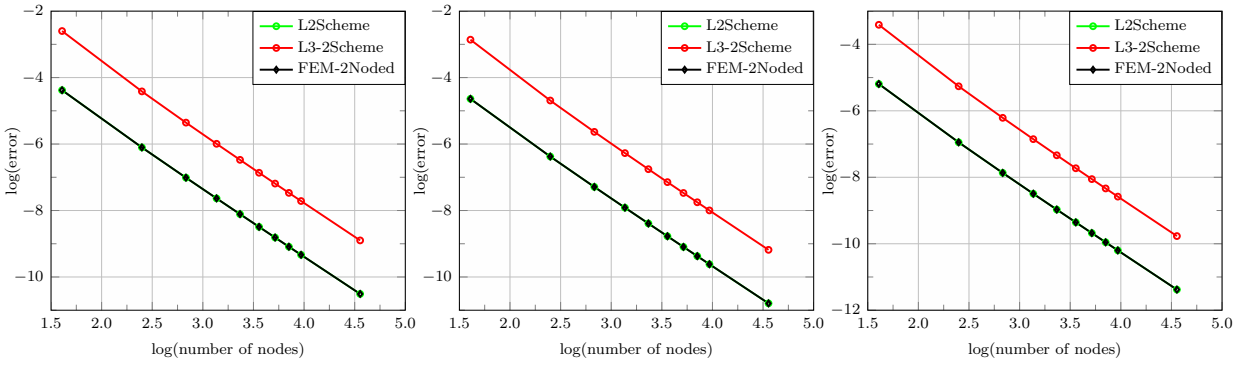

(d) Constant load: $h/L = 0.10$ (e) Constant load: $h/L = 0.50$ (f) Constant load: $h/L = 1.00$

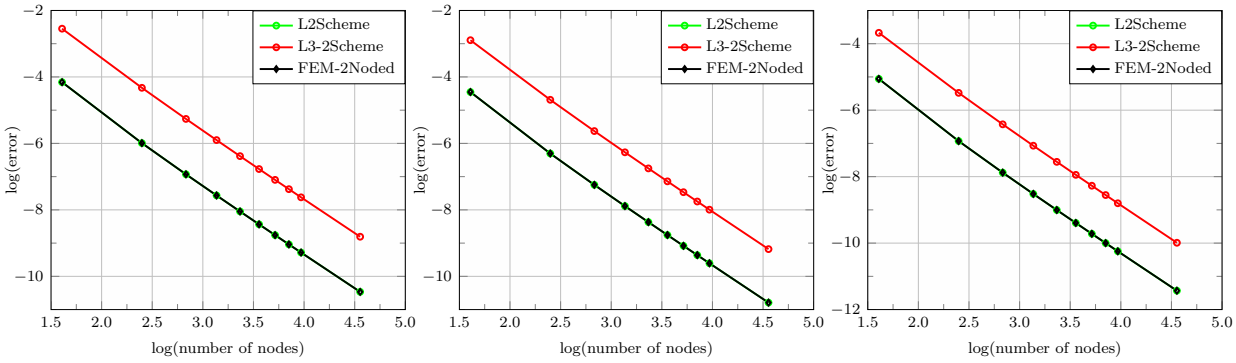

(g) Linear load: $h/L = 0.10$ (h) Linear load: $h/L = 0.50$ (i) Linear load: $h/L = 1.00$

Figure 6.17: Error norm simulations for the fixed-free beam

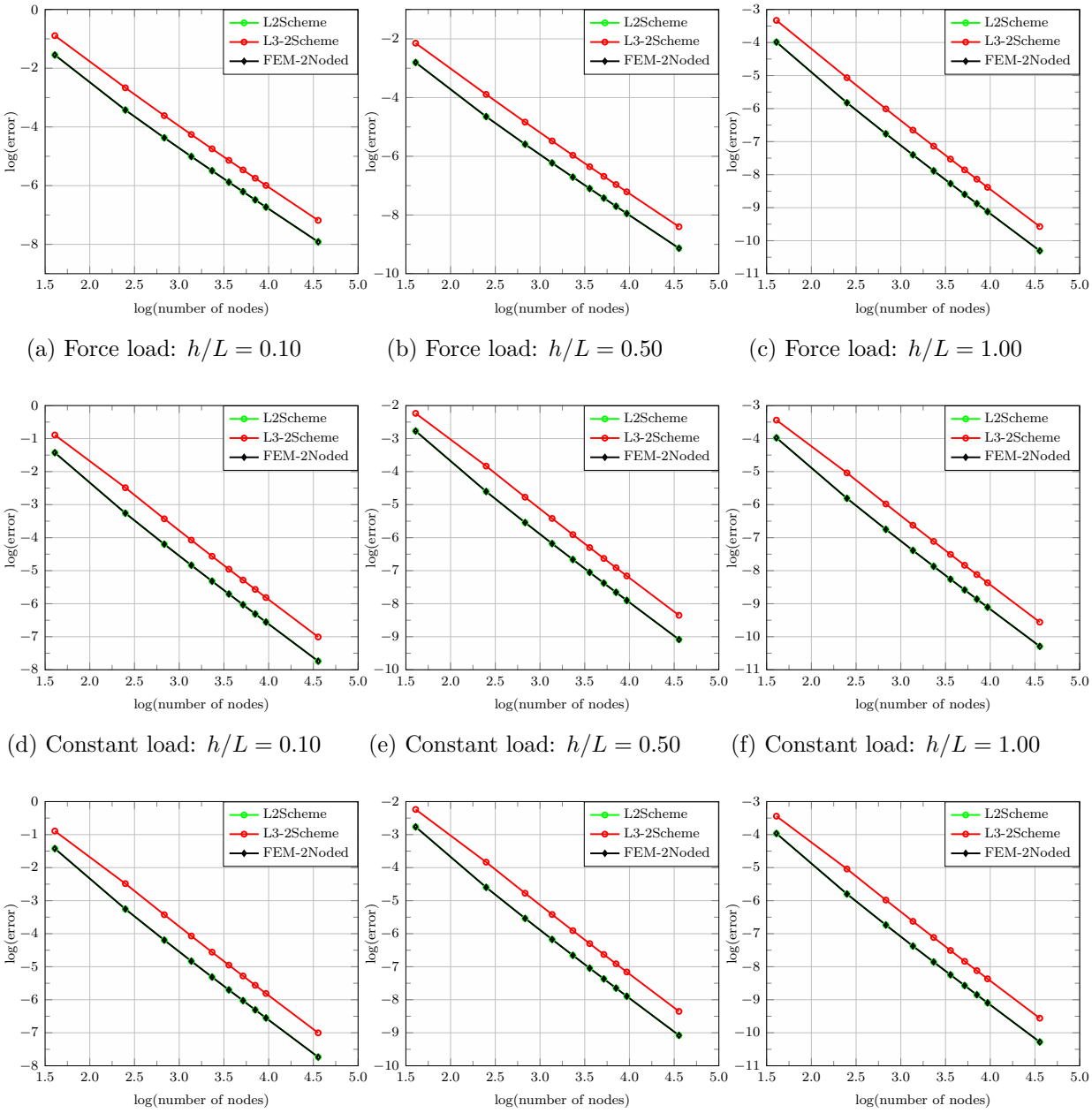

(a) Force load: $h/L = 0.10$ (b) Force load: $h/L = 0.50$ (c) Force load: $h/L = 1.00$

(d) Constant load: $h/L = 0.10$ (e) Constant load: $h/L = 0.50$ (f) Constant load: $h/L = 1.00$

(g) Linear load: $h/L = 0.10$ (h) Linear load: $h/L = 0.50$ (i) Linear load: $h/L = 1.00$

Figure 6.18: Error norm simulations for the fixed-fixed beam

From the error results shown above, one can observe that the L2-scheme simulations exactly reproduce the linear finite element results with one integration point. The L3/2-scheme exhibited the highest errors over all, except for the uniform (Figs. 6.15d to 6.15f) and linear (Figs. 6.15g to 6.15i) loads in the simply supported beam. Both the linear FEM and the L2 and L3/2 schemes exhibited the same rate of convergence.

For the force load case the difference of the L2 and L3/2 error results were similar in all boundary conditions. For the other load cases, the cantilever beam shown the highest differences, while the fixed-pinned beam shown the lower ones. Furthermore, for the simply supported and fixed-fixed beams the difference of error results were similar for

all load cases.

In general, the error for each simulation shown a descendent behaviour with the increasing of the slenderness ratios (h/L), which is in accordance with the results of deflections shown previously, i.e. in general, the errors obtained using $h/L = 0.10$ are higher than the errors using $h/L = 1.00$.

6.3 αPIM simulations

As shown in Section 6.2, the exact solution of the Timoshenko beam is bounded by the SPIM numerical results using the L2 and L3/2 schemes. Hence the alpha PIM shape function presented in Section 5.7 can be used to combine these schemes aiming to improve the outcome.

6.3.1 Alpha calibration

In order to obtain the αPIM results, a proper alpha parameter should be chosen. First, several simulations were performed varying the alpha values from 0.1 to 0.9 aiming to reveal the variation of the deflections when compared to the exact solution. In Figs. 6.20 to 6.23, the variation of the exact deflection at $x = 5\,\text{m}$ is depicted for each load case and boundary condition (*left plots*) using a mesh with 11 nodes and a slenderness ratio of $h/L = 0.10$. One can observe that the displacements vary linearly with the alpha parameter. During this research work, it was found that this is true for all points where a displacement is a non-zero value and this is valid for all meshes, boundary conditions and slenderness ratios. It is clear (see Figs. 6.20 to 6.23 and Eq. (5.68)) that the L2-scheme produces the same results of αPIM when $\alpha = 1.0$ (*stiffer solution*), while the L3/2-scheme is equivalent to αPIM for $\alpha = 0.0$[1] (*softer solution*).

Hence, knowing the exact value of the displacement at $x = 5\,\text{m}$, the "optimal" alpha parameter can be estimated by fitting the displacement values in a linear function $y = ax + b \equiv a \cdot \alpha + b = v$ and seeking for an $\alpha = \alpha_{est.}$ value such that $a \cdot \alpha + b = v^{\text{exact}}$, see Fig. 6.19. Therefore α can be estimated, for a particular position i, as shown in Eq. (6.2). In theory, a simulation using $\alpha_{est.}$ might lead to a result very close to v^{exact} at $x = 5\,\text{m}$, and hopefully to better results in an overall perspective.

[1] It could be the contrary depending of the defined order of the shape functions settled in Eq. (5.68).

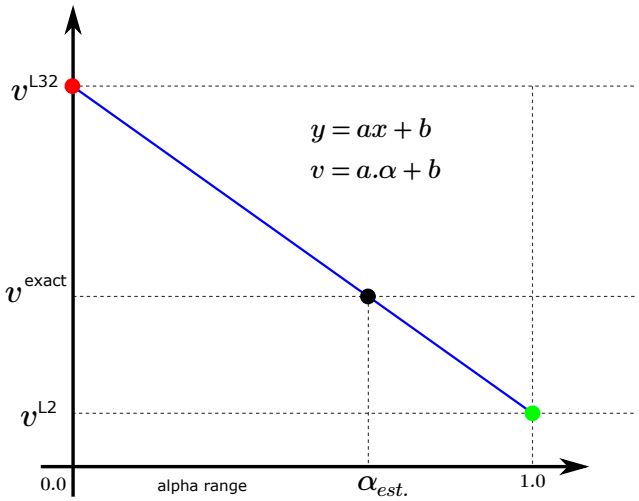

$$\alpha_{est.} = \frac{v_i^{\text{exact}} - v_i^{L3/2}}{v_i^{L2} - v_i^{L3/2}} \qquad (6.2)$$

Figure 6.19: Alpha variation using L2 and L3/2 schemes

In order to standardize the procedure of estimating alpha, the displacement at $x = 5\,\text{m}$ was used to "calibrate" the alpha values for all cases of this chapter, i.e. the results of L2 and L3/2 schemes at $x = 5\,\text{m}$ and the correspondent displacement exact values, were defined as the input parameters in Eq. (6.2) for all meshes[2] and boundary conditions. Twelve meshes were used to map the variation of alpha. The same meshes presented in Section 6.2 to compute the error were used, plus two additional meshes containing 191 and 383 nodes. The outcome of this process is detailed in Figs. 6.20 to 6.23 (*right plots*). From these plots, one can observe that each discretisation possesses its own "optimal" alpha based on the displacement at $x = 5\,\text{m}$. Moreover, a single plot means that each slenderness ratio produced the same results. In Appendix E the calibrated alpha values are shown quantitatively for each case.

[2]The meshes were chosen to guarantee that there is always a node placed in $x = 5\,\text{m}$.

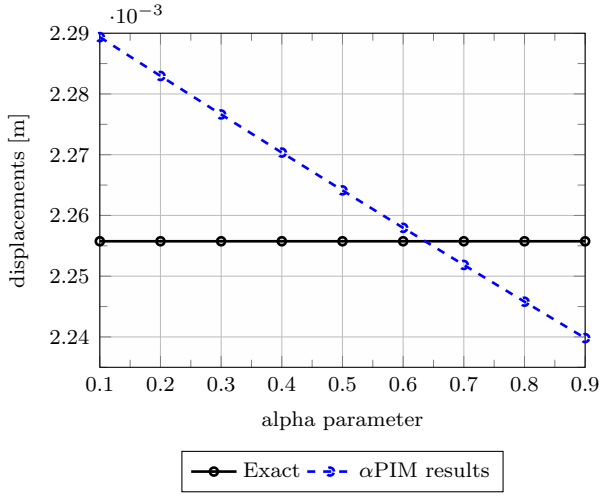

(a) Force load displacements

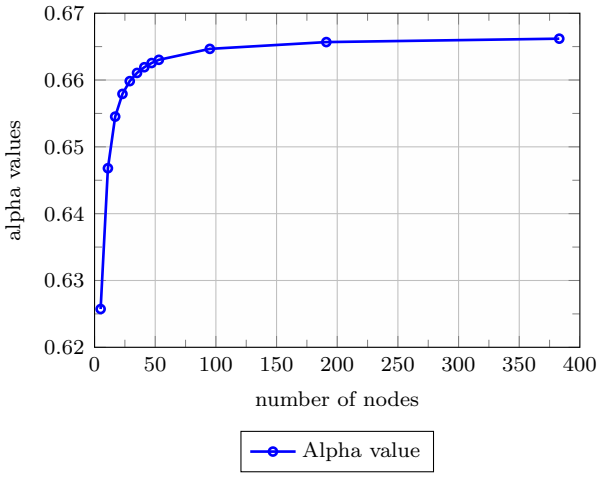

(b) Variation of the alpha parameter with the mesh

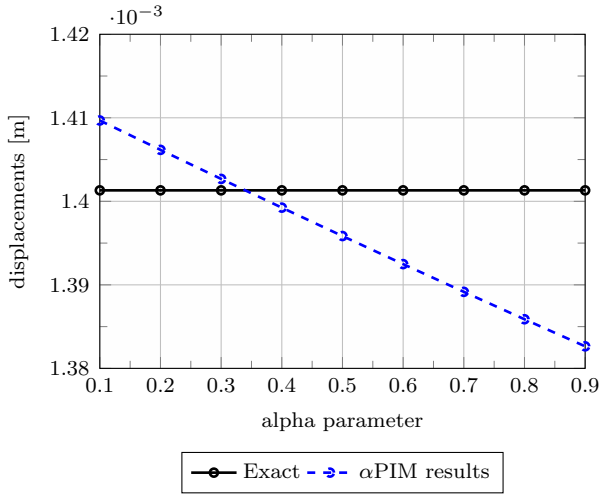

(c) Constant load displacements

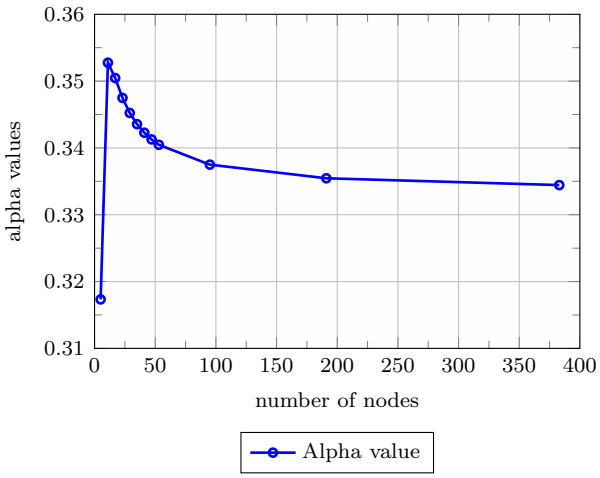

(d) Variation of the alpha parameter with the mesh

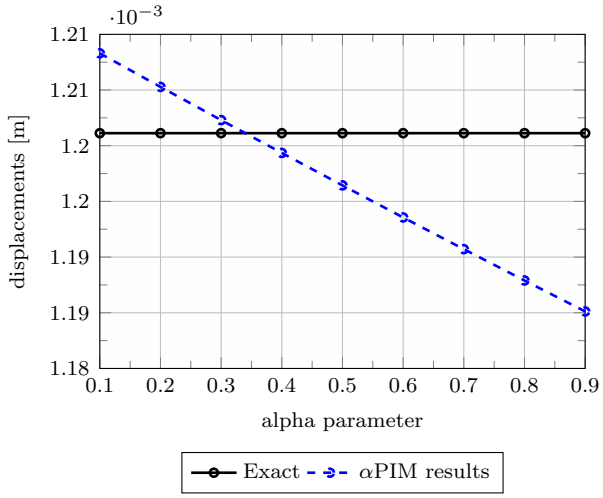

(e) Linear load displacements

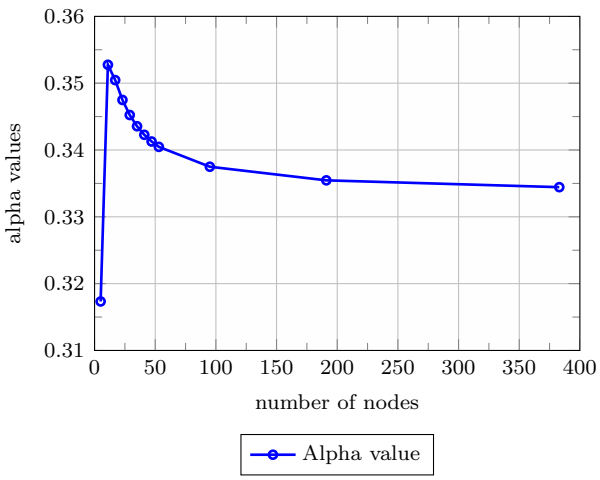

(f) Variation of the alpha parameter with the mesh

Figure 6.20: Alpha analysis for the simply supported beam

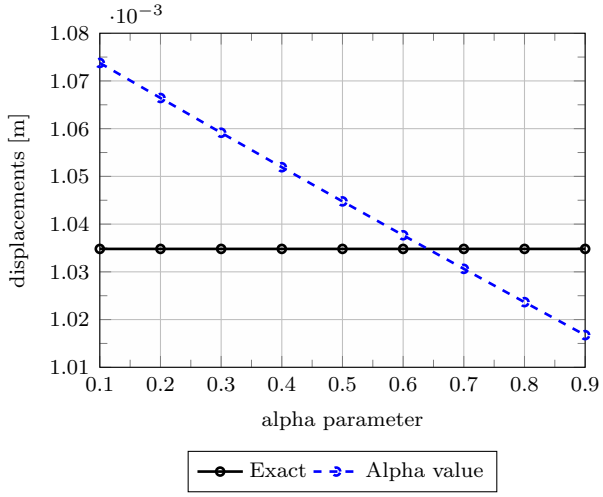

(a) Force load displacements

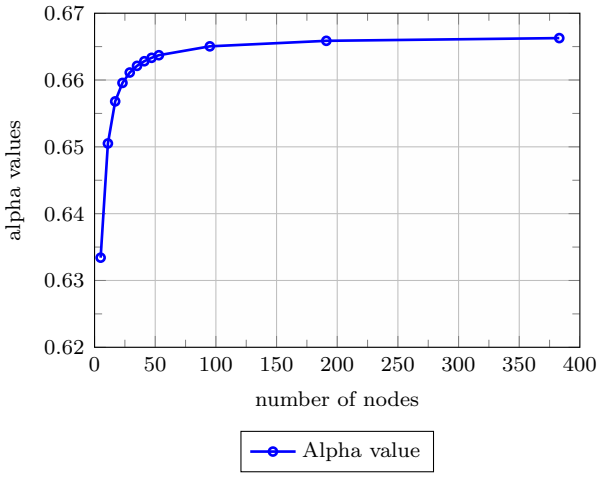

(b) Variation of the alpha parameter with the mesh

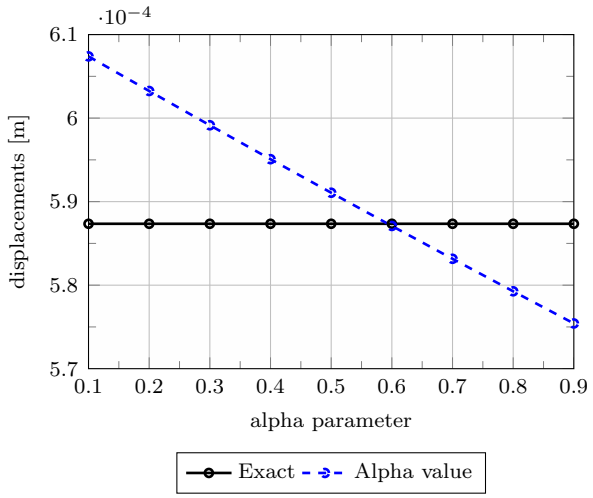

(c) Constant load displacements

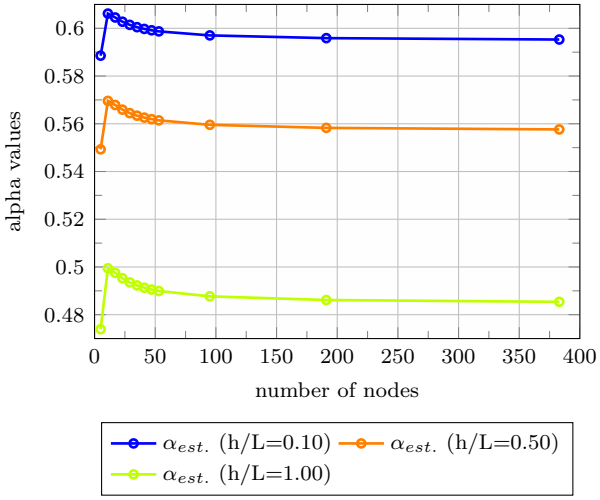

(d) Variation of the alpha parameter with the mesh

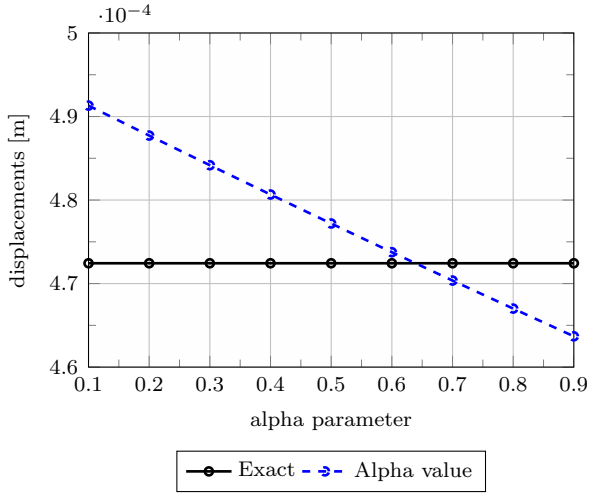

(e) Linear load displacements

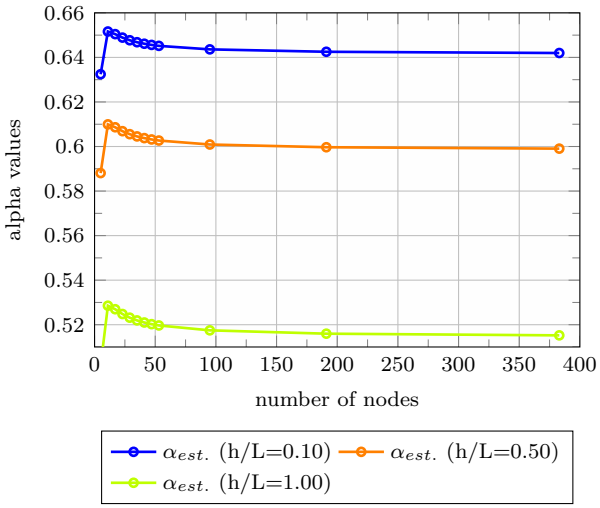

(f) Variation of the alpha parameter with the mesh

Figure 6.21: Alpha analysis for the fixed-pinned beam

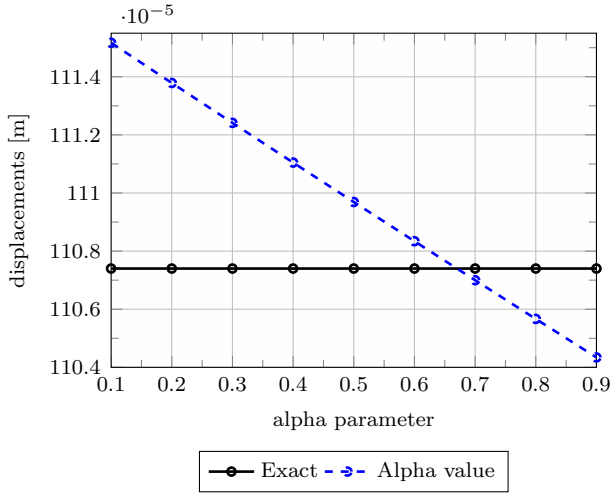

(a) Force load displacements

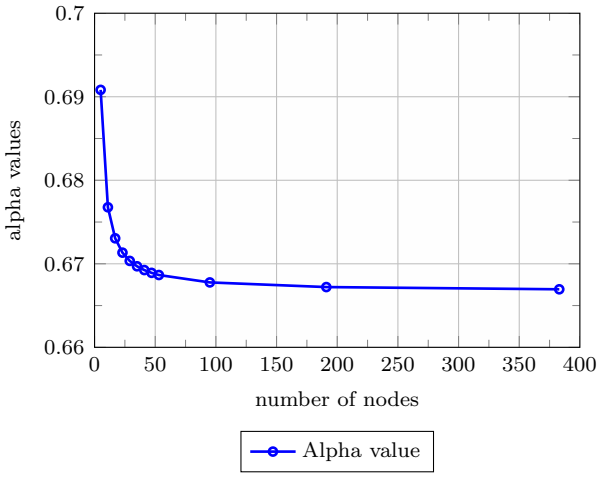

(b) Variation of the alpha parameter with the mesh

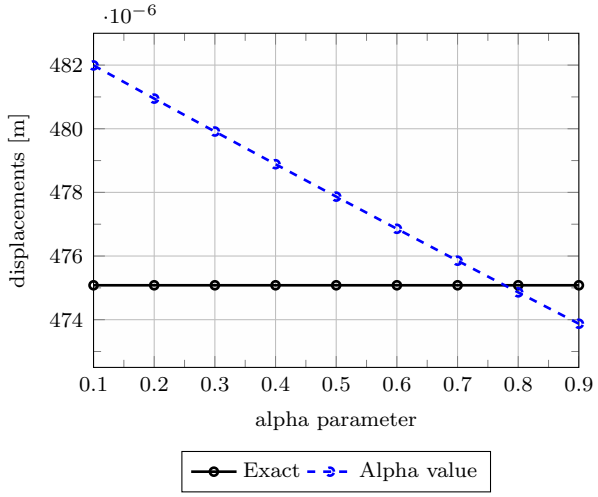

(c) Constant load displacements

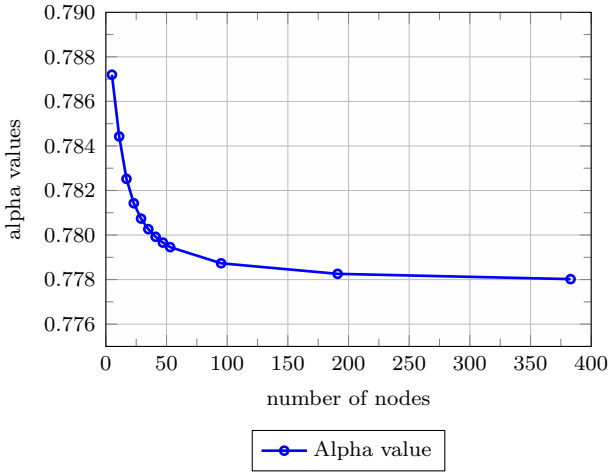

(d) Variation of the alpha parameter with the mesh

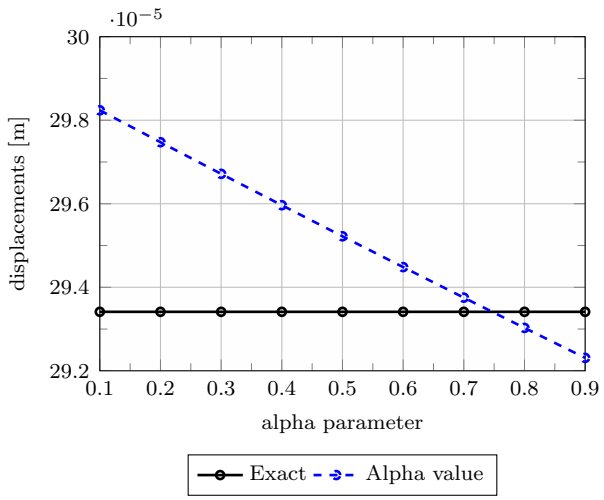

(e) Linear load displacements

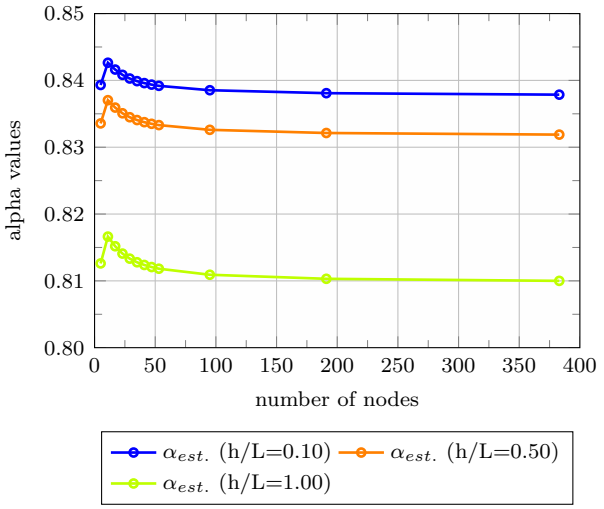

(f) Variation of the alpha parameter with the mesh

Figure 6.22: Alpha analysis for the cantilever beam

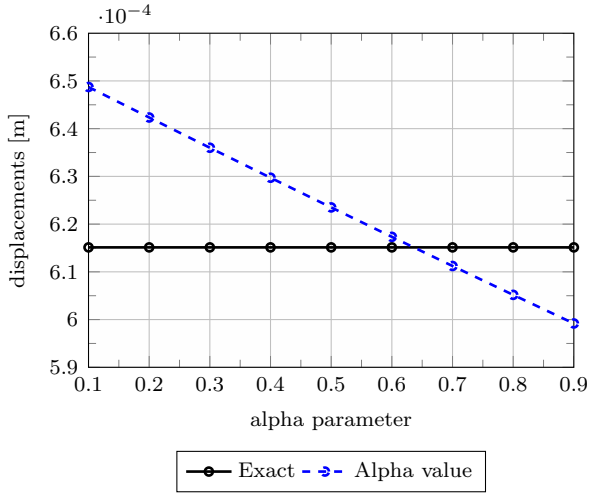

(a) Force load displacements

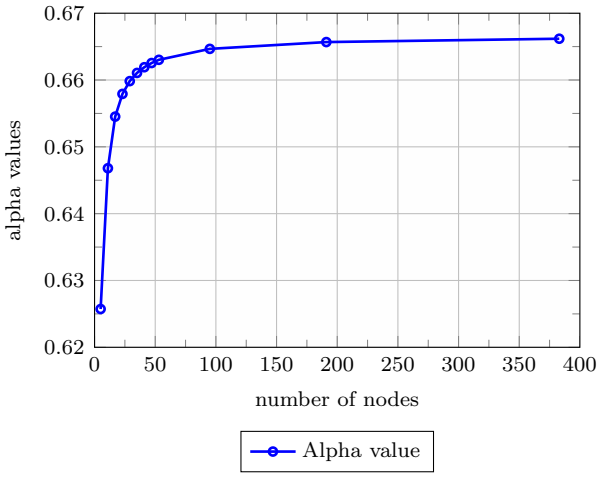

(b) Variation of the alpha parameter with the mesh

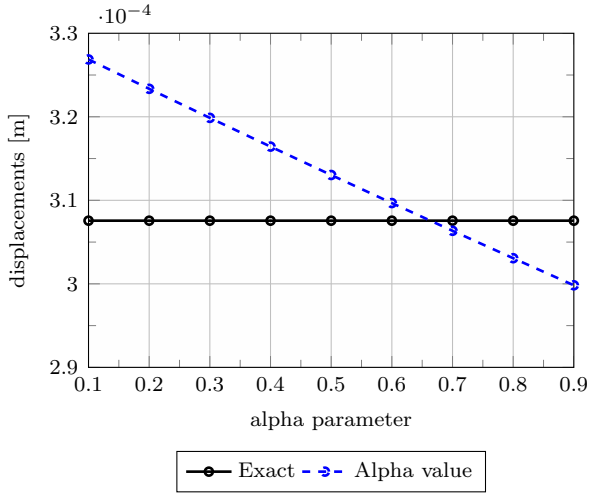

(c) Constant load displacements

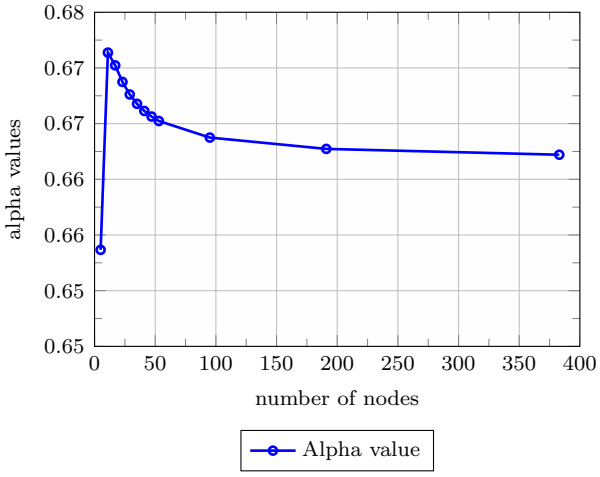

(d) Variation of the alpha parameter with the mesh

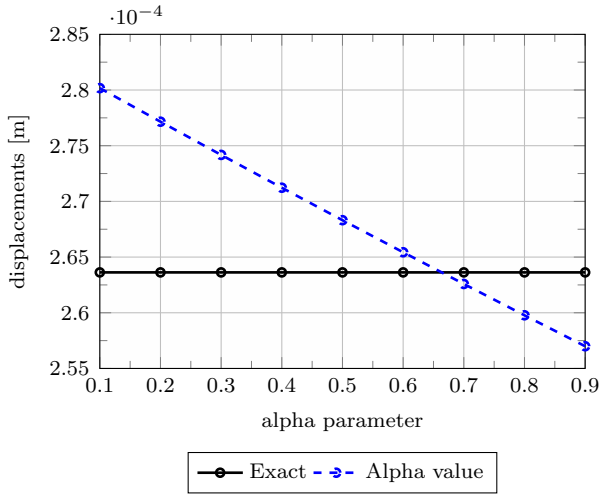

(e) Linear load displacements

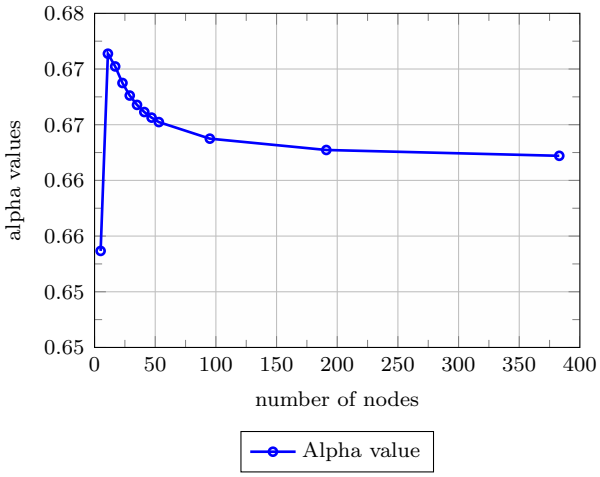

(f) Variation of the alpha parameter with the mesh

Figure 6.23: Alpha analysis for the fixed-fixed beam

From the graphical representation of the alpha values, the following considerations can be drawn: (i) for each boundary condition and load case, $\alpha_{est.}$ exhibits a convergent behaviour with the discretisation, with a small variation from the coarsest to the most refined mesh, (ii) within each boundary condition $\alpha_{est.}$ does not vary too much with the load case, except for the simply supported beam where the results for the force load are quite different from the ones obtained with the uniform and linear loads.

In general, the calibrated alpha parameter varied according to the boundary condition, load case and discretisation. On the other hand, it appeared to be less sensitive to variations of the slenderness ratio. It does not varied with the slenderness ratio (h/L), except for the fixed-pinned beam for the distributed load cases (Fig. 6.21d and Fig. 6.21f) and the cantilever beam with a linearly distributed load (Fig. 6.22f). The convergence behaviour were similar for all boundary conditions, except for the cantilever beam, where the pattern of the plots slightly changed. Moreover, for the symmetric boundary conditions, pinned-pinned and fixed-fixed, the obtained alpha values for the uniformly and linearly distributed load cases were the same.

6.3.2 Error simulations

Using the estimated alpha values obtained in Section 6.3.1, a set of simulations were performed with the αPIM shape functions. The error values were computed, and added to the plots shown in Figs. 6.15 to 6.18. Finite element simulations with three nodes elements were also performed, however, only the error results of the simply supported beam case are shown (Fig. 6.24). As illustrated in the following, the αPIM shapes improve the results of L2 and L3/2 schemes considerably, however even these improved solutions are no match for the quadratic Timoshenko FEM model. This conclusion is extended to the other boundary conditions, therefore, the quadratic FEM was left out of the other cases. As already pointed out in Chapter 5, the computational cost of αPIM and the linear FEM are comparable, since it is truly necessary to evaluate the shape functions *only* at the center of the smoothing domains. The error results including the αPIM simulations are shown Figs. 6.24 to 6.27.

In order to analyse the error results in another perspective, the variation of the error with the alpha parameter was evaluated using a slenderness ratio of $h/L = 0.10$ for all load cases and boundary conditions. In this scenario, the results of the 2-noded FEM model are straight lines for each mesh. Two type of plots are shown: (i) the errors obtained simply using Eq. (6.1), and (ii) the errors obtained disregarding the rotations in Eq. (6.1). The outcome is presented in Figs. 6.28 to 6.39.

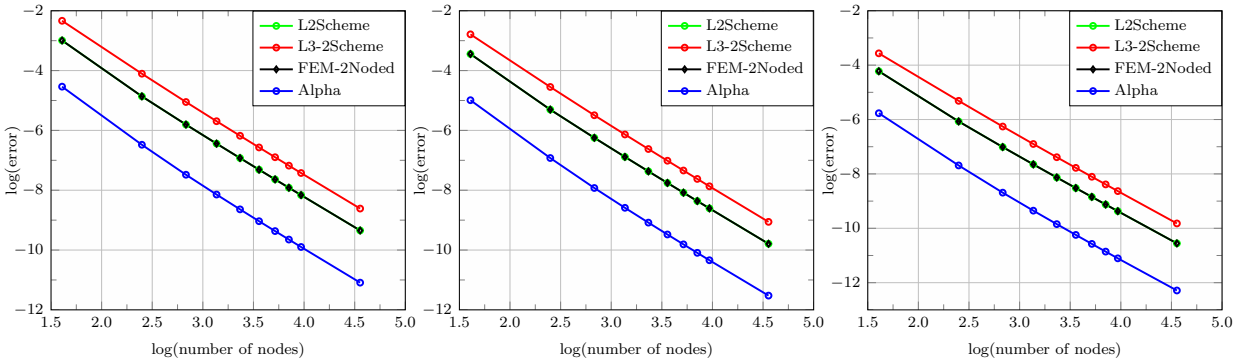

(a) Force load: $h/L = 0.10$ (b) Force load: $h/L = 0.50$ (c) Force load: $h/L = 1.00$

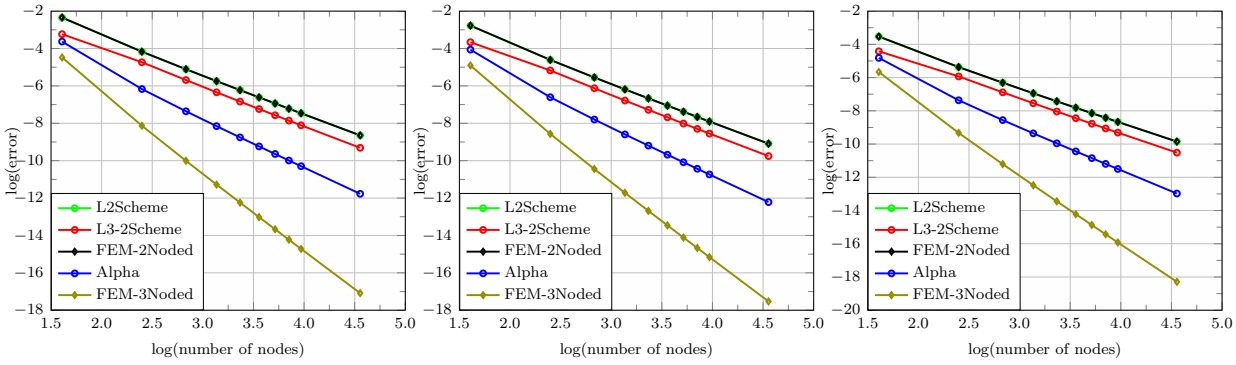

(d) Constant load: $h/L = 0.10$ (e) Constant load: $h/L = 0.50$ (f) Constant load: $h/L = 1.00$

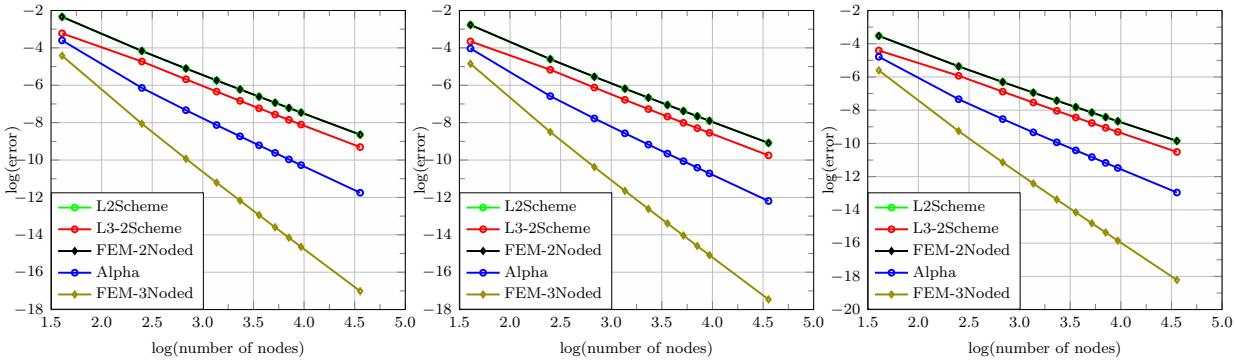

(g) Linear load: $h/L = 0.10$ (h) Linear load: $h/L = 0.50$ (i) Linear load: $h/L = 1.00$

Figure 6.24: Error norm simulations for the simply supported beam

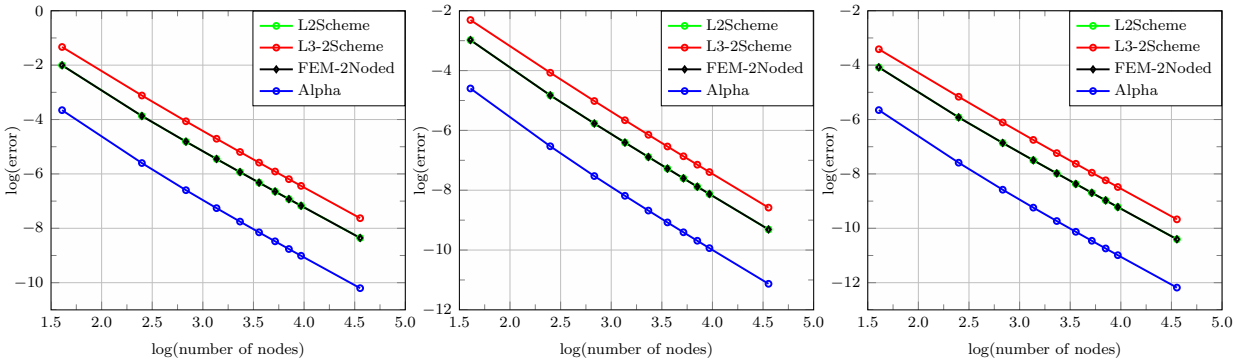

(a) Force load: $h/L = 0.10$ (b) Force load: $h/L = 0.50$ (c) Force load: $h/L = 1.00$

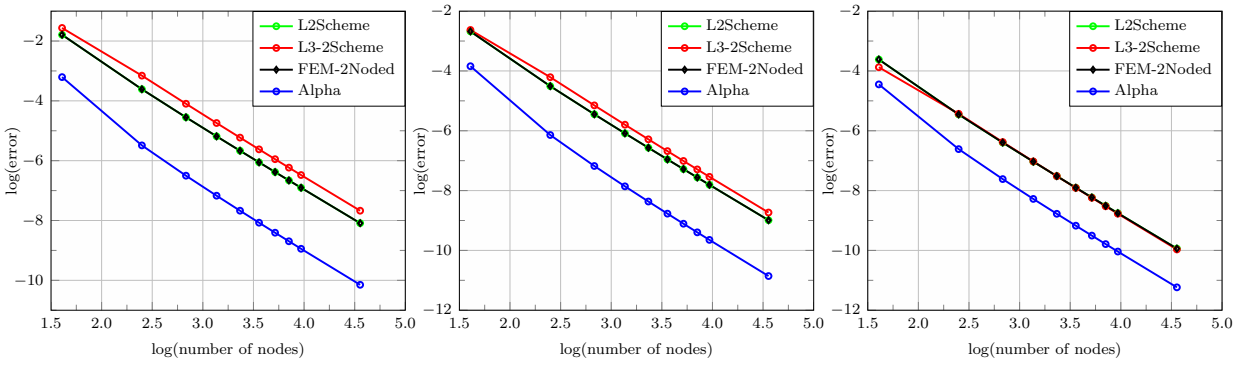

(d) Constant load: $h/L = 0.10$ (e) Constant load: $h/L = 0.50$ (f) Constant load: $h/L = 1.00$

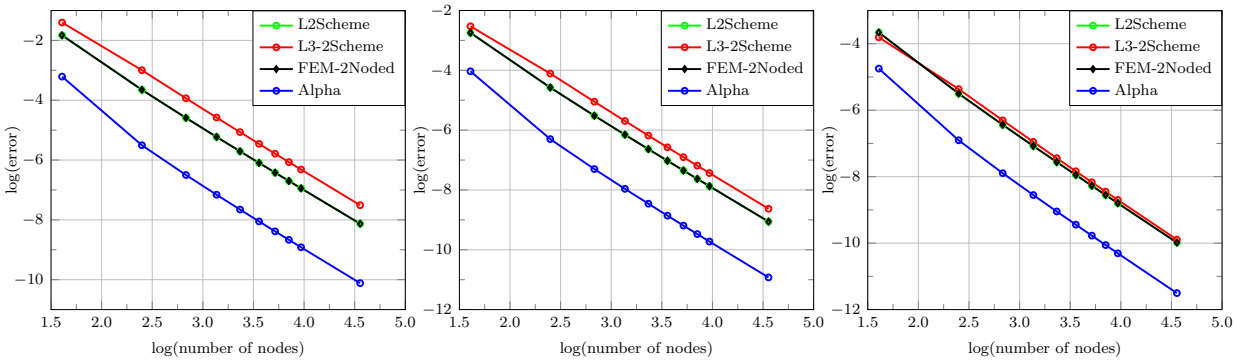

(g) Linear load: $h/L = 0.10$ (h) Linear load: $h/L = 0.50$ (i) Linear load: $h/L = 1.00$

Figure 6.25: Error norm simulations for the fixed-pinned beam

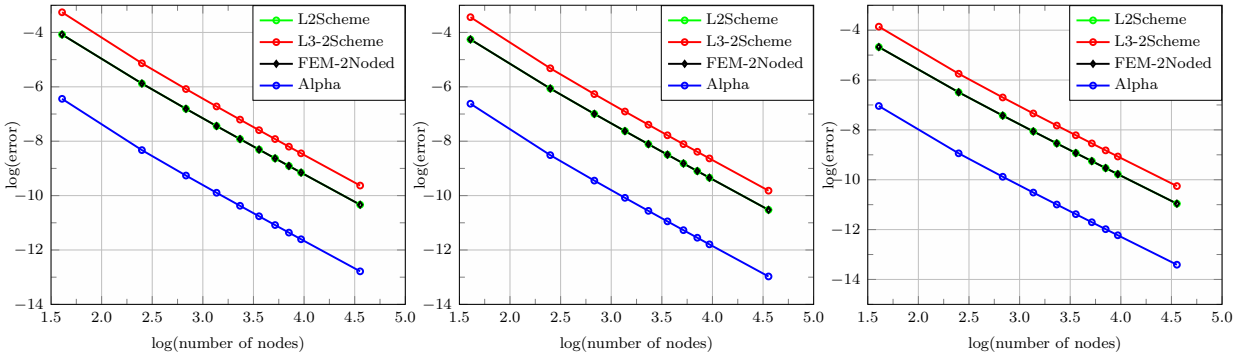

(a) Force load: $h/L = 0.10$ (b) Force load: $h/L = 0.50$ (c) Force load: $h/L = 1.00$

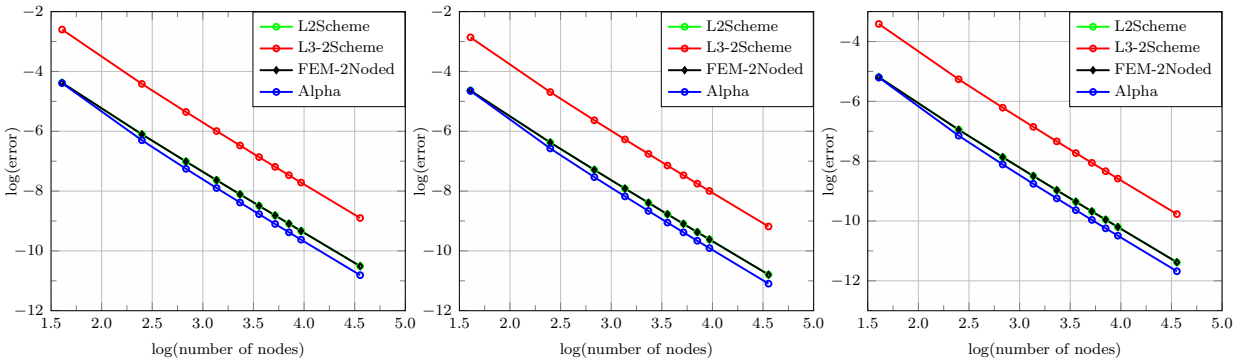

(d) Constant load: $h/L = 0.10$ (e) Constant load: $h/L = 0.50$ (f) Constant load: $h/L = 1.00$

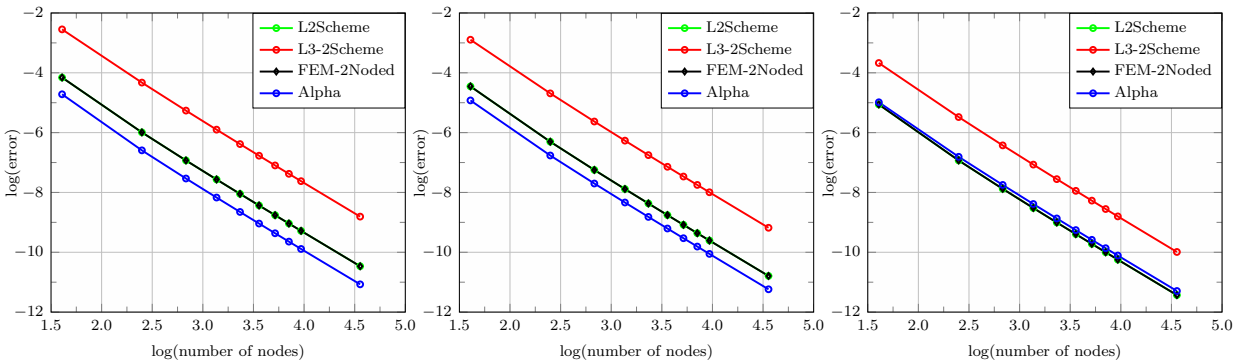

(g) Linear load: $h/L = 0.10$ (h) Linear load: $h/L = 0.50$ (i) Linear load: $h/L = 1.00$

Figure 6.26: Error norm simulations for the fixed-free beam

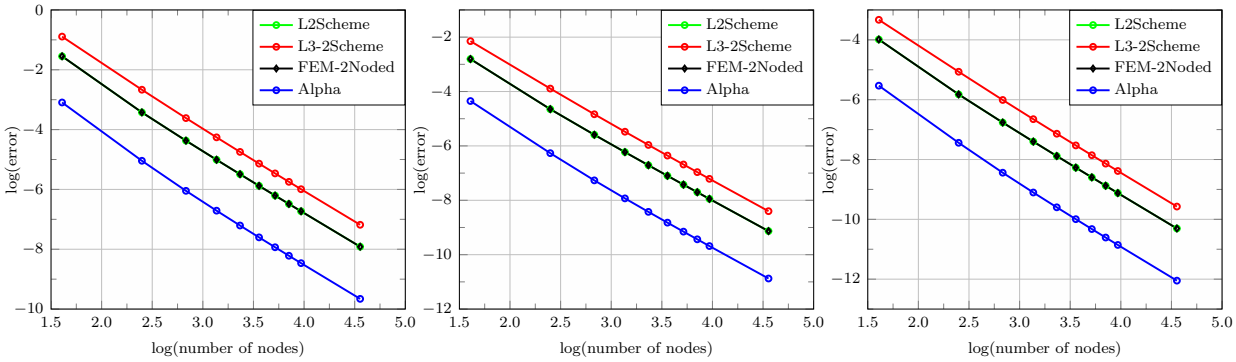

(a) Force load: $h/L = 0.10$ (b) Force load: $h/L = 0.50$ (c) Force load: $h/L = 1.00$

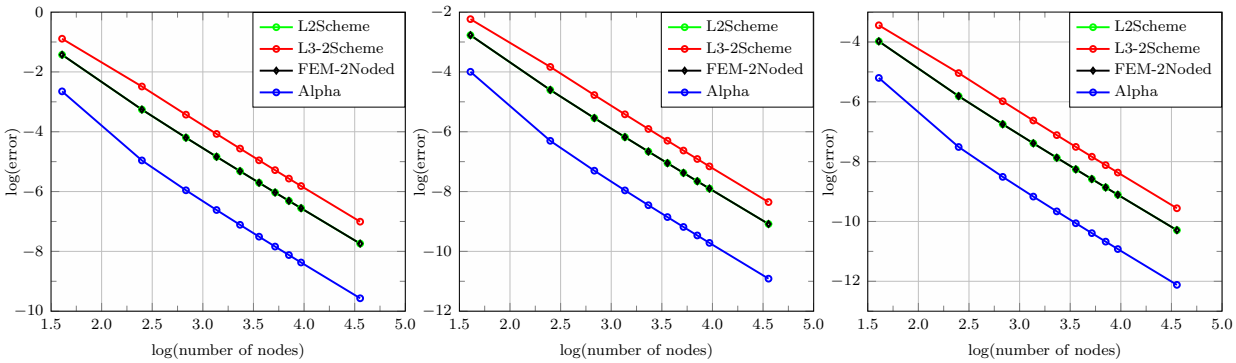

(d) Constant load: $h/L = 0.10$ (e) Constant load: $h/L = 0.50$ (f) Constant load: $h/L = 1.00$

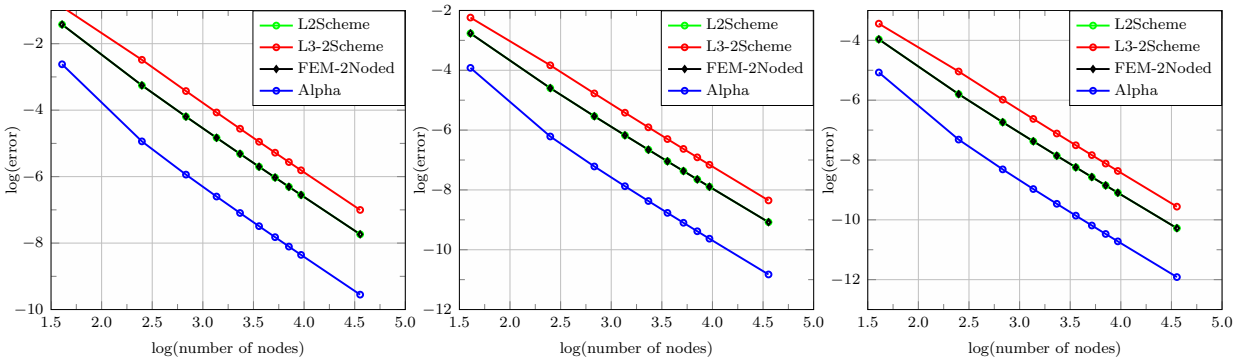

(g) Linear load: $h/L = 0.10$ (h) Linear load: $h/L = 0.50$ (i) Linear load: $h/L = 1.00$

Figure 6.27: Error norm simulations for the fixed-fixed beam

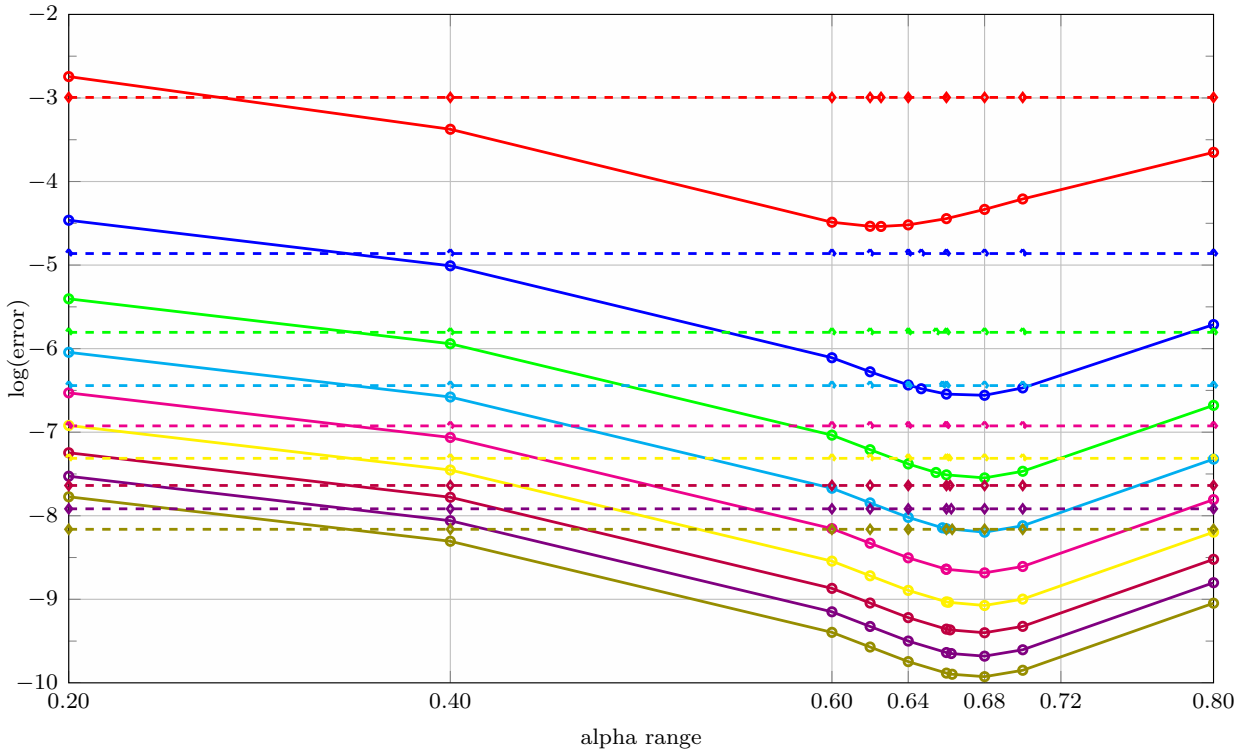

(a) With rotations

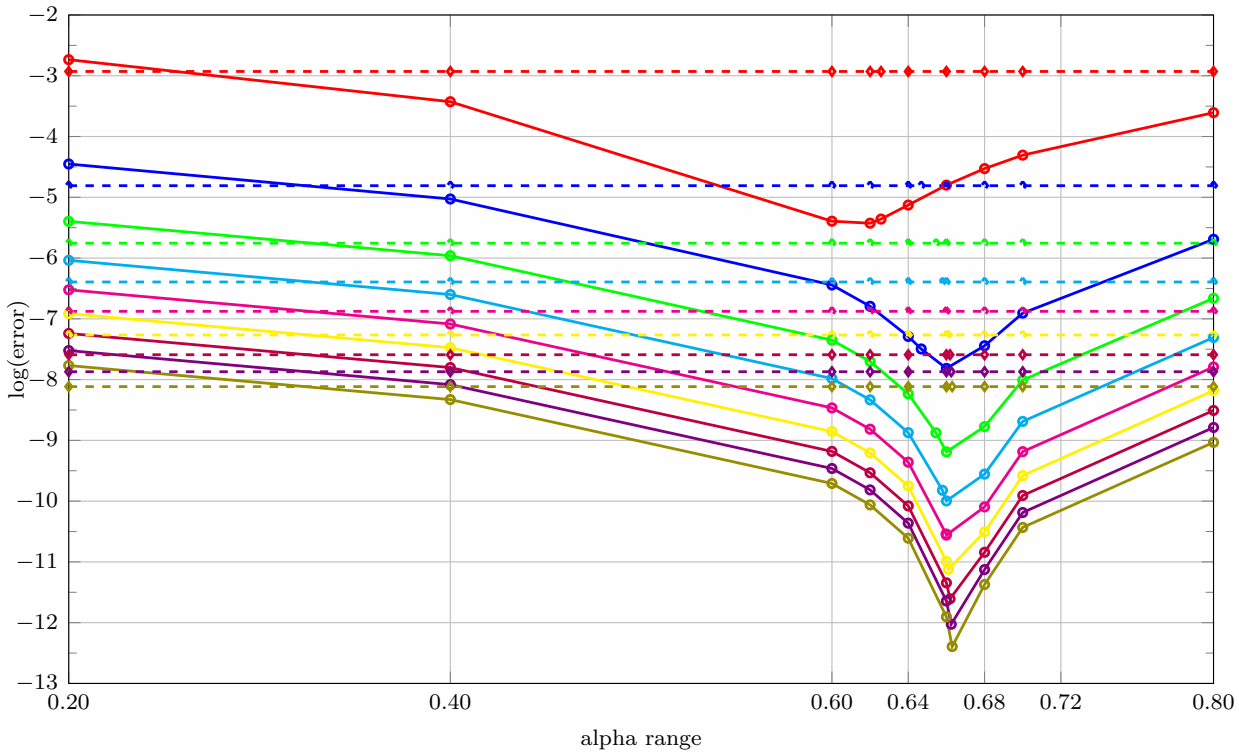

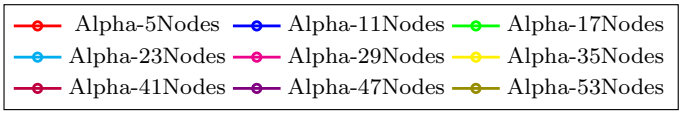

(b) Without rotations

Figure 6.28: Error convergence for a simply supported beam: force load

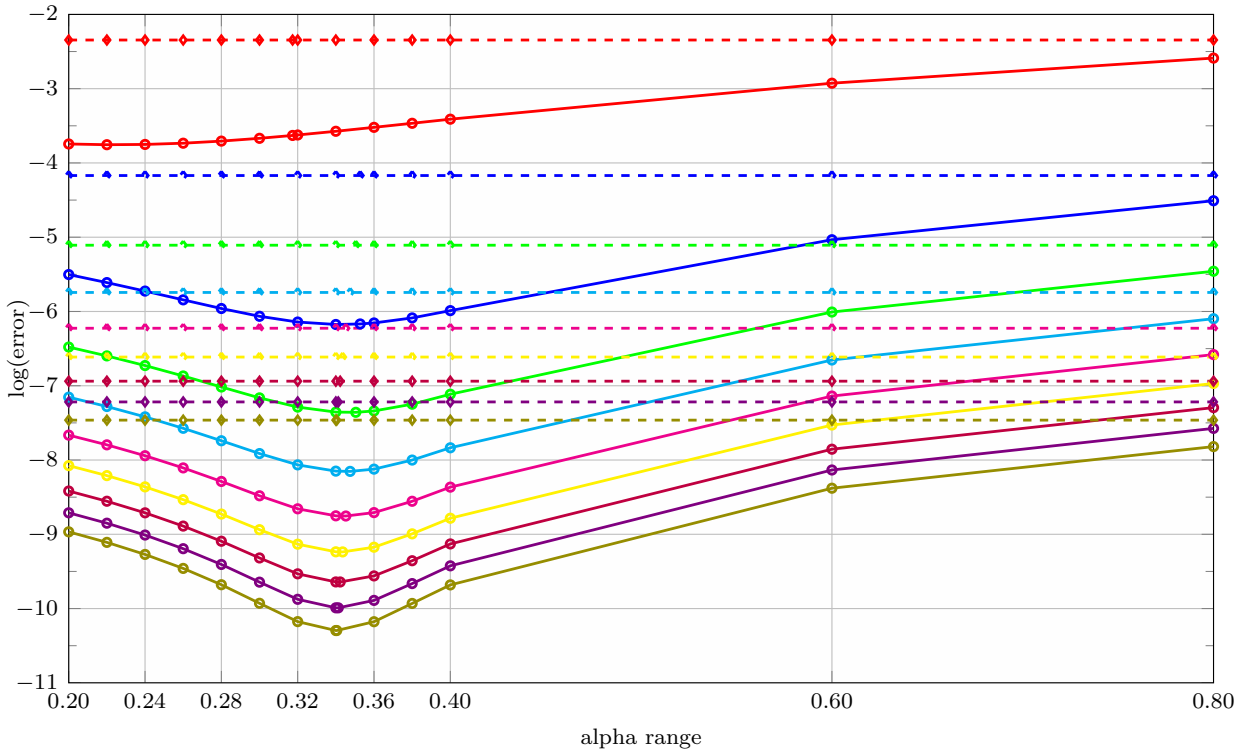

(a) With rotations

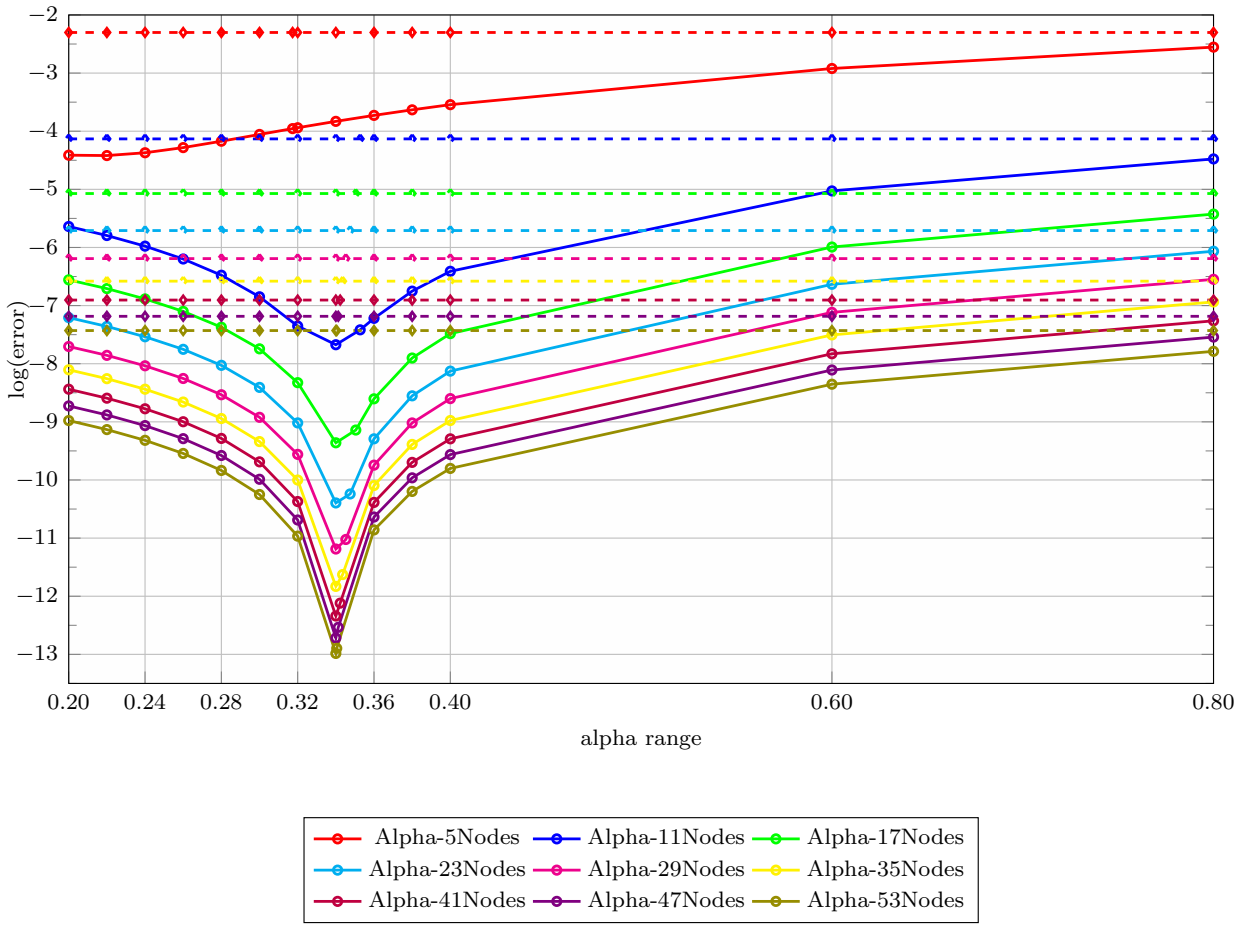

(b) Without rotations

Figure 6.29: Error convergence for a simply supported beam: uniformly distributed load

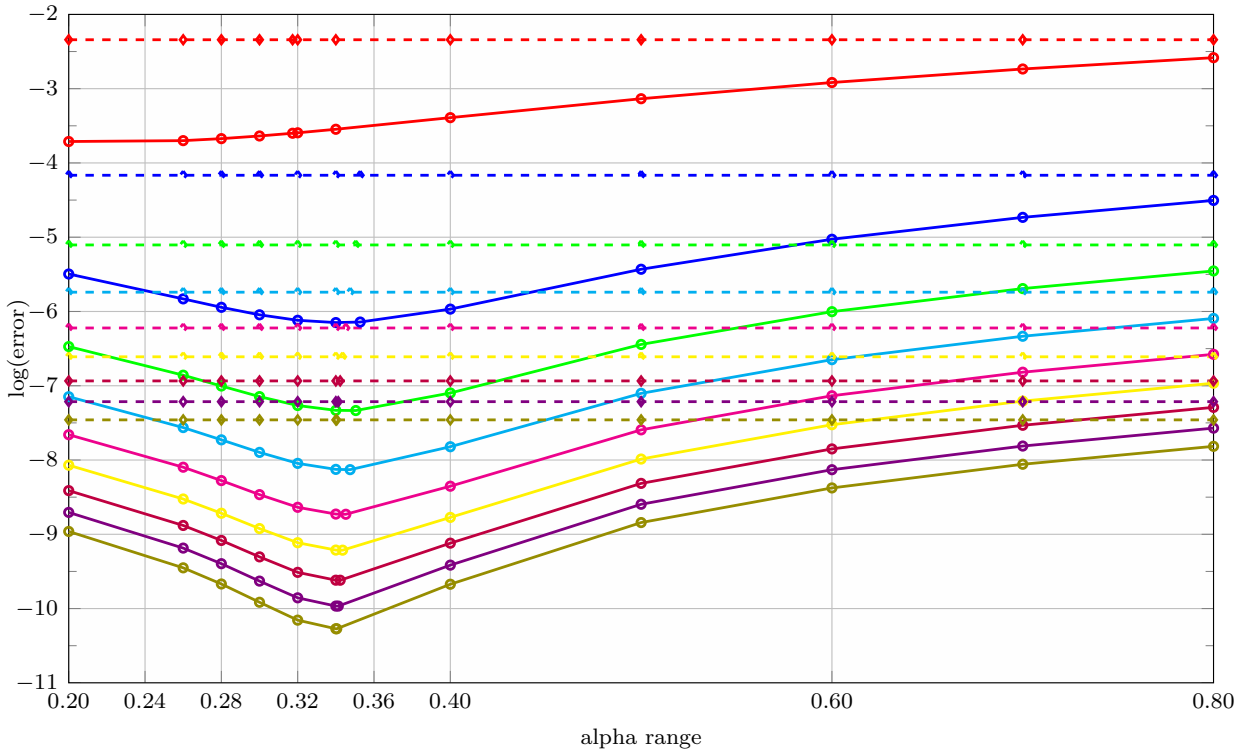

(a) With rotations

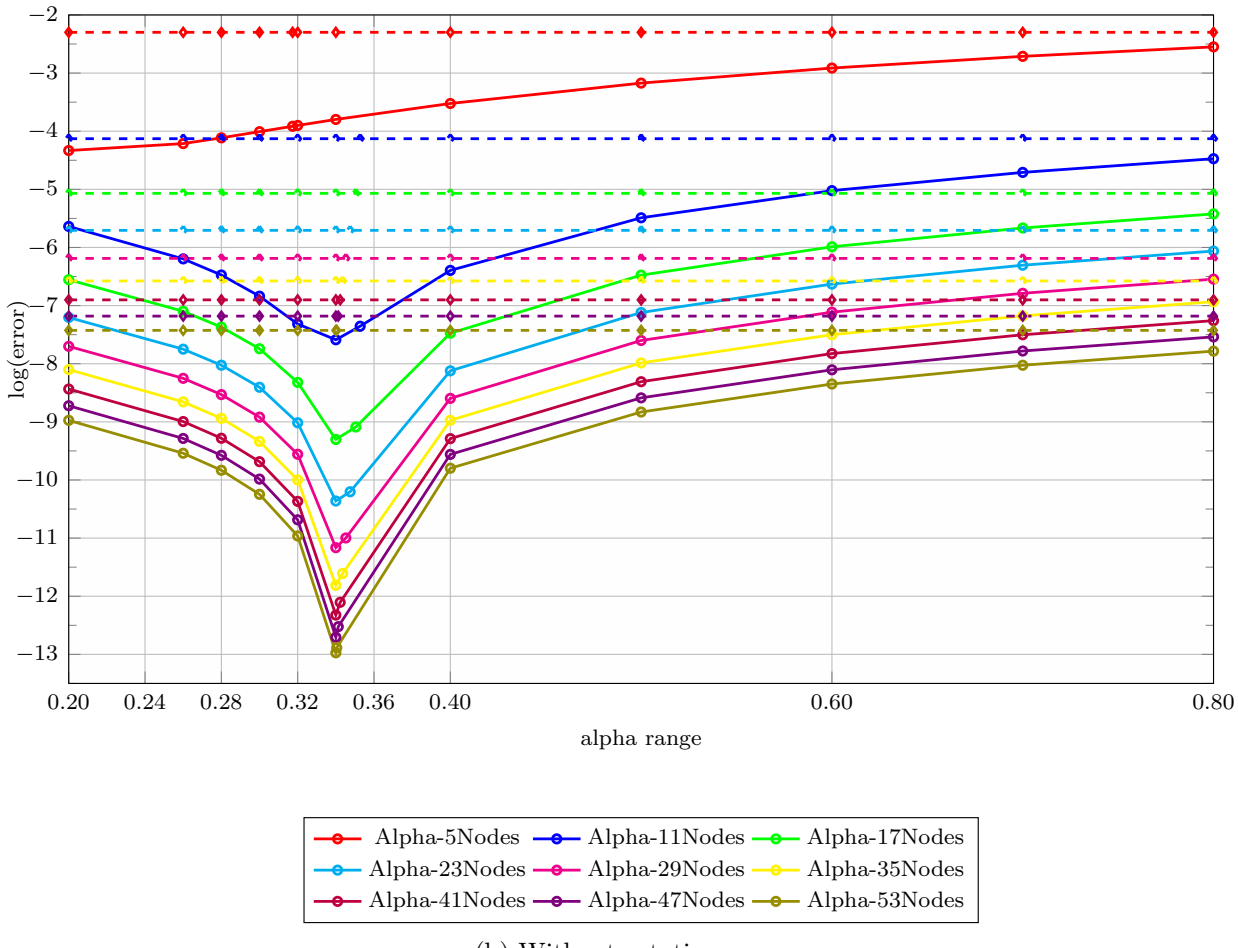

(b) Without rotations

Figure 6.30: Error convergence for a simply supported beam: linearly distributed load

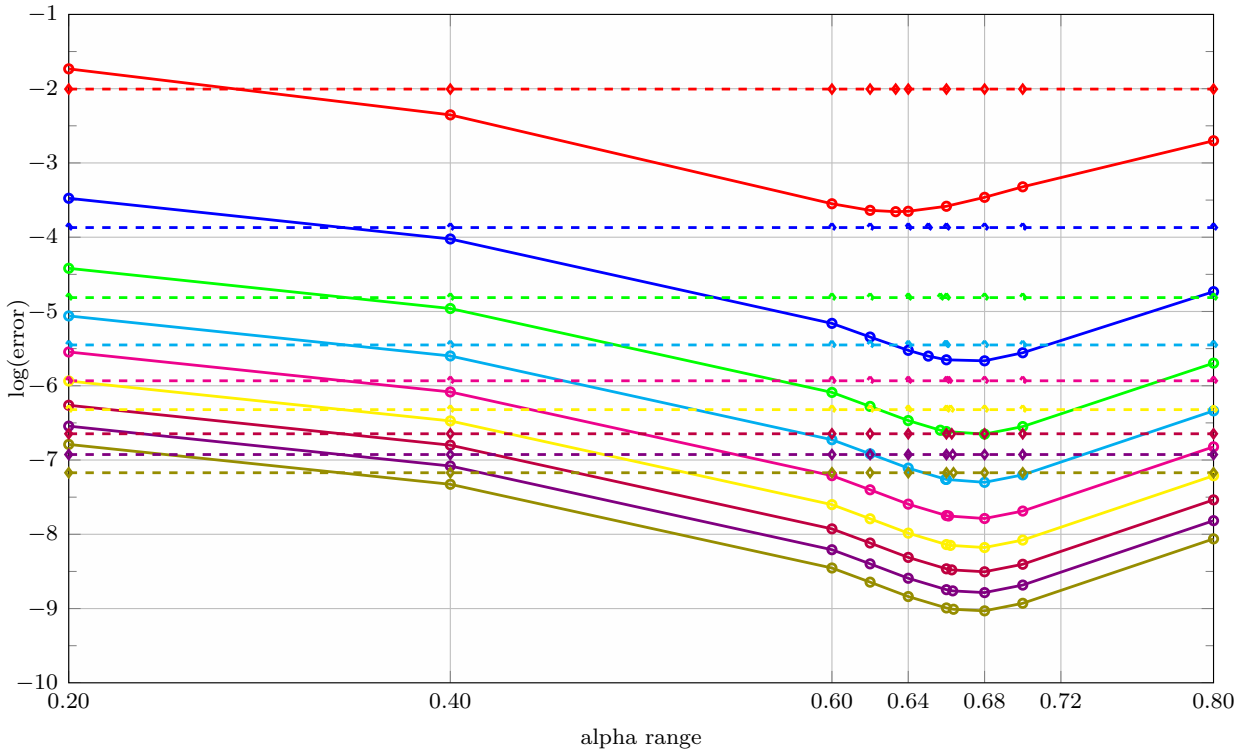

(a) With rotations

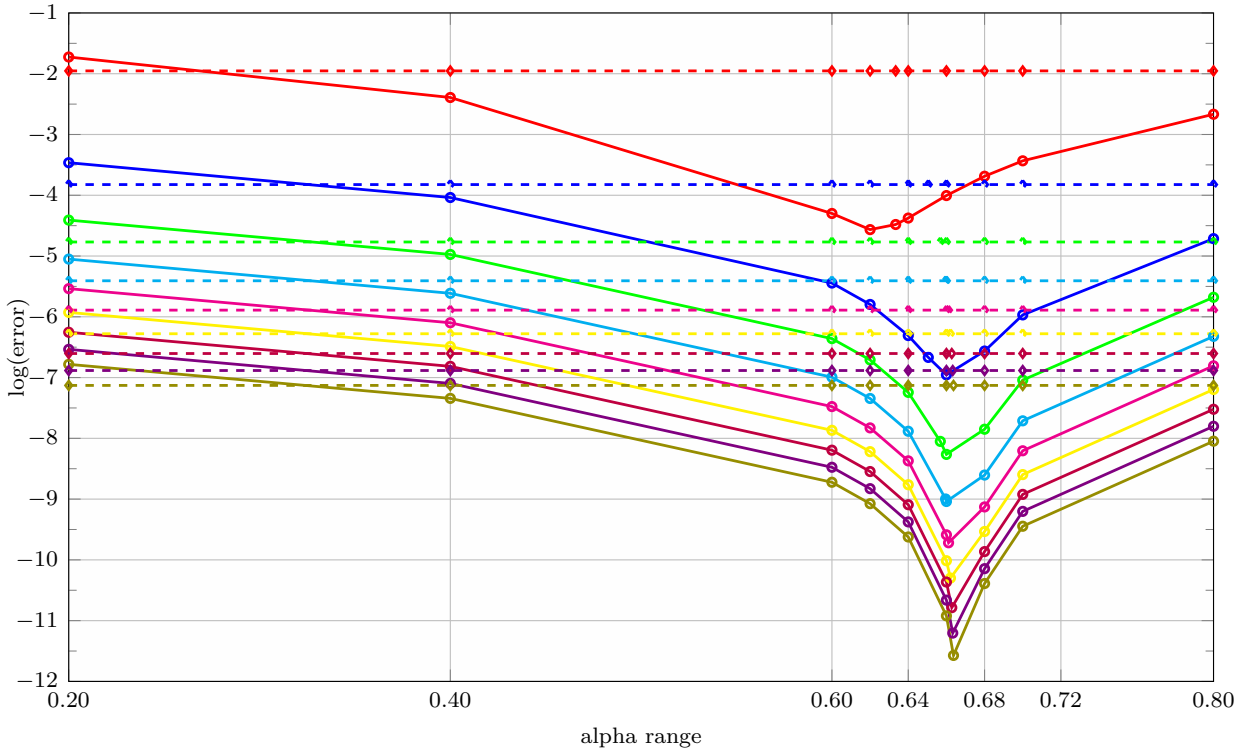

(b) Without rotations

Figure 6.31: Error convergence for a fixed-pinned beam: force load

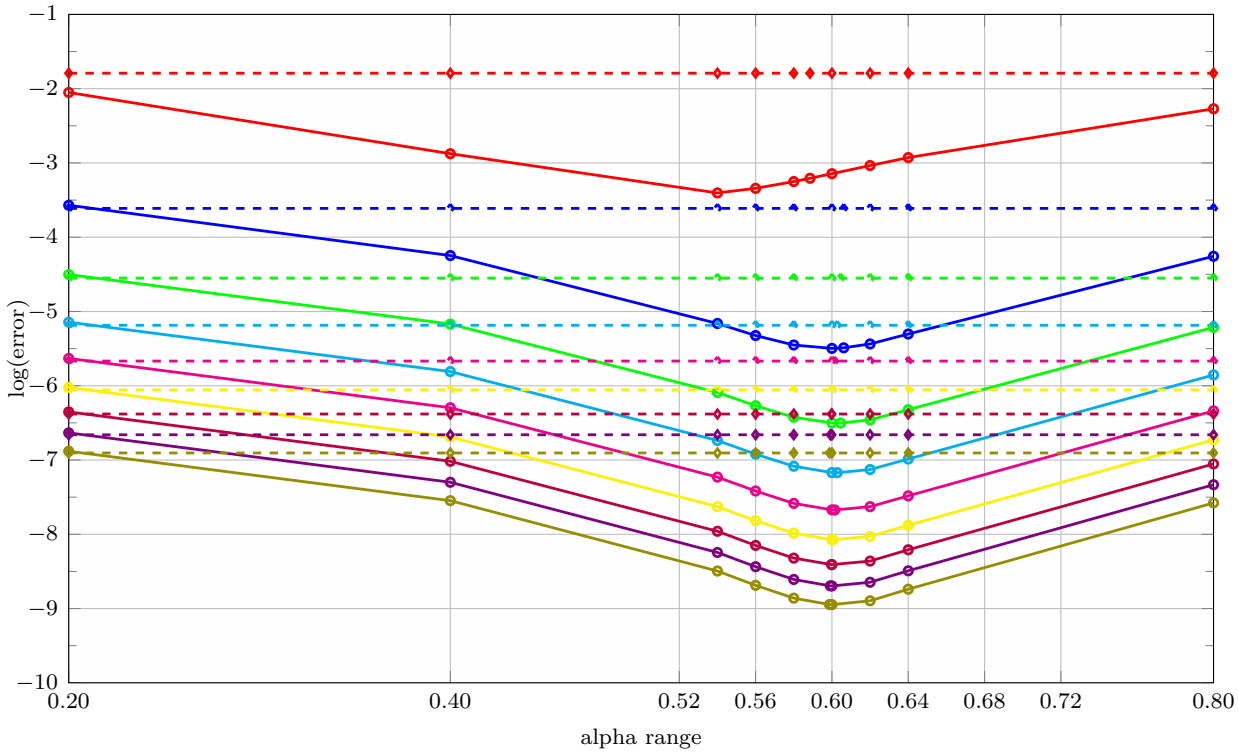

(a) With rotations

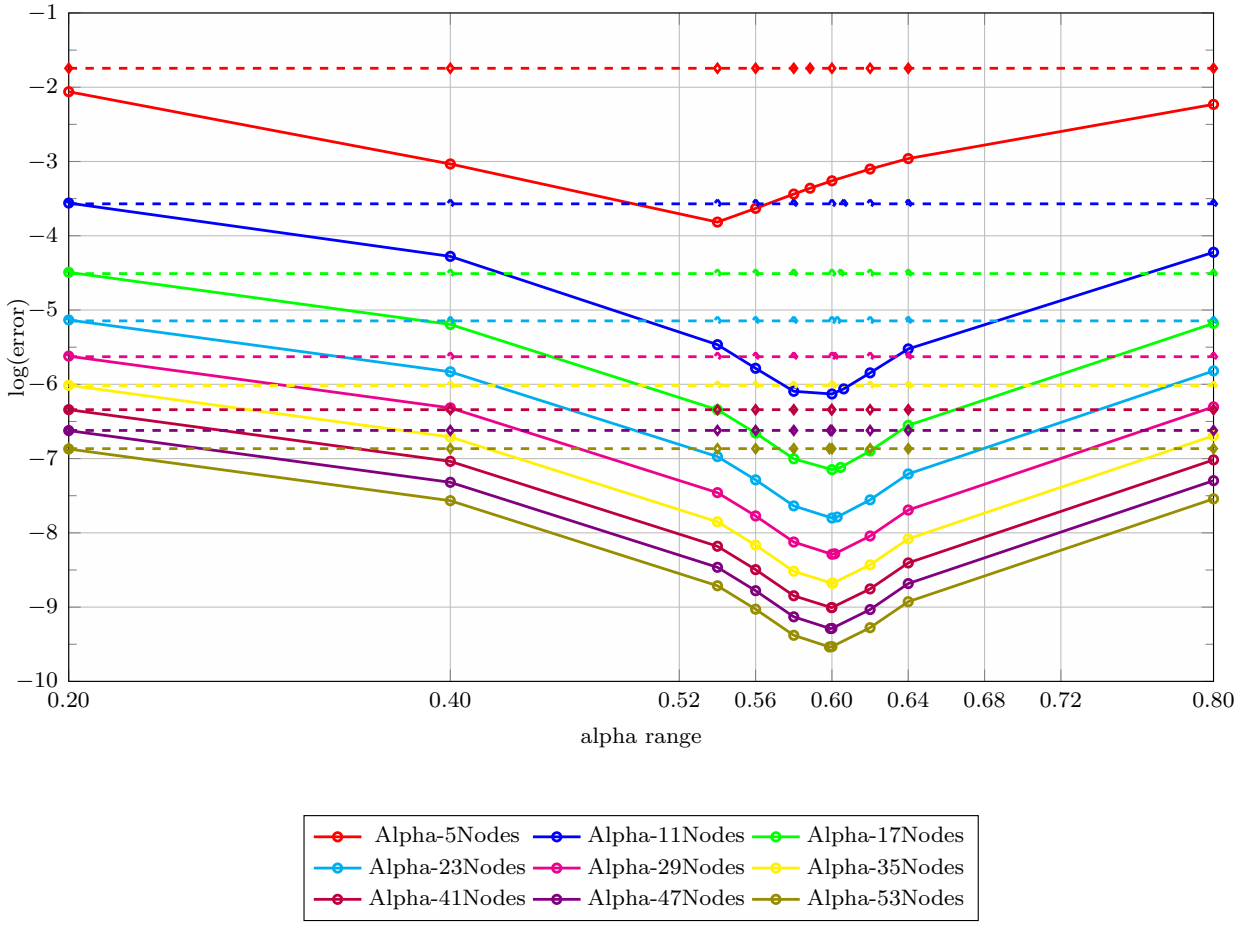

(b) Without rotations

Figure 6.32: Error convergence for a fixed-pinned beam: uniformly distributed load

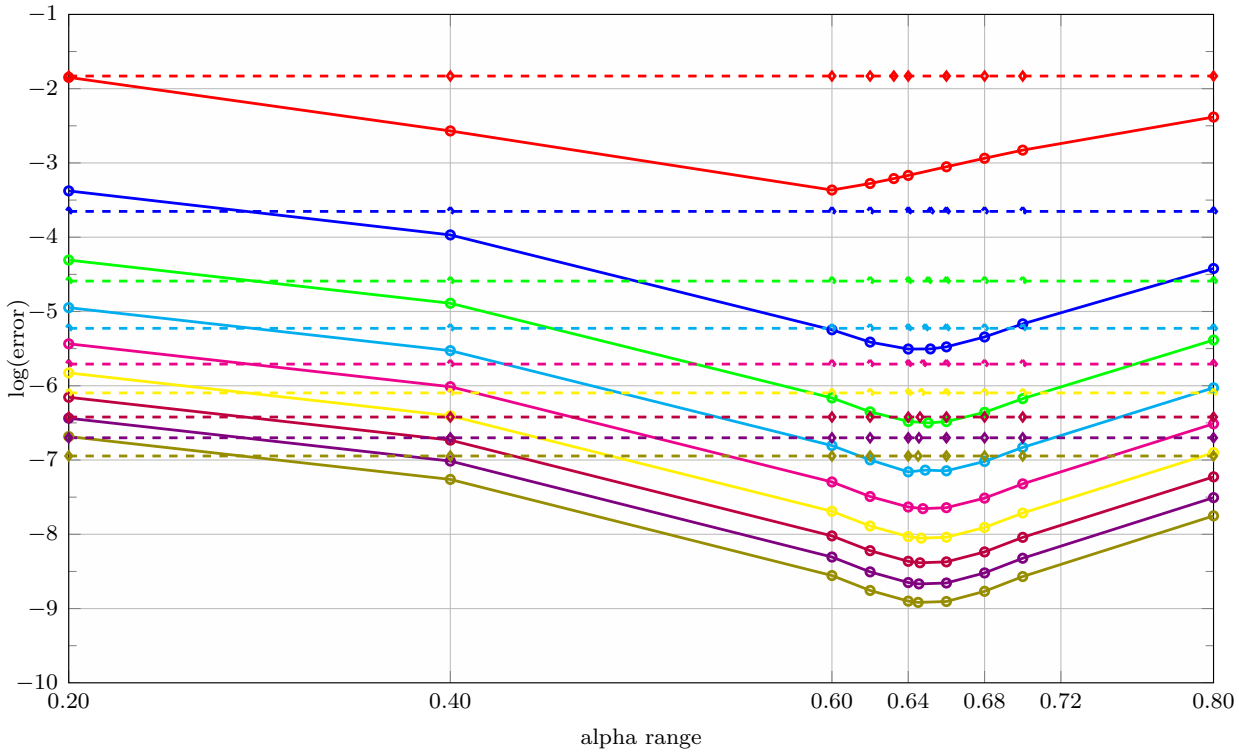

(a) With rotations

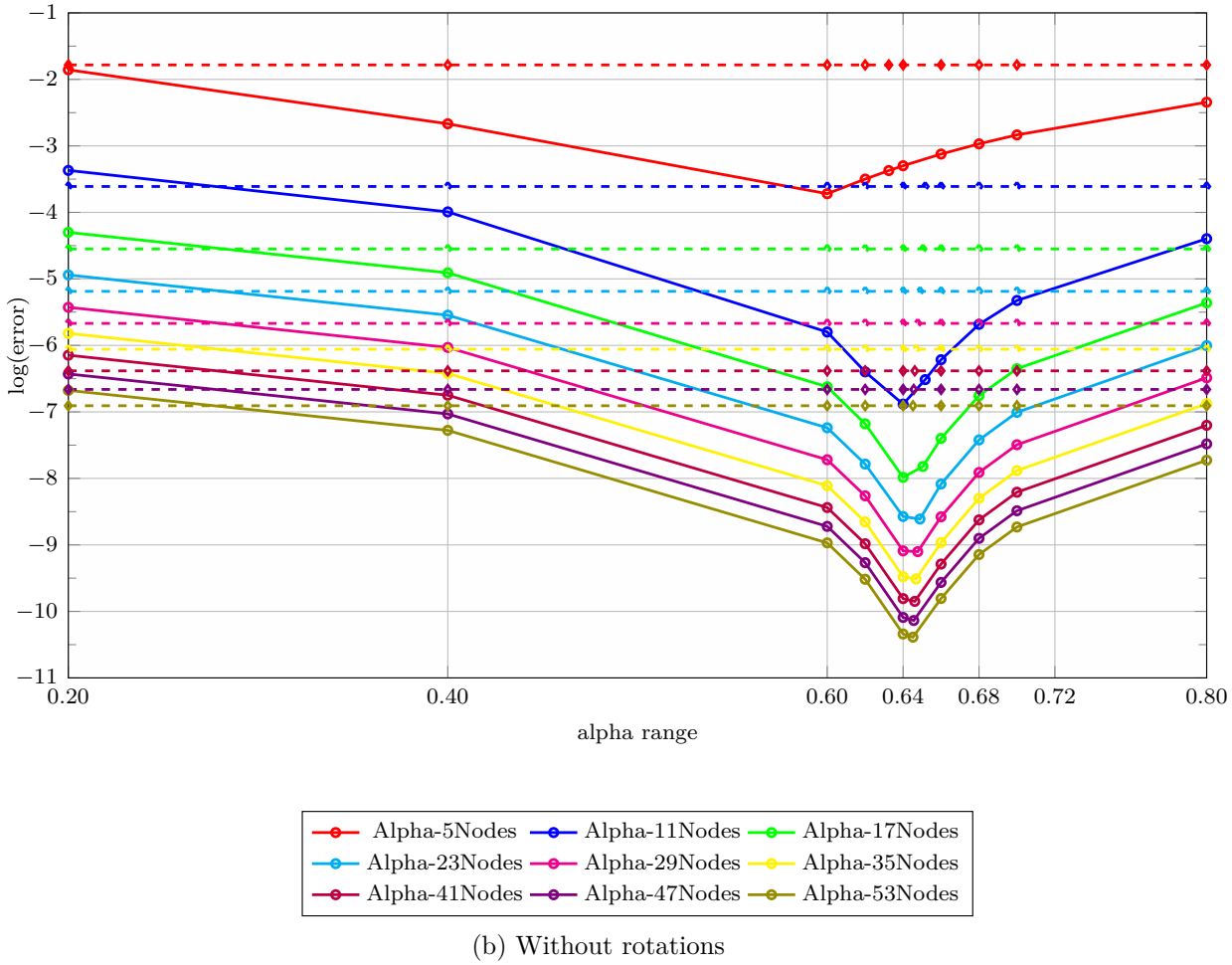

(b) Without rotations

Figure 6.33: Error convergence for a fixed-pinned beam: linearly distributed load

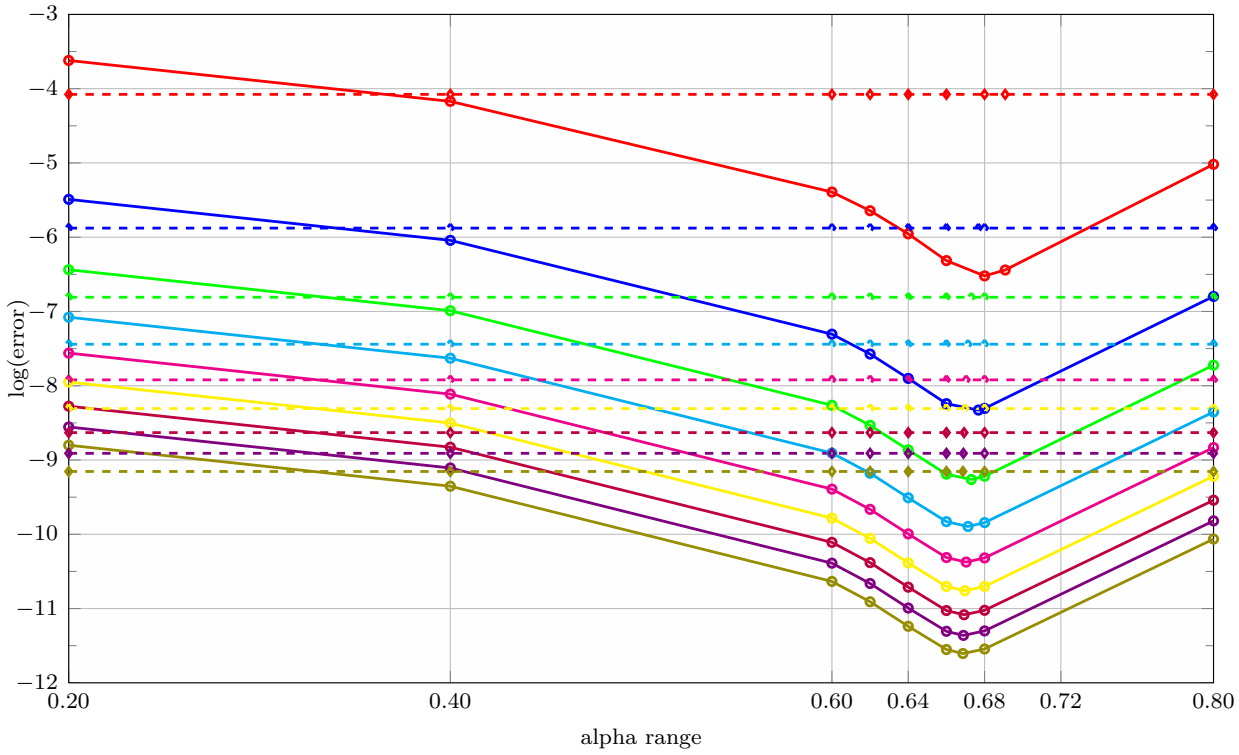

(a) With rotations

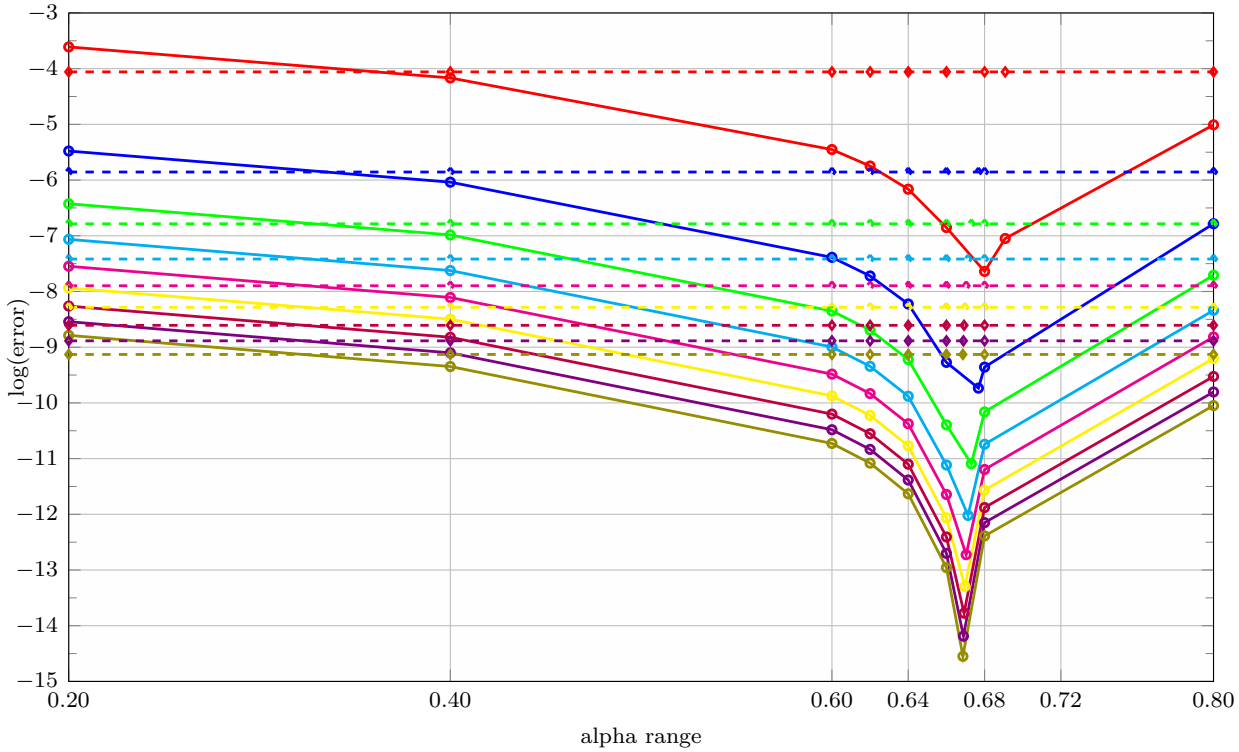

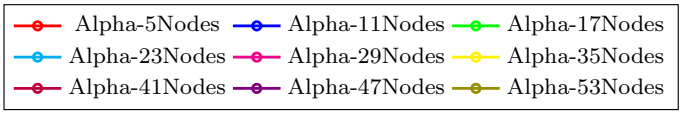

(b) Without rotations

Figure 6.34: Error convergence for a cantilever beam: force load

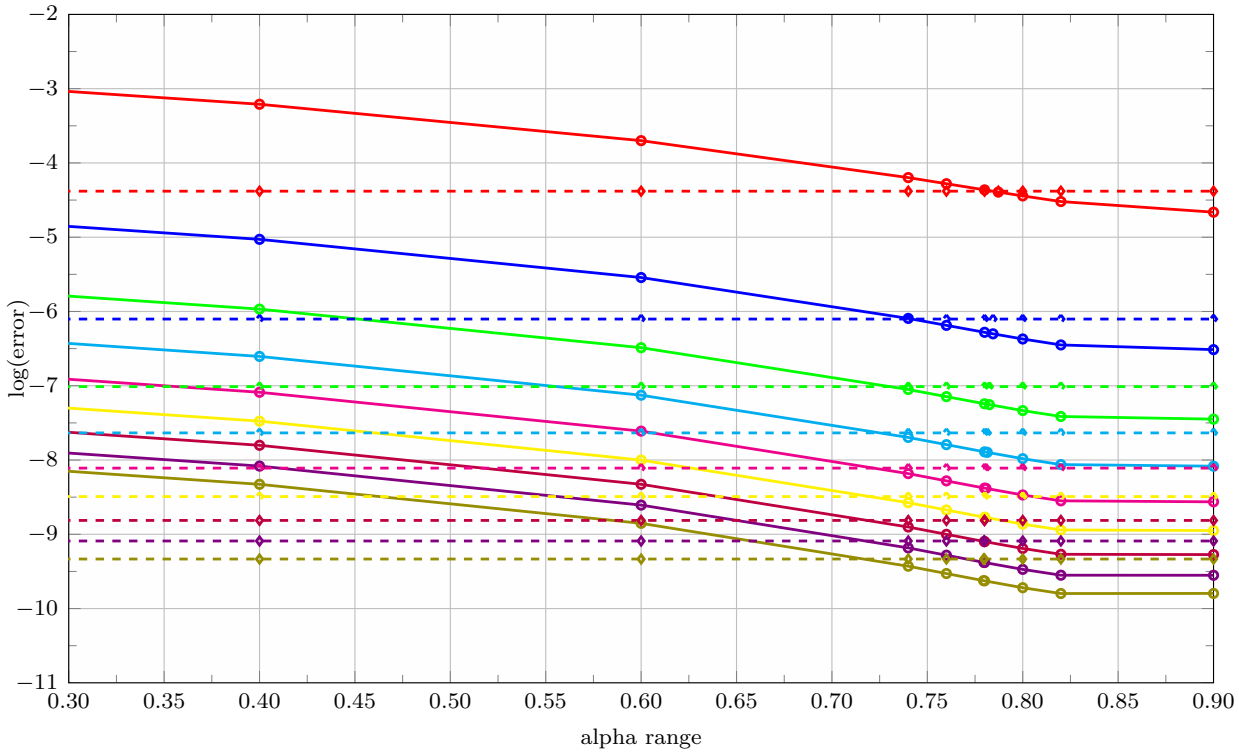

(a) With rotations

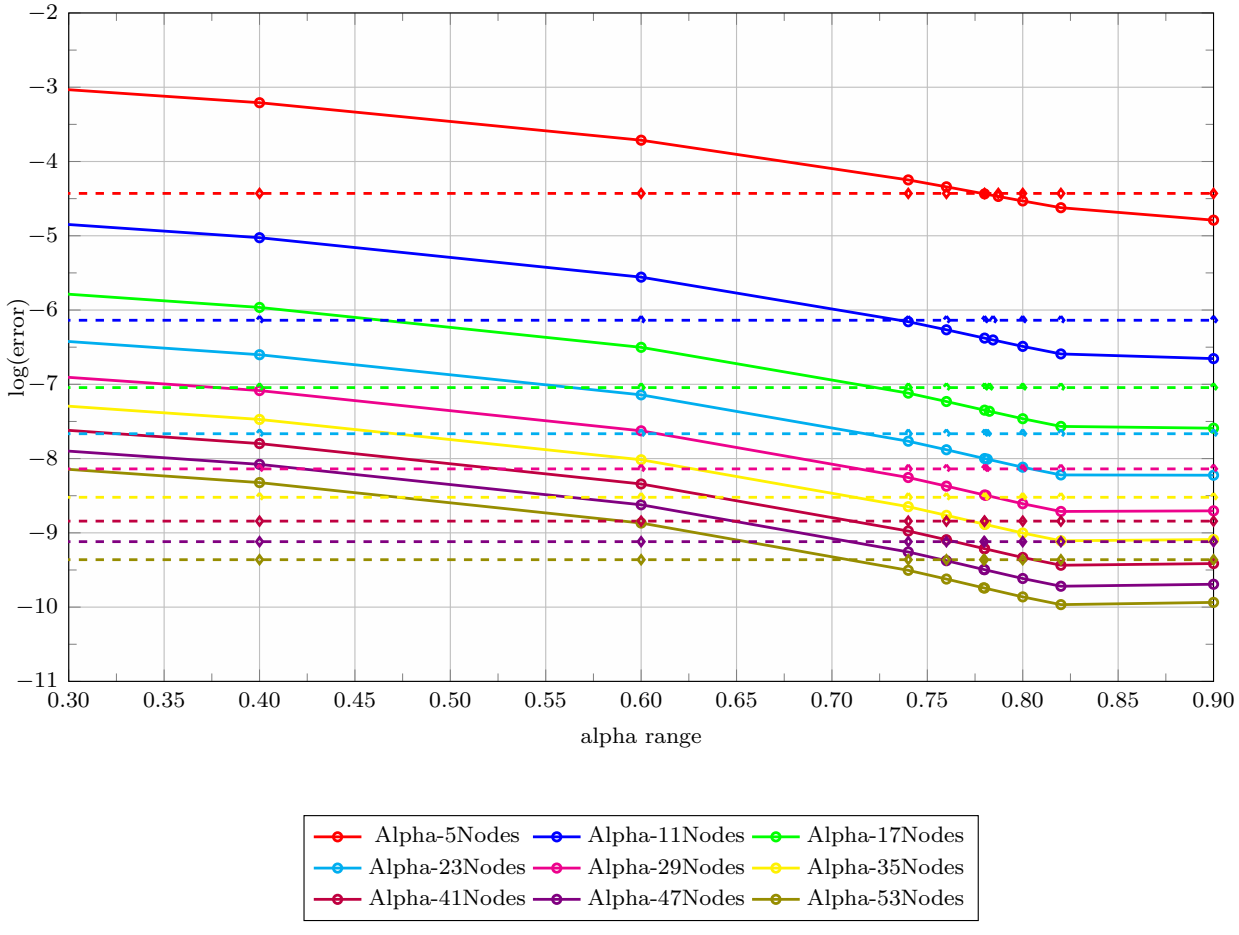

(b) Without rotations

Figure 6.35: Error convergence for a cantilever beam: uniformly distributed load

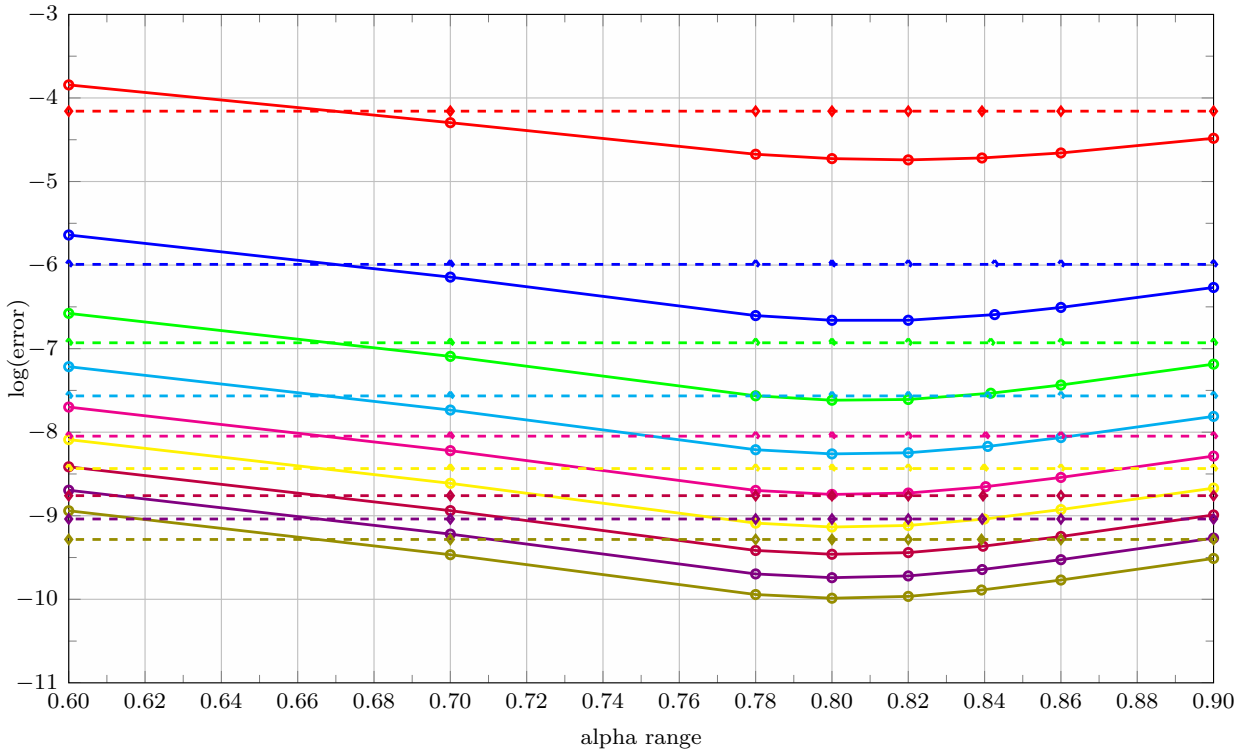

(a) With rotations

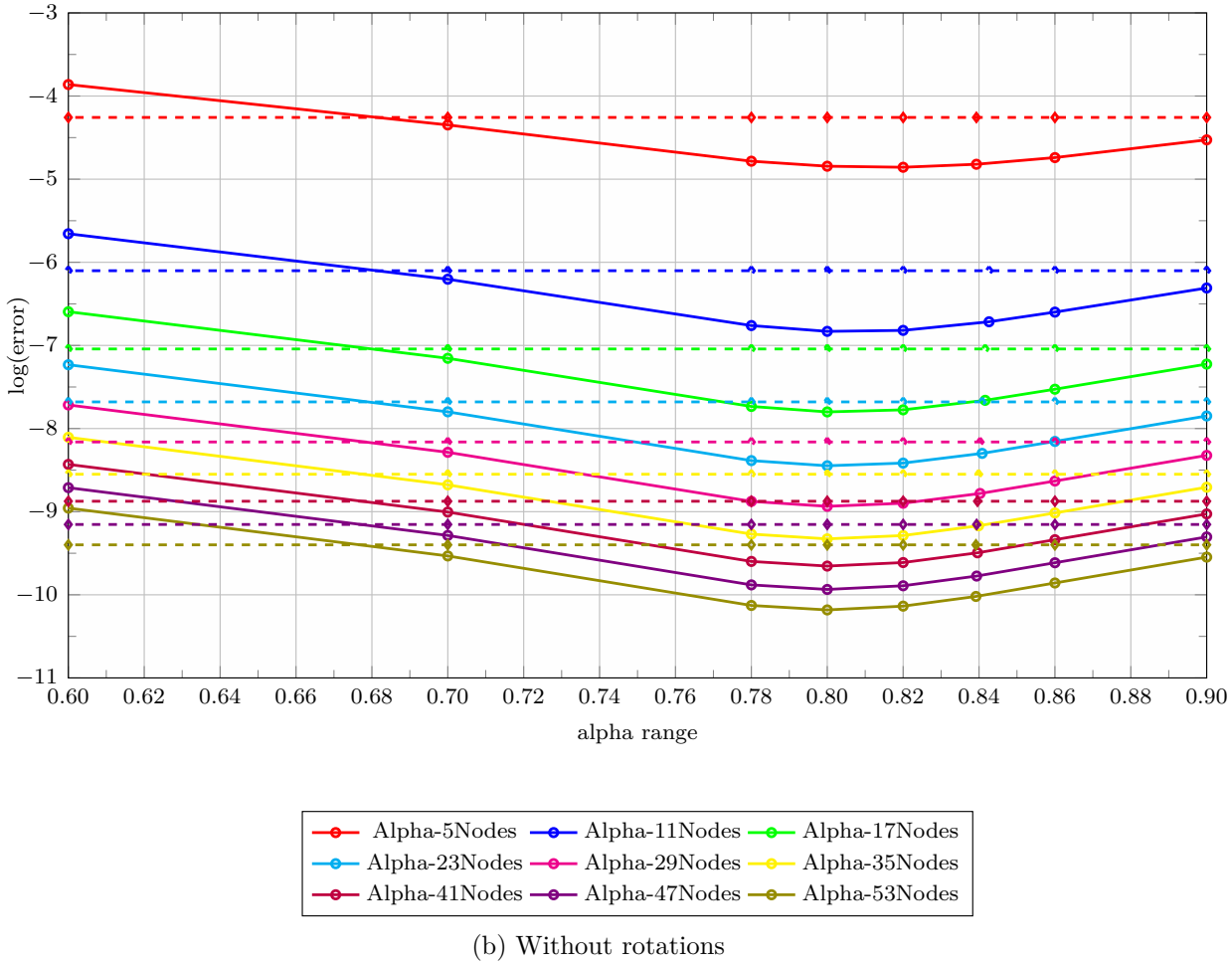

(b) Without rotations

Figure 6.36: Error convergence for a cantilever beam: linearly distributed load

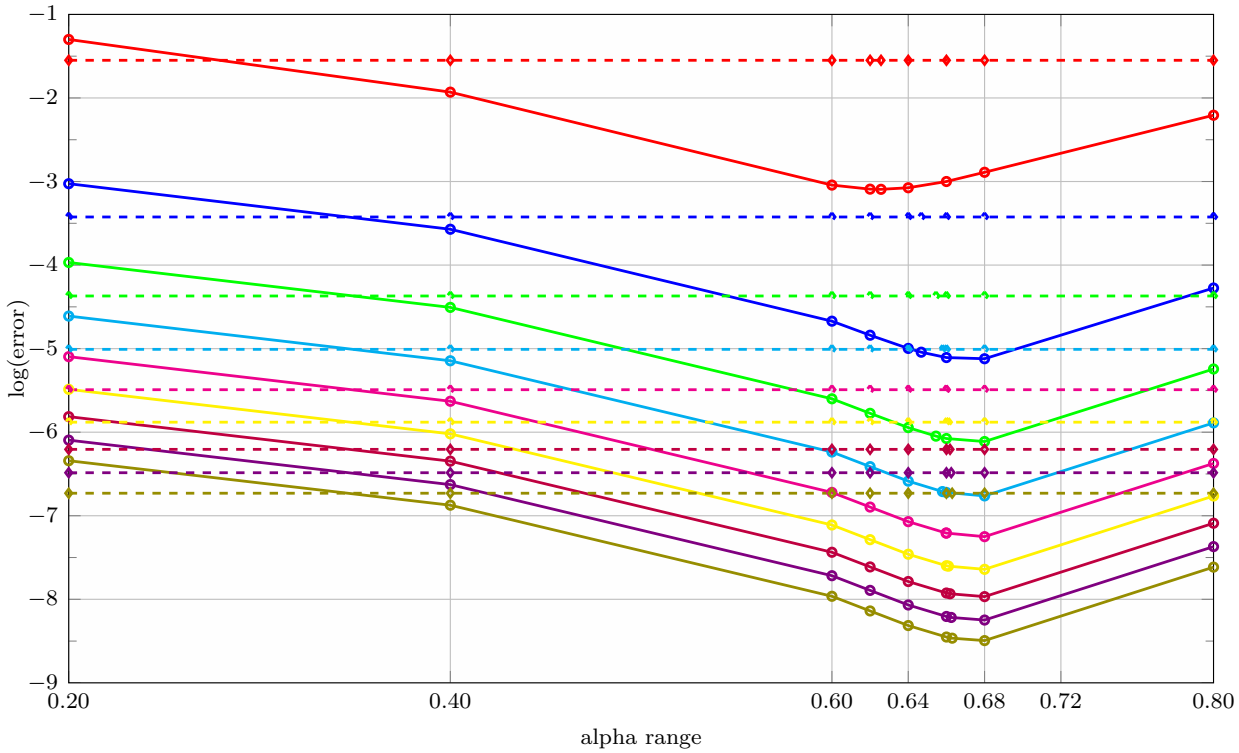

(a) With rotations

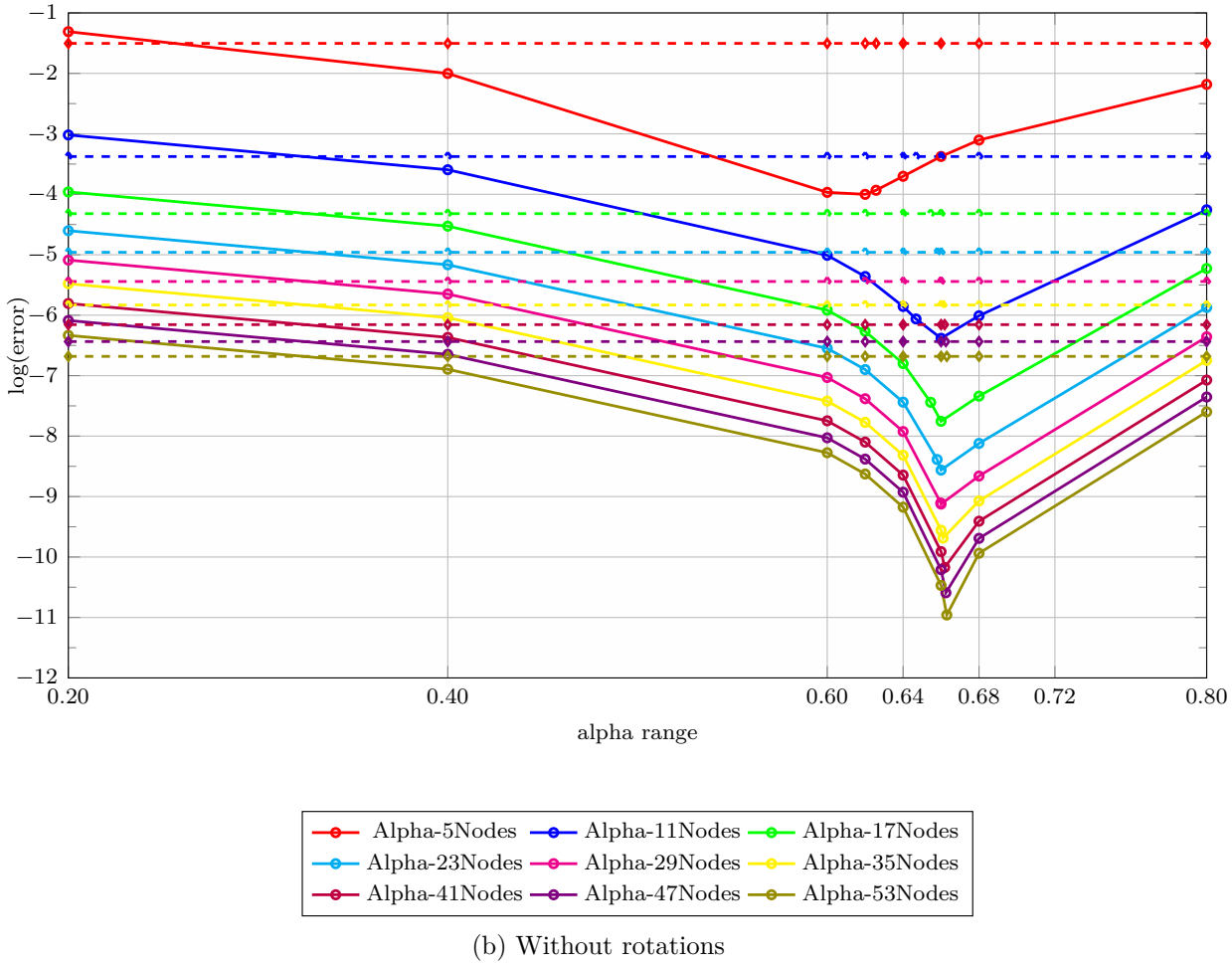

(b) Without rotations

Figure 6.37: Error convergence for a fixed-fixed beam: force load

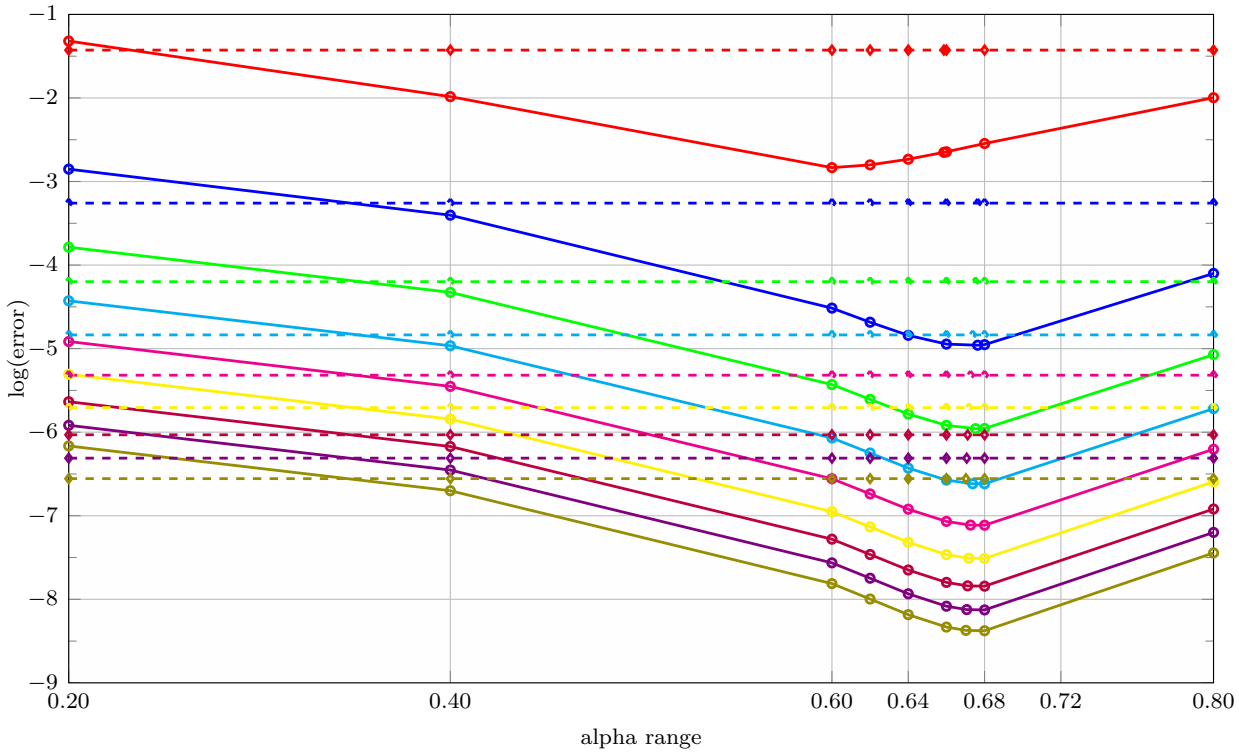

(a) With rotations

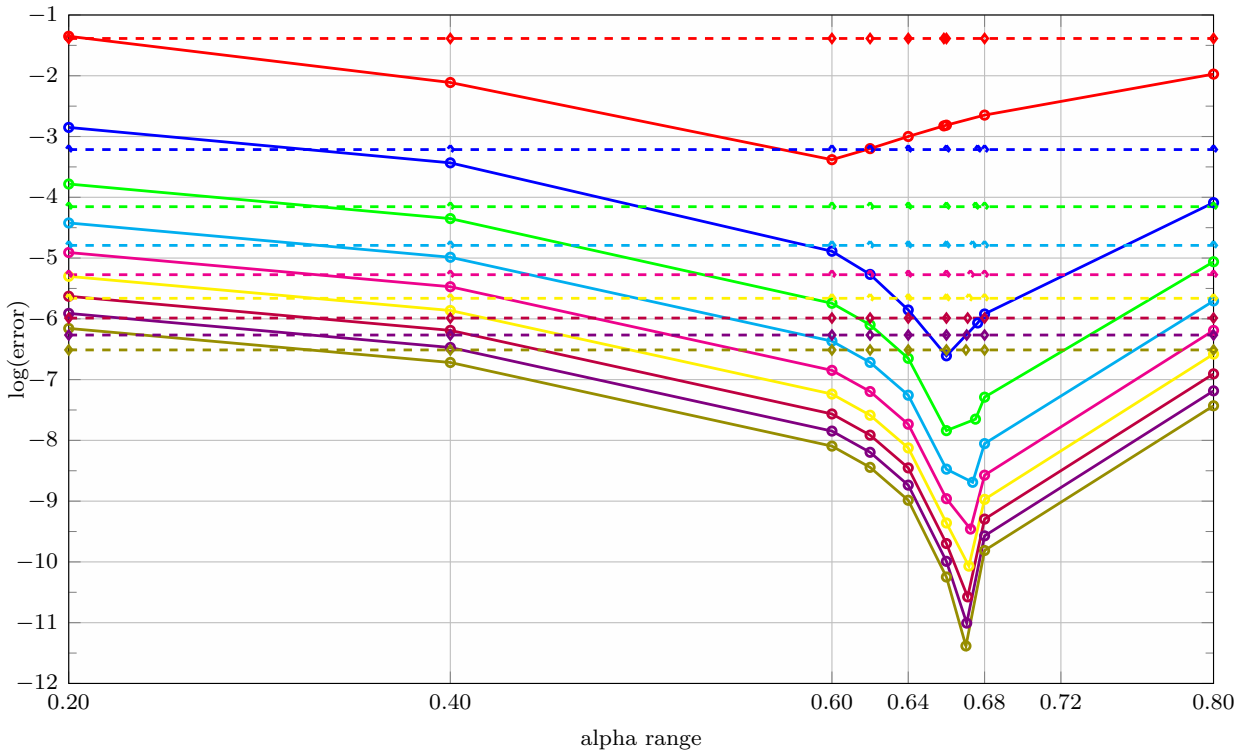

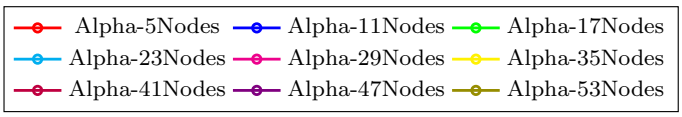

(b) Without rotations

Figure 6.38: Error convergence for a fixed-fixed beam: uniformly distributed load

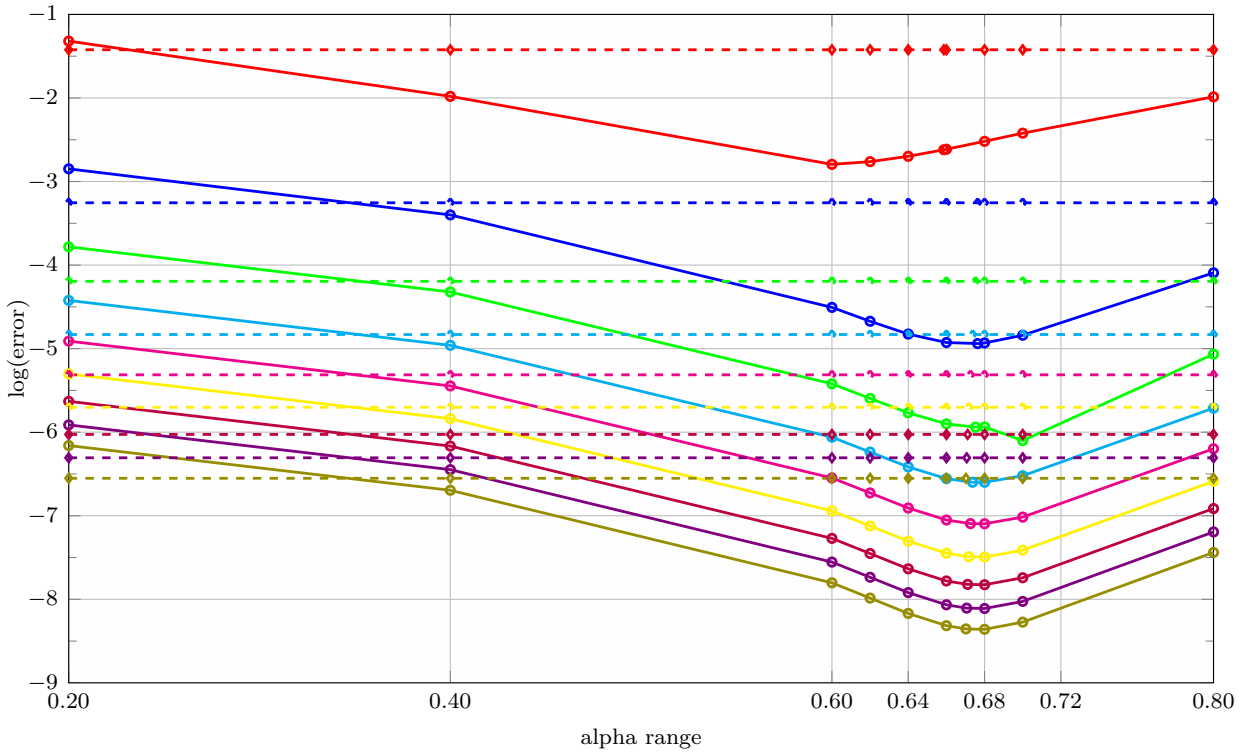

(a) With rotations

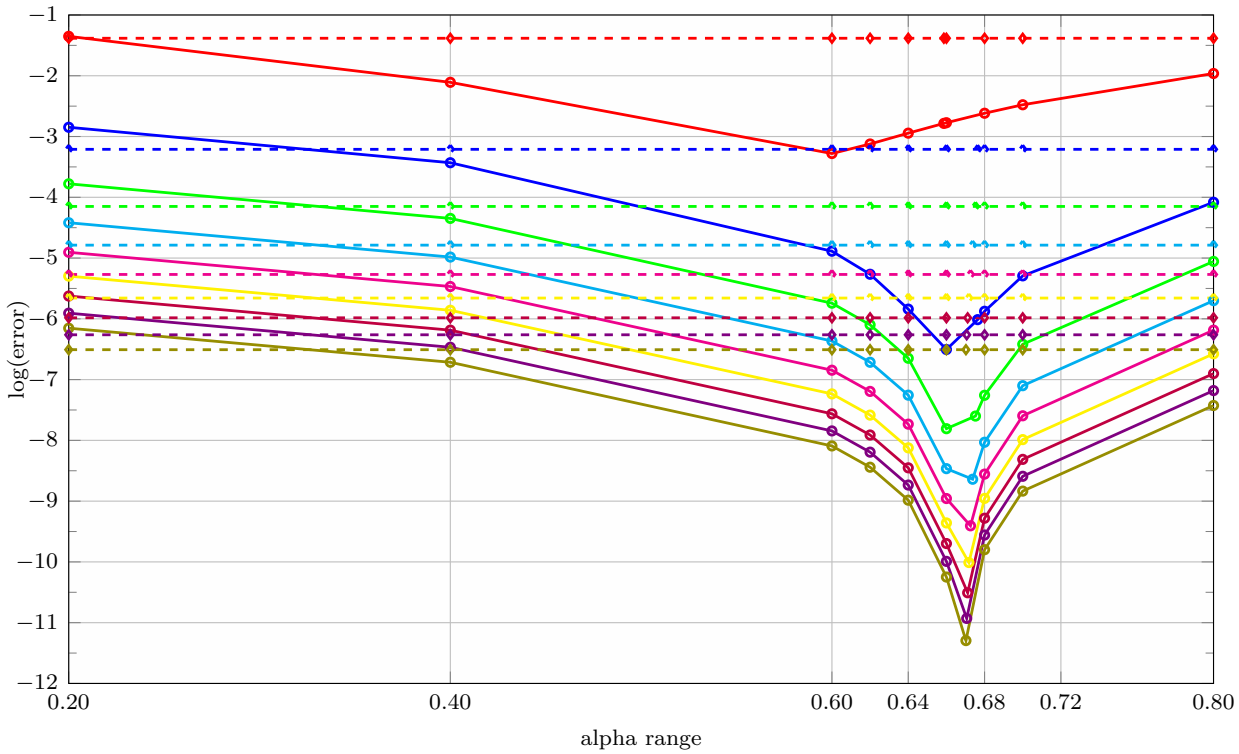

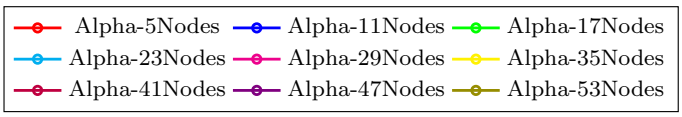

(b) Without rotations

Figure 6.39: Error convergence for a fixed-fixed beam: linearly distributed load

As can be observed in Figs. 6.24a to 6.27g, in general, the use of the alpha parameter resulted in a significant improvement of the error level, though the rate of convergence remained unchanged. When rotations are not considered in equation 6.1, as shown in Figs. 6.28 to 6.39, even better results can be achieved[3]. There are however two exceptions to this general observation.

First, for the uniform (Figs. 6.24d to 6.24f) and linear (Figs. 6.24g to 6.24i) loads in the simply supported beam, the αPIM shape resulted in a convergence rate higher than the one exhibited by the other approximations. Second, for the uniform (Figs. 6.26d to 6.26f) and linear (Figs. 6.26g to 6.26i) loads in the cantilever beam, the improvement of the error due to the use of the αPIM function was smaller that the one obtained in the other configurations. This behaviour in the cantilever beam can be explained by the following considerations: (i) the rotation results of the L2 and L3/2 schemes bound the analytical solution from the same side (Figs. 6.9d to 6.9f and Figs. 6.10d to 6.10f), (ii) the displacement obtained with the L2-scheme (Figs. 6.9a to 6.9c and Figs. 6.10a to 6.10c) are already a good approximation of the exact solution, i.e. there is not too much space for improvement by the αPIM function, (iii) the deflection corresponding to the linear load (Figs. 6.10a to 6.10c) is not bounded by the L2 and L3/2 schemes all along the beam length.

It is worth mentioning that it is not mandatory to find an "optimal" alpha value to achieve better error results than L2 and L3/2 schemes results, because the improvement occurs within a certain interval and not only for a specific alpha value.

6.4 Main conclusions

The main conclusions that can be drawn from the simulations presented in this chapter are addressed in the following:

General: (i) the proposed ES-PIM model showed a good agreement with the exact solution (ii) the L2-scheme models exactly reproduce the results of the linear FEM with one integration point; (iii) the αPIM shape improves the results of L2 and L3/2 schemes considerably without introducing significant computational costs (iv) however even these improved solutions are no match for the quadratic Timoshenko FEM model.

Alpha parameter: (i) all calibrated alpha parameters for the force load case converged to approximately $\alpha = 0.666$ for all boundary conditions, while the distributed load cases did not show this same pattern; (ii) for the fixed-fixed beam the range of alpha values for the force load and the distributed load cases are similar, in the sense that they are confined between $0.63 - 0.68$; (iii) in addition to that, the calibrated alpha parameters converged to different values when varying the ratio h/L for the fixed-pinned distributed load cases;

[3]Which is not a surprisingly outcome, since the alpha parameter was calibrated using a displacement value.

(iv) for the cantilever beam with distributed loads the alpha parameter impacted less on the improvement of the results; (v) Moreover, for the pinned-pinned and fixed-fixed beams the estimated alpha values of the linearly and uniformly distributed load were the same, while the fixed-pinned and fixed-free beams exhibited a different behaviour.

CHAPTER 7

NUMERICAL SIMULATIONS: GEOMETRICALLY EXACT BEAM

In this chapter the results regarding the geometrically exact model are illustrated. Simulations of three classical problems from the literature are performed. Comparisons of the present SPIM results with other authors results are also presented. All examples of this chapter can be found in Simo and Vu-Quoc (1986). In our implementation the convergence criteria of all examples is based on the *unbalanced forces vector*.

In what follows, the numerical results of three examples are illustrated for the L2 and L3/2 schemes. Since, in general, there is no analytical solutions available for nonlinear problems, the alpha PIM is simulated aiming to verify its behaviour when compared to the other two methods. The linear FEM was also simulated, however, as identified previously in this work, its results are the same as the L2-scheme, therefore they have been omitted.

7.1 Pure bending of a cantilever beam

This example consists of an initially straight cantilever beam under a concentrated moment applied at its tip, as shown in Fig. 7.1. This example is the same performed in Simo and Vu-Quoc (1986).

The beam is characterised by a unit length, $L = 1\,\text{mm}$, and by the following geometric and material parameters (see Eq. (2.45) and Eq. (2.46))

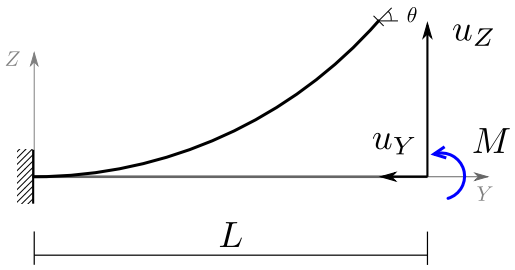

Figure 7.1: Pure bending cantilever beam

$$\left.\begin{array}{ll} A = 1\,\mathrm{mm}^2 & I_1 = 1\,\mathrm{mm}^4 \\ A_1 = 1\,\mathrm{mm}^2 & I_2 = 1\,\mathrm{mm}^4 \\ A_2 = 1\,\mathrm{mm}^2 & J_t = 2\,\mathrm{mm}^4 \end{array}\right| \; E = G = 2\,\mathrm{N/mm}^2 \tag{7.1}$$

Since the bending deformation is constant along the beam, it follows that the exact solution must be coincident with an arc of a circle. One can show that the analytical solutions for the displacement components at the beam tip are given by the following equations[1]:

$$u_Y = L - r\sin\theta = L - \frac{L}{\theta}\sin\theta \tag{7.2}$$

$$u_Z = r - r\cos\theta = \frac{L}{\theta}(1 - \cos\theta) \tag{7.3}$$

where L is the beam length, and the rotation is given by $\theta = (M \cdot L)/EI$.

The discretisation of the model is equivalent to the one adopted in Simo and Vu-Quoc (1986), i.e. 6 equally-spaced nodes where considered along the beam length, resulting in 5 smoothing domains. The bending moment ($M = 8\pi\mathrm{N\,mm}$) is applied in one step, and the convergence is achieved in three iterations for both, L2 and L3/2 schemes.

The expected *closed form configuration* is achieved, hence the numerical results agree with the analytical solution, as shown in Figure 7.2. Due to the magnitude of the bending moment the beam wind around itself *twice*. In Table 7.1, the *unbalanced forces vector* norm is compared with the values obtained by Simo and Vu-Quoc (1986), showing that the L2 and L3/2 schemes simulations are consistent with those results.

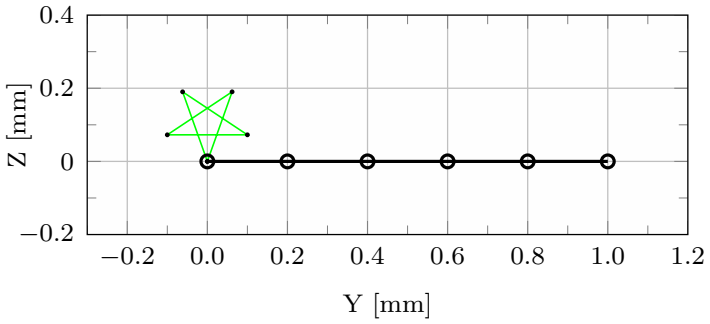

Figure 7.2: Closed form configuration

In order to observe the evolution of the displacements, a bending moment of $M = 4\pi\mathrm{N\,mm}$ is applied in 10 load steps for both the L2 and L3/2 schemes. The results are illustrated in Fig. 7.3.

When a moment of $M = 4\pi\mathrm{N\,mm}$ is applied at the tip of the beam, the exact solution consists in a *closed form configuration*, i.e. the tip coincides with the constrained beam

[1] See Lozzo (2010), for example.

Load step	Iteration	$\|p\|^{L2}$	$\|p\|^{L3/2}$	$\|p\|$ (Simo and Vu-Quoc, 1986)
1	1	$2.51 \times 10^{+1}$	$2.51 \times 10^{+1}$	$2.51 \times 10^{+1}$
	2	$2.83 \times 10^{+1}$	$2.83 \times 10^{+1}$	$4.25 \times 10^{+1}$
	3	1.64×10^{-13}	6.78×10^{-14}	4.41×10^{-14}

Table 7.1: Norm of the unbalanced forces vector

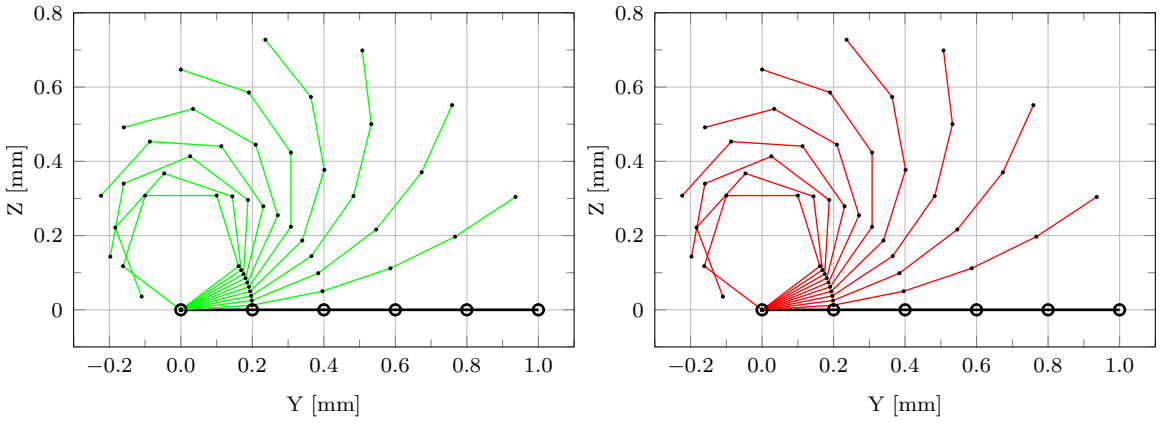

(a) L2-scheme results

(b) L3/2-scheme results

Figure 7.3: Deformed configurations

end. In what follows, the convergence to the exact solution is analysed by computing the distance $d = \|p_f - p_i\|$ between the two beam ends for five meshes: 4, 5, 6, 9 and 11 nodes.

In Table 7.2 the coordinates Y and Z of the beam tip and the distance d between the beam ends are shown, while in Table 7.3 the linear FEM results are presented. As can be observed in these tables, the values of d are nearly constant. The L2 and L3/2 schemes produced a similar outcome. For the first mesh, with only 4 nodes, the beam ends are already very close. In Fig. 7.4 the results are illustrated graphically.

Number of nodes	L2-scheme			L3/2-scheme		
	Y [mm]	Z [mm]	d [mm]	Y [mm]	Z [mm]	d [mm]
4	1.98E-06	3.82E-05	3.83E-05	2.91E-07	3.82E-05	3.82E-05
5	-3.85E-10	1.05E-16	3.85E-10	-3.85E-10	-5.72E-17	3.85E-10
6	-3.71E-10	-9.19E-17	3.71E-10	-3.71E-10	-6.54E-16	3.71E-10
9	-3.56E-10	-7.79E-17	3.56E-10	-3.56E-10	-8.23E-17	3.56E-10
11	-3.53E-10	1.05E-16	3.53E-10	-3.53E-10	-4.30E-16	3.53E-10

Table 7.2: Tip position convergence: SPIM results

Additional results are illustrated in Fig. 7.5, where the displacements of the tip in the Y and Z directions are compared with the analytical solution (see equations 7.2 and 7.3), considering 20 load steps and an applied moment $M = 4\pi$N mm. As it can be observed,

Number of nodes	FEM linear		
	Y [mm]	Z [mm]	d [mm]
4	1.98E-06	3.82E-05	3.83E-05
5	-3.85E-10	-1.19E-16	3.85E-10
6	-3.71E-10	-2.93E-17	3.71E-10
9	-3.56E-10	1.24E-16	3.56E-10
11	-3.53E-10	2.32E-16	3.53E-10

Table 7.3: Tip position convergence: FEM results

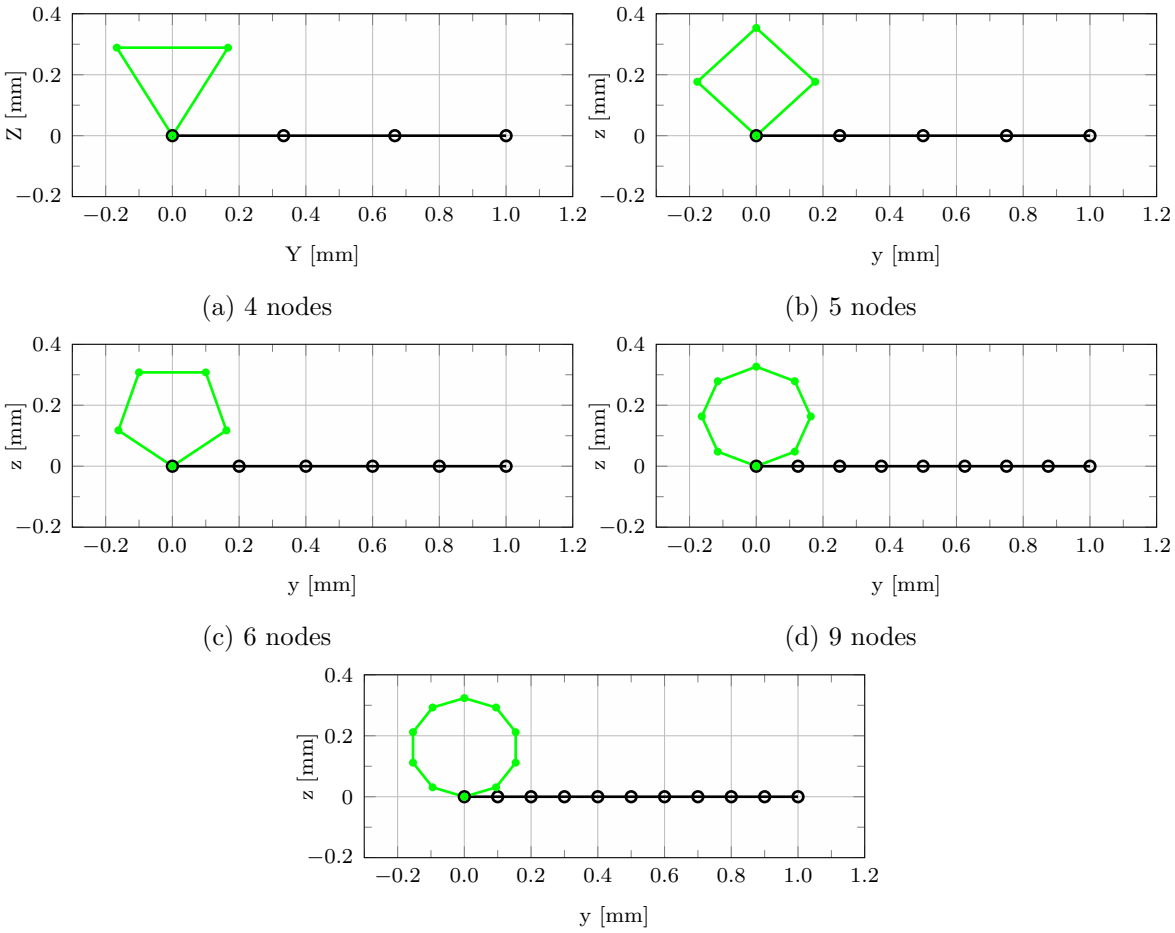

(a) 4 nodes

(b) 5 nodes

(c) 6 nodes

(d) 9 nodes

(e) 11 nodes

Figure 7.4: Convergence analysis

the numerical results are in good agreement with the exact solution.

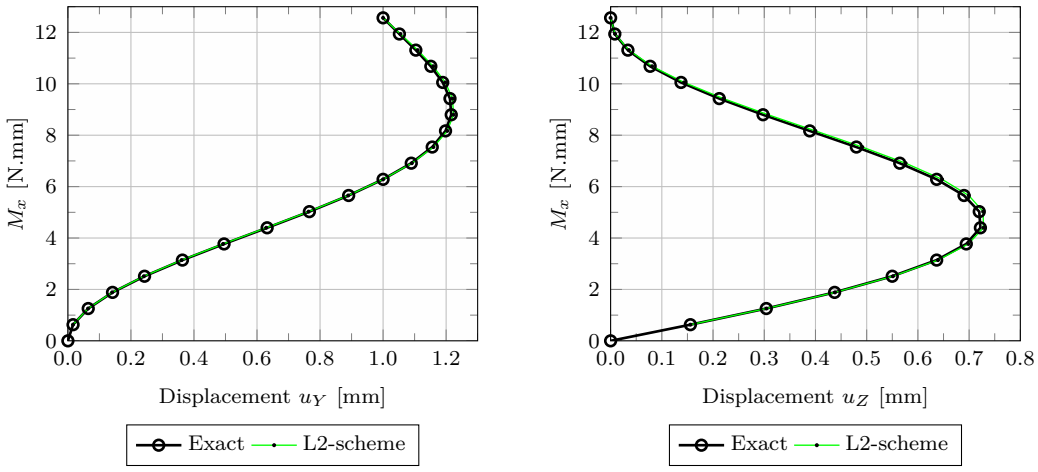

(a) Y direction (b) Z direction

Figure 7.5: Displacements of the beam tip

7.2 Buckling of a hinged right-angle frame

This example is a hinged right-angle frame[2] subjected to a *fixed* load or a *follower* load. The same input data presented in Simo and Vu-Quoc (1986) are adopted in this work. Each component of the frame is discretised in 5 smoothing domains.

The frame is characterised by each component having a length $L = 120\,\text{mm}$, and the following geometric and material parameters

$$\left.\begin{array}{ll} A = 6\,\text{mm}^2 & I_1 = 2\,\text{mm}^4 \\ A_1 = 6\,\text{mm}^2 & I_2 = 2\,\text{mm}^4 \\ A_2 = 6\,\text{mm}^2 & J_t = 4\,\text{mm}^4 \end{array}\right| \begin{array}{l} \\ E = 7\,200\,000\,\text{N/mm}^2 \\ G = 2\,770\,000\,\text{N/mm}^2 \end{array} \tag{7.4}$$

The distance a that defines the point of application of the load (Fig. 7.6) is equal to $1/5L$.

In this work, during the simulations the load was incremented up to the buckling load[3]. The L2 and L3/2 schemes were analysed considering two cases for the load $P = 1000\,\text{N}$ applied to the structure: a *fixed* load, that remains vertical all along the analysis, and a *follower* load, that remains orthogonal to the beam axis as it deforms. During the simulations, the tolerance for the norm of the *unbalanced forces vector* was $1 \cdot 10^{-5}$.

[2]Some authors refer it as the Lee's frame, due to the work of Lee et al. (1968) where this frame was first studied and analytical solutions provided.

[3]Due to the limitations of the *load control* based algorithm used in these simulations, several tests were necessary to determine the buckling load. As a result, different load steps and load increment sizes were employed depending of the load type and number of *support nodes* (L2 or L3/2 schemes) selected to build the shape functions.

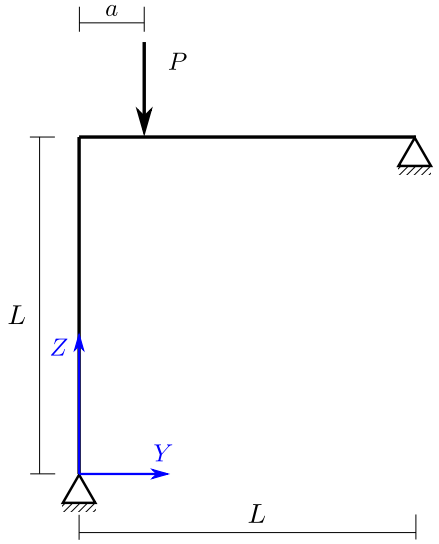

Figure 7.6: Hinged right-angle frame under a force load

Fig. 7.7 and Fig. 7.8 illustrate the results in terms of deformed configurations, obtained with the two load cases, for both the L2 and L3/2 schemes. The load-displacement diagrams are depicted in Fig. 7.9; as it can be observed, the two schemes provided similar results, with the L3/2 schemes characterised by lower values of the buckling load. The analytical solution of the buckling load for this problem for a *fixed* load is available in Lee et al. (1968), and corresponds to $P = 18.552(EI/L^2) = 18\,552\,\text{N}$. Table 7.4 provides a comparison of the buckling load obtained with the L2 and L3/2 schemes, and the values available in Simo and Vu-Quoc (1986).

The behaviour of the SPIM discussed for the Timoshenko beam is propagated for the geometrically nonlinear model, (i) the L2-scheme reproduces the linear FEM; (ii) the L3/2 is *softer* than the L2-scheme (or linear FEM). In other words, the buckling load achieved for the simulation with the L2-scheme is bigger than the L3/2-scheme outcome.

Load	L2-scheme	Simo (1986)	Δ [%]	L3/2-scheme	Simo (1986)	Δ [%]
fixed	19550	18532	5.49	17880	18532	-3.52
follower	39250	35447	10.73	33580	35447	-5.27

Table 7.4: Load buckling values

In order to illustrate the effect of the αPIM shape function, the *fixed* and *follower* load cases were simulated for a value of $\alpha = 0.50$. The deformed shapes produced by the load $P = 14\,000\,\text{N}$ are illustrated in Fig. 7.10. As observed in previous results the alpha PIM produces an intermediate solution bounded by the L2 and L3/2 schemes solutions, i.e. the alpha application is somehow capable of "regulate" the stiffness of the numerical model.

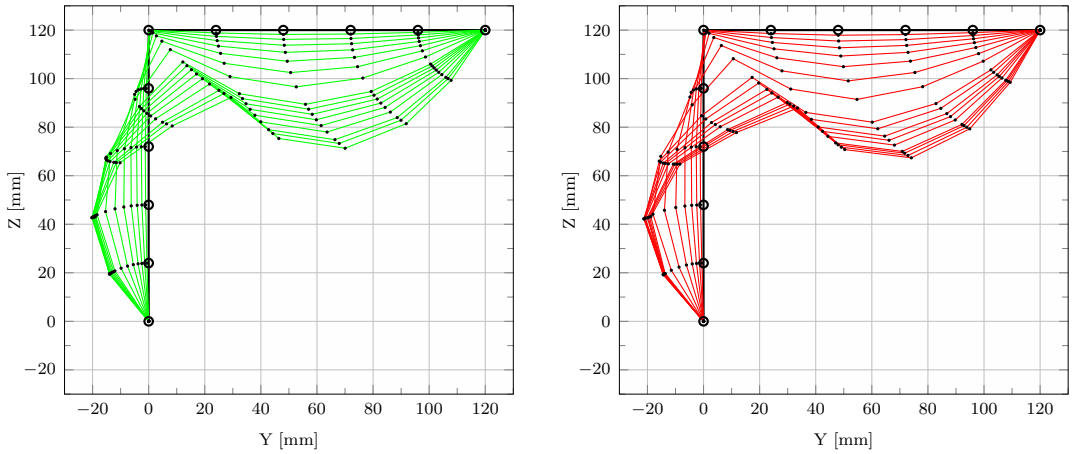

(a) L2-scheme results (b) L3/2-scheme results

Figure 7.7: Fixed load

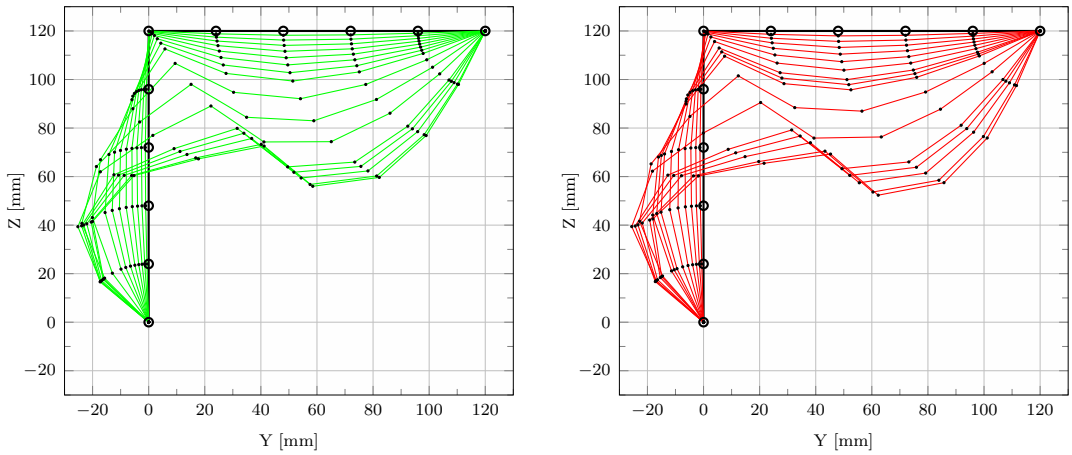

(a) L2-scheme results (b) L3/2-scheme results

Figure 7.8: Follower load

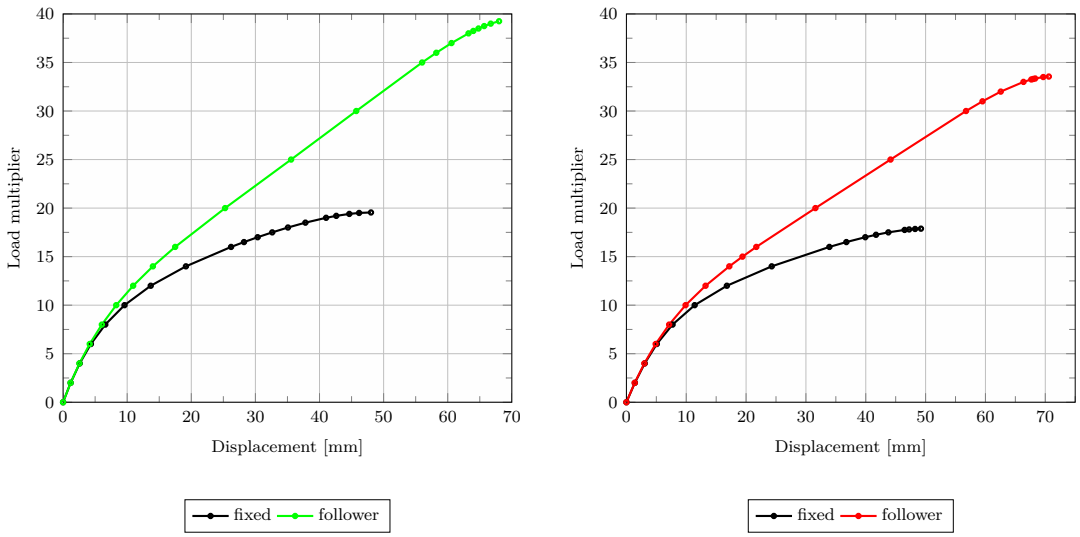

(a) L2-scheme (b) L3/2-scheme

Figure 7.9: Load-displacement diagram

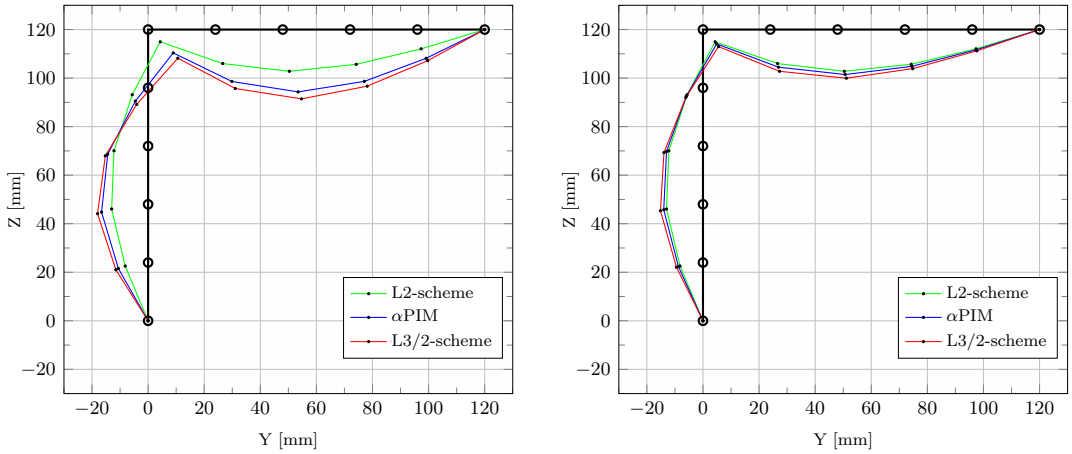

(a) Fixed load (b) Follower load

Figure 7.10: Comparison

7.3 Cantilever 45-degree bend

In this example, a 45-degree bent cantilever beam is considered. The same input data simulated in Simo and Vu-Quoc (1986) are adopted. This structure was first studied in Bathe and Bolourchi (1979). Its initial configuration is depicted in Fig. 7.11.

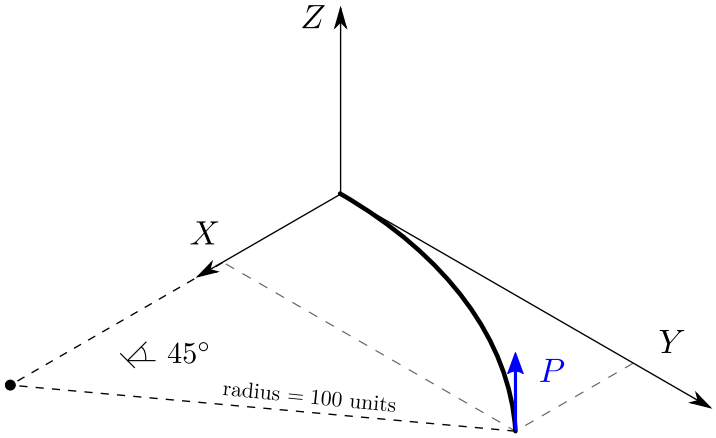

Figure 7.11: 45-degree bent cantilever beam

The beam geometry follows a circle with radius 100 mm and angle of 45° in a X-Y plane, and it is characterised by the following geometric and material parameters

$$\begin{array}{ll|l} A = 1\,\text{mm}^2 & I_1 = 0.00833\text{mm}^4 & \\ A_1 = 0.833\,\text{mm}^2 & I_2 = 0.00833\text{mm}^4 & E = 10\,000\,000\,\text{N/mm}^2 \\ A_2 = 0.833\,\text{mm}^2 & J_t = 0.16667\text{mm}^4 & G = 5\,000\,000\,\text{N/mm}^2 \end{array} \tag{7.5}$$

The beam is discretised in 8 smoothing domains. A point force load of $P = 600\,\text{N}$ is applied at its tip in the Z direction. In Simo and Vu-Quoc (1986) this load value is reached in three load steps with the following load factors: 0.50, 0.75 and 1.00. For these particular load steps the L3/2-scheme did not achieved convergence. Aiming to perform

a comparison with the results commonly presented in the literature, a tiny perturbation equal to 0.00394 was added to these three load factors. In this new scenario, the convergence was reached, and the displacement results could be compared.

In Fig. 7.12 the displacements in each axis direction are represented in detail up to a load value of $P = 3000\,\mathrm{N}$. Both, L2 and L3/2 results are consistent with the same plot shown Simo and Vu-Quoc (1986). A perspective view of the deformed configurations due to the loads $P = 300\,\mathrm{N}$, $P = 450\,\mathrm{N}$ and $P = 600\,\mathrm{N}$ are illustrated in Fig. 7.13a and Fig. 7.13b for the L2 and L3/2 schemes respectively. In Fig. 7.14 the results for $P = 600\,\mathrm{N}$ are compared with a αPIM simulation with $\alpha = 0.10$. As observed in previous applications, in this case the L3/2 model is *softer* than the L2 model, and the αPIM is bounded by both.

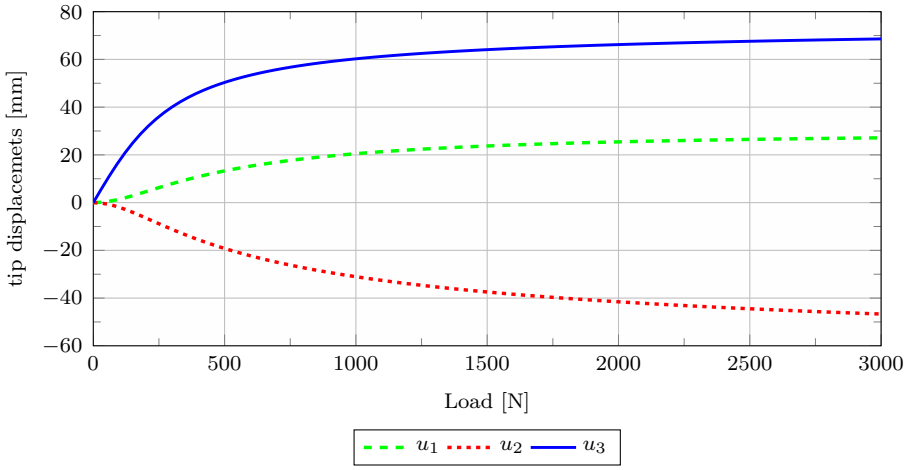

(a) L2-scheme

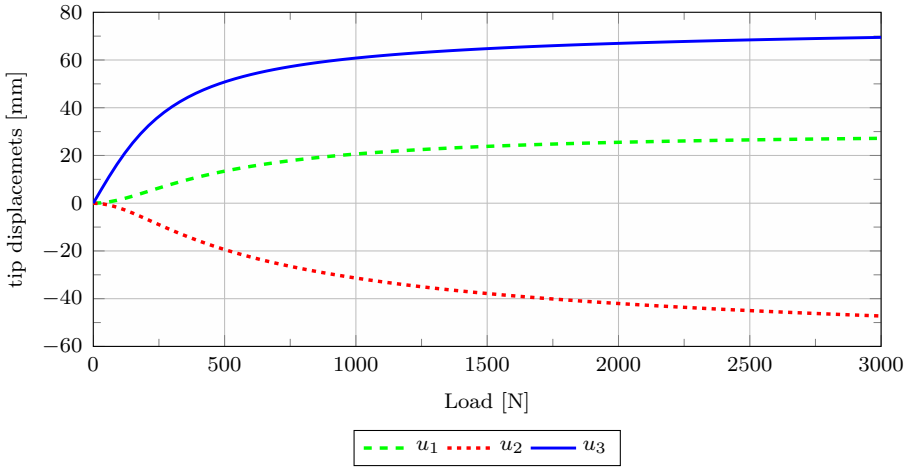

(b) L3/2-scheme

Figure 7.12: Tip displacements

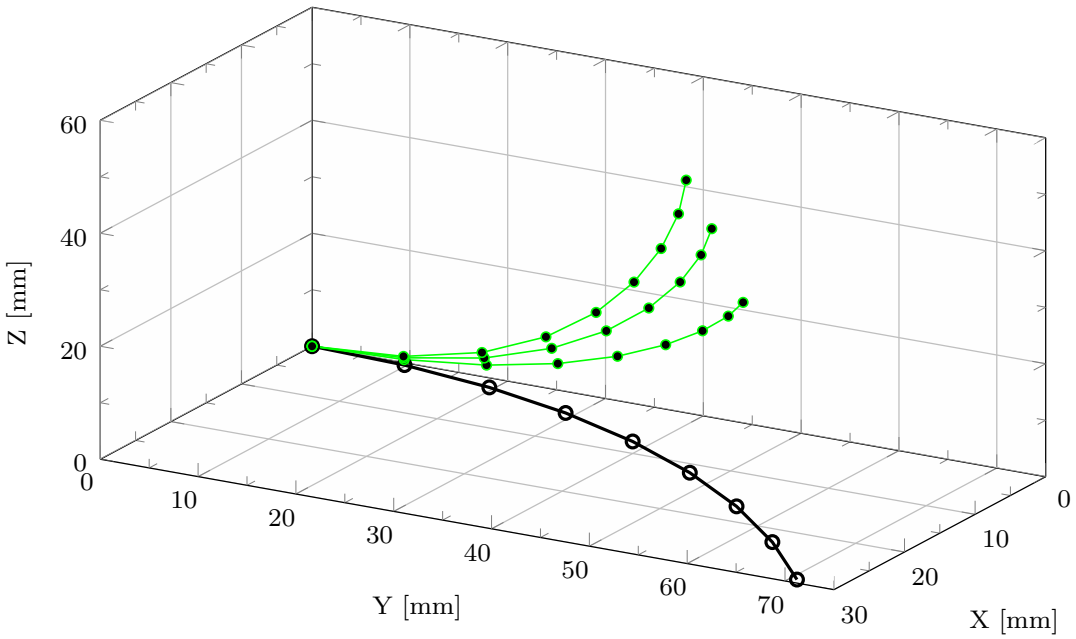

(a) L2-scheme

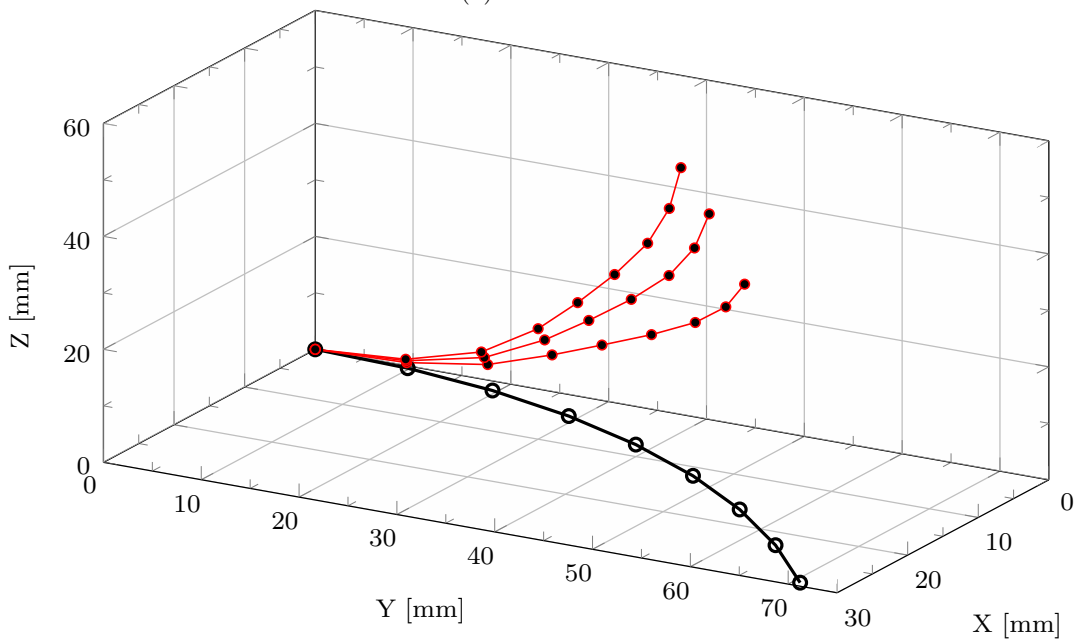

(b) L3/2-scheme

Figure 7.13: Deformed shapes for 3 load cases: $P = 300\,\mathrm{N}$, $P = 450\,\mathrm{N}$ and $P = 600\,\mathrm{N}$

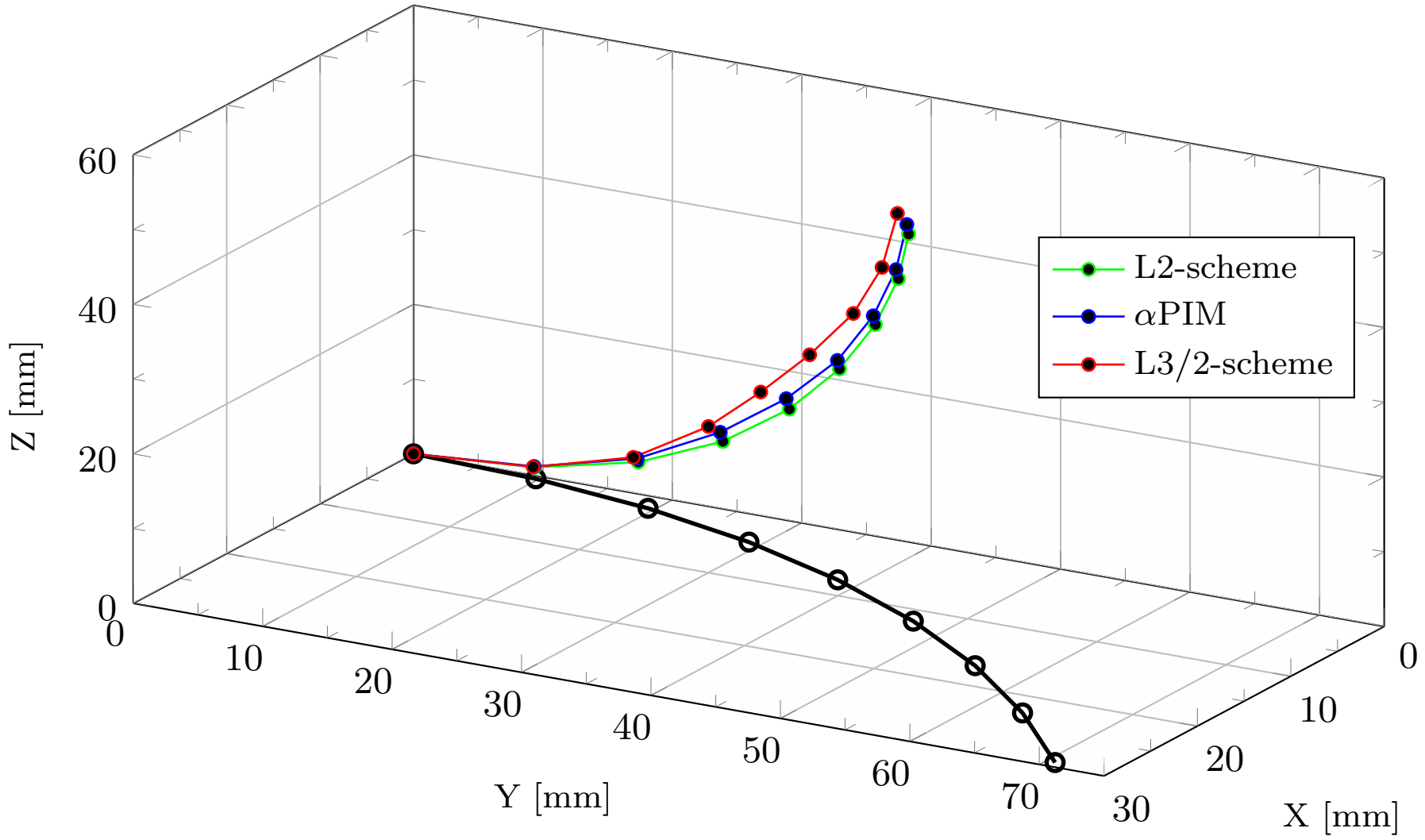

Figure 7.14: Comparison of L2, L3/2 and alpha PIM results for $P = 600\,\mathrm{N}$

In Table 7.5 the results of X, Y and Z nodes positions are compared with different results available in the literature. As it can be observed, the results obtained with the proposed SPIM strategy are in good agreement with the ones obtained by other authors.

Load level [N]	L2-scheme			Geradin and Cardona (1988)			Bathe and Bolourchi (1979)			Simo and Vu-Quoc (1986)		
	X	Y	Z	X	Y	Z	X	Y	Z	X	Y	Z
300	21.12	59.39	40.21	22.14	58.64	40.35	22.50	59.20	39.50	22.33	58.84	40.08
450	17.04	53.16	48.53	18.38	52.11	48.59	- - -	- - -	- - -	18.62	52.32	48.39
600	13.89	48.27	53.52	15.55	47.04	53.50	15.90	47.20	53.40	15.79	47.23	53.37

Load level [N]	L3/2-scheme			Geradin and Cardona (1988)			Bathe and Bolourchi (1979)			Simo and Vu-Quoc (1986)		
	X	Y	Z	X	Y	Z	X	Y	Z	X	Y	Z
300	20.10	58.40	42.92	22.14	58.64	40.35	22.50	59.20	39.50	22.33	58.84	40.08
450	16.20	51.97	50.78	18.38	52.11	48.59	- - -	- - -	- - -	18.62	52.32	48.39
600	13.29	46.98	55.48	15.55	47.04	53.50	15.90	47.20	53.40	15.79	47.23	53.37

Table 7.5: Position X[mm], Y [mm] and Z [mm] of the beam tip

CHAPTER 8

CONCLUSION

The main goal of this master's thesis was to extend the application of smoothed point interpolation methods to two shear-deformable beam theories, namely the linear Timoshenko beam theory and the geometrically-exact beam proposed in Simo (1985), Simo and Vu-Quoc (1986). This application was made possible by the extension of the concept of weakened-weak form proposed by Liu (2009) to these beam models. The concept of αPIM shape function proposed by Liu et al. (2013) was also considered, as a mean to improve the convergence of these methods. Comprehensive simulations were performed with the Timoshenko beam model, considering different boundary conditions, different load conditions, and different slenderness ratios. The simulations obtained with the L2 and L3/2 schemes were in good agreement with the analytical solutions, with convergence properties similar to the linear FEM. They also pointed out that the L2 and L3/2 schemes provide, in general, different bounds to the analytical solution; while the L2-scheme provided a *lower* bound to the solution in terms of deflections (like the linear FEM), the L3/2-scheme provided an *upper* bound to the deflection. This property allowed to take advantage of the concept of αPIM shape function already introduced by Liu et al. (2013). With this concept the approximation was built as a blend of the L2 and L3/2 schemes, resulting in an improved convergence.

Numerical simulations were also performed with the geometrically exact model, considering three classic problems from the literature on this topic. The results were in good agreement with the ones from the literature. It is worth noting that the behaviour of the L2 and L3/2 schemes observed in the linear model was also observed in the nonlinear case, in the sense that the two schemes provided different bounds to the solution, the L3/2-scheme showing a *softer* behaviour with respect to the L2-scheme.

In terms of implementations, the SPIMs applications of the INSANE software now accounts for the Timoshenko beam model, where the proposed nodes support selection schemes can be used in future applications. Regarding the nonlinear implementation, the present MATLAB® code can be improved to widen the simulation possibilities aiming to comprehend more complex load cases, structures and behaviours.

With the advent of this master's thesis, and aiming future developments, the following research topics are suggested as branches of the present work:

- Extend the Timoshenko SPIMs implementation to plane and spatial frames in INSANE
- Test the applicability of the node-based smoothed point interpolation methods for the proposed beam models
- Investigate the use of shape functions constructed using radial basis functions with or without polynomial reproduction
- Investigate the performance of the αPIM in more complex structures, such as, continuous beams, plane frames and spatial frames
- Derive a procedure to estimate the alpha values without the need for an analytical solution
- Extend the proposed strategies to dynamic problems
- Investigate the performance of the SPIMs in *physically* nonlinear beam models

BIBLIOGRAPHY

Argyris, J. (1982), 'An excursion into large rotations', *Computer methods in applied mechanics and engineering* vol. 32(1-3), 85–155.

Argyris, J. and Poterasu, V. F. (1993), 'Large rotations revisited application of lie algebra', *Computer methods in applied mechanics and engineering* vol. 103(1-2), 11–42.

Bathe, K.-J. (1996), *Finite Element Procedures*, Klaus-Jurgen Bathe.

Bathe, K.-J. and Bolourchi, S. (1979), 'Large displacement analysis of three-dimensional beam structures', *International journal for numerical methods in engineering* vol. 14(7), 961–986.

Belytschko, T., Lu, Y., Gu, L. and Tabbara, M. (1995), 'Element-free galerkin methods for static and dynamic fracture', *International Journal of Solids and Structures* vol. 32(17-18), 2547–2570.

Chen, J., Yoon, S. and Wu, C. (2002), 'Non-linear version of stabilized conforming nodal integration for Galerkin mesh-free methods', *International Journal for Numerical Methods in Engineering* vol. 53, 2587–2615.

Cui, X., Liu, G., Li, G. and Zheng, G. (2008), 'A rotation free formulation for static and free vibration analysis of thin beams using gradient smoothing technique', *CMES-Comput. Model. Eng. Sci* vol. 38, 217–229.

Du, C., Zhang, D., Li, L. and Liu, G. (2018), 'A node-based smoothed point interpolation method for dynamic analysis of rotating flexible beams', *Acta Mechanica Sinica* vol. 34(2), 409–420.

Elishakoff, I. (2020), 'Who developed the so-called timoshenko beam theory?', *Mathematics and Mechanics of Solids* vol. 25(1), 97–116.

Fleischfresser, S. A. (2012), Uma formulação do método dos elementos de contorno para a análise de vigas de Timoshenko, PhD thesis, Universidade Federal do Paraná.

Gallier, J. and Quaintance, J. (2020), *Differential Geometry and Lie Groups: A Computational Perspective*, Springer Nature.

Geradin, M. and Cardona, A. (1988), 'A beam finite element non-linear theory with finite rotations', *International Journal for Numerical Methods in Engineering* vol. 26.

Gori, L. (2014), Geometrically exact three-dimensional beam theory: Fem implementation and applications, Master's thesis, Universitá degli Studi di Firenze.

Gori, L. (2018), Failure analysis of quasi-brittle media using the micropolar continuum theory, elastic-degrading constitutive models, and smoothed point interpolation methods, PhD thesis, Federal University of Minas Gerais.

Gori, L., Silva Penna, S. and da Silva Pitangueira, R. L. (2019), 'G-space theory and weakened-weak form for micropolar media: Application to smoothed point interpolation methods', *Engineering Analysis with Boundary Elements* vol. 101, 318–329.
URL: *https://linkinghub.elsevier.com/retrieve/pii/S0955799718305794*

Hale, J. (2013), Meshless methods for shear-deformable beams and plates based on mixed weak forms, PhD thesis, Imperial College London.

He, C., Wu, X., Wang, T. and He, H. (2019), 'Geometrically nonlinear analysis for elastic beam using point interpolation meshless method', *Shock and Vibration* vol. 2019.

Hodges, D. H. (1990), 'A mixed variational formulation based on exact intrinsic equations for dynamics of moving beams', *International journal of solids and structures* vol. 26(11), 1253–1273.

Lee, S.-L., Manuel, F. S. and Rossow, E. C. (1968), 'Large deflections and stability of elastic frames', *Journal of the Engineering Mechanics Division* vol. 94(2), 521–548.

Liu, G. and Gu, Y. (2002), 'Comparisons of two meshfree local point interpolation methods for structural analyses', *Computational Mechanics* vol. 29(2), 107–121.

Liu, G.-R. (2008), 'A generalized gradient smoothing technique and the smoothed bilinear form for galerkin formulation of a wide class of computational methods', *International Journal of Computational Methods* vol. 5(02), 199–236.

Liu, G.-R. (2009), *Meshfree Methods: moving beyond the the finite element method*, Taylor & Francis.

Liu, G.-R. (2010*a*), 'A g space theory and a weakened-weak (w^2) form for a unified formulation of compatible and incompatible methods: Part i theory', *International Journal for Numerical Methods in Engineering* vol. 81(9), 1093–1126.

Liu, G.-R. (2010*b*), 'A g space theory and a weakened-weak (w^2) form for a unified formulation of compatible and incompatible methods: Part ii applications to solid mechanics problems', *International Journal for Numerical Methods in Engineering* vol. 81(9), 1127–1156.

Liu, G.-R. and Zhang, G.-y. (2013), *Smoothed point interpolation methods: G space theory and weakened weak forms*, World Scientific.

Liu, G., Zhang, G., Zong, Z. and Li, M. (2013), 'Meshfree cell-based smoothed alpha radial point interpolation method (cs-α rpim) for solid mechanics problems', *International Journal of Computational Methods* vol. 10(04), 1350020.

Lozzo, E. C. D. (2010), Geometrically exact three-dimensional beam theory: modeling and fem implementation for statics and dynamics analysis, Master's thesis, Università degli Studi di Pavia.

Mäkinen, J. (2007), 'Total Lagrangian Reissner's geometrically exact beam element without singularities', *International Journal for Numerical Methods in Engineering* vol. 70, 1009–1048.

Marino, E. (2016), 'Isogeometric collocation for three-dimensional geometrically exact shear-deformable beams', *Computer Methods in Applied Mechanics and Engineering* vol. 307, 383–410.

Marsden, J. E. and Hughes, T. J. (1994), *Mathematical foundations of elasticity*, Courier Corporation.

Moreira, M. d. L. T. (2009), Parametrização das rotações em teorias de barras e cascas, PhD thesis, University of São Paulo.

Öchsner, A. and Merkel, M. (2018), *One-Dimensional Finite Elements: An Introduction to the FE Method*, second edn, Springer.

Oñate, E. (2013), *Structural analysis with the finite element method. Linear statics: volume 2: beams, plates and shells*, Springer Science & Business Media.

Panchore, V., Ganguli, R. and Omkar, S. (2016), 'Meshless local petrov-galerkin method for rotating timoshenko beam: a locking-free shape function formulation', *CMES-COMPUTER MODELING IN ENGINEERING & SCIENCES* vol. 108(4), 215–237.

Pimenta, P. and Campello, E. (2003), 'A fully nonlinear multi–parameter rod model incorporating general cross-section in–plane changes and out-of-plane warping', *Latin American Journal of Solids and Structures* pp. 119–140.

Pimenta, P. M. and Yojo, T. (1993), 'Geometrically exact analysis of spatial frames', *Applied Mechanics Reviews* vol. 46(11S), S118–S128.

Reddy, J. (2010), *An introduction to the finite element method*, Vol. 1221, McGraw-Hill New York.

Reissner, E. (1972), 'On one-dimensional finite-strain beam theory: the plane problem', *Journal of Applied Mathematics and Physics (ZAMP)* vol. 23.

Roque, C., Ferreira, A. and Reddy, J. (2011), 'Analysis of timoshenko nanobeams with a nonlocal formulation and meshless method', *International Journal of Engineering Science* vol. 49(9), 976–984.

Simo, J. (1985), 'A finite strain beam formulation. the three-dimensional dynamic problem. part i', *Computer Methods in Applied Mechanics and Engineering* vol. 49(1), 55–70. **URL:** *https://linkinghub.elsevier.com/retrieve/pii/0045782585900507*

Simo, J. and Vu-Quoc, L. (1986), 'A three-dimensional finite-strain rod model. Part II: Computational Aspects', *Computer Methods in Applied Mechanics and Engineering* .

Tiago, C. and Pimenta, P. (2005), Geometrically exact analysis of space frames by a meshless method, *in* 'Proceedings of the ECCOMAS Thematic Conference on Meshless Methods, Lisboa, Portugal'.

Tootoonchi, A. and Khoshghalb, A. (2016), A cell-based smoothed point interpolation method for flow-deformation analysis of saturated porous media, *in* 'VII European Congress on Computational Methods in Applied Sciences and Engineering', Crete Island, Greece.

Wang, C., Reddy, J. N. and Lee, K. (2000), *Shear deformable beams and plates: Relationships with classical solutions*, Elsevier.

Wang, J. and Liu, G. (2000), Radial point interpolation method for elastoplastic problems, *in* 'ICSSD 2000: 1 st Structural Conference on Structural Stability and Dynamics', pp. 703–708.

Wang, J. and Liu, G. (2002), 'A point interpolation meshless method based on radial basis functions', *International Journal for Numerical Methods in Engineering* vol. 54(11), 1623–1648.

Wriggers, P. (2008), *Nonlinear finite element methods*, Springer Science & Business Media.

Xiao, J. and McCarthy, M. (2003), 'Meshless analysis of timoshenko beams based on a locking-free formulation and variational approaches', *Computer methods in applied mechanics and engineering* vol. 192(39-40), 4403–4424.

Appendices

APPENDIX A

WEAK FORM OF THE TIMOSHENKO BEAM MODEL

In what follows, the derivation of the weak form of the Timoshenko beam is achieved by a weighted residual procedure, starting from the model governing differential equations (Eq. (2.3) and Eq. (2.4)):

$$\frac{\partial}{\partial x}\left(EI\omega\right) + GA_s\gamma = 0 \tag{A.1}$$

$$\frac{\partial}{\partial x}\left(GA_s\gamma\right) = -q_y(x) \tag{A.2}$$

Proposition A.1. The strong form of the problem depicted in Eqs. (A.1) and (A.2) can be recasted in the following weak form:

$$\begin{aligned}\int_0^L \frac{\partial\delta\theta}{\partial x} EI \frac{\partial\theta}{\partial x} dx + \int_0^L \left(\frac{\partial\delta v}{\partial x} - \delta\theta\right) GA_s \left(\frac{\partial v}{\partial x} - \theta\right) dx = \\ \int_0^L \delta v q_y(x) dx + \left[\delta v GA_s \left(\frac{\partial v}{\partial x} - \theta\right)\right]\Bigg|_0^L + \left(\delta\theta EI\frac{\partial\theta}{\partial x}\right)\Bigg|_0^L\end{aligned} \tag{A.3}$$

Proof.

First of all, the shear differential equation (Eq. (A.2)*) is multiplied by a deflection weight function δv and integrated over the domain as follows*

$$\int_0^L \delta v \left[\frac{\partial}{\partial x}\left[GA_s\left(\frac{\partial v}{\partial x} - \theta\right)\right] + q_y(x)\right] dx = 0 \tag{A.4}$$

The weighted residual procedure performed in this work uses trial functions that satisfy the essential boundary conditions of the problem. The trial function defined above, δv, must be equal to v at the boundaries of the problem domain.

If GA_s is constant in equation A.4, the above equation can be recasted as follows

$$\int_0^L \delta v \left[GA_s\left(\frac{\partial^2 v}{\partial x^2} - \frac{\partial\theta}{\partial x}\right) + q_y(x)\right] dx = 0 \tag{A.5}$$

Performing an integration by parts of both the expressions in the round brackets leads to

$$\int_0^L \delta v GA_s \frac{\partial^2 v}{\partial x^2} dx = \delta v GA_s \frac{\partial v}{\partial x}\Big|_0^L - \int_0^L \frac{\partial\delta v}{\partial x} GA_s \frac{\partial v}{\partial x} dx \tag{A.6}$$

$$-\int_0^L \delta v G A_s \frac{\partial \theta}{\partial x} dx = -\left(\delta v G A_s \theta\right)\Big|_0^L + \int_0^L \frac{\partial \delta v}{\partial x} G A_s \theta dx \tag{A.7}$$

Next, the bending differential (equation A.1) is multiplied with a rotation weight function $\delta\theta(x)$ and integrated over the domain (for a constant EI)

$$\int_0^L \delta\theta \left[EI \frac{\partial^2 \theta}{\partial x^2} + G A_s \cdot \left(\frac{\partial v}{\partial x} - \theta \right) \right] dx = 0 \tag{A.8}$$

Again, performing an integration by parts of the first expression in above equation leads to

$$\int_0^L \delta\theta EI \frac{\partial^2 \theta}{\partial x^2} dx = \left(\delta\theta EI \frac{\partial \theta}{\partial x} \right)\Big|_0^L - \int_0^L \frac{\partial \delta\theta}{\partial x} dx EI \frac{\partial \theta}{\partial x} dx \tag{A.9}$$

now equation A.8 can be rewritten as follows

$$\left(\delta\theta EI \frac{\partial \theta}{\partial x} \right)\Big|_0^L - \int_0^L \frac{\partial \delta\theta}{\partial x} EI \frac{\partial \theta}{\partial x} dx + \int_0^L \delta\theta G A_s \left(\frac{\partial v}{\partial x} - \theta \right) dx \tag{A.10}$$

Summation of equations A.6, A.7, A.10 and $\int_0^L \delta v q_y(x) dx$ (from Eq. (A.4)), results in

$$\begin{aligned} &\delta v G A_s \frac{\partial v}{\partial x}\Big|_0^L - \int_0^L \frac{\partial \delta v}{\partial x} G A_s \frac{\partial v}{\partial x} dx - \left(\delta v G A_s \theta\right)\Big|_0^L \\ &+ \int_0^L \frac{\partial \delta v}{\partial x} G A_s \theta dx + \int_0^L \delta v q_y(x) dx + \left(\delta\theta EI \frac{\partial \theta}{\partial x} \right)\Big|_0^L \\ &- \int_0^L \frac{\partial \delta\theta}{\partial x} EI \frac{\partial \theta}{\partial x} dx + \int_0^L \delta\theta G A_s \left(\frac{\partial v}{\partial x} - \theta \right) dx = 0 \end{aligned} \tag{A.11}$$

Rearranging above equation the weak form of the searched beam model is achieved

$$\begin{aligned} &\int_0^L \frac{\partial \delta\theta}{\partial x} EI \frac{\partial \theta}{\partial x} dx + \int_0^L \left(\frac{\partial \delta v}{\partial x} - \delta\theta \right) G A_s \left(\frac{\partial v}{\partial x} - \theta \right) dx = \\ &\int_0^L \delta v q_y(x) dx + \left[\delta v G A_s \left(\frac{\partial v}{\partial x} - \theta \right) \right]\Big|_0^L + \left(\delta\theta EI \frac{\partial \theta}{\partial x} \right)\Big|_0^L \end{aligned} \tag{A.12}$$

□

APPENDIX B

COMPOUND ROTATIONS

B.1 Introduction to rotations in three dimensions

Let us consider the rotation operator $\underline{\boldsymbol{R}}$ introduced in equation 2.18. It belongs to the Lie group of proper orthogonal linear transformations and satisfies the following

$$\begin{gathered}\underline{\boldsymbol{R}}: \mathbb{R}^3 \rightarrow \mathbb{R}^3 \\ \underline{\boldsymbol{R}}^T \underline{\boldsymbol{R}} = \underline{\boldsymbol{R}}\underline{\boldsymbol{R}}^T = \underline{\boldsymbol{I}}; \det \underline{\boldsymbol{R}} = 1\end{gathered} \tag{B.1}$$

This group contemplates all rotations about the origin of the three-dimensional Euclidean space under the operation of composition. Frequently, it is denoted by SO(3) which stands for special orthogonal group in the three-dimensional space. The SO(3) group is characterized by the following properties Argyris and Poterasu (1993)

- $\underline{\boldsymbol{R}}_1 \underline{\boldsymbol{R}}_2 = \underline{\boldsymbol{R}}_3 \in \mathrm{SO}(3), \forall \underline{\boldsymbol{R}}_1, \underline{\boldsymbol{R}}_2 \in \mathrm{SO}(3)$
- $\exists\, \underline{\boldsymbol{R}}^{-1}$ such that $\underline{\boldsymbol{R}}\underline{\boldsymbol{R}}^{-1} = \underline{\boldsymbol{R}}^{-1}\underline{\boldsymbol{R}} = \underline{\boldsymbol{I}}$
- $\underline{\boldsymbol{R}}_1(\underline{\boldsymbol{R}}_2\underline{\boldsymbol{R}}_3) = (\underline{\boldsymbol{R}}_1\underline{\boldsymbol{R}}_2)\underline{\boldsymbol{R}}_3, \forall \underline{\boldsymbol{R}}_1, \underline{\boldsymbol{R}}_2, \underline{\boldsymbol{R}}_3 \in \mathrm{SO}(3)$
- $\exists\, \underline{\boldsymbol{I}} \in \mathrm{SO}(3)$ such that $\underline{\boldsymbol{I}}\underline{\boldsymbol{R}} = \underline{\boldsymbol{R}}\underline{\boldsymbol{I}} = \underline{\boldsymbol{R}}, \forall \underline{\boldsymbol{R}} \in \mathrm{SO}(3)$

In addition, we quote the work of (Gallier and Quaintance, 2020, p. 16)

> "The inventors of Lie groups and Lie algebras (starting with Lie!) regarded Lie groups as groups of symmetries of various topological or geometric objects. Lie algebras were viewed as the "infinitesimal transformations" associated with the symmetries in the Lie group. For example, the group SO(n) of rotations is the group of orientation-preserving isometries of the Euclidean space $\mathbb{E}^n$. The Lie algebra $\mathrm{so}(\mathrm{n};\mathbb{R})$ consisting of real skew symmetric $n \times n$ matrices is the corresponding set of infinitesimal rotations. The geometric link between a Lie group and its Lie algebra is the fact that the Lie algebra can be viewed as the tangent space to the Lie group at the identity. There is a map from the tangent space to the Lie group, called the exponential map. The Lie algebra can be

considered as a linearisation of the Lie group (near the identity element), and the exponential map provides the "delinearisation", i.e., it takes us back to the Lie group."

Let us consider a point P defined by its position vector $\bar{\boldsymbol{a}}$. Next, consider another point P' represented by its position vector $\bar{\boldsymbol{b}}$. Figure B.1 illustrates the referred quantities.

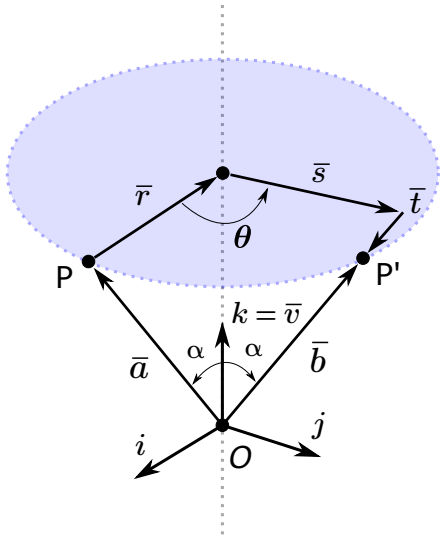

Figure B.1: Vector Rotation.

The vector $\bar{\boldsymbol{b}}$ can be achieved by a rotation of the vector $\bar{\boldsymbol{a}}$. First, based on the quantities illustrated in Figure B.1 the vector $\bar{\boldsymbol{b}}$ can be described by a vectorial summation, as follows

$$\bar{\boldsymbol{b}} = \bar{\boldsymbol{a}} + \bar{\boldsymbol{r}} + \bar{\boldsymbol{s}} + \bar{\boldsymbol{t}} \tag{B.2}$$

then, using Figure B.1 and geometric observations the vectors $\bar{\boldsymbol{r}}$, $\bar{\boldsymbol{s}}$ and $\bar{\boldsymbol{t}}$ can be expressed in terms of $\bar{\boldsymbol{a}}$, $\bar{\boldsymbol{v}}$ and θ. Hence, equation B.2 can be rewritten in the form

$$\bar{\boldsymbol{b}} = \bar{\boldsymbol{a}} + \sin\theta(\bar{\boldsymbol{v}} \times \bar{\boldsymbol{a}}) + (1 - \cos\theta)(\bar{\boldsymbol{v}} \times (\bar{\boldsymbol{v}} \times \bar{\boldsymbol{a}})) \tag{B.3}$$

finally $\bar{\boldsymbol{b}}$ can be expressed as

$$\bar{\boldsymbol{a}} = \underline{\boldsymbol{R}}\bar{\boldsymbol{b}} \tag{B.4}$$

where the quantity $\underline{\boldsymbol{R}}$ in equation B.4 is the rotation tensor and it assumes the form (see Moreira (2009))

$$\underline{\boldsymbol{R}} = \underline{\boldsymbol{I}} + \sin\theta\underline{\boldsymbol{V}} + (1 - \cos\theta)\underline{\boldsymbol{V}}^2 \tag{B.5}$$

in above equation, $\underline{\boldsymbol{V}}$ is a skew-symmetric tensor and $\bar{\boldsymbol{v}}$ is the correspondent axial vector.

Considering $\underline{\boldsymbol{\theta}}$ the skew-symmetric tensor and $\bar{\boldsymbol{\theta}}$ its associated axial vector with $\|\bar{\boldsymbol{\theta}}\| = \theta$, equation B.5 can be expressed as

$$\underline{\boldsymbol{R}} = \underline{\boldsymbol{I}} + \frac{\sin\theta}{\theta}\underline{\boldsymbol{\theta}} + \frac{1}{2}\left[\frac{\sin(\theta/2)}{\theta/2}\right]^2 \underline{\boldsymbol{\theta}}^2 \tag{B.6}$$

An expansion in power of series of the trigonometric quantities in equation B.6 leads to

$$\underline{\boldsymbol{R}} = \boldsymbol{I} + \underline{\boldsymbol{\theta}} + \frac{1}{2!}\underline{\boldsymbol{\theta}}^2 \cdots = \exp(\underline{\boldsymbol{\theta}}) \tag{B.7}$$

Equation B.7 is the exponential representation of rotations or the exponential map.

Let us consider equation 2.18 again which is a map from the reference configuration to the current configuration by means of $\underline{\boldsymbol{R}}$ and can be physically interpreted as a rigid body rotation from a frame to another. Now, consider an incremental rotation applied to the current configuration $\{\boldsymbol{t}_I\}$. This incremental rotation can be described in two ways, as follows Geradin and Cardona (1988)

- Via a left translation: left-application of an incremental rotation operator $\underline{\boldsymbol{R}}_{(r)}$ to the actual rotation $\underline{\boldsymbol{R}}$

$$\begin{aligned} \underline{\boldsymbol{R}}' &= \underline{\boldsymbol{R}}_{(\ell)}\underline{\boldsymbol{R}} \\ \bar{\boldsymbol{t}}' &= \underline{\boldsymbol{R}}_{(\ell)}\boldsymbol{t}_I = \underline{\boldsymbol{R}}_{(\ell)}\underline{\boldsymbol{R}}\bar{\boldsymbol{E}}_I \end{aligned} \tag{B.8}$$

- Via a right translation: right-application of an incremental rotation operator $\underline{\boldsymbol{R}}_{(r)}$ to the actual rotation $\underline{\boldsymbol{R}}$

$$\begin{aligned} \underline{\boldsymbol{R}}' &= \underline{\boldsymbol{R}}\underline{\boldsymbol{R}}_{(r)} \\ \bar{\boldsymbol{t}}' &= \underline{\boldsymbol{R}}_{(r)}\bar{\boldsymbol{E}}_I \end{aligned} \tag{B.9}$$

The left and right rotation operators can be represented by an exponential map similar to the relation shown in equation B.7. Let us consider $\underline{\boldsymbol{\theta}}$ as a spatial skew-symmetric tensor and $\underline{\boldsymbol{\Theta}}$ as a material skew-symmetric tensor, then, one can write

$$\underline{\boldsymbol{R}}_{(\ell)} = \exp(\underline{\boldsymbol{\theta}}), \quad \underline{\boldsymbol{\theta}} \in \mathrm{so}(3) \tag{B.10}$$

$$\underline{\boldsymbol{R}}_{(r)} = \exp(\underline{\boldsymbol{\Theta}}), \quad \underline{\boldsymbol{\Theta}} \in \mathrm{so}(3) \tag{B.11}$$

The *compound rotation* is defined as a rotation obtained from a combination of two other rotations in the sense of equation B.8 or alternatively by equation B.9.

Given a known rotation $\underline{\boldsymbol{R}}$ and a spatial, $\bar{\boldsymbol{\theta}}$, or a material, $\bar{\boldsymbol{\Theta}}$, incremental rotation vector, corresponding to the spatial rotation $\underline{\boldsymbol{R}}_{(\ell)} = \exp(\underline{\boldsymbol{\theta}})$ and to the material rotation $\underline{\boldsymbol{R}}_{(r)} = \exp(\underline{\boldsymbol{\Theta}})$ respectively, the description of the new compound rotation tensor, $\underline{\boldsymbol{R}}_c$, is obtained from the left or the right translation map as follows

$$\underline{\boldsymbol{R}}_c = \exp(\underline{\boldsymbol{\theta}})\underline{\boldsymbol{R}} \tag{B.12}$$

$$\underline{\boldsymbol{R}}_c = \underline{\boldsymbol{R}}\exp(\underline{\boldsymbol{\Theta}}) \tag{B.13}$$

where $\bar{\boldsymbol{\theta}}$ is the axial vector associated with the spatial skew-symmetric tensor $\underline{\boldsymbol{\theta}}$ and $\bar{\boldsymbol{\Theta}}$ is the axial vector associated with the material skew-symmetric tensor $\underline{\boldsymbol{\Theta}}$. In addition to that, one can demonstrate that the following relation stands

$$\bar{\boldsymbol{\theta}} = \underline{\boldsymbol{R}}\bar{\boldsymbol{\Theta}} \tag{B.14}$$

B.2 Corotated Rate

We highlight that while the spatial and the material strain measures are related through the rotation operator,[1] $\underline{\boldsymbol{R}}(S,t)$, the time derivatives of these quantities do not follow the same relation, in other words

$$\frac{\partial\bar{\boldsymbol{\gamma}}}{\partial t}(S,t) \neq \underline{\boldsymbol{R}}(S,t)\frac{\partial\bar{\boldsymbol{\Gamma}}(S,t)}{\partial t} \tag{B.15}$$

$$\frac{\partial\bar{\boldsymbol{\omega}}}{\partial t}(S,t) \neq \underline{\boldsymbol{R}}(S,t)\frac{\partial\bar{\boldsymbol{\Omega}}(S,t)}{\partial t} \tag{B.16}$$

instead, the material quantities from above equations, on the right hand side, are related to the spatial quantities as follows

$$\overset{\triangledown}{\bar{\boldsymbol{\gamma}}}(S,t) = \underline{\boldsymbol{R}}(S,t)\frac{\partial\bar{\boldsymbol{\Gamma}}(S,t)}{\partial t} \tag{B.17}$$

$$\overset{\triangledown}{\bar{\boldsymbol{\omega}}}(S,t) = \underline{\boldsymbol{R}}(S,t)\frac{\partial\bar{\boldsymbol{\Omega}}(S,t)}{\partial t} \tag{B.18}$$

where the corotated rate is defined in the following

$$\overset{\triangledown}{\bar{\boldsymbol{\gamma}}}(S,t) = \frac{\partial\bar{\boldsymbol{\gamma}}(S,t)}{\partial t} - \bar{\boldsymbol{w}}(S,t)\times\bar{\boldsymbol{\gamma}}(S,t) \tag{B.19}$$

[1] See equation 2.25 and compare equations 2.35 and 2.37.

$$\overset{\triangledown}{\bar{\boldsymbol{\omega}}}(S,t) = \frac{\partial \bar{\boldsymbol{\omega}}(S,t)}{\partial t} - \bar{\boldsymbol{w}}(S,t) \times \bar{\boldsymbol{\omega}}(S,t) \tag{B.20}$$

and for an arbitrarily vectorial quantity

$$\overset{\triangledown}{(\cdot)} = \frac{\partial (\cdot)}{\partial t} - \bar{\boldsymbol{w}} \times (\cdot) \tag{B.21}$$

As pointed out by Simo (1985) the physical significance of equation B.21 is that it computes the rate of change of the quantity $(\cdot)$ relative to an observer which moves with the spatial frame $\bar{\boldsymbol{t}}_I$. Note that the spin $\bar{\boldsymbol{w}}$ of the moving frame is subtracted from the time derivative and therefore the observer does not experiment rotations.

B.3 Linearisation procedure

This appendix is devoted to demonstrate how to obtain some of the results of the linearisation procedure presented in section 2.2.6. The variables (S,t) of the quantities are omitted by convenience. All linearisations of this section is performed using the spatial rotation increment. However they could be achieved using the material rotation increment. Before proceeding with the linearisation, let us define the following perturbed quantities for the left (or spatial) translation map in the following

$$\underline{\boldsymbol{R}}_\varepsilon \coloneqq \exp(\varepsilon \underline{\boldsymbol{\theta}}) \underline{\boldsymbol{R}} \tag{B.22}$$

$$\underline{\boldsymbol{R}}_\varepsilon^T \coloneqq \underline{\boldsymbol{R}}^T \exp(-\varepsilon \underline{\boldsymbol{\theta}}) \tag{B.23}$$

Proposition B.1. The linearisation of the spatial curvature tensor is given by (equation 2.66)

$$D\underline{\boldsymbol{\omega}} \cdot \underline{\boldsymbol{\theta}} \coloneqq \left. \frac{\partial \underline{\boldsymbol{\omega}}_\varepsilon}{\partial \varepsilon} \right|_{\varepsilon=0} = \underline{\boldsymbol{\theta}}' + \underline{\boldsymbol{\theta}}\underline{\boldsymbol{\omega}} - \underline{\boldsymbol{\omega}}\underline{\boldsymbol{\theta}} \tag{B.24}$$

Proof. *Let us consider the perturbed spatial curvature tensor*

$$\underline{\boldsymbol{\omega}}_\varepsilon = \frac{\partial \underline{\boldsymbol{R}}_\varepsilon}{\partial S} \underline{\boldsymbol{R}}_\varepsilon^T$$

taking the directional derivative results in

$$\left. \frac{\partial \underline{\boldsymbol{\omega}}_\varepsilon}{\partial \varepsilon} \right|_{\varepsilon=0} = \left[\frac{\partial}{\partial S} \left(\frac{\partial \underline{\boldsymbol{R}}_\varepsilon}{\partial \varepsilon} \right) \underline{\boldsymbol{R}}_\varepsilon^T + \frac{\partial \underline{\boldsymbol{R}}_\varepsilon}{\partial S} \frac{\partial \underline{\boldsymbol{R}}_\varepsilon^T}{\partial \varepsilon} \right] \Bigg|_{\varepsilon=0}$$

using equations B.22 and B.23, leads to,

$$\left. \frac{\partial \underline{\boldsymbol{\omega}}_\varepsilon}{\partial \varepsilon} \right|_{\varepsilon=0} = \frac{\partial (\underline{\boldsymbol{\theta}} \underline{\boldsymbol{R}})}{\partial S} \underline{\boldsymbol{R}}^T + \frac{\partial \underline{\boldsymbol{R}}}{\partial S} (-\underline{\boldsymbol{R}}^T \underline{\boldsymbol{\theta}})$$

$$= \left(\frac{\partial \underline{\boldsymbol{\theta}}}{\partial S}\underline{\boldsymbol{R}}\right)\underline{\boldsymbol{R}}^T + \left(\underline{\boldsymbol{\theta}}\frac{\partial \underline{\boldsymbol{R}}}{\partial S}\right)\underline{\boldsymbol{R}}^T - \frac{\partial \underline{\boldsymbol{R}}}{\partial S}\underline{\boldsymbol{R}}^T\underline{\boldsymbol{\theta}}$$

recalling that $\underline{\boldsymbol{R}}\underline{\boldsymbol{R}}^T = \boldsymbol{I}$ *and* $(\partial \underline{\boldsymbol{R}}/\partial \boldsymbol{S})\underline{\boldsymbol{R}}^T = \underline{\boldsymbol{\omega}}$ *(equation 2.20) we obtain*

$$\left.\frac{\partial \underline{\boldsymbol{\omega}}_\varepsilon}{\partial \varepsilon}\right|_{\varepsilon=0} = \underline{\boldsymbol{\theta}}' + \underline{\boldsymbol{\theta}}\underline{\boldsymbol{\omega}} - \underline{\boldsymbol{\omega}}\underline{\boldsymbol{\theta}}$$

□

The symbol $(\cdot)'$ represents the derivative of the quantity $(\cdot)$ relative to S.

Proposition B.2. The linearisation of the material curvature tensor is given by (equation 2.67)

$$D\underline{\boldsymbol{\Omega}} \cdot \underline{\boldsymbol{\theta}} := \left.\frac{\partial \bar{\underline{\boldsymbol{\Omega}}}_\varepsilon}{\partial \varepsilon}\right|_{\varepsilon=0} = \underline{\boldsymbol{R}}^T\underline{\boldsymbol{\theta}}'\underline{\boldsymbol{R}} \tag{B.25}$$

Proof. *Let us consider the following perturbed material curvature tensor*

$$\underline{\boldsymbol{\Omega}}_\varepsilon = \underline{\boldsymbol{R}}_\varepsilon^T\frac{\partial \underline{\boldsymbol{R}}_\varepsilon}{\partial S}$$

taking the directional derivative

$$\left.\frac{\partial \underline{\boldsymbol{\Omega}}_\varepsilon}{\partial \varepsilon}\right|_{\varepsilon=0} = \frac{\partial \underline{\boldsymbol{R}}_\varepsilon^T}{\partial \varepsilon}\frac{\partial \underline{\boldsymbol{R}}_\varepsilon}{\partial S} + \underline{\boldsymbol{R}}_\varepsilon^T\left(\frac{\partial}{\partial \varepsilon}\frac{\partial \underline{\boldsymbol{R}}_\varepsilon}{\partial S}\right)$$

the derivative relative to S *of the perturbed rotation tensor is*

$$\begin{aligned}\frac{\partial \underline{\boldsymbol{R}}_\varepsilon}{\partial S} = \frac{\partial}{\partial S}[\exp(\varepsilon\underline{\boldsymbol{\theta}})\underline{\boldsymbol{R}}] &= \frac{\partial exp(\varepsilon\underline{\boldsymbol{\theta}})}{\partial S}\underline{\boldsymbol{R}} + exp(\varepsilon\underline{\boldsymbol{\theta}})\frac{\partial \underline{\boldsymbol{R}}}{\partial S} \\ &= \varepsilon\frac{\partial \underline{\boldsymbol{\theta}}}{\partial S}exp(\varepsilon\underline{\boldsymbol{\theta}})\underline{\boldsymbol{R}} + exp(\varepsilon\underline{\boldsymbol{\theta}})\frac{\partial \underline{\boldsymbol{R}}}{\partial S}\end{aligned}$$

using equations B.22 and B.23 we obtain

$$\begin{aligned}\left.\frac{\partial \underline{\boldsymbol{\Omega}}_\varepsilon}{\partial \varepsilon}\right|_{\varepsilon=0} = -\underline{\boldsymbol{R}}^T\underline{\boldsymbol{\theta}}exp(-\varepsilon\underline{\boldsymbol{\theta}})\frac{\partial \underline{\boldsymbol{R}}_\varepsilon}{\partial S} + \underline{\boldsymbol{R}}^T exp(-\varepsilon\underline{\boldsymbol{\theta}})\,[&\underline{\boldsymbol{\theta}}' exp(\varepsilon\underline{\boldsymbol{\theta}})\underline{\boldsymbol{R}} \\ &+ \varepsilon\underline{\boldsymbol{\theta}}'\underline{\boldsymbol{\theta}}exp(\varepsilon\underline{\boldsymbol{\theta}})\underline{\boldsymbol{R}} + \underline{\boldsymbol{\theta}}exp(\varepsilon\underline{\boldsymbol{\theta}})\frac{\partial \underline{\boldsymbol{R}}}{\partial S}\Big]\end{aligned}$$

making $\varepsilon = 0$ *and analysing the terms above, results in*

$$\begin{aligned}\left.\frac{\partial \underline{\boldsymbol{R}}_\varepsilon}{\partial S}\right|_{\varepsilon=0} = \frac{\partial \underline{\boldsymbol{R}}}{\partial S} - \underline{\boldsymbol{R}}^T\underline{\boldsymbol{\theta}}exp(-\varepsilon\underline{\boldsymbol{\theta}})\Big|_{\varepsilon=0} = -\underline{\boldsymbol{R}}^T\underline{\boldsymbol{\theta}}\;\underline{\boldsymbol{R}}^T exp(-\varepsilon\underline{\boldsymbol{\theta}})\Big|_{\varepsilon=0} = \\ \underline{\boldsymbol{R}}^T\left[\underline{\boldsymbol{\theta}}' exp(\varepsilon\underline{\boldsymbol{\theta}})\underline{\boldsymbol{R}} + \varepsilon\underline{\boldsymbol{\theta}}'\underline{\boldsymbol{\theta}}exp(\varepsilon\underline{\boldsymbol{\theta}})\underline{\boldsymbol{R}} + \underline{\boldsymbol{\theta}}exp(\varepsilon\underline{\boldsymbol{\theta}})\frac{\partial \underline{\boldsymbol{R}}}{\partial S}\right]\Big|_{\varepsilon=0} = \underline{\boldsymbol{\theta}}'\underline{\boldsymbol{R}} + \underline{\boldsymbol{\theta}}\frac{\partial \underline{\boldsymbol{R}}}{\partial S}\end{aligned}$$

finally we obtain the searched equation

$$\left.\frac{\partial \underline{\boldsymbol{\Omega}}_\varepsilon}{\partial \varepsilon}\right|_{\varepsilon=0} = -\underline{\boldsymbol{R}}^T\underline{\boldsymbol{\theta}}\frac{\partial \underline{\boldsymbol{R}}}{\partial S} + \underline{\boldsymbol{R}}^T\left(\underline{\boldsymbol{\theta}}'\underline{\boldsymbol{R}} + \underline{\boldsymbol{\theta}}\frac{\partial \underline{\boldsymbol{R}}}{\partial S}\right) = \underline{\boldsymbol{R}}^T\underline{\boldsymbol{\theta}}'\underline{\boldsymbol{R}}$$

□

Proposition B.3. The linearisation of the material version of the shear and axial deformations is given by (table 2.1)

$$(D\bar{\boldsymbol{\Gamma}}\cdot\bar{\boldsymbol{\eta}}_0) \coloneqq \left.\frac{\partial\bar{\boldsymbol{\Gamma}}_\varepsilon}{\partial\varepsilon}\right|_{\varepsilon=0} = \underline{\boldsymbol{R}}^T\left(\frac{\partial\bar{\boldsymbol{\eta}}_0}{\partial S} - \bar{\boldsymbol{\theta}}\times\frac{\partial\varphi_0}{\partial S}\right) \tag{B.26}$$

Proof. *Let us consider the perturbed material version of the shear and axial deformations*

$$\bar{\boldsymbol{\Gamma}}_\varepsilon = \underline{\boldsymbol{R}}_\varepsilon^T\frac{\partial\varphi_{0\varepsilon}}{\partial S} - \bar{\boldsymbol{E}}_3$$

and the following results

$$\varphi_{0\varepsilon} = \varphi_0 + \varepsilon\bar{\boldsymbol{\eta}}_0 \rightarrow \frac{\partial\varphi_{0\varepsilon}}{\partial S} = \frac{\partial\varphi_0}{\partial S} + \varepsilon\frac{\partial\bar{\boldsymbol{\eta}}_0}{\partial S} \xrightarrow{\varepsilon=0} \frac{\partial\varphi_0}{\partial S}$$

$$\underline{\boldsymbol{R}}_\varepsilon^T = \underline{\boldsymbol{R}}^T\exp[-\varepsilon\underline{\boldsymbol{\theta}}] \xrightarrow{\varepsilon=0} = \underline{\boldsymbol{R}}^T$$

taking the derivative of $\bar{\boldsymbol{\Gamma}}_\varepsilon$ *with respect to* ε *and using the above results leads to*

$$\left.\frac{\partial\bar{\boldsymbol{\Gamma}}_\varepsilon}{\partial\varepsilon}\right|_{\varepsilon=0} = \left.\left[\frac{\partial\underline{\boldsymbol{R}}_\varepsilon^T}{\partial\varepsilon}\frac{\partial\varphi_{0\varepsilon}}{\partial S} + \underline{\boldsymbol{R}}_\varepsilon^T\frac{\partial}{\partial\varepsilon}\frac{\partial\varphi_{0\varepsilon}}{\partial S}\right]\right|_{\varepsilon=0} = -\underline{\boldsymbol{R}}^T\underline{\boldsymbol{\theta}}\frac{\partial\varphi_0}{\partial S} + \underline{\boldsymbol{R}}^T\frac{\partial\bar{\boldsymbol{\eta}}_0}{\partial S}$$

therefore

$$\left.\frac{\partial\bar{\boldsymbol{\Gamma}}_\varepsilon}{\partial\varepsilon}\right|_{\varepsilon=0} = \underline{\boldsymbol{R}}^T\left(\frac{\partial\bar{\boldsymbol{\eta}}_0}{\partial S} - \bar{\boldsymbol{\theta}}\times\frac{\partial\varphi_0}{\partial S}\right)$$

where $\bar{\boldsymbol{\theta}}$ *is the axial vector associated with the skew-symmetric tensor* $\underline{\boldsymbol{\theta}}$.

□

Proposition B.4. The linearisation of the spatial version of the bending and torsional strain measures is given by (table 2.1)

$$(D\bar{\boldsymbol{\omega}}\cdot\bar{\boldsymbol{\theta}}) \coloneqq \left.\frac{\partial\bar{\boldsymbol{\omega}}_\varepsilon}{\partial\varepsilon}\right|_{\varepsilon=0} = \frac{\partial\bar{\boldsymbol{\theta}}}{\partial S} + \bar{\boldsymbol{\theta}}\times\bar{\boldsymbol{\omega}} \tag{B.27}$$

Proof. *With the aid of equation B.24 one can write*

$$(D\underline{\boldsymbol{\omega}}\cdot\underline{\boldsymbol{\theta}})\boldsymbol{h} \equiv \left.\frac{\partial(\underline{\boldsymbol{\omega}}_\varepsilon\boldsymbol{h})}{\partial\varepsilon}\right|_{\varepsilon=0} = \underline{\boldsymbol{\theta}}'\boldsymbol{h} + [\underline{\boldsymbol{\theta}}\underline{\boldsymbol{\omega}} - \underline{\boldsymbol{\omega}}\underline{\boldsymbol{\theta}}]\boldsymbol{h}$$

where $[\cdot,\cdot]$ *is the Lie bracket commutator of two skew-symmetric matrices. Now, let us consider the following equation for a given vector* $\boldsymbol{h}$

$$[\underline{\boldsymbol{\theta}},\underline{\boldsymbol{\omega}}]\boldsymbol{h} \coloneqq [\underline{\boldsymbol{\theta}}\underline{\boldsymbol{\omega}} - \underline{\boldsymbol{\omega}}\underline{\boldsymbol{\theta}}]\boldsymbol{h} = (\bar{\boldsymbol{\theta}}\times\bar{\boldsymbol{\omega}})\times\boldsymbol{h} \quad \forall\boldsymbol{h}\in\mathbb{R}^3$$

Considering $\bar{\boldsymbol{\theta}}$ *the correspondent axial vector of the skew-symmetric tensor* $\underline{\boldsymbol{\theta}}$ *leads to the relation* $\underline{\boldsymbol{\theta}}'\boldsymbol{h} = \bar{\boldsymbol{\theta}}'\times\boldsymbol{h}$. *Taking these results and the Lie bracket identity into account we obtain*

$$(D\bar{\boldsymbol{\omega}} \cdot \bar{\boldsymbol{\theta}}) \times \boldsymbol{h} = \left(\frac{\partial \bar{\boldsymbol{\theta}}}{\partial S} + \bar{\boldsymbol{\theta}} \times \bar{\boldsymbol{\omega}} \right) \times \boldsymbol{h} \quad \forall \boldsymbol{h} \in \mathbb{R}^3$$

above equation is precisely the one of proposition B.4.

□

B.4 Weak form of momentum balance

The goal of this section is demonstrate how to achieve equation 2.68 presented in section 2.2.7. We recall that $\bar{\boldsymbol{\eta}} \in T_{\varphi}\mathcal{C}$ vanishes at the boundary (see equation 2.62).

Proposition B.5. The spatial version of the weak form of momentum balance is given by

$$G(\varphi, \bar{\boldsymbol{\eta}}) \coloneqq \int_{[0,L]} \left\{ \bar{\boldsymbol{f}} \cdot \left[\frac{\partial \bar{\boldsymbol{\eta}}_0}{\partial S} - \bar{\boldsymbol{\theta}} \times \frac{\partial \varphi_0}{\partial S} \right] + \bar{\boldsymbol{m}} \cdot \frac{\partial \bar{\boldsymbol{\theta}}}{\partial S} \right\} dS - \int_{[0,L]} (\bar{\boldsymbol{q}}_{\bar{\boldsymbol{f}}} \cdot \bar{\boldsymbol{\eta}}_0 + \bar{\boldsymbol{q}}_{\bar{\boldsymbol{m}}} \cdot \bar{\boldsymbol{\theta}}) dS \quad \text{(B.28)}$$

Proof. *Let us consider equations 2.31 and 2.32 again*

$$\frac{\partial \bar{\boldsymbol{f}}}{\partial S} + \bar{\boldsymbol{q}}_{\bar{\boldsymbol{f}}} = 0$$

$$\frac{\partial \bar{\boldsymbol{m}}}{\partial S} + \frac{\partial \varphi_0}{\partial S} \times \bar{\boldsymbol{f}} + \bar{\boldsymbol{q}}_{\bar{\boldsymbol{m}}} = 0 \qquad S \in \boldsymbol{I}$$

and the arbitrary admissible variation:

$$\bar{\boldsymbol{\eta}}(S,t) \equiv (\bar{\boldsymbol{\eta}}_0(S,t), \bar{\boldsymbol{\theta}}(S,t)) \in T_{\varphi}\mathcal{C}$$

Multiplying equations above by $\bar{\boldsymbol{\eta}}(S,t)$ as a weighted residual procedure (integrating over the domain) we obtain

$$G(\boldsymbol{\varphi}, \bar{\boldsymbol{\eta}}) \coloneqq \int_{[0,L]} \left[\left(\frac{\partial \bar{\boldsymbol{f}}}{\partial S} + \bar{\boldsymbol{q}}_{\bar{\boldsymbol{f}}} \right) \cdot \bar{\boldsymbol{\eta}}_0 + \left(\frac{\partial \bar{\boldsymbol{m}}}{\partial S} + \frac{\partial \varphi_0}{\partial S} \times \bar{\boldsymbol{f}} + \bar{\boldsymbol{q}}_{\bar{\boldsymbol{m}}} \right) \cdot \bar{\boldsymbol{\theta}} \right] dS = 0 \quad \text{(B.29)}$$

Let us rewrite the first term on the right hand side of equation B.29 in the following

$$\int_0^L \left[\left(\frac{\partial \bar{\boldsymbol{f}}}{\partial S} + \bar{\boldsymbol{q}}_{\bar{\boldsymbol{f}}} \right) \cdot \bar{\boldsymbol{\eta}}_0 \right] dS = \int_0^L \left[\frac{\partial \bar{\boldsymbol{f}}}{\partial S} \cdot \bar{\boldsymbol{\eta}}_0 \right] dS + \int_0^L \left[\bar{\boldsymbol{q}}_{\bar{\boldsymbol{f}}} \cdot \bar{\boldsymbol{\eta}}_0 \right] dS$$

performing the integration by parts of the first term on the right hand side in equation above leads to

$$\int_0^L \left[\frac{\partial \bar{\boldsymbol{f}}}{\partial S} \cdot \bar{\boldsymbol{\eta}}_0 \right] dS = \cancel{[\bar{\boldsymbol{f}} \cdot \bar{\boldsymbol{\eta}}_0]_0^L} \overset{0}{} - \int_0^L \left[\bar{\boldsymbol{f}} \cdot \frac{\partial \eta_0}{\partial S} \right] dS$$

therefore we can write

$$\int_0^L \left[\left(\frac{\partial \bar{\boldsymbol{f}}}{\partial S} + \bar{\boldsymbol{q}}_{\bar{\boldsymbol{f}}}\right) \cdot \bar{\boldsymbol{\eta}}_0\right] dS = \int_0^L \left[\bar{\boldsymbol{q}}_{\bar{\boldsymbol{f}}} \cdot \bar{\boldsymbol{\eta}}_0\right] dS - \int_0^L \left[\bar{\boldsymbol{f}} \cdot \frac{\partial \bar{\boldsymbol{\eta}}_0}{\partial S}\right] dS \tag{B.30}$$

Now, let us consider the second term on the right hand side of equation B.29 and rewritte it as follows

$$\int_0^L \left[\left(\frac{\partial \bar{\boldsymbol{m}}}{\partial S} + \frac{\partial \varphi_0}{\partial S} \times \bar{\boldsymbol{f}} + \bar{\boldsymbol{q}}_{\bar{\boldsymbol{m}}}\right) \cdot \bar{\boldsymbol{\theta}}\right] dS =$$
$$\int_0^L \left[\frac{\partial \bar{\boldsymbol{m}}}{\partial S} \cdot \bar{\boldsymbol{\theta}}\right] dS + \int_0^L \left[\bar{\boldsymbol{q}}_{\bar{\boldsymbol{m}}} \cdot \bar{\boldsymbol{\theta}}\right] dS + \int_0^L \left[\left(\frac{\partial \varphi_0}{\partial S} \times \bar{\boldsymbol{f}}\right) \cdot \bar{\boldsymbol{\theta}}\right] dS$$

taking the integration by parts of the first term on the right hand side of above equation, we have

$$\int_0^L \left[\frac{\partial \bar{\boldsymbol{m}}}{\partial S} \cdot \bar{\boldsymbol{\theta}}\right] dS = \cancel{[\bar{\boldsymbol{m}} \cdot \bar{\boldsymbol{\theta}}_0]|_0^L} \overset{0}{} - \int_0^L \left[\bar{\boldsymbol{m}} \cdot \frac{\partial \bar{\boldsymbol{\theta}}}{\partial S}\right] dS$$

therefore we obtain

$$\int_0^L \left[\left(\frac{\partial \bar{\boldsymbol{m}}}{\partial S} + \frac{\partial \varphi_0}{\partial S} \times \bar{\boldsymbol{f}} + \bar{\boldsymbol{q}}_{\bar{\boldsymbol{m}}}\right) \cdot \bar{\boldsymbol{\theta}}\right] dS = -\int_0^L \left[\bar{\boldsymbol{m}} \cdot \frac{\partial \bar{\boldsymbol{\theta}}}{\partial S}\right] dS$$
$$+ \int_0^L \left[\bar{\boldsymbol{q}}_{\bar{\boldsymbol{m}}} \cdot \bar{\boldsymbol{\theta}}\right] dS + \int_0^L \left[\left(\frac{\partial \varphi_0}{\partial S} \times \bar{\boldsymbol{f}}\right) \cdot \bar{\boldsymbol{\theta}}\right] dS$$

recalling the properties of the scalar triple product (or mixed product), the following equally stands

$$\left(\frac{\partial \varphi_0}{\partial S} \times \bar{\boldsymbol{f}}\right) \cdot \bar{\boldsymbol{\theta}} = \bar{\boldsymbol{f}} \cdot \left(\bar{\boldsymbol{\theta}} \times \frac{\partial \varphi_0}{\partial S}\right)$$

therefore

$$\int_0^L \left[\left(\frac{\partial \bar{\boldsymbol{m}}}{\partial S} + \frac{\partial \varphi_0}{\partial S} \times \bar{\boldsymbol{f}} + \bar{\boldsymbol{q}}_{\bar{\boldsymbol{m}}}\right) \cdot \bar{\boldsymbol{\theta}}\right] dS = -\int_0^L \left[\bar{\boldsymbol{m}} \cdot \frac{\partial \bar{\boldsymbol{\theta}}}{\partial S}\right] dS$$
$$+ \int_0^L \left[\bar{\boldsymbol{q}}_{\bar{\boldsymbol{m}}} \cdot \bar{\boldsymbol{\theta}}\right] dS + \int_0^L \left[\bar{\boldsymbol{f}} \cdot \left(\bar{\boldsymbol{\theta}} \times \frac{\partial \varphi_0}{\partial S}\right)\right] dS \tag{B.31}$$

substituting equations B.30 and B.31 in equation B.29 and rearranging the terms, we obtain B.28.

□

APPENDIX C

PIM SHAPE FUNCTIONS EXPRESSIONS

Following the procedures described in Chapter 4 and Chapter 5, it is possible to obtain analytical solutions for the one-dimensional SPIM shape functions aiming to reduce the computation costs, hence improving the performance of the implementation.

C.1 Shape Functions

As shown in Section 5.1, the SPIM shape functions are obtained by the product between the matrix of polynomials and the inverse of the *moment matrix*:

$$\boldsymbol{\Phi}(x) = \boldsymbol{p}^T(x)\boldsymbol{P}_Q^{-1} \tag{C.1}$$

We recall that the *moment matrix* is constructed by enforcing the polynomial basis to be satisfied at each *support node*. For a *support domain* with two *support nodes* (linear shapes) the following procedure leads to the searched shape functions. The starting point is to obtain the matrix of polynomials and the *moment matrix*:

$$\boldsymbol{p}^T(x) = \begin{bmatrix} 1 & x \end{bmatrix}, \quad \boldsymbol{P}_Q = \begin{bmatrix} 1 & x_1 \\ 1 & x_2 \end{bmatrix} \tag{C.2}$$

hence, the inverse of the *moment matrix* is

$$\boldsymbol{P}_Q^{-1} = \begin{bmatrix} x_2 & -x_1 \\ -1 & 1 \end{bmatrix} \frac{1}{x_2 - x_1} \tag{C.3}$$

performing the matrix multiplication of Eq. (C.1) results in

$$\boldsymbol{\Phi}(x) = \boldsymbol{p}^T(x)\boldsymbol{P}_Q^{-1} = \begin{bmatrix} 1 & x \end{bmatrix} \begin{bmatrix} x_2 & -x_1 \\ -1 & 1 \end{bmatrix} \frac{1}{x_2 - x_1} \tag{C.4}$$

therefore the linear shape functions can be written as

$$\boldsymbol{\Phi}(x) = \begin{bmatrix} \dfrac{x_2 - x}{x_2 - x_1} & \dfrac{x - x_1}{x_2 - x_1} \end{bmatrix} \tag{C.5}$$

Similarly, for a *support domain* with three *support nodes* (quadratic shapes) the following procedure leads to the searched shape functions. The matrix of polynomials and the *moment matrix* are the following

$$\boldsymbol{p}^T(x) = \begin{bmatrix} 1 & x & x^2 \end{bmatrix}, \quad \boldsymbol{P}_Q = \begin{bmatrix} 1 & x_1 & x_1^2 \\ 1 & x_2 & x_2^2 \\ 1 & x_3 & x_3^2 \end{bmatrix} \tag{C.6}$$

the inverse of the *moment matrix* is

$$\boldsymbol{P}_Q^{-1} = \begin{bmatrix} -\dfrac{x_2 x_3}{(x_2 - x_3)} & \dfrac{x_1 x_3}{(x_1 - x_3)} & -\dfrac{x_1 x_2}{(x_1 - x_2)} \\ (x_2 + x_3)(x_2 - x_3) & -(x_1 + x_3)(x_1 - x_3) & (x_1 + x_2)(x_1 - x_2) \\ (x_3 - x_2) & (x_1 - x_3) & (x_2 - x_1) \end{bmatrix} \frac{1}{\det[\boldsymbol{P}_Q]} \tag{C.7}$$

where

$$\det[\boldsymbol{P}_Q] = \frac{1}{(x_2 - x_1)(x_1 - x_3)(x_2 - x_3)} \tag{C.8}$$

Hence, performing the matrix multiplication of Eq. (C.1) results in

$$\boldsymbol{\Phi}(x) = \begin{bmatrix} \dfrac{(x - x_2)(x - x_3)}{(x_1 - x_2)(x_1 - x_3)} & -\dfrac{(x - x_1)(x - x_3)}{(x_1 - x_2)(x_2 - x_3)} & \dfrac{(x - x_1)(x - x_2)}{(x_1 - x_3)(x_2 - x_3)} \end{bmatrix} \tag{C.9}$$

Lastly, for a *support domain* with four *support nodes* (cubic shapes), following the principles described above leads to the searched shape functions:

$$\boldsymbol{\Phi}(x) = \boldsymbol{p}^T(x)\boldsymbol{P}_Q^{-1} = \begin{bmatrix} \phi_1(x) & \phi_2(x) & \phi_3(x) & \phi_4(x) \end{bmatrix} \tag{C.10}$$

with the components of Eq. (C.10) explicit represented as follows

$$\phi_1(x) = \frac{(x - x_2)(x - x_3)(x - x_4)}{(x_1 - x_2)(x_1 - x_3)(x_1 - x_4)} \tag{C.11}$$

$$\phi_2(x) = -\frac{(x - x_1)(x - x_3)(x - x_4)}{(x_1 - x_2)(x_2 - x_3)(x_2 - x_4)} \tag{C.12}$$

$$\phi_3(x) = \frac{(x - x_1)(x - x_2)(x - x_4)}{(x_1 - x_3)(x_2 - x_3)(x_3 - x_4)} \tag{C.13}$$

$$\phi_4(x) = -\frac{(x - x_1)(x - x_2)(x - x_3)}{(x_1 - x_4)(x_2 - x_4)(x_3 - x_4)} \tag{C.14}$$

In Figure C.1 the shape functions are represented graphically for each set of *support*

nodes containing two, three and four nodes in it.

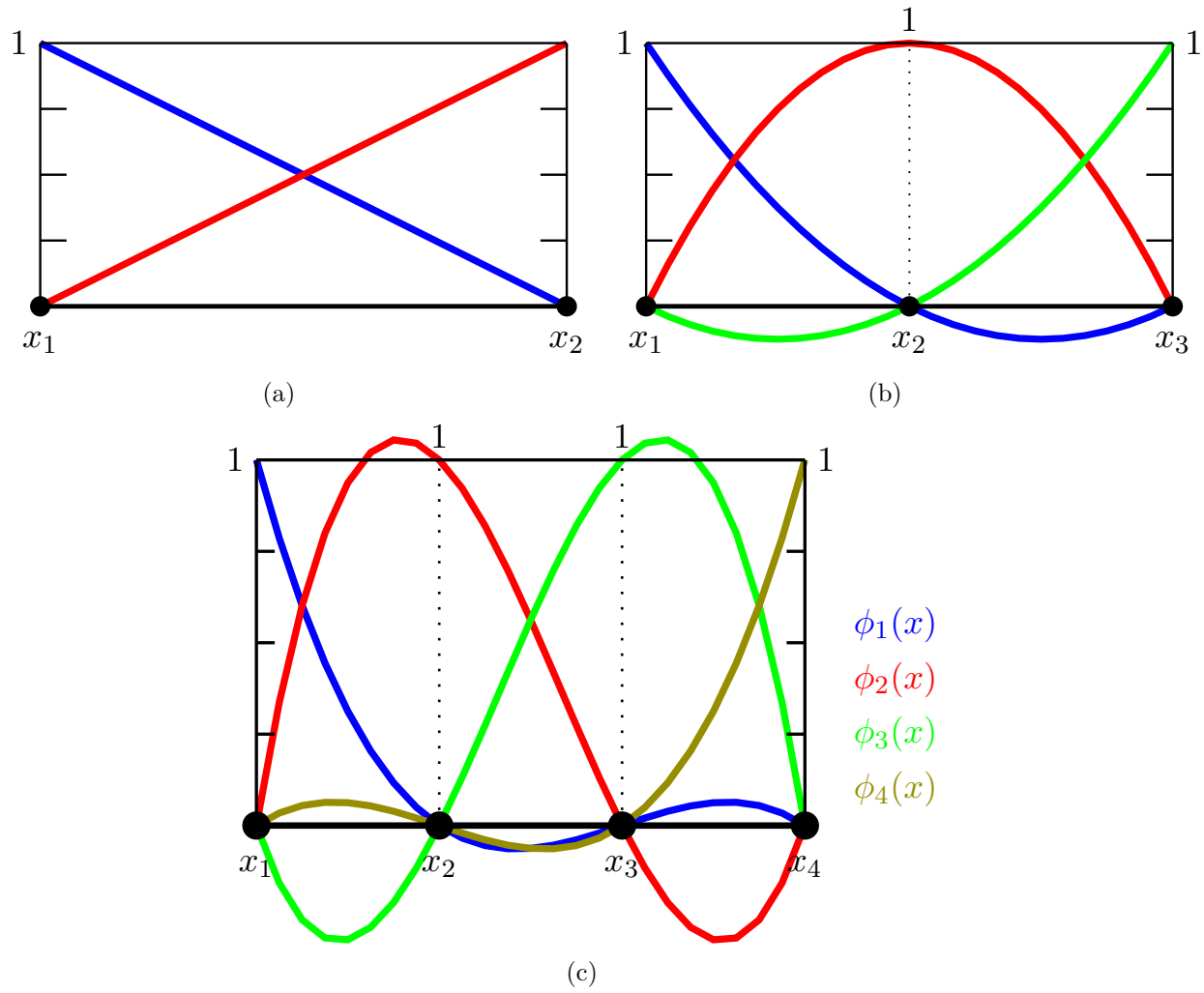

Figure C.1: SPIM shape functions

In order to illustrate the discontinuities of PIM shape functions, a beam with four evenly distributed nodes is considered in Fig. C.2a. A node-based tessellation (see Section 5.3) is constructed giving rise to four smoothing domains. For the boundary smoothing domains, the two extreme nodes are chosen to compose the nodes of the *support domain*, while for interior smoothing domains, three nodes are selected as *support nodes*, which are the center node and the nodes from the *left* and *right* sides of the smoothing domain. This process can be referred as mixed linear-quadratic interpolation (Liu and Zhang, 2013). After constructing all shape functions for each smoothing domain, the outcome is shown in Fig. C.2a. The dotted vertical lines are delimiting the node-based smoothing domains, and the discontinuities can be identified on the smoothing domain boundaries. In Fig. C.2b, for the same domain discretisation, the shape function corresponding to the node x_2 is illustrated for the edge-based approach. Different from the node-based tessellation, in this case the discontinuities are within the smoothing domains.

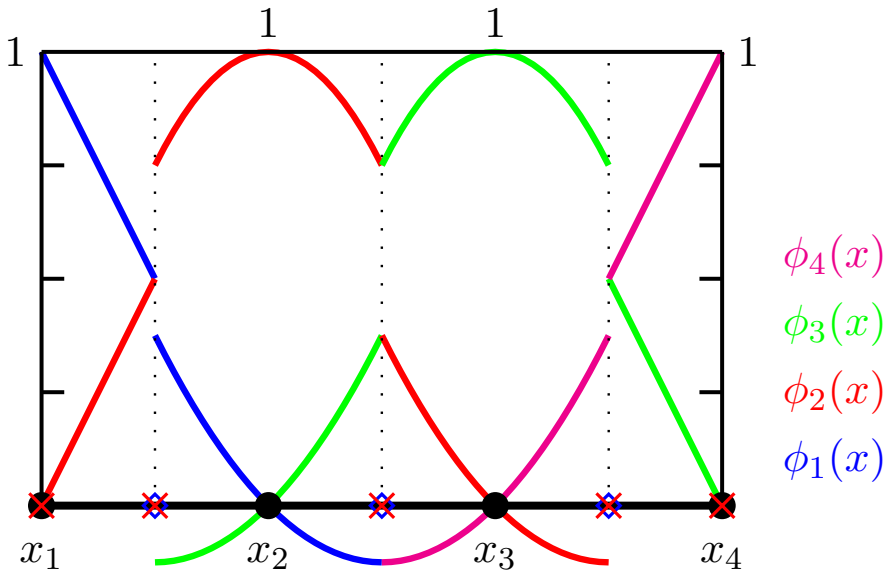

(a) Node-based

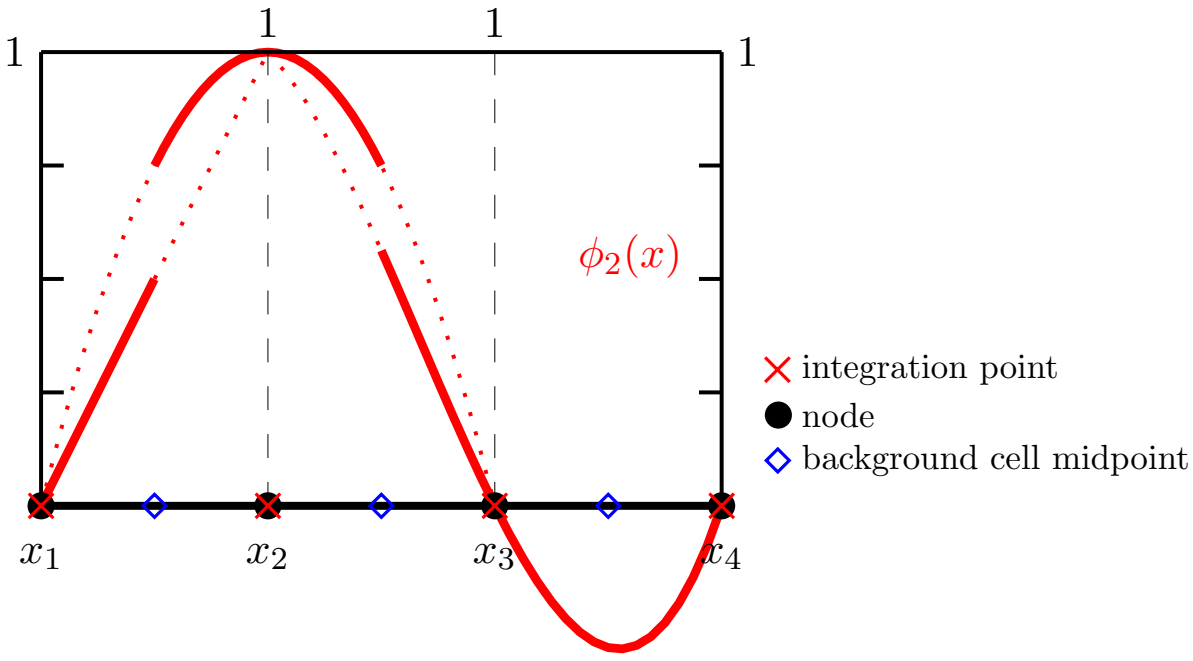

(b) Edge-based

Figure C.2: Shape functions discontinuity example

The procedure illustrated above to obtain the analytical shape functions was performed through the MATLAB® software.

APPENDIX D

ANALYTICAL SOLUTIONS FOR THE TIMOSHENKO BEAM

In this appendix, a methodology[1] to derive the analytical solutions for the Timoshenko beam is presented. These analytical solutions were used to enhance the numerical simulations analysis shown in Chapter 6. In the following, a *homogeneous prismatic* beam is considered, as a consequence the Young's modulus E, the shear modulus G, and the inertia moment I are constants.

D.1 Distributed loads

In order to obtain the searched expressions, first of all the problem governing differential equations (Eq. (2.3) and Eq. (2.4)) are recalled:

$$\frac{\partial}{\partial x}\left(EI\frac{\partial \theta}{\partial x}\right) + GA_s\left(\frac{\partial v}{\partial x} - \theta\right) = 0 \tag{D.1}$$

$$\frac{\partial}{\partial x}\left(GA_s\left(\frac{\partial v}{\partial x} - \theta\right)\right) = -q_y(x) \tag{D.2}$$

with the aid of Fig. 2.1 and under the kinematics, equilibrium and constitutive assumptions of the model, one can show that the following relations are valid for the Timoshenko beam theory (see Öchsner and Merkel (2018)).

$$\frac{\partial Q_y}{\partial x} = q_y, \quad \frac{\partial M}{\partial x} = -Q_y \tag{D.3}$$

$$M = EI\frac{\partial \theta}{\partial x}, \quad Q_y = -k_s GA\gamma \tag{D.4}$$

where Q_y and M are the applied shearing forces and bending moments, respectively, A is the beam cross-section area, $A_s = k_s A$ is the shearing area, and k_s is the shearing factor. Substituting equations D.3 and D.4 in the problem governing differential equations (Eq. (D.1) and Eq. (D.2)) results in

[1] The procedure shown in this appendix was based on the work of Fleischfresser (2012).

$$EI\frac{\partial^2\theta}{\partial x^2} - GA_s\theta + GA_s\frac{\partial v}{\partial x} = 0 \tag{D.5}$$

$$EI\frac{\partial^3\theta}{\partial x^3} = q_y \tag{D.6}$$

above equations can be recasted in a compacted form as follows

$$EI\theta'' - GA_s\theta + GA_s v' = 0 \tag{D.7}$$

$$EI\theta''' = q_y \tag{D.8}$$

next, equation D.8 is integrated successively

$$\begin{aligned} EI\theta'' &= q_y x + C_1 \\ EI\theta' &= \frac{q_y}{2}x^2 + C_1 x + C_2 \\ EI\theta &= \frac{q_y}{6}x^3 + \frac{C_1}{2}x^2 + C_2 x + C_3 \end{aligned} \tag{D.9}$$

therefore the *rotations* can be expressed as

$$\theta = \frac{1}{EI}\left(\frac{q_y}{6}x^3 + \frac{C_1}{2}x^2 + C_2 x + C_3\right) \tag{D.10}$$

With the aid of equations D.10, Equation D.7 can be rewritten as

$$GA_s v' = \frac{GA_s}{EI}\left(\frac{q_y}{6}x^3 + \frac{C_1}{2}x^2 + C_2 x + C_3\right) - EI\left(q_y x + C_1\right) \tag{D.11}$$

integrating above equation results in

$$GA_s v = \frac{GA_s}{EI}\left(\frac{q_y}{24}x^4 + \frac{C_1}{6}x^3 + \frac{C_2}{2}x^2 + C_3 x\right) - \left(\frac{q_y}{2}x^2 + C_1 x\right) + C_4 \tag{D.12}$$

therefore the *displacements* can be expressed as

$$v = \frac{1}{EI}\left(\frac{q_y}{24}x^4 + \frac{C_1}{6}x^3 + \frac{C_2}{2}x^2 + C_3 x\right) - \frac{1}{GA_s}\left(\frac{q_y}{2}x^2 + C_1 x - C_4\right) \tag{D.13}$$

Taking into account the boundary conditions shown in Fig. D.1, the following equations for shearing forces, bending moments, rotations and displacements, in the following, can be used to determine the unknown constants C_1, C_2, C_3 and C_4:

$$\boxed{EI\theta'' = -Q_y = (q_y x + C_1)} \tag{D.14}$$

$$\boxed{EI\theta' = M = \left(\frac{q_y}{2}x^2 + C_1 x + C_2\right)} \tag{D.15}$$

$$\boxed{\theta = \frac{1}{EI}\left(\frac{q_y}{6}x^3 + \frac{C_1}{2}x^2 + C_2 x + C_3\right)} \tag{D.16}$$

$$\boxed{v = \frac{1}{EI}\left(\frac{q_y}{24}x^4 + \frac{C_1}{6}x^3 + \frac{C_2}{2}x^2 + C_3 x\right) - \frac{1}{GA_s}\left(\frac{q_y}{2}x^2 + C_1 x - C_4\right)} \tag{D.17}$$

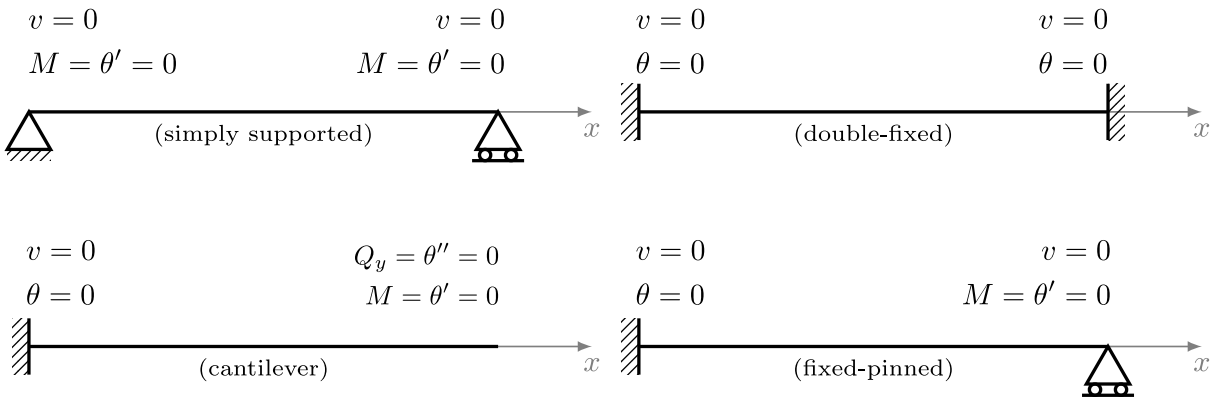

Figure D.1: Beam boundary conditions

Equations Eqs. (D.14) to (D.17) were derived for an uniformly distributed load, however the procedure is analogous for any type of distributed load over the beam span. It suffices to substitute q_y for the desired $q(x)$ at the beginning of the process. For instance, let us consider a linearly distributed load defined by $q(x) = ax + b$. Equation D.8 is rewritten with the new load function, and it is integrated successively:

$$\begin{aligned} EI\theta'' &= \left(\frac{a}{2}x^2 + bx\right) + C_1 \\ EI\theta' &= \left(\frac{a}{6}x^3 + \frac{b}{2}x^2\right) + C_1 x + C_2 \\ EI\theta &= \left(\frac{a}{24}x^4 + \frac{b}{6}x^3\right) + \frac{C_1}{2}x^2 + C_2 x + C_3 \end{aligned} \tag{D.18}$$

therefore the *rotations* can be expressed as

$$\boxed{\theta = \frac{1}{EI}\left[\left(\frac{a}{24}x^4 + \frac{b}{6}x^3\right) + \frac{C_1}{2}x^2 + C_2 x + C_3\right]} \tag{D.19}$$

with the aid of equations D.19, Equation D.7 can be rewritten as

$$GA_s v' = \frac{GA_s}{EI}\left[\left(\frac{a}{24}x^4 + \frac{b}{6}x^3\right) + \frac{C1}{2}x^2 + C_2 x + C_3\right] - \left[\left(\frac{a}{2}x^2 + bx\right) + C_1\right] \tag{D.20}$$

integrating above equation results in

$$\begin{aligned} GA_s v = \frac{GA_s}{EI}&\left[\left(\frac{a}{120}x^5 + \frac{b}{24}x^4\right) + \frac{C1}{6}x^3 + \frac{C2}{2}x^2 + C_3 x\right] \\ &- \left[\left(\frac{a}{6}x^3 + \frac{b}{2}x^2\right) + C_1 x\right] + C_4 \end{aligned} \tag{D.21}$$

therefore the *displacements* can be expressed as

$$\boxed{\begin{aligned} v = \frac{1}{EI}&\left[\left(\frac{a}{120}x^5 + \frac{b}{24}x^4\right) + \frac{C1}{6}x^3 + \frac{C2}{2}x^2 + C_3 x\right] \\ &- \frac{1}{GA_s}\left[\left(\frac{a}{6}x^3 + \frac{b}{2}x^2\right) + C_1 x - C_4\right] \end{aligned}} \tag{D.22}$$

Besides being more complex, the equations Eq. (D.19) and Eq. (D.22) possess the same number of unknown constants as the uniformly distributed load, hence the same boundary conditions illustrated in Fig. D.1 can be used to determine these constants. In order to illustrate the methodology shown above, the following example is considered.

Example 1: Derive the analytical solutions of *rotations* and *displacements* for the simply supported beam shown in Fig. D.2.

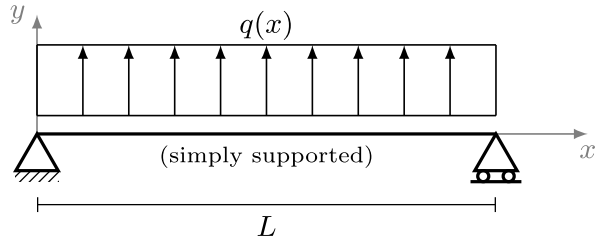

Figure D.2: Simply supported beam: distributed load case

Solution:

Based in Fig. D.1, if $x = 0$, then $M = 0$. Entering these values in equation D.15 leads to $\boxed{C_2 = 0}$. At the same point $v = 0$, hence from equation D.17 results in $\boxed{C_4 = 0}$. Another boundary conditions is in $x = L$, where $M = 0$. Substituting these values in equation D.15 results in

$$\frac{q_y}{2}L^2 + C_1 L = 0 \rightarrow \boxed{C_1 = -\frac{q_y L}{2}}$$

The last condition is if $x = L$, then $v = 0$. Substituting these values in equation D.17 and using the *known* constants (C_1, C_2 and C_4) leads to:

$$\begin{aligned}
0 &= \frac{1}{EI}\left[\frac{q_y}{24}L^4 + \left(-\frac{q_y L}{2}\right)\frac{1}{6}L^3 + C_3 L\right] - \frac{1}{GA_s}\left[\frac{q_y}{2}L^2 + \left(-\frac{q_y L}{2}\right)L\right] \\
0 &= \frac{1}{EI}\left[\frac{q_y}{24}L^4 - \frac{q_y}{12}L^4 + C_3 L\right] + 0 \\
0 &= \frac{1}{EI}\left[-\frac{q_y}{24}L^4 + C_3 L\right] \rightarrow \boxed{C_3 = \frac{q_y L^3}{24}}
\end{aligned}$$

Finally, substituting the constants C_1, C_2, C_3 and C_4 in equations D.16 and D.17 results in the following analytical expressions for the *rotations* and *displacements*:

$$\boxed{\theta = \frac{q_y}{24EI}\left(4x^3 - 6x^2 + L^3\right)} \tag{D.23}$$

$$\boxed{v = \frac{q_y}{24EI}\left(x^4 - 2Lx^3 + 3L^3 x\right) + \frac{q_y}{2GA_s}\left(-x^2 + Lx\right)} \tag{D.24}$$

D.2 Force loads

In this section, a methodology to obtain the analytical expressions of rotations and displacements for a force load case is illustrated. A generic force load applied in a point a at the beam span is considered. The procedure to obtain the searched expressions is a little different from the distributed load cases. First, from D.7 and D.8, the starting problem differential equations are rewritten as

$$Q_y = GA_s\left(v' - \theta\right) \tag{D.25}$$

$$EI\theta'' = -Q_y \tag{D.26}$$

In this type of problem, due to the applied load at a particular position within the beam span, two analysis are necessary. The first one is performed before the load position, while the second on is performed after it. Hence, the number of *unknown* constants naturally increase. However, taking advantage of the continuity of the beam, a set of new conditions can be established to overcome this inconvenient. Aside from the ones shown in Fig. D.1, the following conditions can be used at the point a

$$\begin{aligned} \theta_1'(a) &= \theta_2'(a) \quad \text{from the conituity of } \textit{bending moments} \\ \theta_1(a) &= \theta_2(a) \quad \text{from the conituity of } \textit{rotations} \\ v_1(a) &= v_2(a) \quad \text{from the conituity of } \textit{displacements} \end{aligned} \tag{D.27}$$

where the sub-index 1 indicates the patch *before* the load position a, while the sub-index 2 refers to the patch *after* it.

Example 2: Derive the analytical solutions for the *rotations* and *displacements* of the cantilever beam shown in Fig. D.3.

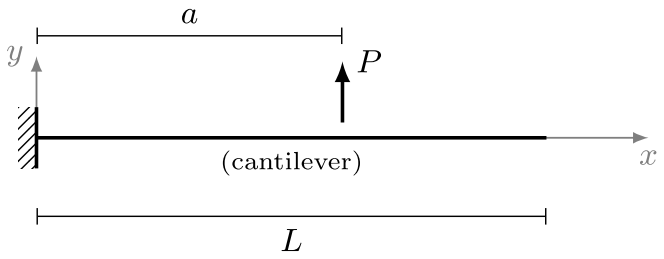

Figure D.3: Cantilever beam: force load case

Solution:

Before the load P: $x \in [0\ a]$

First, equation D.26 is integrated successively:

$$\begin{aligned} EI\theta_1' &= -Q_{1y}x + C_1 \\ EI\theta_1 &= -\frac{Q_{1y}}{2}x^2 + C_1x + C_2 \end{aligned} \tag{D.28}$$

when $x = 0$, $\theta_1 = 0$, hence from equation above $\boxed{C_2 = 0}$.

Now, equation D.25 is rearranged and integrated:

$$\begin{aligned} v_1' &= -\frac{Q_{1y}}{2EI}x^2 + \frac{C_1}{EI}x + \frac{Q_{1y}}{GA_s} \\ v_1 &= -\frac{Q_{1y}}{6EI}x^3 + \frac{C_1}{2EI}x^2 + \frac{Q_{1y}}{GA_s}x + C_3 \end{aligned} \tag{D.29}$$

again, when $x = 0$, $v_1 = 0$, hence from equation above $\boxed{C_3 = 0}$.

After the load P: $x \in [a\ L]$

Similarly, equation D.26 is integrated successively:

$$\begin{aligned} EI\theta_2' &= -Q_{2y}x + C_4 \\ EI\theta_2 &= -\frac{Q_{2y}}{2}x^2 + C_4 x + C_5 \end{aligned} \tag{D.30}$$

When $x = L$, $\theta_2' = 0$, hence from the first equation above $\boxed{C_4 = Q_{2y}L}$. However, Q_2 must be zero in the second patch, therefore $Q_2 = C_4 = 0$ and $Q_1 = P$. Therewith, equation D.26 becomes simply:

$$v_2' = \frac{C_5}{EI} \tag{D.31}$$

integrating above equation results in

$$v_2 = \frac{C_5}{EI}x + C_6 \tag{D.32}$$

In order to obtain the remaining constants, the conditions of continuity in $x = a$ can be used.

First, the *bending moments* are equal in $x = a$:

$$\theta_1'(a) = \theta_2'(a) \rightarrow \frac{1}{EI}\left(-Q_{1y}a + C_1\right) = 0 \quad \therefore \boxed{C_1 = Pa} \tag{D.33}$$

next, the *rotations* are equal in $x = a$:

$$\theta_1(a) = \theta_2(a) \rightarrow -\frac{P}{2EI}a^2 + \frac{Pa}{EI}a = \frac{C_5}{EI} \quad \therefore \boxed{C_5 = \frac{P}{2}a^2} \tag{D.34}$$

now, the *displacements* are equal in $x = a$:

$$\begin{aligned} v_1(a) = v_2(a) \rightarrow -\frac{P}{6EI}a^3 + \frac{Pa}{2EI}a^2 + \frac{P}{GA_s}a = \frac{Pa^2}{2EI}a + C_6 \\ \therefore \boxed{C_6 = -\frac{P}{6EI}a^3 + \frac{P}{GA_s}} \end{aligned} \tag{D.35}$$

Finally, the expressions for rotations and displacements are obtained after substituting the constants in the correspondent equations. As result, the *rotations* and *displacements* are the following expressions defined by parts:

$$\theta(x) = \begin{cases} \dfrac{1}{EI}\left(-\dfrac{P}{2}x^2 + Pax\right) & x \in [0\ a] \\ \\ \dfrac{P}{2EI}a^2 & x \in [a\ L] \end{cases} \tag{D.36}$$

$$v(x) = \begin{cases} \dfrac{P}{6EI}\left(-x^3 + 3ax^2\right) + \dfrac{P}{GA_s}x & x \in [0\ a] \\ \\ \dfrac{Pa^2}{6EI}\left(3x - a\right) + \dfrac{Pa}{GA_s} & x \in [a\ L] \end{cases} \tag{D.37}$$

Based on the procedures shown throughout this appendix, the analytical expressions for the *rotations* and *displacements* regarding the Timoshenko beam model, were obtained for the point force, uniformly distributed and linearly distributed load cases applied in all boundary conditions shown in Fig. D.1.

APPENDIX E

ALPHA TABLES

In the following tables, the plots shown in Figs. 6.20 to 6.23 (*right plots*) are represented through their numerical values, i.e. the actual values of the estimated alpha parameters according to the number of nodes. In all tables which alpha varies with the slenderness ratio (h/L) are explicit indicated.

E.1 Simply supported beam

Mesh	Alpha	Mesh	Alpha
5	0.625730994152046	41	0.661912308501584
11	0.646799116997489	47	0.662540119296967
17	0.654520917680695	53	0.663021465283246
23	0.657920310947208	95	0.664659959295801
29	0.659832953718178	191	0.665676197431680
35	0.661059190444920	383	0.666186733535444

Table E.1: Force load

Mesh	Alpha	Mesh	Alpha
5	0.317333333333325	41	0.342274292189959
11	0.352750809062166	47	0.341271694335000
17	0.350459879480149	53	0.340467694849007
23	0.347489046122188	95	0.337494552471722
29	0.345234366979236	191	0.335457286161415
35	0.343554799357901	383	0.334438272729140

Table E.2: Uniformly distributed load

Mesh	Alpha	Mesh	Alpha
5	0.317333333333314	41	0.342274292163100
11	0.352750809060498	47	0.341271694492765
17	0.350459879476329	53	0.340467694988065
23	0.347489046119782	95	0.337494562185642
29	0.345234366987607	191	0.335457506136241
35	0.343554799329244	383	0.334436300026086

Table E.3: Linearly distributed load

E.2 Fixed-fixed beam

Mesh	Alpha	Mesh	Alpha
5	0.625730994152047	41	0.661912308480469
11	0.646799116997752	47	0.662540119133596
17	0.654520917678483	53	0.663021465999079
23	0.657920310979023	95	0.664659977706902
29	0.659832953689419	191	0.665676822272606
35	0.661059190114914	383	0.666177675219863

Table E.4: Force load

Mesh	Alpha	Mesh	Alpha
5	0.658666666666668	41	0.671137146063260
11	0.676375404530718	47	0.670635847066161
17	0.675229939739555	53	0.670233848346730
23	0.673744523084864	95	0.668747303720630
29	0.672617183431079	191	0.667729641249653
35	0.671777399293255	383	0.667206820633372

Table E.5: Uniformly distributed load

Mesh	Alpha	Mesh	Alpha
5	0.658666666666671	41	0.671137146065082
11	0.676375404530735	47	0.670635847070440
17	0.675229939739634	53	0.670233848411683
23	0.673744523085746	95	0.668747304316187
29	0.672617183430300	191	0.667729653519156
35	0.671777399287819	383	0.667206517158981

Table E.6: Linearly distributed load

E.3 Cantilever beam

Mesh	Alpha	Mesh	Alpha
5	0.690821256038911	41	0.669250646304116
11	0.676767676770099	47	0.668915884126875
17	0.673052362751302	53	0.668657910816459
23	0.671335200723898	95	0.667771188137824
29	0.670345842252864	191	0.667214436541085
35	0.669702489460423	383	0.666948465566915

Table E.7: Force load

Mesh	Alpha	Mesh	Alpha
5	0.787198669991778	41	0.779921253175297
11	0.784424683374650	47	0.779660799296509
17	0.782520972726283	53	0.779456595934448
23	0.781428168212960	95	0.778731473171188
29	0.780737633119671	191	0.778257912978723
35	0.780264689515928	383	0.778021247737339

Table E.8: Uniformly distributed load

Mesh	Alpha	Mesh	Alpha
5	0.839309567981347	41	0.839594131903283
11	0.842642261618775	47	0.839367000403874
17	0.841621379459191	53	0.839186501860373
23	0.840830300899719	95	0.838529529030538
29	0.840281656121307	191	0.838088021425181
35	0.839888058248994	383	0.837864491567394

Table E.9: Linearly distributed load: $h/L = 0.10$

Mesh	Alpha	Mesh	Alpha
5	0.833560282587747	41	0.833748017805211
11	0.837037524520309	47	0.833503716698985
17	0.835930913373028	53	0.833309593595937
23	0.835078310120062	95	0.832603104317794
29	0.834487704333950	191	0.832127882542743
35	0.834064202223725	383	0.831885281301689

Table E.10: Linearly distributed load: $h/L = 0.50$

Mesh	Alpha	Mesh	Alpha
5	0.812608349026056	41	0.812379336449734
11	0.816627085297122	47	0.812066959650932
17	0.815179297442153	53	0.811818795514927
23	0.814082748445449	95	0.810915896641854
29	0.813325818688778	191	0.810308746327780
35	0.812783769574460	383	0.809999946268061

Table E.11: Linearly distributed load: $h/L = 1.00$

E.4 Fixed-pinned beam

Mesh	Alpha	Mesh	Alpha
5	0.633414596283830	41	0.662809138555847
11	0.650508025770618	47	0.663318831311630
17	0.656800835009432	53	0.663709551121989
23	0.659565897853724	95	0.665039148077435
29	0.661120301876204	191	0.665863854105215
35	0.662116372762056	383	0.666271303816654

Table E.12: Force load

Mesh	Alpha	Mesh	Alpha
5	0.588530667935364	41	0.599742143907526
11	0.606168164415925	47	0.599169816777263
17	0.604535846110522	53	0.598712093375434
23	0.602758370125353	95	0.597027524796216
29	0.601444257525700	191	0.595880158791093
35	0.600475943184836	383	0.595294333099830

Table E.13: Uniformly distributed load: $h/L = 0.10$

Mesh	Alpha	Mesh	Alpha
5	0.549286408764475	41	0.562577864595384
11	0.569594915918963	47	0.561941716884377
17	0.567871921699315	53	0.561432602144949
23	0.565919281990305	95	0.559556609262005
29	0.564466279965028	191	0.558276848924293
35	0.563392689189962	383	0.557628532728131

Table E.14: Uniformly distributed load: $h/L = 0.50$

Mesh	Alpha	Mesh	Alpha
5	0.473930326500457	41	0.491299892006021
11	0.499439523812470	47	0.490541467022039
17	0.497550055351868	53	0.489933862895325
23	0.495263543939139	95	0.487690854330726
29	0.493544998874189	191	0.486156971449634
35	0.492269899726791	383	0.485395934750166

Table E.15: Uniformly distributed load: $h/L = 1.00$

Mesh	Alpha	Mesh	Alpha
5	0.632453306615516	41	0.646138200106682
11	0.651626784129163	47	0.645607882510319
17	0.650446342157357	53	0.645182321519640
23	0.648888530685320	95	0.643606600030137
29	0.647701246403728	191	0.642526080159721
35	0.646814882950922	383	0.641971261374838

Table E.16: Linearly distributed load: $h/L = 0.10$

Mesh	Alpha	Mesh	Alpha
5	0.588066859793833	41	0.603766059616003
11	0.609946108348508	47	0.603165335193207
17	0.608636830173392	53	0.602683185692452
23	0.606878581330575	95	0.600897362768277
29	0.605535708247047	191	0.599672120097625
35	0.604532374275632	383	0.599047697176292

Table E.17: Linearly distributed load: $h/L = 0.50$

Mesh	Alpha	Mesh	Alpha
5	0.501611729984496	41	0.520992868539790
11	0.528531795156330	47	0.520256722766794
17	0.526954605245675	53	0.519665829166083
23	0.524805032412456	95	0.517476935476974
29	0.523160863467894	191	0.515974399414162
35	0.521931806383839	383	0.515224051030151

Table E.18: Linearly distributed load: $h/L = 1.00$